



Università Politecnica delle Marche
Scuola di Dottorato di Ricerca in Scienze dell'Ingegneria
Curriculum in Ingegneria Civile, Ambientale, Edile e Architettura

**Experimental and numerical characterisation of the
mechanical properties of the
titanium alloy-lightweight concrete interface**

PhD Dissertation of:
Diletta Maracci

Advisor:
Prof. Stefano Lenci

Curriculum supervisor:
Prof. Stefano Lenci

XXXI edition

Università Politecnica delle Marche
Dipartimento di Ingegneri Civile, Ambientale, Edile e Architettura
Via Brezze Bianche – 60131, Ancona, Italy

Acknowledgments

I would like to acknowledge Calvi S.p.A. for funding part of my PhD and providing the material for the tests. In particular, I would express my gratitude to Eng. Alessandro Fendoni, who has always supported my work and spent time on this research, despite his many commitments.

I would like to thank TiFast s.r.l. for providing part of the material used for the experiments and Eng. Marco Costanzi, whose profound expertise and knowledge in the field of titanium helped me in this new topic.

I would like to thank also Eng. Massimo Belcecchi, who conceived first the main idea of this research and cooperated during these three years.

Further, I want to thank So.Mi s.r.l. and, particularly, Eng. Michele Mingo. His patience and kindness, as well as his expertise and knowledge, were fundamental for realising the fibres used in this work.

Many thanks also to the Department of Materials, Environmental Sciences and Urban Planning of Università Politecnica delle Marche. Particularly, I would like to acknowledge Prof. Giacomo Moriconi, Prof. Tiziano Bellezze, Eng. Ph.D Jacopo Donnini, and, particularly, Roberto Mancini. Their contribution was fundamental for carrying out the experimental tests.

I would like to thank Prof. Stefano Lenci for giving me the opportunity to attend the PhD under his supervision, for the trust demonstrated and for his stimulating cooperation.

I would like to express my gratitude to Prof. Giulio Alfano for allowing me to live a great experience at Brunel University in London. His constant supervision, his patience in explaining me new concepts, and his knowledge and professionalism were essential to develop some concepts of this research.

I would like to sincerely thank Prof. Roberto Serpieri for his extreme professionalism and expertise and, especially, for his constant help during the last year.

And last, but not least, I would like to thank Susanna with all my heart, for supporting, encouraging, and reassuring me more than everyone. Without her, I would not have been able to get to the end of this journey.

Abstract

The possibility to use titanium as alternative reinforcement for concrete is investigated in this thesis by focusing on the interfacial behaviour that the two materials develop when they are combined in a composite structural material. Therefore, experimental and numerical characterisation of the structural interface between titanium alloys and concrete is addressed in this research. To this end, several experimental programs were conducted. The first one concerns the pull-out behaviour of plain bars made of the titanium alloy Ti6Al4V from two different concrete mixtures, i.e. Normal and Light Weigh Concrete (NWC and LWC, respectively). The second experimental program investigates the pull-out behaviour of Ti6Al4V fibres from LWC specimens. Straight and Hooked-end configurations were tested in order to quantify the contribution of the geometrical deformation on the bond performance. Straight fibres and plain bars bond behaviour is compared, leading to the conclusion that, although the size effect is present, the micro-mechanisms acting at the interface during debonding are the same. The third and last series of experiments regards the fracture toughness characterisation of a fibre reinforced concrete material made of LWC and titanium fibres. In this case, fibres of two titanium alloys are tested for the distributed reinforcement phase, i.e. the alloy Ti6Al4V (Titanium Grade 5) and the unalloyed titanium (Titanium Grade 2), realising Ti-gr5FRC and Ti-gr2FRC respectively. Three-point bending tests on standardised specimens demonstrate that Ti-gr5FRC has better performance than Ti-gr2FRC in terms of flexural strength peak and residual values. Therefore, a full-scale beam made of Ti-gr5FRC, without any other reinforcement, has been built and tested under three-point load conditions in order to measure the size effect on the flexural strength.

The experimental results concerning the pull-out tests are supported by Finite Element (FE) analyses. Particularly, the results of the bar pull-out tests, combined with Scanning Electron Microscope (SEM) analyses, show that, although the employed rebars are plain, the debonding process is strongly affected by defects-induced surface roughness present at the microscopic level, which activates mechanical interlocking responsible for the dilatant behaviour of the interface. Therefore, a novel Cohesive Zone Model micromechanics-based formulation is implemented in the FE model in order to account for such aspects. The introduced *enhanced degrading M-CZM*, accounting for damage, friction, mechanical interlocking and dilatancy, is used to carry out sensitivity analyses and identification procedures on the FE models simulating the bar pull-out tests. The proposed modelling strategy is further validated by performing FE simulation of straight fibres pull-out tests.

The obtained results demonstrate that the *enhanced degrading M-CZM* is capable of describing and explaining the pull-out mechanisms under different conditions, underlining differences among bars and fibres that are consistent with the physics of the phenomena. In fact, FE analyses are here considered a tool to better understand the interfacial micromechanisms acting at the reinforcement-matrix interface during debonding processes.

Sommario

La possibilità di utilizzare il titanio come materiale alternativo per il rinforzo del calcestruzzo è stata affrontata in questa tesi dal punto di vista del comportamento di interfaccia che i due materiali sviluppano quando sono combinati in un materiale composito strutturale. La tesi si occupa dunque della caratterizzazione delle proprietà meccaniche dell'interfaccia titanio-calcestruzzo, sia sperimentalmente che numericamente. A tal fine sono state eseguite diverse campagne sperimentali. La prima riguarda prove di sfilamento di barre lisce in lega di titanio Ti6Al4V da provini di due diverse tipologie di calcestruzzo: di peso normale e alleggerito (rispettivamente NWC e LWC). La seconda serie di prove consiste in prove di sfilamento di fibre della stessa lega di titanio (Ti6Al4V) da provini in calcestruzzo alleggerito. In questo caso sono state realizzate e testate fibre di due diverse configurazioni geometriche, rispettivamente dritte e doppiamente uncinato alle estremità. Questo al fine di avere un termine di paragone tra il comportamento di interfaccia di barre e fibre nel caso delle fibre dritte e di quantificare il contributo meccanico fornito dalla presenza dell'uncino. Il terzo ed ultimo programma di prove riguarda la caratterizzazione della resistenza alla frattura di un materiale fibrorinforzato costituito da una matrice di calcestruzzo alleggerito e da fibre di titanio, qui denominato TiFRC. In questo caso sono state realizzate fibre doppiamente uncinato in lega di titanio Ti6Al4V (o titanio grado 5) e fibre di titanio commercialmente puro (o titanio grado 2). I test di flessione su tre punti condotti su provini standardizzati dei due materiali risultanti, denominati Ti-gr5FRC e Ti-gr2FRC, hanno evidenziato una performance migliore del Ti-gr5FRC rispetto al Ti-gr2FRC in termini sia di resistenza a flessione di picco che residua. Dunque il Ti-gr5FRC è stato utilizzato per realizzare una trave di dimensioni realistiche da sottoporre ad un ulteriore test di flessione. I risultati ottenuti da questo ultimo test, sebbene lo stesso sia stato condotto in controllo di forza, hanno permesso di quantificare l'effetto scala sulla resistenza a flessione di picco che risulta inferiore a quella calcolata sui provini dello stesso materiale. Tuttavia, i meccanismi di frattura riscontrati sui provini sono stati osservati anche nel caso della trave, confermando l'azione migliorativa delle fibre sulla resistenza a flessione.

I risultati delle prove sperimentali sono stati supportati dall'analisi numerica per ciò che riguarda i test di pull-out (sfilamento). In particolare, i risultati dei test condotti sulle barre in lega di titanio, coadiuvati da analisi al microscopio elettronico (SEM) e ottico, hanno evidenziato che, nonostante siano state impiegate barre lisce, il processo di rottura dell'interfaccia è fortemente influenzato dalla formazione di asperità all'interfaccia, dovuta prevalentemente alla presenza di materiale matriciale residuo sulla superficie delle barre. Quando dunque le barre vengono sfilate le nuove asperità si rompono generando un ingranamento meccanico a livello microscopico, a sua volta responsabile del comportamento dilatante dell'interfaccia. Per descrivere numericamente questo processo è stato formulato un nuovo modello coesivo definito *enhanced degrading M-CZM*, in grado di tener conto dell'azione combinata di danno, attrito, ingranamento meccanico e dilatanza. Con tale modello, sono state condotte analisi di sensitività e una procedura di identificazione per riprodurre i risultati sperimentali delle prove di pull-out delle barre.

Un'ulteriore validazione del modello è stata ottenuta simulando numericamente le prove di pull-out delle fibre dritte.

I risultati ottenuti dimostrano che il modello coesivo *enhanced degrading M-CZM* è in grado di descrivere e spiegare i meccanismi di frattura dell'interfaccia in molteplici situazioni, evidenziando anche differenze tra il comportamento di barre e fibre che risultano consistenti con la fisica dei fenomeni. Infatti, in questo lavoro le analisi agli elementi finiti sono state utilizzate come strumento per meglio interpretare i micro-meccanismi agenti all'interfaccia tra rinforzo e matrice durante il processo di frattura della stessa.

Contents

Chapter 1

Introduction	1
1.1 Research significance and objectives.....	3
1.2 Thesis outline	4

Chapter 2

Literature review	7
--------------------------------	----------

Part 1 - Titanium and titanium alloys: main characteristics and existing uses in civil structural engineering	7
--	----------

2.1 Main properties of titanium and its alloys.....	7
2.2 Applications of titanium and its alloys in civil structural engineering.....	8
2.2.1 Monumental restoration	9
2.2.2 Cathodic protection systems	11
2.2.3 Strengthening of reinforced concrete beams.....	11
2.2.4 Concluding considerations	13

Part 2 - Reinforcement-to-concrete interface behaviour: from reinforcing bars to fibres	14
--	-----------

2.3 Bond behaviour between reinforcing bars and concrete	14
2.3.1 General concepts	14
2.3.2 Experimental determination of bond behaviour.....	15
2.3.3 Steel rebars-concrete interaction	17
2.3.3.1 Factors influencing bond.....	19
2.3.3.2 Influence of steel reinforcement corrosion on bond behaviour.....	20
2.3.4 Interaction between concrete and alternative reinforcement.....	23
2.3.4.1 Galvanised steel reinforcement	23
2.3.4.2 Epoxy-coated reinforcement	23
2.3.4.3 Stainless steel reinforcement.....	24
2.3.4.4 FRP reinforcement	24
2.3.5 Plain rebars behaviour under pull-out conditions	26
2.3.5.1 The role of surface roughness	27

2.3.6 Influence of the matrix nature on bond behaviour	28
2.4 Bond modelling.....	29
2.4.1 Analytical formulation	30
2.4.1.1 Steel reinforcement	30
2.4.1.2 Non-metallic reinforcement	31
2.4.2 Numerical modelling.....	32
2.4.2.1 Layer models.....	32
2.4.2.2 Fracture mechanics models	33
2.4.2.3 Bond elements	34
2.4.2.4 Damage mechanics approach.....	35
2.5 Cohesive zone models.....	35
2.5.1 The framework of Fracture Mechanics	36
2.5.1.1 Linear Elastic Fracture Mechanics	36
2.5.1.2 Non-Linear Elastic Fracture Mechanics.....	38
2.5.1.3 Damage and fracture	39
2.5.2 The cohesive zone model.....	40
2.5.2.1 FE formulation of CZMs.....	42
2.5.2.2 Traction-separation law.....	43
2.5.2.2.1 Dugdale and Barenblatt models	44
2.5.2.2.2 Alfano and Crisfield nonpotential-based bilinear CZM.....	45
2.5.2.2.3 Xu and Needleman potential-based exponential CZM	47
2.5.3 CZMs accounting for friction.....	49
2.5.4 CZMs for description of bond-slip behaviour in RC structures	57
2.6 Reinforcement-to-concrete interface in fibre-reinforced concrete.....	59
2.6.1 Introduction to fibre-reinforced concrete	59
2.6.1.1 Physical and mechanical properties of fibres and matrix.....	60
2.6.1.2 The fibre-matrix interface	63
2.6.2 Fibre-matrix bond and pull-out mechanism	64
2.6.3 Differences between reinforcing bars and fibres in terms of bond behaviour ..	65
2.6.4 Bond modelling for FRC.....	65

Chapter 3

Characterisation of the bond behaviour between concrete and titanium alloy bars through pull-out tests..... 67

3.1 Pull-out test experimental methodology	67
3.2 Materials.....	67
3.2.1 Concrete	68
3.2.1.1 Compression test	68
3.2.1.2 Indirect tensile test	69
3.2.2 Titanium alloy Ti6Al4V.....	70
3.3 Specimen preparation and testing set-up.....	71
3.4 Test results and discussion	73
3.4.1 Bond stress-slip relationship	74
3.4.2 SEM observations	77
3.4.3 Influence of concrete mixtures.....	84
3.4.4 Comparison with other reinforcement materials	86
3.5 Concluding remarks after experimental testing	91

Chapter 4

Finite Element Modelling of the pull-out behaviour between titanium bars and concrete 93

4.1 Description of the numerical model	93
4.1.1 Material models.....	95
4.1.2 Interface model.....	96
4.1.2.1 Interface delamination.....	96
4.1.3.1.1 Xu and Needleman model.....	97
4.1.3.1.2 Alfano and Crisfield model.....	98
4.1.3 Analysis settings.....	100
4.2 Results with exponential and bilinear CZMs	101
4.3 CZM accounting for friction	104
4.3.1 Model formulation	104
4.3.2 Model implementation in the FE code ANSYS R16	105
4.3.3 Results with CZM accounting for friction	106

4.3.4 Further validation	112
4.4 Concluding remarks	113
Chapter 5	
New cohesive models for the characterisation of the interface between plain Ti6Al4V bars and concrete	115
5.1 A new CZM derived from the Alfano and Crisfield bilinear model	115
5.1.1 Results with the modified Alfano and Crisfield model	117
5.2 M-CZM and ‘enhanced degrading M-CZM’	120
5.2.1 Original M-CZM	120
5.2.1.1 Formulation of the interface constitutive law	121
5.2.1.1.1 Modelling of the finite depth of the asperities	124
5.2.1.1.2 Modelling of interlocking degradation	125
5.2.2 Enhanced degrading M-CZM	125
5.3 Numerical results and discussion	128
5.3.1 Characteristics of pull-out response with the enhanced degrading M-CZM ..	129
5.3.2 Influence of the multiplane-structure of the interface	133
5.3.3 Contribution of the degradation of the asperities depth	134
5.3.4 Sensitivity analysis and identification	135
5.3.4.1 Preliminary sensitivity analyses	135
5.3.4.1.1 Sensitivity to the microplanes number	136
5.3.4.1.2 Sensitivity to the microplanes area fractions	137
5.3.4.2 Sensitivity to initial microplanes inclination angle and identification ..	139
5.3.4.3 Sensitivity to final microplanes inclination angle and identification	141
5.3.4.4 Sensitivity to characteristic energy value and identification	143
5.3.4.5 Sensitivity to asperities depth and identification	145
5.3.4.6 Sensitivity to friction coefficient and identification	147
5.3.4.7 Results of the identification procedure	149
5.3.4.8 Validation	151
5.3.5 Stress distribution along the interface	152
5.4 Concluding remarks	154

Chapter 6

Single fibre pull-out tests of straight and hooked-end Ti6Al4V fibres.....	157
6.1 Introduction to the single fibre pull-out test.....	157
6.1.1 Relevance of the test results	157
6.1.2 Test configurations.....	158
6.1.3 Pull-out test typical results	158
6.2 Experimental single fibre pull-out test.....	160
6.2.1 Materials.....	161
6.2.2 Geometrical configuration of the fibres	162
6.2.3 Specimen preparation and test set-up.....	163
6.2.4 Experimental results.....	165
6.2.4.1 Bond stress-slip relationships.....	166
6.2.4.2 Influence of fibre geometry.....	169
6.2.4.3 Hook contribution	172
6.2.4.4 Experimental scattering and curve averaging procedure	173
6.3 Comparison between bar and fibre pull-out tests.....	175
6.4 Modelling of the single fibre pull-out behaviour: a review on straight and hooked end fibres.....	176
6.3.1 Models for straight fibres.....	176
6.3.2 Models for hooked-end fibres	177
6.3.3 Numerical implementation.....	177
6.5 Finite element analysis of single fibre pull-out tests.....	178
6.5.1 Finite element simulation of straight single fibre pull-out test	178

Chapter 7

Titanium Alloy-Fibre Reinforced Lightweight Concrete: a preliminary experimental study	183
7.1 Some concepts on steel fibre reinforced concrete.....	183
7.1.1 Mix design.....	184
7.1.2 Mechanical properties	184
7.2.2.1 Hardening and softening responses.....	185
7.2.3 Durability	187

7.3 Overview of standardised test methods to characterise SFRC.....	188
7.3.1 Three-Point Bending Test (EN 14651)	189
7.4 Experimental tests on TiFRC specimens	191
7.4.1 Materials and fibres geometrical configuration	192
7.4.2 Specimen preparation and test set-up.....	192
7.5 Experimental test results	196
7.5.1 Compression and indirect tensile tests	198
7.5.2 Three-point bending tests.....	199
7.5.3 Comparison between TiFRC and SFRC	205
7.6 Experimental test on a Ti-gr5FRC full-scale beam.....	208
7.6.1 Materials and geometrical details.....	208
7.6.2 Test set-up	209
7.6.3 Test results	209
7.6.3.1 Flexural strength.....	210
7.6.3.2 Failure mechanisms.....	211
Chapter 8	
Conclusions and future research	213
8.1 Overview of findings and conclusions.....	214
8.2 Objectives achievement discussion.....	217
8.3 Future research.....	218
References.....	221

List of Figures

Figure 2.1 - Applications of titanium in monumental restoration: a) titanium bars into pre-drilled holes in the columns of the Parthenon of Athens (Karanassos, 2014); b) restoration of the Column of Marco Aurelio in Rome with titanium bars and plates (Masiani and Tocci, 2012); c) consolidation of the foundations of the San Marco bell tower in Venice with titanium bars (Cecconi et al., 2008).....	9
Figure 2.2 - Titanium belts for hooping historical columns: a) Monastery of Santa Monica, Cremona (Dolce et al., 2001); and b) Abbey of San Pietro, Perugia (Vetturini, 2014)	10
Figure 2.3 - Shape memory alloy devices installed in the Basilica of San Francesco, Assisi (Castellano, 2005)	10
Figure 2.4 - a) Nitinol bars applied as further reinforcement in a RC beam; stress-strain response: b) without nitinol bars; and c) with nitinol bars	11
Figure 2.5 - Flexural Strengthening of RC beam with titanium rods in the experiment by Higgins et al. [taken in (Higgins et al., 2017)].....	12
Figure 2.6 - a) Scheme of pull-out test according to the standard RILEM RC6; and b) typical bond-slip relationship derived from a pull-out test	16
Figure 2.7 - Typical stages of a bond-slip relationship for ribbed and plain steel reinforcing bars [based on (CEB-FIP Report, 2000)]	19
Figure 2.8 - Scheme of the influence of corrosion on bond performance for plain and ribbed reinforcing bars	22
Figure 2.9 - Typical stages of a bond-slip relationship for deformed FRP bars [based on (CEB-FIP Report, 2000)]	26
Figure 2.10 - Analytical bond-slip relationship for steel reinforcing bar-to-concrete interface.....	31
Figure 2.11 - Analytical bond-slip relationship for FRP reinforcing bar-to-concrete interface.....	32
Figure 2.12 - Geometry and strain energy released of a double-ended crack of length $2c$ in an infinite plate of unit width under a uniformly applied stress σ_a	37
Figure 2.13 - Fracture Modes: (a) Mode I – opening; (b) Mode II – in plane-shear (sliding), and (c) Mode III – out-of-plane shear (tearing)	38
Figure 2.14 - a) Scheme of the cohesive zone ahead of a tensile crack; b) Barenblatt's crack model; and c) Dugdale's crack model	41
Figure 2.15 - a) Scheme of the cohesive zone [taken in (Cornec et al., 2003)]; b) FE implementation of CZM [taken in (Cornec et al., 2003)]; and c) typical traction-separation law (TSL) for describing the cohesive behaviour.....	43
Figure 2.16 - TSL: a) Barenblatt's model; and b) Dugdale's model.....	45
Figure 2.17 - Alfano and Crisfield model: a) mode I TSL; and b) mode II TSL.....	46
Figure 2.18 - Xu and Needleman model: a) TSL in mode I; and b) TSL in mode II.....	48
Figure 2.19 - Tvergaard's interface model accounting for friction: a) under normal loading; and b) under tangential loading [taken in (Tvergaard, 1990)].....	49

Figure 2.20 - Schematic behaviour of the Chaboche et al.'s model under tangential loading [taken in (Chaboche et al., 1997)]	50
Figure 2.21 - Lin et al.'s model: a) uncoupled TSL in mode I; and b) uncoupled TSL in mode II accounting for friction [taken in (Lin et al., 2001)]	52
Figure 2.22 - RCCM model accounting for friction: a) TSL in mode I; and b) TSL in mode II [taken in (Raous et al., 1999)]	53
Figure 2.23 - Del Piero and Raous model accounting for friction and viscosity: a) TSL in mode I; and TSL in mode II [taken in (Del Piero and Raous, 2010)]	53
Figure 2.24 - Scheme of the bipartition of the REA into damaged and undamaged parts	54
Figure 2.25 - Alfano and Sacco model accounting for friction: TSL in mode II [taken in (Alfano and Sacco, 2006)]	56
Figure 2.26 - Multiscale approach of the Serpieri and Alfano model (Serpieri and Alfano, 2011): a) smooth macro-interface; b) real micro-interface; and b) periodic micro-pattern of a repeating unit through which the interface is described.....	56
Figure 2.27 - Finite depth of the asperities in the M-CZM	57
Figure 2.28 - Typical stress–strain curves for conventional and high performance FRC [after (ACI Committee 544, 1999)].....	60
Figure 2.29 - Examples of fibre distribution and orientation: a) unidirectional in-plane distribution of continuous long fibres; b) bidirectional in-plane distribution of continuous long fibres; and c) random distribution of discrete short fibres.....	62
Figure 2.30 - a) Toughening effects and crack front debonding, the Cook-Gordon effect (Cook and Gordon, 1964), and debonding and sliding in the crack wake; b) matrix spalling and matrix cracking; c) plastic bending of inclined fibre during pull-out at the crack and at the end-anchor [based on (Löfgren, 2005)].....	64
Figure 2.31 - a) Fibre normal to and bridging a matrix tensile crack in a real composite; and b) simulation of the real situation through single fibre pull-out test	65
Figure 3.1 - a) Pull-out scheme; b) Pull-out test set-up	71
Figure 3.2 - Specimen identification.....	72
Figure 3.3 - $\phi 16$ mm bar specimens: a) initial configuration, b) final configuration with cut position; $\phi 8$ mm bar specimens: c) initial configuration, d) final configuration with cut position	73
Figure 3.4 - Pull-out results: $\phi 8$ mm Ti6Al4V rebar from NWC specimen.....	74
Figure 3.5 - Pull-out results: $\phi 16$ mm Ti6Al4V rebar from NWC specimen.....	75
Figure 3.6 - Pull-out results: $\phi 8$ mm Ti6Al4V rebar from LWC specimen	75
Figure 3.7 - Pull-out results: $\phi 16$ mm Ti6Al4V rebar from LWC specimen	76
Figure 3.8 - Examples of local increases in the bond stress noticed in the experimental pull-out curve responses	76
Figure 3.9 - a) Partial pull-out test and cut position; b) cross-section; c) bar-matrix interface intended for SEM observations	77
Figure 3.10 - SEM observation: specimen N/8-2.....	79
Figure 3.11 - SEM observation: specimen N/16-2.....	80
Figure 3.12 - SEM observation: specimen L/8-2	81

Figure 3.13 - SEM observation: specimen L/16-2	82
Figure 3.14 - SEM observations: a) Bar-matrix interfaces of N/8-2, N/16-2, L/8-2 and L/16-2 specimens with indication of the main features; b) Zoom on the interface of N/8-2, N/16-2 and L/16-2 specimens with the indication of the interface measures; c) Legend.....	84
Figure 3.15 - Indirect tensile test fracture surface: a) scheme; b) NWC; c) LWC.....	85
Figure 3.16 - a) Visual and b) Microscopic Analysis of Ti6Al4V bars pulled out from NWC specimens; c) Visual and d) Microscopic Analysis of Ti6Al4V bars pulled out from LWC specimens	86
Figure 3.17 - Bond Strength comparison for Plain rebars.....	89
Figure 4.1 - FE model of the specimens with 8 mm bar diameter: a) Geometry; b) Interface details and boundary conditions; and c) Mesh discretisation.....	94
Figure 4.2 - FE model of the specimens with 16 mm bar diameter: a) Geometry; b) Interface details and boundary conditions; and c) Mesh discretisation.....	95
Figure 4.3 - Scheme of the interface: a) initial configuration; and b) deformed configuration	96
Figure 4.4 - a) Mode I and Mode II Exponential CZM laws; b) Mode I and Mode II Bilinear CZM laws.....	97
Figure 4.5 - Applied displacement in two substeps for the models with $\phi 8$ and $\phi 16$ bars	100
Figure 4.6 - $\phi 8$ mm rebars pull-out from NWC specimens: Comparison between Bilinear (Alfano and Crisfield, 2001) and Exponential (Xu and Needleman, 1994) CZMs and experimental curves.....	101
Figure 4.7 - $\phi 16$ mm rebars pull-out from NWC specimens: Comparison between Bilinear (Alfano and Crisfield, 2001) and Exponential (Xu and Needleman, 1994) CZMs and experimental curves.....	102
Figure 4.8 - $\phi 8$ and 16 mm rebars pull-out from NWC specimens, zoom on the elastic branch: Comparison between Bilinear (Alfano and Crisfield, 2001) and Exponential (Xu and Needleman, 1994) CZMs and experimental curves.....	102
Figure 4.9 - $\phi 8$ mm rebars pull-out from LWC specimens: Comparison between Bilinear (Alfano and Crisfield, 2001) and Exponential (Xu and Needleman, 1994) CZMs and experimental curves.....	103
Figure 4.10 - $\phi 16$ mm rebars pull-out from LWC specimens: Comparison between Bilinear (Alfano and Crisfield, 2001) and Exponential (Xu and Needleman, 1994) CZMs and experimental curves.....	103
Figure 4.11 - $\phi 8$ and 16 mm rebars pull-out from LWC specimens, zoom on the elastic branch: Comparison between Bilinear (Alfano and Crisfield, 2001) and Exponential (Xu and Needleman, 1994) CZMs and experimental curves.....	104
Figure 4.12 - $\phi 8$ mm rebars pull-out from NWC specimens: Comparison between CZM accounting for friction (Alfano and Sacco, 2006) and experimental curves.....	106
Figure 4.13 - $\phi 16$ mm rebars pull-out from NWC specimens: Comparison between CZM accounting for friction (Alfano and Sacco, 2006) and experimental curves.....	107

Figure 4.14 - $\phi 8$ mm rebars pull-out from LWC specimens: Comparison between CZM accounting for friction (Alfano and Sacco, 2006) and experimental curves	107
Figure 4.15 - $\phi 16$ mm rebars pull-out from LWC specimens: Comparison between CZM accounting for friction (Alfano and Sacco, 2006) and experimental curves	108
Figure 4.16 - a) scheme of the interface; evolution of the normal stress on bar and matrix portions and along the interface: b) substep 10; c) substep 66; d) substep 67; and e) substep 250.....	109
Figure 4.17 - a) bar and matrix strain distribution along the interface during the bonding stage; and b) bar and matrix strain distribution along the interface during the debonding stage.....	110
Figure 4.18 - a) Purely linear softening CZM: a perfect bond at the beginning of the analysis; b) bar and matrix normal strain and directional deformation distributions along the interface during the bonding stage.....	111
Figure 4.19 - a) Bilinear softening CZM with finite stiffness at the linear-elastic branch; b) bar and matrix normal strain and directional deformation distributions along the interface during the bonding stage	111
Figure 4.20 - FE model of the specimens with 16 mm bar diameter and the applied lateral pressure σ_a	112
Figure 4.21 - Pull-out curve response (up to 5 mm of slip) of $\phi 16$ mm titanium alloy rebar from NWC specimen, with a CZM accounting for friction and a constant lateral pressure $\sigma_a = 100$ MPa.....	112
Figure 5.1 - Alfano and Crisfield Bilinear CZM vs Modified law (tangential law)	117
Figure 5.2 - $\phi 8$ mm rebars pull-out from NWC specimens: Comparison between Modified Alfano and Crisfield CZM and experimental curves	118
Figure 5.3 - $\phi 16$ mm rebars pull-out from NWC specimens: Comparison between Modified Alfano and Crisfield CZM and experimental curves	118
Figure 5.4 - $\phi 8$ mm rebars pull-out from LWC specimens: Comparison between Modified Alfano and Crisfield CZM and experimental curves	119
Figure 5.5 - $\phi 16$ mm rebars pull-out from LWC specimens: Comparison between Modified Alfano and Crisfield CZM and experimental curves	119
Figure 5.6 - a) body without interface; b) interface model in the initial (undeformed) configuration; and c) interface model in the deformed configuration.....	120
Figure 5.7 - a) the multiscale approach for describing the smooth macro-interface through a periodic pattern of RIA; and b) RIA scheme.....	121
Figure 5.8 - a) RIA initial configuration; RIA deformed configuration: b) reduction in contact area depending on the opening displacement with HN kept constant; and c) HN is updated according to θ_k degradation law and then the reduction in contact area is computed.....	126
Figure 5.9 - a) M-CZM with constant area fractions among the microplanes; e) b) higher area fraction for the horizontal microplane; c) higher area fractions for the inclined microplanes; and d) different area fractions among the microplanes.....	126

Figure 5.10 - RIA scheme: a) 3 microplanes; and b) five microplanes.....	127
Figure 5.11 - Typical pull-out curve obtained by employing the enhanced degrading M-CZM: a) whole curve; and b) enlargement on the first 5 mm of slip.....	130
Figure 5.12 - Identification of the most significant substeps	131
Figure 5.13 - Damage variable trend on the three microplanes	131
Figure 5.14 - Progressive loss of adhesion on the RIA microplanes during loadstep 1: a) substep 1; b) substep 110; and c) substep 175.....	132
Figure 5.15 - Evolution of: a) inclination angle (θ_1); and b) asperities depth (H_{N1}) on microplane 1 during loadsteps 1 and 2.....	132
Figure 5.16 - Influence of the microplane-structured interface.....	133
Figure 5.17 - Comparison between the response curves obtained by using the M-CZM (Serpieri et al., 2015a) and the enhanced degrading M-CZM	134
Figure 5.18 - Sensitivity to N_p : pull-out curves for the model with $\phi 16$ mm and NWC obtained by using a RIA consisting of 3 and 5 microplanes	137
Figure 5.19 - Sensitivity to γ_{ok} : pull-out curves for the model with $\phi 16$ mm and NWC obtained by using three combination of area fractions.....	138
Figure 5.20 - Sensitivity to θ_0 : a) NWC; b) LWC.....	140
Figure 5.21 - Sensitivity to θ_f : a) NWC; b) LWC	142
Figure 5.22 - Sensitivity to ζ_0 : a) NWC; b) LWC	144
Figure 5.23 - Sensitivity to H_{N0} : a) NWC; b) LWC	146
Figure 5.24 - Sensitivity to μ : a) NWC; b) LWC.....	148
Figure 5.25 - Numerical-experimental comparison: $\phi 16$ rebar, NWC.....	150
Figure 5.26 - Numerical-experimental comparison: $\phi 16$ rebar, LWC	150
Figure 5.27 - Numerical-experimental comparison: $\phi 8$ rebar, NWC.....	151
Figure 5.28 - Numerical-experimental comparison: $\phi 8$ rebar, LWC	151
Figure 5.29 - Substep identification for computing stress distributions at the interface.	152
Figure 5.30 - Normal (σ_x) and tangential (τ_{xy}) stress distributions along the interface at different substeps.....	153
Figure 5.31 - Normal stress evolution: a) Loadstep 1 - substep 30 (bonding phase); b) Loadstep 1 - substep 68 (pull-out force peak); and c) Loadstep 2 - substep 100 (post-debonding/frictional phase).....	154
Figure 5.32 - Tangential stress evolution: a) Loadstep 1 - substep 30 (bonding phase); b) Loadstep 1 - substep 68 (pull-out force peak); and c) Loadstep 2 - substep 100 (post-debonding/frictional phase).....	154
Figure 6.1 - Pull-out test configurations: a), b) and c) single-sided specimens; d) double-sided specimens.....	158
Figure 6.2 - Typical bond-slip response curve of: a) straight fibre; and b) hooked-end fibre; c) comparison between straight and hooked-end fibre in terms of bond-slip response curve.....	160
Figure 6.3 - Geometric details of: a) smooth straight; and b) hooked-end Ti6Al4V fibres	163

Figure 6.4 - Cast of the specimens	163
Figure 6.5 - Geometrical details of the specimens for the single fibre pull-out test: a) perspective view; b) longitudinal cross-section (Section V-V'); and c) transversal cross-section (Section H-H')	164
Figure 6.6 - Pull-out test set-up: a) scheme of the test; b) execution of the test	164
Figure 6.7 - Pull-out test details: a) testing machine; b) metallic frame; c) clamping device; and d) strain gauges.....	165
Figure 6.8 - Specimen identification.....	165
Figure 6.9 - Single fibre pull-out test results: Straight fibre	167
Figure 6.10 - Zoom on the first 5 mm of slip of the single fibre pull-out test results: Straight fibre	167
Figure 6.11 - Single fibre pull-out test results: Hooked-end fibre	168
Figure 6.12 - Zoom on the first 10 mm of slip of the single fibre pull-out test results: Hooked-end fibre.....	168
Figure 6.13 - Hooked-end fibres after pull-out test.....	169
Figure 6.14 - Bond-slip response curve comparison between straight and hooked-end fibres	169
Figure 6.15 - Fibre pull-out mechanism: a) rigid sliding of straight fibres; and b) plastic deformation (strengthening) of the hook of hooked-end fibres.....	171
Figure 6.16 - Plastic hinges: a) hooked-end fibre with two curvatures; and b) hooked-end fibre with three curvature	171
Figure 6.17 - Comparison between pull-out response curves of hooked-end fibres: a) hook plastic deformation response; and b) hook rupture response	172
Figure 6.18 - a) plastically deformed hook (specimen L/PO_HE-7); and b) broken hook (specimen L/PO_HE-6).....	172
Figure 6.19 - Average curve: a) straight fibres series; and b) hooked-end fibres series .	174
Figure 6.20 - Pull-out Load-slip average curves: a) ϕ 16 mm bar in LWC specimens (L/PO_B16); b) ϕ 8 mm bar in LWC specimens (L/PO_B8); and c) ϕ 1.2 mm fibres in LWC specimens (L/PO_S1.2).....	175
Figure 6.21 - 2D axisymmetric FE model of the single straight fibre pull-out tests: a) geometry, b) boundary conditions; and c) mesh discretisation	178
Figure 6.22 - Comparison between the experimental average curve and the numerical curve obtained with the enhanced degrading M-CZM: curve until a slip equal to 12.5 mm; and zoom on the first 2.5 mm of slip	180
Figure 7.1 - Typical profiles of steel fibres used in concrete according to Naaman (Naaman, 2003)	184
Figure 7.2 - Softening and hardening behaviour of FRC: a) tension-softening; b) deflection-softening; c) tension-hardening; and d) deflection-hardening.....	186
Figure 7.3 - Corrosion mechanisms on: a) un-cracked concrete; b) cracked concrete at an early stage; c) cracked concrete after autogenous healing; d) cracked concrete with critical corrosion on fibres [based on (Marcos-Meson et al., 2017)].	188

Figure 7.4 - Three-point bending test set-up according to EN 14651 (EN 14651, 2005): a) set up and specimen dimensions; b) details of the notch and the transducer	190
Figure 7.5 - Example of the load- <i>CMOD</i> response of a 3PBT with the indication of <i>FL</i> , <i>CMOD_j</i> and the respective <i>F_j</i>	191
Figure 7.6 - Fibres geometry hooked-end configurations: a) Titanium Grade 2; b) Titanium Grade 5	192
Figure 7.7 - Cast #1 (Ti-gr2FRC) scheme	193
Figure 7.8 - Cast #2 (Ti-gr5FRC) scheme	194
Figure 7.9 - Cast #3 (Plain concrete) scheme	194
Figure 7.10 - Test set-up and execution: a) compression test; b) indirect tensile test.....	195
Figure 7.11 - Specimen dimensions for the three-point bending test.....	195
Figure 7.12 - Three-point bending test set-up	196
Figure 7.13 - Compression test broken specimens: a) Ti-gr2_CT-1; b) Ti-gr5_CT-1; c) P_CT-1	199
Figure 7.14 - Results of the 3PBT on Ti-gr2FRC (complete curves and zoom on the first part up to <i>CMOD</i> =0.5 mm)	199
Figure 7.15 - Results of the 3PBT on Ti-gr5FRC (complete curves and zoom on the first part up to <i>CMOD</i> =0.5 mm)	200
Figure 7.16 - Results of the 3PBT on Plain Concrete (complete curves and zoom on the first part up to <i>CMOD</i> =0.5 mm)	200
Figure 7.17 - Broken specimens after the 3PBT on Ti-gr2FRC	203
Figure 7.18 - Broken specimens after the 3PBT on Ti-gr5FRC	204
Figure 7.19 - Broken specimens after the 3PBT on Plain Concrete (P).....	205
Figure 7.20 - Geometry of the Ti-gr5FRC full-scale beam.....	208
Figure 7.21 - Test set-up: a) test apparatus with load steps indication; b) position of the extensometer 1; c) position of the extensometer 2; and c) detail of the steel beam used to transfer the load	209
Figure 7.22 - Beam under progressive load-step.....	210
Figure 7.23 - Failure mechanisms: a) multiple and diffusive cracking; b) plastic deformation of the fibres hook; and c) bridging action of the fibres.....	211

List of Tables

Table 2.1 - Main mechanical properties of Titanium Grade 2 and 5	8
Table 2.2 - Layer models review for bond modelling.....	33
Table 2.3 - Review of fracture mechanics approaches to bond modelling	34
Table 2.4 - Review of potential and nonpotential-based formulation of CZMs	44
Table 2.5 - Comparison among different materials used as fibre reinforcement for concrete	61
Table 3.1 - NWC and LWC concrete mixtures mix design	68
Table 3.2 - Control specimens' characteristics - compression test	68
Table 3.3 - Mechanical properties of concrete: Compression test results.....	69
Table 3.4 - Control specimens' characteristics - indirect tensile test.....	69
Table 3.5 - Mechanical properties of concrete: Indirect Tensile test results.....	70
Table 3.6 - Mechanical properties of Titanium alloy: Tensile test results	70
Table 3.7 - Properties of Ti6Al4V bars: manufacturer specifications and experimental results	71
Table 3.8 - Specimens for the pull-out test	72
Table 3.9 - Experimental pull-out test results	74
Table 3.10 - Bond strength values comparison for plain rebars.....	87
Table 3.11 - Bond strength values comparison for ribbed rebars	90
Table 4.1 - Material properties for the FE analysis.....	95
Table 4.2 - Experimental interface delamination parameters for Mode II dominated fracture behaviour.....	97
Table 4.3 - Parameter values for Exponential CZM	98
Table 4.4 - Parameter values for Bilinear CZM.....	100
Table 4.5 - Analysis settings	100
Table 4.6 - Input parameters for the CZM accounting for friction proposed by Alfano and Sacco (Alfano and Sacco, 2006)	106
Table 5.1 - Input parameters for the modified Alfano and Crisfield model.....	117
Table 5.2 - Input parameters for the enhanced degrading M-CZM	127
Table 5.3 - Initial set of enhanced degrading M-CZM input parameters.....	129
Table 5.4 - Fixed input parameters for the enhanced degrading M-CZM	135
Table 5.5 - Enhanced degrading M-CZM input parameters for sensitivity analysis to Np	136
Table 5.6 - Enhanced degrading M-CZM input parameters for sensitivity analysis to $\gamma_0 k$	138
Table 5.7 - Enhanced degrading M-CZM input parameters for sensitivity analysis to θ_0	139

Table 5.8 - Enhanced degrading M-CZM input parameters for sensitivity analysis to θf	141
Table 5.9 - Enhanced degrading M-CZM input parameters for sensitivity analysis to ζ_0	143
Table 5.10 - Enhanced degrading M-CZM input parameters for sensitivity analysis to HN_0	145
Table 5.11 - Enhanced degrading M-CZM input parameters for sensitivity analysis to μ	147
Table 5.12 - Final values of enhanced degrading M-CZM input parameters after identification procedure	149
Table 6.1 - Most used steel fibre profiles	159
Table 6.2 - LWC mix design	161
Table 6.3 - Mechanical properties of LWC	161
Table 6.4 - Mechanical properties of the titanium wires (provided by the manufacturer)	162
Table 6.5 - Single fibre pull-out test results	166
Table 6.6 - Hook contribution	173
Table 6.7 - Comparison between bar and fibre pull-out tests	175
Table 6.8 - Material properties for the FE analysis	179
Table 6.9 - Enhanced degrading M-CZM input parameters for the single fibre pull-out test FE simulation	179
Table 7.1 - Mechanical properties of the titanium wires provided by the manufacturer	192
Table 7.2 - Cast details and specimen identification for each batch	193
Table 7.3 - Specific weight of the three concrete batches	197
Table 7.4 - Compression and indirect tensile tests results	198
Table 7.5 - 3PBT results	201
Table 7.6 - <i>LOP</i> comparison	202
Table 7.7 - Flexural strength and residual flexural strength comparison between Ti-gr5FRC and SFRC	206
Table 7.8 - Mechanical properties of the concrete batch	208
Table 7.9 - Results of the test on the full-scale Ti-gr5FRC beam	210

Chapter 1

Introduction

Corrosion of reinforcement in reinforced concrete structures has been recognised as the predominant factor causing premature deterioration of concrete buildings worldwide (Böhni, 2005). Carbonation-induced and chloride-induced corrosion prevails as the most serious mechanisms leading to loss of bearing capacity of reinforced concrete civil structures around the globe (Zhou et al., 2014). Direct consequences of reinforcement corrosion are the severe reduction of reinforcement cross-sectional area and the formation of expansive products formation at the reinforcement-concrete interface, which in turn causes the cracking and spalling in concrete cover. Aggressive environments, such as the marine environment, weather conditions, fatigue and changing of loading conditions on reinforced concrete structures have been established as major factors promoting chloride penetration and carbonation phenomenon (Zhou et al., 2014), (Apostolopoulos, 2016). Recently, the impact of global warming on chloride ingress has been also reported to be a crucial factor that has to be accounted for in the assessment of the structural behaviour of reinforced concrete structures (Bastidas-Arteaga, 2018).

All the previous considerations are actually translated in the need of repairing or replacing those structures that suffer by steel corrosion. This appears to be imperative in the case of those buildings which are places of large gatherings such as schools and hospitals (Apostolopoulos, 2016), and in the case of civil infrastructures, such as bridges, highways, on-shore and off-shore structures, which moreover are severely exposed to the environmental action (Zhou et al., 2014). The poor durability of many concrete infrastructures, which results in short structural service lives, is not sustainable neither in social nor in economic terms (Navarro et al., 2018). In a recent study published by NACE International, called ‘IMPACT - International measures of prevention, application, and economics of corrosion technologies study’ (Koch et al., 2016), it is reported that “*the global cost of corrosion is estimated to be US\$2.5 trillion, which is equal to 3.4% of Global Domestic Product (GDP)*”.

Therefore, it appears clear how novel strategies for preventing corrosion and protecting reinforced structures of various types and importance (e.g. bridges, nuclear structures, hospitals, schools etc.) in order to guarantee structural safety, are encouraged and often crucial. In this background, over decades many efforts have been made by researchers to improve the durability of reinforced concrete structures. The possibility of adding corrosion inhibitors in the concrete mixture, as well as coating the steel rebar surface with both metallic and organic films oriented to improve the reinforcement corrosion resistance, has been largely investigated. Moreover, a vast amount of research is oriented to the replacement of traditional steel reinforcement with reinforcement that does not corrode, such as stainless steel rebars and non-metallic ones (e.g. Fibre Reinforced Polymers). Thus, the need of alternative solutions and strategies able to limit the problem of reinforcement corrosion in reinforced concrete structures is increasingly crucial.

A material that has never been thoroughly investigated as potential reinforcement for concrete structures is titanium, clearly because of its cost. However, titanium and its alloys have outstanding properties in terms of corrosion resistance and excellent strength-to-specific weight ratio. Thus, for special designs where avoiding reinforcement corrosion and reducing structure self-weight are crucial to the point to justify high costs, titanium may become a realistic option.

In the present thesis the possibility to use titanium and its alloys as concrete reinforcement has been investigated by starting from the main prerequisite of understanding the behaviour that titanium and concrete develop when they are in contact, i.e. the bond performance. Therefore, experimental tests and numerical analyses aimed to the comprehension of the titanium-concrete interface mechanisms have been carried out by focusing not just on traditional reinforcing bars, but also on diffused reinforcement, i.e. discrete fibres randomly distributed in the concrete matrix. To emphasise the high strength-to-weight ratio of titanium alloys, lightness has been another pursued objective. In this respect, lightweight aggregate concrete mixes have been taken into account, considering also that they usually suffer corrosion of embedded reinforcement (reinforcing bars or fibres) even more than normal-weight concrete due to their higher porosity.

A first evaluation of the bond performance is made between plain reinforcing bars and normal and lightweight concrete matrices, by carrying out experimental pull-out tests. Plain bars were selected in order to better understand the influence that the particular material used for the reinforcement and the different types of concrete batches designed have on the pull-out response. Additionally, by using plain rebars and analysing the problem from a micro-mechanical point of view, the role of surface roughness can be more easily identified. To this end, the experimental tests have been supported by finite element analyses in which the debonding process has been described through several cohesive zone models. The known formulations of exponential (Xu and Needleman, 1994) and bilinear (Alfano and Crisfield, 2001) cohesive zone models, and those accounting for friction (e.g. the model proposed by Alfano and Sacco in (Alfano and Sacco, 2006)) have been considered and implemented in order to verify their capacity of describing the phenomenon under exam. However, by applying these models, unsatisfactory results have been obtained, underlining the necessity of using a model able to account for the micromechanisms

actually acting at the interface during pull-out. Therefore, other modelling strategies have been adopted, by formulating and implementing into the finite element software two novel cohesive zone models. The first one is derived by the bilinear model formulation introduced by Alfano and Crisfield (Alfano and Crisfield, 2001) and accounts for a further exponential branch which simulates the combined action of friction and dilatancy in a phenomenological manner. Even though this model has led to very good agreement between experimental and numerical results, its empirical approach could not allow the comprehension of the real mechanisms governing the debonding. Thus, the micromechanics-based formulation of the angle-degrading multiplane cohesive zone model developed by Serpieri et al. in (Serpieri et al., 2015a) has been adopted and enhanced by introducing, as a novel mechanical feature, the reduction of the asperities depth induced by wear and degradation. The resulting model, here denominated ‘*enhanced degrading M-CZM*’, permits to outline the individual role of each damaging mechanism in the overall system response, considering also effects induced by the rebar surface roughness which are usually neglected in the finite element simulation of pull-out tests.

Secondly, the possibility to include titanium alloy fibres into a lightweight concrete matrix is investigated. To this end, single fibre pull-out tests have been carried out to estimate the bond behaviour between titanium-alloy fibres and concrete and evaluate the differences between bars and fibres behaviour under pull-out conditions. The numerical analysis by employing cohesive zone models for the debonding simulation is again used as a tool to better identify the interfacial micromechanisms. Straight and deformed configurations of reinforcing fibres were tested, resulting in different failure modes that strongly affect the behaviour of a composite fibre reinforced material. Therefore, after analysing both experimentally and numerically the behaviour of single fibres embedded in lightweight concrete, a titanium-alloy-fibre reinforced (lightweight) concrete (TiFRC) has been designed and tested. A series of three-point bending tests on TiFRC specimens and a bending test on a TiFRC full-scale beam have been carried out in order to quantify the flexural performance of the new material proposed and compare it to the flexural behaviour of the well-known steel fibre reinforced concrete. Tests on specimens of reduced dimensions and on a full-scale beam allowed also to quantify the size effect on the flexural strength.

1.1 Research significance and objectives

Despite the well-known high cost of titanium and its alloys, some novel applications in the field of civil structural engineering have been recently proposed and realised (Higgins et al., 2017), demonstrating that titanium alloys can be a realistic alternative to traditional materials used for reinforcing concrete. The applications proposed in (Higgins et al., 2017) concern the flexural and shear strengthening of reinforced concrete beams. Nevertheless, there still is lack of information about the bond relationship that titanium and concrete can develop, which, however, represents a crucial step towards the possibility to combine them in a composite structural material, either when longitudinal reinforcing bars and distributed short fibres are concerned.

The present thesis is intended as a preliminary study towards the possibility of combining titanium alloys and concrete, providing a series of experimental results and a comprehensive comparison with the literature on the same tests on more traditional materials. The objectives of the thesis are summarised as follows:

- characterise the bond behaviour between titanium alloys and concrete from the mechanical point of view;
- understand the micromechanisms acting at the interface during debonding in the case of plain smooth reinforcement;
- use numerical analysis as a tool to better understand the mechanisms governing the reinforcement-matrix failure, by implementing also novel cohesive zone models able to account for such mechanics;
- compare the bond performance of bars of different diameters and fibres with respect to different concrete matrices from both the experimental and numerical point of view;
- design and test a lightweight fibre reinforced concrete material with titanium alloy fibres, evaluating the flexural strength and the post-peak behaviour of the novel material.

1.2 Thesis outline

The outline of the thesis is as follows: Chapter 2 is a literature survey on the fundamental topics analysed in the present research. It consists of two parts, the first of which reports the main characteristics of titanium and its alloys and their existing applications in the field of civil structural engineering. Part 2 of the literature review, instead, is focused on the importance of bond behaviour between concrete and various types of reinforcement either in the case of traditional reinforced concrete structures and in the case of fibre reinforced concrete materials. Experimental methods and numerical techniques developed to evaluate and predict the bond performance are discussed. Moreover, particular attention is focused on the behaviour of plain bars under pull-out conditions, since its importance in understanding the basic mechanisms acting at the reinforcement-concrete interface. Chapter 3 reports the experimental tests carried out on plain titanium alloy bars from two different concrete matrices, differing only for the coarse aggregates phase, which consists of normal and lightweight aggregates, respectively. Pull-out test results provided the so-called *bond-slip relationships*, that have been used to compare the bond performance of the titanium alloy-concrete interface with that provided by employing more traditional reinforcement materials (steel, fibre reinforced polymers, etc.) found in the literature. Further investigations concern the analysis of the broken interfaces by means of the scanning electron microscope, which provided useful information to catch the micromechanisms acting at the interface during debonding. Chapters 4 and 5 report the finite element analyses carried out in order to simulate the experimental testes carried out and presented in Chapter 3. Cohesive zone models are employed in the finite element analyses to simulate the interface fracture. Chapter 4 presents the numerical models and analysis settings adopted for the analysis, and the results obtained by using some of the

most widely used cohesive zone models (i.e. Xu and Needleman exponential model (Xu and Needleman, 1994), and Alfano and Crisfield bilinear formulation (Alfano and Crisfield, 2001)), including one model accounting for friction (Alfano and Sacco, 2006). Thus, their limitations in describing the problem under exam have been analysed and Chapter 5 reports two novel formulations of cohesive zone models, able to describe the experimental results. Particularly, sensitivity analyses, identification and validation procedures for the enhanced degrading M-CZM here formulated are included in Chapter 5.

Chapters 6 and 7 concern the characterisation of the mechanical properties of lightweight concrete reinforced with distributed titanium alloy fibres (TiFRC). Particularly, Chapter 6 reports the results of single fibre pull-out tests carried out on titanium fibres of two different geometrical configurations from lightweight concrete specimens. The experimental tests are supported by finite element analyses which include the cohesive zone models formulated in Chapter 5. Chapter 7, instead, presents preliminary experimental results of three-point bending tests on TiFRC specimens and a final experimental test on a TiFRC full-scale beam. Conclusions are drawn in Chapter 8, where open issues and suggestions for future research that would investigate titanium as potential reinforcement for concrete are also discussed.

Chapter 2

Literature review

This chapter contains a literature survey on the fundamental topics discussed in the present thesis. It consists of two main sections here called ‘Part 1’ and ‘Part 2’, respectively. In Part 1 the general properties of titanium and its alloys, as well as their existing uses in the field of civil-structural engineering, are analysed. Part 2, instead, reviews several essential aspects at the basis of the applications here hypothesised for titanium, such as bond behaviour between concrete and reinforcement, numerical modelling techniques adopted for interface problems, and fibre-reinforced cementitious materials.

Part 1 - Titanium and titanium alloys: main characteristics and existing uses in civil structural engineering

2.1 Main properties of titanium and its alloys

Titanium is a low-density element (Symbol ‘Ti’; atomic number 22; and atomic weight 47.9) discovered in 1791 by the British reverend, mineralogist and chemist, William Gregor (Leyens and Peters, 2003). Four years later, Martin Klaproth, a Berlin chemist, isolated titanium oxide. However, it took more than 100 years to isolate the proper metal. The first alloys, including today’s most popular Ti6Al4V (i.e. Titanium, 6% Aluminium and 4% Vanadium), were developed in the late 1940s in the United States and commercial production of titanium did not begin until the 1950s (RTI, 2013). Today, the peculiar properties of titanium and its alloys are exploited in many industrial applications, especially in the field of aerospace and chemical industries. But other markets such as architecture, chemical processing, medicine, power generation, marine and offshore, sports and leisure, and transportation are experimenting increasing application of titanium.

Titanium is not actually a rare substance, as it ranks as the fourth most plentiful structural metal in the Earth's crust exceeded only by aluminium, iron, and magnesium. Nevertheless, it is never found in a pure state, since it usually occurs in mineral sands containing ilmenite (FeTiO_3) or rutile (TiO_2). Thus, the difficulties in processing titanium makes it expensive.

Titanium and its alloys exhibit a unique combination of mechanical and physical properties and excellent corrosion resistance. The primary attributes of these alloys are:

- Elevated strength-to-density ratio (high structural efficiency);
- Low density (roughly half the weight of steel, nickel and copper alloys);
- Exceptional corrosion resistance to vast range of chemical environments (excellent resistance to chlorides and seawater);
- Excellent elevated temperature properties (up to 600°C);
- Essentially nonmagnetic.

Mill products, available in both commercially pure and alloy grades, can be grouped into three categories according to the predominant phase or phases in their microstructure, i.e. α , α - β , and β . Each category offers a unique suite of properties which may be advantageous for a given application, despite it requires a specific mill processing methodology.

Among the numerous available titanium alloys, titanium Grade 2, i.e. unalloyed titanium (also called “Commercially Pure”), and titanium Grade 5, i.e. α - β alloy consisting of titanium, aluminium and vanadium (the alloy Ti6Al4V), represent the most widely adopted grades of titanium. Their main mechanical properties are summarised in Table 2.1.

Table 2.1 - Main mechanical properties of Titanium Grade 2 and 5

Designation	Grade	Nominal Composition		Density (kg/dm^3)	Tensile Strength	Yield Strength (0.2 % Offset)	Elongation in 4D	Reduction of Area
		mass fraction (wt %)			(min) (MPa)	(min) (MPa)	(min) (%)	(min) (%)
		Al	V					
CP	2	-	-	4.40	345	275	20	30
Ti6Al4V	5	6	4	4.40	895	828	10	25

2.2 Applications of titanium and its alloys in civil structural engineering

The major fields of application of titanium and its alloys are those requiring high level of sophistication, such as biomedical, aerospace and mechanical engineering, mainly due to their cost. Concerning applications in civil structural engineering, currently the panorama is quite limited, but there are some particular cases where titanium has been chosen for its peculiar characteristics.

2.2.1 Monumental restoration

Because of its lightness, its compatibility with materials such as marble and stone and, above all, its outstanding resistance to corrosion, titanium has been used for the consolidation of monumental buildings of historical-artistic importance. The main applications concern the replacement of existing steel bars with titanium ones, and the consolidation of damaged portions with titanium plates and bars. Some examples of this kind of restoration, shown in Fig. 2.1, are the Parthenon of Athens (Karanassos, 2014), (Dakanali et al., 2016), the Column of Marco Aurelio in Rome (Masiani and Tocci, 2012), and the bell tower of San Marco in Venice (Cecconi et al., 2008).

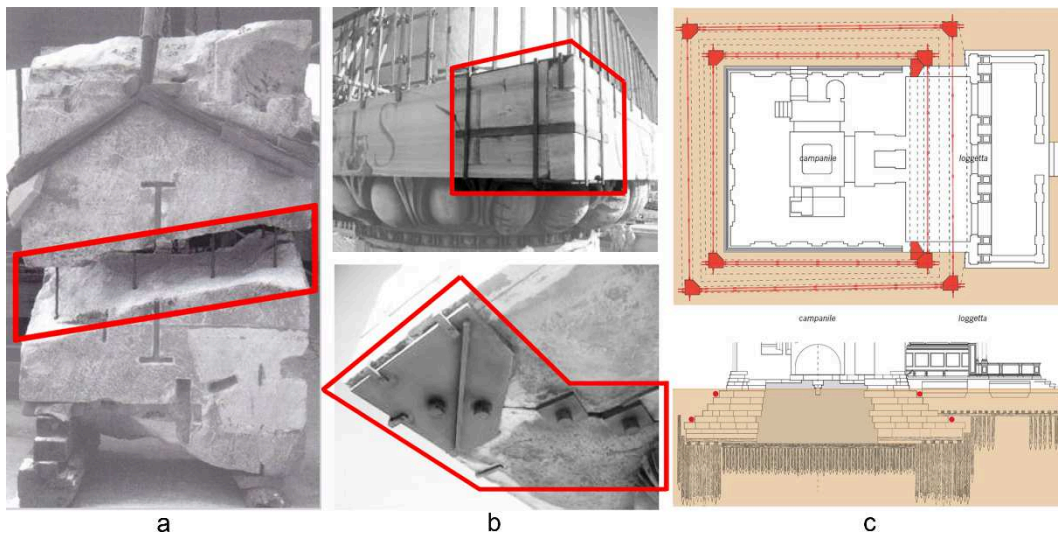


Figure 2.1 - Applications of titanium in monumental restoration: a) titanium bars into pre-drilled holes in the columns of the Parthenon of Athens (Karanassos, 2014); b) restoration of the Column of Marco Aurelio in Rome with titanium bars and plates (Masiani and Tocci, 2012); c) consolidation of the foundations of the San Marco bell tower in Venice with titanium bars (Cecconi et al., 2008)

As for the restoration of the Acropolis of Athens, the technique used consists in re-joining the fractured marble elements by inserting titanium bars into pre-drilled holes. Then the holes are filled with a particular cement-based paste. To assess the compatibility between titanium and marble some investigations on the pull-out behaviour of the rod from marble elements have been carried out in (Dakanali et al., 2016), concluding that the cement-threaded bar interface does not fail during the whole loading procedure, contrary to what happens to the marble-cement interface.

Since the possibility to use the 'near surface mounted reinforcement' (NSM) technique, the hooping of columns by means of titanium belts is a type of consolidation that has been applied in the case of the Monastery of Santa Monica in Cremona (Dolce et al., 2001) and the Abbey of San Pietro in Perugia (Vetturini, 2014), as shown in Figs. 2.2a and 2.2b, respectively.

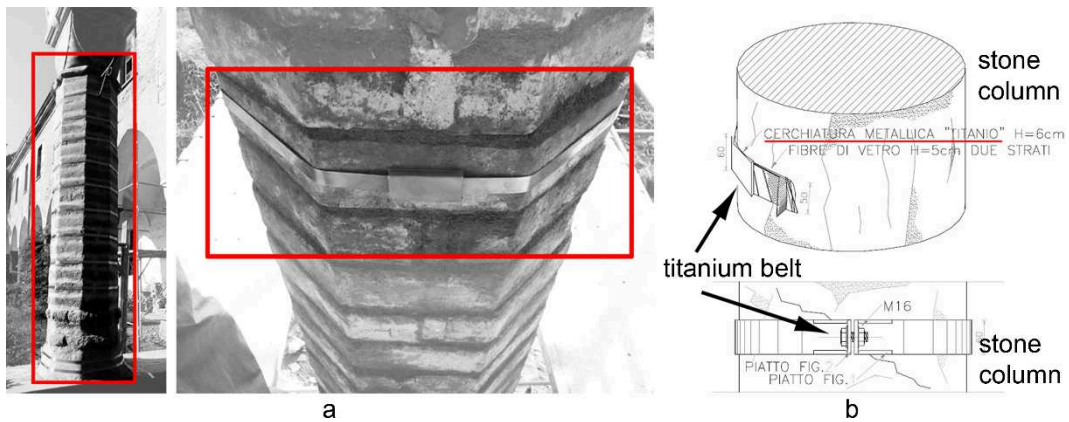


Figure 2.2 - Titanium belts for hooping historical columns: a) Monastery of Santa Monica, Cremona (Dolce et al., 2001); and b) Abbey of San Pietro, Perugia (Vetturini, 2014)

Another titanium-based intervention in the field of monumental restoration that it is worth mentioning, is represented by the devices made of Shape Memory Alloys (SMAs) applied to the Basilica of San Francesco in Assisi (Croci, 1998), (Castellano and Martelli, 2000), (Castellano, 2005) (Fig. 2.3). SMAs are a unique class of metal alloys that can recover apparent permanent strains at the moment in which the load is removed (pseudoelasticity) or when they are heated above a certain temperature (shape memory effect). Among other SMAs, the most used one is the so-called *nitinol*, constituted approximately by 56% of Nickel and 44% of Titanium (Abdulridha et al., 2013). Due to these characteristics, devices in SMA are able to greatly improve the dissipative capacity of buildings (Fig. 2.4).



Figure 2.3 - Shape memory alloy devices installed in the Basilica of San Francesco, Assisi (Castellano, 2005)

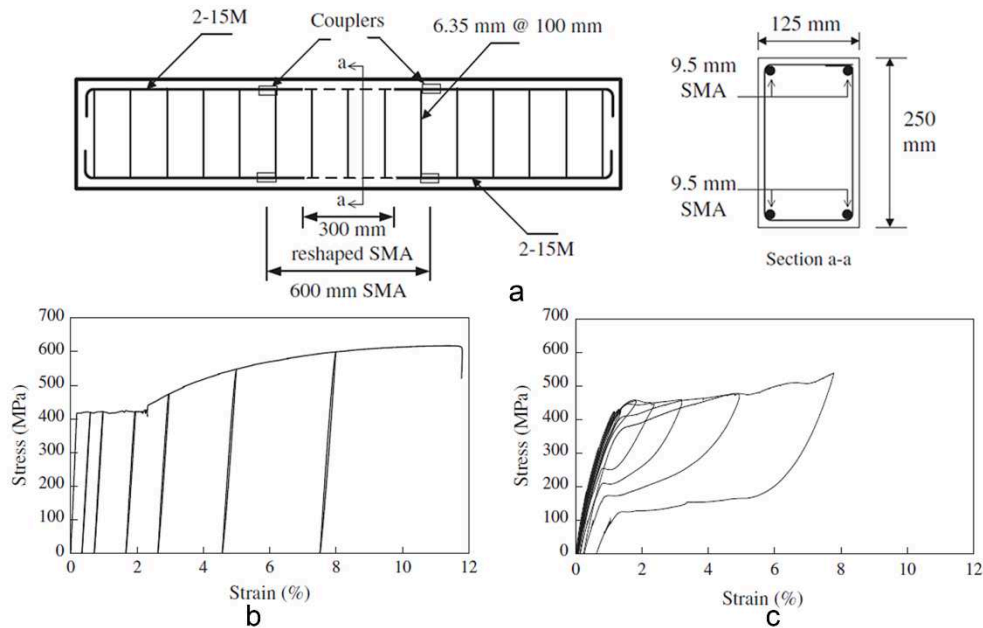


Figure 2.4 - a) Nitinol bars applied as further reinforcement in a RC beam; stress-strain response: b) without nitinol bars; and c) with nitinol bars

2.2.2 Cathodic protection systems

A non-negligible field of application of titanium in civil engineering and, particularly, in reinforced concrete structures is represented by cathodic protection systems of reinforcements. In this case the exploited characteristics of titanium are its excellent corrosion resistance and its capacity to behave as an ‘anode’, i.e. the capacity of distributing the protective current across the structure (Clemena and Jackson, 2002). A cathodic protection system for reinforced concrete consists of a number of basic components, including the reinforcement to be protected, an anode, a power source, concrete surrounding the steel, a monitoring system, and cabling to carry the system power and monitoring signals (Chess and Grønvold & Karnov, 1998). Each cathodic protection system contains two types of anodes, i.e. the ‘anode conductor’ acting as a contact point and a power supply line for the secondary anode, and the proper ‘anode’ that distributes the current over the surface of the structure (Kepler and Locke, 2000). The most used types of proper anodes are: platinum anodes and expanded titanium mesh anodes. Titanium mesh anodes consist of a titanium grid, coated with a metal oxide catalyst (Hayfield and Warne, 1989) (Virmani and Clemena, 1998).

2.2.3 Strengthening of reinforced concrete beams

In the field of civil structural engineering the strengthening of older structures plays a major and fundamental role. A new method of supplemental reinforcing involving titanium for use in a near-surface mounting (NSM) application has been recently proposed by

Higgins et al. (Higgins et al., 2017). In this method, titanium alloy bars are bonded with structural adhesive within grooves that are cut into the surface of the concrete member. The materials and implementation approach were demonstrated in the laboratory on full-size specimens (Fig. 2.5) and were then applied to a RC bridge in the US that contained poorly detailed flexural steel reinforcement and exhibited significant distress. The behaviour of the whole structure after this intervention resulted in a significant improving of the structural capacity in terms of flexure and shear resistance (Higgins et al., 2017).

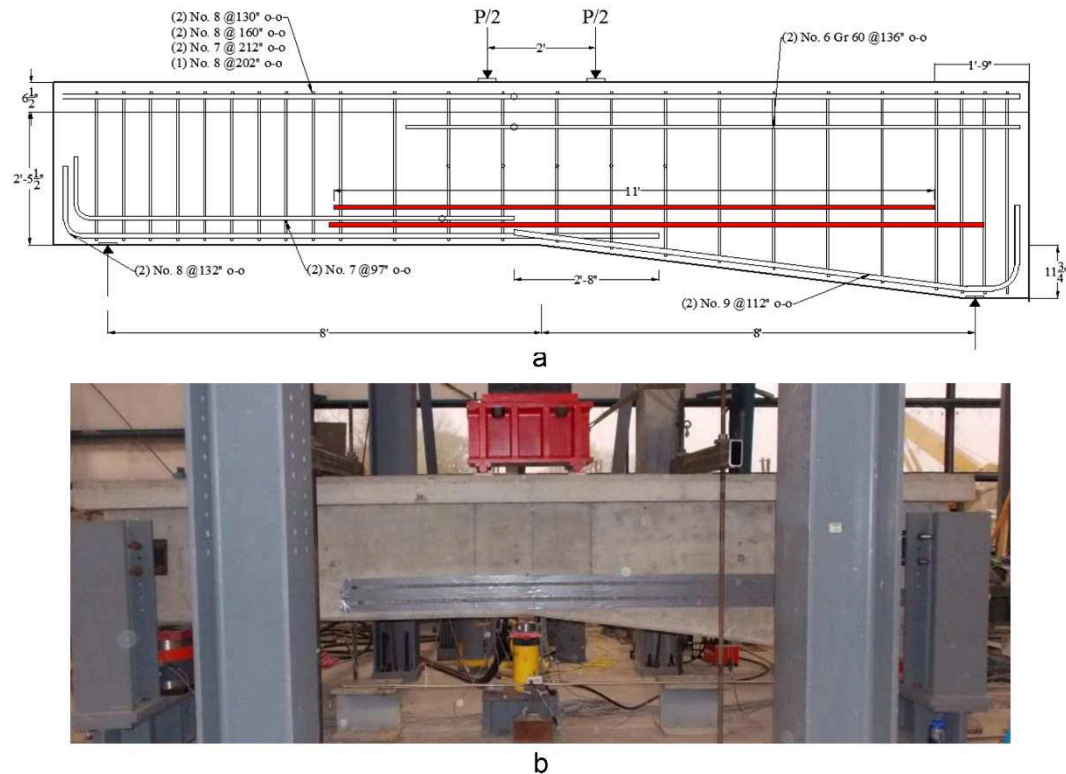


Figure 2.5 - Flexural Strengthening of RC beam with titanium rods in the experiment by Higgins et al. [taken in (Higgins et al., 2017)]

In the application proposed by Higgins et al. (Higgins et al., 2017), it is worth underlining that the near surface mounting technique was possible only due to the excellent corrosion resistance characterising the titanium rods. Moreover, since the yield strength of the titanium alloy selected is more than double than that of steel (i.e. ~ 1000 MPa vs. 450 MPa), only four 16 mm bars were needed to provide the required member strengthening.

The experiment carried out by Higgins et al. (Higgins et al., 2017) led the authors to conclude that the application of only four titanium alloy bars increased both the girder strength by a factor of two and its deformation capacity. In addition, titanium reinforcing bars have been also developed for the shear strengthening by adopting also in this case the NSM technique. Particularly, tests were carried out on T-shaped cross-section beams. The

results of the test confirmed an improvement of 40% in the shear performance of the beam. Therefore, the titanium-based shear strengthening would have shifted from non-ductile shear failure to ductile flexural failure.

The flexural strengthening technique tested in the laboratory was then applied to a real bridge, obtaining very successful results not only in terms of technical performance but also from the economic point of view. In fact, no shoring or posting techniques were required and the final cost of the operation was 30% lower than the possible alternatives, i.e. stainless steel and carbon fibre bars (Higgins et al., 2017), (Knudtsen, 2016).

Thus, Higgins et al. (Higgins et al., 2017) concluded in their study that titanium can be considered a promising material for strengthening civil infrastructures.

2.2.4 Concluding considerations

Few applications of titanium and titanium alloys in the field of civil-structural engineering have been found in the literature, due to the high cost of the material. However, for some restorations of historical monuments, the advantages obtained by using different titanium alloys reinforcing strategies could overcome the high costs of this class of metals.

Furthermore, a recent application of titanium alloy bars demonstrated the remarkable advantages that can be obtained by employing this material in reinforced concrete structures. The possibility to use a near surface mounting technique due to the excellent corrosion resistance and the reduction in the number of bars due to the high strength of the considered titanium alloys, revealed that this material could be a valuable alternative to other materials traditionally employed for the same scope. Moreover, an economic analysis carried out in (Knudtsen, 2016) highlighted that, even though the cost of the material itself is higher, for some applications the labour cost is much higher when other materials, such as carbon fibre and stainless steel, are used.

Part 2 - Reinforcement-to-concrete interface behaviour: from reinforcing bars to fibres

The second part of the literature review investigates the aspects related to the concrete-reinforcement interface behaviour. In the present research, the considered types of reinforcement are both traditional bars for reinforced concrete (RC) structures and fibres for reinforced cementitious materials. Thus, in the first instance, the bond behaviour between rebars and concrete is examined from the experimental and numerical point of view, with particular attention to the factors affecting bond and to the mechanisms acting in the case of plain steel reinforcing bars. Moreover, with regard to steel rebars, the influence of corrosion on the bond performance is taken in consideration. In fact, corrosion is the main reason why alternative materials for reinforcement have been proposed in the literature. A review of the most widely adopted alternative reinforcements in terms of bond performance is also made here.

In the second instance, the general behaviour of fibre reinforced cementitious materials is considered with regard to the mechanisms governing the fracture process. Among these mechanisms, especially those concerning the fibre-matrix interface failure are analysed.

2.3 Bond behaviour between reinforcing bars and concrete

2.3.1 General concepts

Reinforcement-to-concrete bond is the phenomenon which allows longitudinal forces to be transferred from the reinforcement to the surrounding concrete in a RC structure (CEB-FIP Report, 2000). Reliable and efficient force transfer is essential to make RC to behave as a composite structural material. The force transfer process does not involve the whole reinforcement uniformly, so that the force in a reinforcing bar changes along its length, as the force does in the concrete cover. To prevent the discontinuity, i.e. the separation of the two materials, the reinforcing element has to undergo the same strain as the surrounding matrix. Wherever this does not happen, i.e. reinforcement strains differ from concrete ones, a relative displacement (slip) between the two occurs (CEB-FIP Report, 2000).

A vast amount of research has been carried out over the last decades, providing an ever-improving understanding of this aspect of reinforced concrete behaviour. Unsurprisingly, bond behaviour has been widely investigated with regard to steel reinforcing bars, and the resistant mechanisms upon which the steel-concrete bond is based, are well known (CEB-FIP Report, 2000). However, the rebar-matrix interface represents a very complex and inhomogeneous zone (Angst et al., 2017), and bond performance is still a crucial topic under investigation. As for steel reinforcement, many studies are focused on the influence of corrosion on bond performance (Almusallam et al., 1996), (Lundgren, 2005), (Cairns et al., 2007), (Coccia et al., 2016). In addition, especially in the last decades, a vast amount of research has investigated the bond performance between both different reinforcements

and several types of concrete mixtures. In fact, the growing attention to durability of structures has led to investigate the possibility to substitute traditional steel reinforcing bars with alternative ones, such as fibre reinforced polymers (Bakis et al., 2002), stainless steel bars (Ahlborn and DenHartigh, 2002), etc. On the other hand, different matrices have been also proposed to lighten structures (Lightweight concrete (ACI Committee 213, 2003)), or increase strength (High-strength concrete (ACI Committee 211, 1998)), or reduce cracking process (Fibre-reinforced concrete (CNR, 2007)), etc. For all these cases, bond behaviour has to be investigated in order to characterise the novel interfaces originated from different materials in contact.

In the next paragraphs the following aspects are analysed:

- The experimental determination of the bond performance;
- Steel reinforcement-to-concrete interaction;
- Bond behaviour between reinforcements alternative to steel and concrete;
- Plain rebars of different materials under pull-out conditions.

2.3.2 Experimental determination of bond behaviour

Concerning the experimental investigation of the bond performances of RC, a primary method for understanding the failure mechanisms is represented by *pull-out tests* (Yeih et al., 1997) which provide the so-called *bond stress-slip relationships*. A bond stress-slip (or simply bond-slip) relationship describes the average bond stress trend with respect to the slip occurring between the reinforcement and the concrete surrounding it, namely the tangential separation at the interface.

Pull-out tests concerning the rebar-concrete interface characterisation consist of applying a force to the free end of a rebar embedded in a prismatic concrete specimen. Then, by pulling the bar out of the specimen under controlled displacements, it is possible to track the force trend and therefore to compute the bond stress. The maximum measured pull-out force corresponds to the bond strength between the two surfaces in contact. A scheme of the pull-out test according to the standard RILEM RC6 (RILEM TC, 1983) is reported in Fig. 2.6a, while a typical response curve (bond-slip relationship) is shown in Fig. 2.6b.

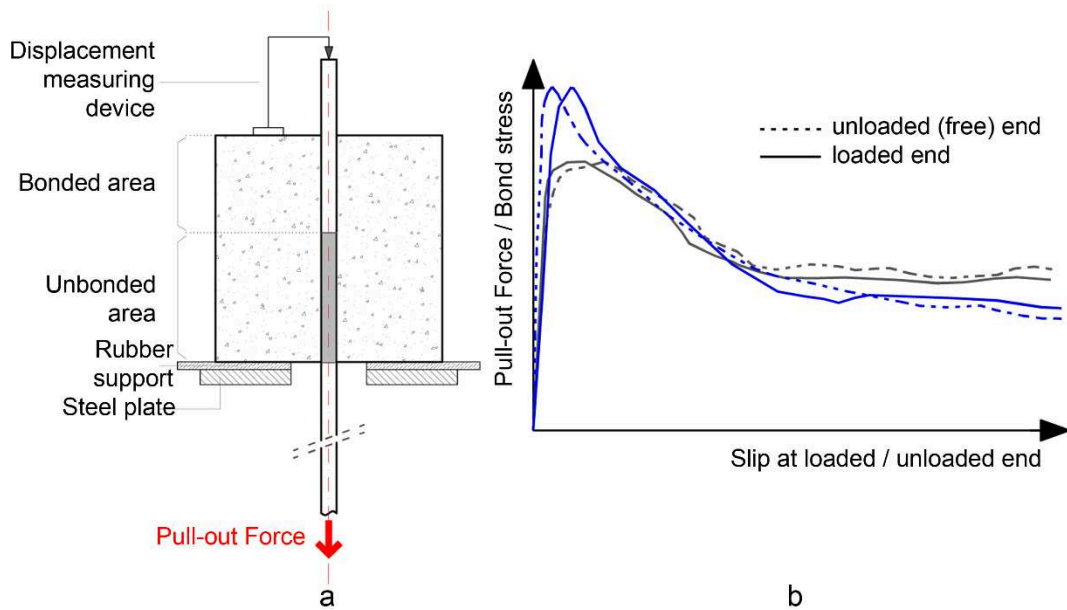


Figure 2.6 - a) Scheme of pull-out test according to the standard RILEM RC6; and b) typical bond-slip relationship derived from a pull-out test

It is worth underlining that a bond-slip relationship represents the whole behaviour of the interface under pull-out conditions, describing the force trend during the bonded phase and the debonding process. Therefore, pull-out results can be viewed as the macroscopic response of simultaneous failure micro-mechanisms acting at the interface.

As far as bond between reinforcement and concrete is concerned, the main mechanisms governing the transfer of forces from the bar to the surrounding concrete are (ACI Committee 408, 2003):

- chemical adhesion;
- friction;
- mechanical interlocking.

Depending on numerous factors and, above all, on bar and matrix geometrical characteristics, each of the three previous mechanisms is more or less involved in the debonding process.

Detailed aspects of the interaction between several types of reinforcement and concrete are reported below in order to better understand which factors influence bond behaviour in different situations. Moreover, particular attention has been dedicated to the case of plain rebars, highlighting some aspects that have not been thoroughly investigated in the literature with respect to the bond mechanisms involved in this particular case.

2.3.3 Steel rebars-concrete interaction

Traditional reinforcement for RC consists of steel reinforcing bars, thus, a vast amount of research has been focused on the mechanisms developed at the interface between steel and concrete. Despite this, the understanding of the influence of local characteristics of the Steel-Concrete Interface (SCI) still presents uncertainties. In fact, as recently noted by Angst et al. in (Angst et al., 2017), the rebar-matrix interface represents a very complex zone. It exhibits significant spatial inhomogeneity in terms of material composition and physical and chemical properties. The occurrence of features such as voids, honeycombs, cracks, bleed water zones and the microstructures both of bar material and concrete contributes to inhomogeneity of the SCI. Moreover, these features span over a large range of dimensions which goes from the nanometre scale (e.g. passive layer at steel reinforcement surface) to the order of centimetres (e.g. voids or aggregates occurring at the interface). All these aspects strongly affect the rebar-matrix bond-slip behaviour, which becomes even more a crucial aspect to analyse.

Steel bars-to-concrete interaction has been largely investigated in terms of bond behaviour (for a detailed review, see (CEB-FIP Report, 2000)) both experimentally and theoretically (Meaud et al., 2014) (Kabir and Islam, 2014) due to the great impact that this aspect has on the structural performance of the whole RC structure. The FIB bulletin n°10, ‘*Bond of reinforcement in concrete*’ (CEB-FIP Report, 2000), describes the stages of a bond-slip relationship with regard to both plain and deformed steel reinforcements subjected to a pull-out force from a concrete matrix. The four different stages identified in the FIB bulletin n°10 are shown in Fig. 2.7 and described below (CEB-FIP Report, 2000):

- **Stage I (uncracked concrete):** for low bond-stress values, bond efficiency is assured mostly by chemical adhesion. At this stage, almost no bar slip occurs, but highly localised stresses arise close to the lugs for ribbed bars. Chemical adhesion is also associated with the micromechanical interaction due to the microscopically rough steel surface. However, this mechanism still plays a minor role on the whole chemical and physical adhesion.
- **Stage II (first cracking):** for higher bond stress values, the chemical adhesion breaks down. For deformed (ribbed) bars, the lugs induce large bearing stresses in the concrete and transverse microcracks originate at the tips of the lugs allowing the bar to slip, but the wedging action of the lugs remains limited and there is no concrete splitting.
- **Stage III:** as the bond stress increases, the longitudinal cracks (splitting cracks) start to spread radially, owing to the wedging action promoted by the crushed concrete at the front of the ribs. The surrounding concrete carries out a confinement action on the bar, and bond strength and stiffness are assured mostly by the interlocking among the reinforcement, the concrete struts radiating from the bar and the undamaged outer concrete cover. In the case of poor transverse reinforcement, this stage ends as soon as concrete splitting reaches the outer surface of the concrete member. Afterwards, a sudden failure occurs depending on transverse confinement (Stage IVb, *splitting failure*). However, in relatively-long

anchorage with moderate confinement, a pull-out failure usually occurs after splitting. Hence, bond failure may be defined as '*splitting-induced pull-out failure*'. As for the case presenting heavy transverse reinforcement or large concrete cover, splitting is prevented by their confining action, and concrete splitting remains limited to a cracked core around the bar (Stage IVc, *pull-out failure*).

- Stage IVa: for plain bars this stage immediately follows the significant reduction of chemical adhesion. The force transfer is mostly provided by friction and is strongly affected by the transverse pressure. Concrete shrinkage and bar roughness favour friction, while interface wear along the sliding plane reduces the radial compressive stresses, eventually leading to the progressive reduction of the bond stress.
- Stage IVb: for deformed bars confined by light-to-medium transverse reinforcement, the longitudinal cracks (splitting cracks) break out through the whole cover, and the bond tends to fail abruptly. Conversely, a sufficient amount of transverse reinforcement (namely stirrups) can guarantee a confinement action able to assure bond efficiency in spite of concrete splitting. At increasing slip values, the bond strength reaches a peak and then starts to decrease, maintaining significant values also for very large slip. In the end, bond behaviour tends to become of the dry-friction type (Coulomb type), since the wedging action between the ribs and concrete does not increase appreciably any more.
- Stage IVc: in the case of deformed bars heavily confined by, splitting does not occur and bond failure is caused by bar pull-out. The transfer mechanism of the forces changes from rib bearing to friction. Under increasing loading, the interface is smoothed due to wear and concrete crush, eventually leading to a further decrease of bond stress.

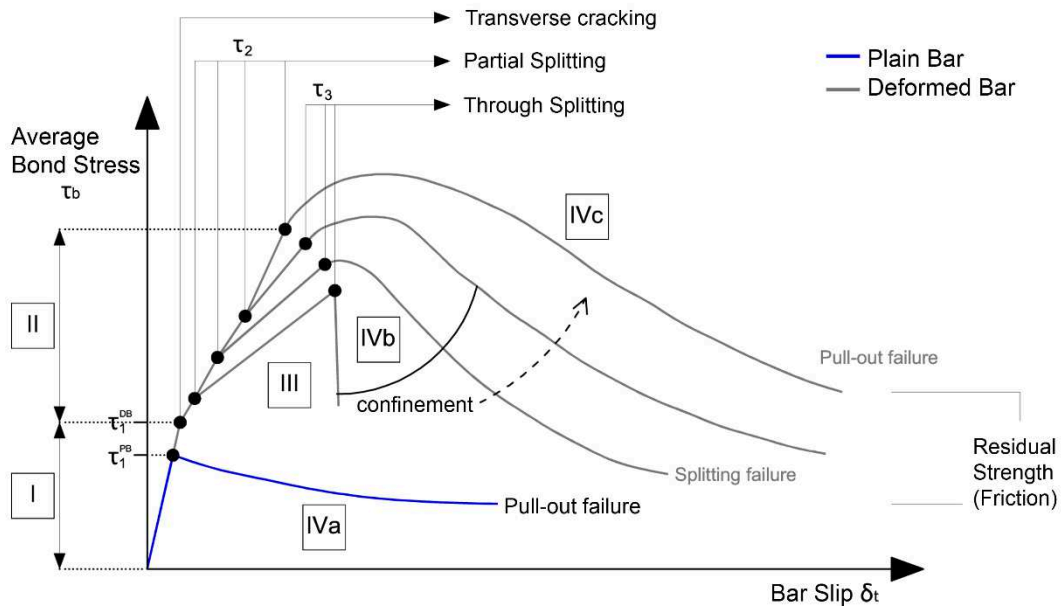


Figure 2.7 - Typical stages of a bond-slip relationship for ribbed and plain steel reinforcing bars [based on (CEB-FIP Report, 2000)]

The main mechanisms here identified as those governing the pull-out process, i.e. chemical adhesion, friction, and mechanical interlocking, can be considered not just related specifically to steel-concrete interfaces, but a general guide to explain pull-out responses of several reinforcement materials with respect to concrete matrices. Nevertheless, depending on the type of interface under investigation (in terms of materials, geometry and size of reinforcement), some mechanisms can prevail on others, resulting in different shapes of the bond-slip relationship.

2.3.3.1 Factors influencing bond

Many factors affect the bond between reinforcing bars and concrete. They can be grouped into three categories, i.e. structural characteristics, bar properties, and concrete properties. An extended and detailed list of these factors is included in (CEB-FIP Report, 2000) and (ACI Committee 408, 2003). Some of the main parameters affecting bond are reported and discussed in this paragraph.

Among the structural characteristics, it is worth mentioning the bond length. Extending the bond length of a reinforcing bar results in an increase in bond strength, that is not proportional to the increase in bonded length due to the not uniform distribution of bond forces along the bar. It has been demonstrated (ACI Committee 408, 2003) that, although the relationship between the bond force and the bonded length is not proportional, it is nearly linear. Another factor influencing bond and classified under the structural characteristics, is represented by the transverse reinforcement. The presence of transverse reinforcement is able to increase the confinement, which leads to higher bond strengths,

eventually converting a splitting failure to a pull-out failure (see Fig. 2.7). However, if transverse reinforcement is above that needed to cause the transition from a splitting to a pull-out failure, it becomes progressively less effective, resulting in no bond strength increase (Orangun et al., 1977).

As far as bar properties are concerned, the main factors influencing bond are the bar size and geometry and the bar surface features. As the bar size (diameter) increases, a longer bond length is required to fully develop a given stress; but, at the same time, for a given splice length, larger bars achieve higher bond forces than smaller bars for the same degree of confinement (ACI Committee 408, 2003). Thus, the relationship between bar size and bond performance is not always appreciable. When evaluated in terms of bond stress, bars with smaller diameters appear to provide greater strengths than larger bars (ACI Committee 408, 2003). Bar geometry, i.e. deformation pattern, affects bond performance in terms of both achieved bond strengths and failure modes. Many researches focused on the differences between plain (or smooth) and ribbed rebars and also between ribbed bars with different geometric deformation patterns. Generally, it can be assessed that the presence of ribs strongly increases the bond strength. Particularly, among the ribs geometrical characteristics, height and spacing have been found to be the most influencing parameters for bond performance, while rib inclination and rib face angle have a minor effect on bond (Silva Filho et al., 2012).

With regard to concrete properties, strength is certainly the first aspect to take into consideration. Both the compressive and tensile strengths have been found to play a non-negligible role in the development of bond performance. An increase in the concrete compressive strength corresponds to higher bearing capacity, resulting in better bond performances. In this context, for values of the compressive strength up to 55 MPa, the effect of concrete properties on bond strength can be represented using the square root of the compressive strength, $\sqrt{f'_c}$ (CEB-FIP Report, 2000), (ACI Committee 408, 2003). As for the concrete tensile strength, instead, it is involved in the development of bond strength because it is the main parameter governing the (splitting) cracking phenomenon of the concrete surrounding the reinforcement. The higher is the concrete tensile strength, the slower is the cracking formation process.

The last aspect mentioned with reference to the concrete properties, is the aggregate type and quantity. The studies carried out by Darwin et al. (Darwin et al., 1998) and Zuo and Darwin (Zuo and Darwin, 2000) demonstrated that for bars not confined with transverse reinforcement, the increasing in the strength of coarse aggregates resulted in higher bond strengths. As for confined bars, instead, the increase in both the strength and the quantity of the coarse phase of the aggregates improved the bond performances.

2.3.3.2 Influence of steel reinforcement corrosion on bond behaviour

As far as steel reinforcement is concerned, a non-negligible aspect is represented by corrosion, which is expected to affect bond in several ways (CEB-FIP Report, 2000).

Generally, the effects of corrosion on residual structural capacity can be divided into three main categories, i.e. those aspects affecting the reinforcement itself, those influencing

the surrounding concrete, and those which affect the interaction between the two (Cairns et al., 2007). Some of the most relevant aspects belonging to these three groups are here discussed in order to outline the bond performance of the bar-matrix interface under growing corrosion level (CL).

It is well-known that corrosion products, i.e. oxides, occupy a larger volume than that occupied by non-corroded steel bar (Jaffer and Hansson, 2009). The formation of expansive oxides at the bar surface generates radial pressure around the bars, and can originate cracking due to tensile stresses in the surrounding concrete (Coccia et al., 2016). Another direct effect of corrosion is the progressive loss of bar cross-section (Cairns et al., 2007), which can be also associated to the degradation of the ribs height. As a consequence, the reduction of the effective bearing area of the rebar significantly weakens the mechanisms governing bond behaviour, i.e. chemical adhesion, friction and mechanical interlocking. However, several studies on this topic ((Al-Sulaimani et al., 1990), (Almusallam et al., 1996), (Cabrera, 1996)) reported an increase of bond strength for low values of corrosion. In fact, the surface roughness increased by rust and the presence of oxides around the bar, actually generate higher radial stresses that, at the beginning, increase the frictional component of bond. Particularly, Al-Sulaimani et al. (Al-Sulaimani et al., 1990), related the mass loss of the bar to the effects induced by corrosion on bond. As a results of their experiments, they noted an increase of the bond stress for corrosion levels up to about 1 % in mass loss; for higher corrosion levels a sharp reduction of bond strength was measured (of about 50 % for mass loss of 5–6 %). Similar results were obtained by Almusallam et al. (Almusallam et al., 1996), who reported an increase of bond (maximum increase around 17 %) for corrosion levels up to 5 % in mass loss. Afterward, an abrupt decrease of strength was observed with bond reduction of about 80 % for 10% of mass loss. The results obtained by Lee et al. in (Lee et al., 2002) confirmed this trend, relating also the corrosion-induced bond performance to the degree of confinement of the considered specimen. They highlighted that, at first, for both confined and unconfined specimens the bond strength increases, whereas for growing corrosion level the failure of the confined specimens was less influenced by corrosion than that exhibited by unconfined specimens.

Another aspect that has been found to be relevant when the influence of corrosion on bond is concerned, is the bar type. Plain (or smooth) and ribbed rebars have been tested by Fang et al. (Fang et al., 2004) and Lundgren (Lundgren, 2007) in order to understand the differences in their bond behaviour under corrosion actions. The main mechanism activated by (uncorroded) ribbed bars under pull-out conditions is the mechanical interlocking, which may lead to the splitting failure (see Fig. 2.7), especially for unconfined (or low-confined) specimens. On the contrary, as plain bars generate far lower splitting stresses than ribbed bars, it is quite rare for uncorroded plain bars to notice the cracking of surrounding concrete under pull-out conditions. However, for both ribbed and plain bars, corrosion causes an initial increase in bond strength, which is much remarkable in the case of plain bars. This is because the higher surface roughness enhances the initial adhesion, and the increase in radial stresses has a direct influence on the bond stresses that can be carried by friction. Adhesion and friction, which are directly influenced by the corrosion action, play a much more significant role in the pull-out mechanism of plain bars than that

of ribbed bars. Fang et al. (Fang et al., 2004) found out that for plain rebars at corrosion level of around 5%, the bond strength increase is 20%, while no substantial increase has been noticed for ribbed bars, whose bond strength had already decreased (12% of the initial value) at corrosion level of 6%. Larger corrosion levels, instead, always abruptly weaken the bond capacity and ductility, especially when elements are not sufficiently confined (Lundgren, 2007). Moreover, growing corrosion levels lead to the development of longitudinal cracking, which are exhibited from both plain and ribbed bars.

To conclude, it can be assessed that corrosion has basically the same effect on plain and ribbed bars, i.e. the appearance of splitting stresses due to the bar volume increase (Lundgren, 2007). However, it affects the behaviour of plain and ribbed bars in a different manner. As long as the concrete cover is not cracked, corrosion improves bond capacity of plain bars, whereas it might increase the bond capacity of ribbed bars, but only to a minor extent. High corrosion levels, instead, results in longitudinal cracking of the concrete cover, damaging the bond. Moreover, if not sufficient transversal reinforcement is supplied, the corrosion action is even more detrimental, because no confinement prevents the splitting cracks that may arise due to the corrosion (Lundgren, 2007).

A general scheme of the corrosion influence on bond performance is provided in Fig. 2.8.

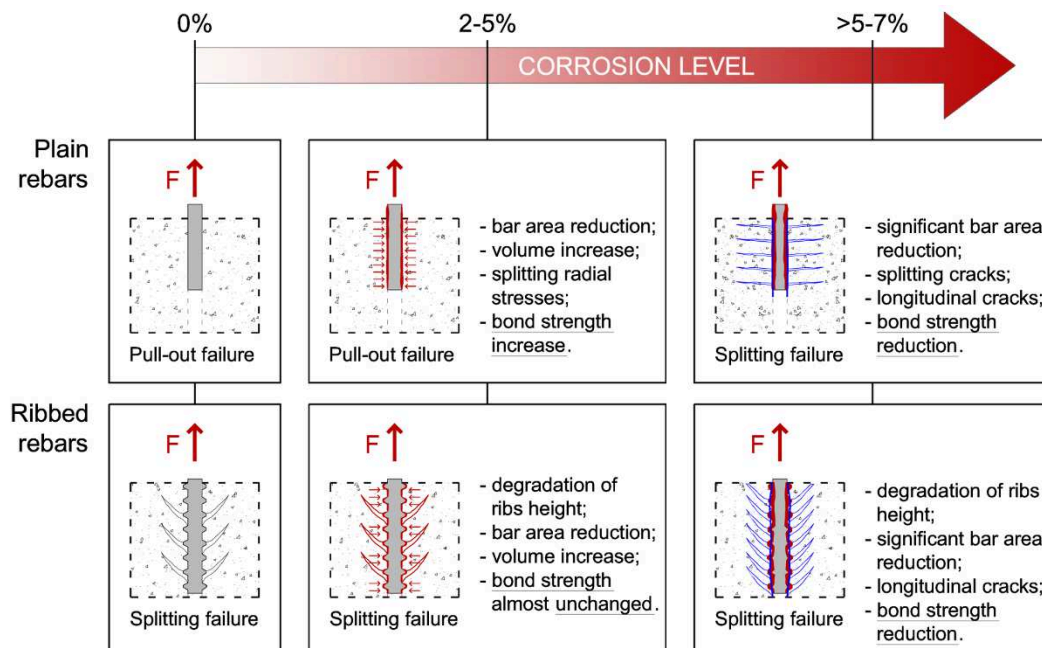


Figure 2.8 - Scheme of the influence of corrosion on bond performance for plain and ribbed reinforcing bars

2.3.4 Interaction between concrete and alternative reinforcement

As mentioned in the introduction, many efforts have been made by researchers to improve the durability of RC structures, such as adding corrosion inhibitors in the concrete mixture (Hansson et al., 1998), (Söylev and Richardson, 2008) and coating the steel rebar surface with both metallic (galvanized steel (Yeomans, 2013)) and organic (epoxy-coated steel (Dong et al., 2012)) films so as to increase corrosion resistance of reinforcement. In addition, the possibility to reinforce concrete with alternative materials less susceptible to corrosion than carbon steel, has been also explored. Among metal reinforcements, some studies have investigated the behaviour of nickel-iron alloys (Kepler and Locke, 2000) and, particularly, of stainless steel reinforcing bars (Ahlborn and DenHartigh, 2002), (Ertzibengoa et al., 2012). A considerable amount of research has been also focused on non-metallic materials, especially concerning Fibre Reinforced Polymers (FRP) (Bank et al., 2003), such as the better known Carbon (CFRP), Glass (GFRP) and Aramid (AFRP) Fibre Reinforced Polymers (Uomoto et al., 2002), and, more recently, the Basalt Fibre Reinforced Plastics (BFRPs) (Urbanski et al., 2013).

2.3.4.1 Galvanised steel reinforcement

One of the most used method for reducing corrosion of rebars is represented by hot-dip galvanising systems (Cheng et al., 2005). Steel rebars are coated with zinc, which acts as sacrificial anode in the corrosion cell and generates much less volume change of corrosion products than carbon steel. As the zinc-coating is applied to the rebar surface, the interface properties between reinforcement and concrete are expected to change. Cheng et al. (Cheng et al., 2005) reported that the bond strength of uncoated rebars is 5–10% less than zinc-coated ones before the exposure to an aggressive environment. Then, during the durability test, the reduction of bond strength for zinc-coated rebars is less important than that exhibited by uncoated rebars. However, other studies on zinc-coating influence on bond strength (Pernicova et al., 2017), (Dong et al., 2012) have unearthed some problems concerning the initial corrosion of zinc surface in fresh concrete, with the subsequent formation of hydrogen. The latter irreversibly increases porosity of concrete at rebar-matrix interface, resulting in significant decreasing of the bond strength.

2.3.4.2 Epoxy-coated reinforcement

Epoxy-coated reinforcing bars are used in concrete structures where corrosion protection is one of the principal design requirements. The negative impact of epoxy coating on the bond strength between reinforcing steel and concrete is well established ((Treece and Jirsa, 1989), (Choi et al., 1991); (Hester et al., 1993); (Hadj-Ghaffari et al., 1994)). This is because an epoxy coating is much smoother than the normal mill scale surface of a 'black' (i.e. non-coated) bar and is chemically inert. Chemical adhesion and friction between bar and concrete are therefore reduced by coating (CEB-FIP Report, 2000), (Hester et al., 1993).

2.3.4.3 Stainless steel reinforcement

A detailed and extended review of the research findings on the possibility to substitute traditional carbon steel rebars with stainless steel ones has been provided by Mc Donald et al. in (McDonald et al., 1995). They discussed the potentialities of both using solid stainless steel and stainless steel-clad reinforcing bars in terms of durability and costs with respect to traditional steel rebars. However, the bond behaviour between this material and concrete had not been investigated for several years. Data provided by D. Ertzibengoa et al. (Ertzibengoa et al., 2012) on bond performance of flat stainless steel rebars in concrete, in fact, are quite recent (2012). They concluded that, the use of stainless steel instead of carbon steel is not considerably influencing the bond capacity of the reinforcement when ribbed rebars are used, while parameters as reinforcement shape or rib pattern are far more deterministic (Ertzibengoa et al., 2012). As far as plain rebars are concerned, instead, bond strength values in the case of stainless steel reinforcements have been found to be lower than those related to carbon steel-concrete interface. They also found out that increasing micro-roughness of plain stainless steel rebars results in enhanced bond performance.

2.3.4.4 FRP reinforcement

A considerable amount of research investigating FRP materials as an effective solution for the replacement of steel reinforcement in RC structures has been conducted in the last decades (Achillides and Pilakoutas, 2004), (Baena et al., 2009), (Antonietta Aiello et al., 2007). In most of the cases, the FRP products consist of continuous glass, carbon or aramid fibres embedded in a resin matrix (epoxy, vinyl ester and polyester). Bond between concrete and FRP reinforcing bars is the key to understand the composite action of FRP RC. Thus, sufficient bond must be mobilised between reinforcement and concrete for successful transfer of forces from reinforcement to concrete (CEB-FIP Report, 2000). The bond behaviour of FRP bars to concrete is expected to vary from that of conventional steel bars, since various key parameters that influence bond performance are significantly different. The main differences, identified in (Achillides, 1998) and (Muñoz, 2011), are:

- the modulus of elasticity of FRP bars is generally lower than that of steel, both in the lateral and longitudinal directions. With reference to the polymers more used in the form of bars for reinforcing concrete, Glass FRP, usually, exhibit the lowest elastic modulus (i.e. around 20-30% of that of steel), while Carbon FRP the highest (i.e. around 50-70% of that of steel);
- the shear stiffness of FRP is much lower than that of steel;
- the resin matrix has lower shear strength than steel.

The bond performance between FRP bars and concrete along the anchorage length is described in the FIB bulletin n°10 (CEB-FIP Report, 2000), which highlights the differences between plain and deformed FRP bars in terms of bond performance:

- Bond of plain bars is mainly provided by the chemical adhesion mechanism, as it happens in the other analysed cases (steel, stainless steel, epoxy-coated bars, etc.). However, for plain FRP reinforcement, the inter-laminar shear strength between adjacent layers of fibres might govern the failure process if the chemical adhesion

between FRP and concrete is sufficiently high. Since no tensile cracking is expected to occur along the plain bar, splitting bond forces with consequent splitting failure are unlikely to originate.

- Deformed FRP bar-to-concrete interaction is described in Fig. 2.9 (CEB-FIP Report, 2000). The graph is similar to that reported for steel reinforcement, since the mechanisms for a deformed bar subjected to pull-out are mostly depending on bar size and geometry, surface pattern, etc., and not on the nature of the reinforcement material. A brief description of the graph reported in Fig. 2.9 is here provided, referring to (CEB-FIP Report, 2000) and (Achillides, 1998) for more details.

At the beginning of loading (Section OA), the main mechanism is the chemical adhesion between FRP and concrete. As the load increases (Section AB), i.e. for higher bond stress $\tau > \tau_a$, adhesion breaks down and the bond mechanism changes. The slip at the loaded end of the bar gradually increases and bearing stresses arise in the concrete cover due to the deformed pattern of the bar, giving birth to the microcracking process. However, since the surface deformations of FRP bars are much ‘softer’ than those of steel bars, it is believed that the initiation of transverse microcracks is delayed with respect to steel bars behaviour. For growing slips (Section BC), the bearing stress from the bar deformations (or ribs) to the surrounding concrete considerably increases. The splitting resistance, τ_{sp} , is influenced by the confinement provided by the concrete cover, transverse reinforcement and pressure. If the value of the tensile hoop stress exceeds the tensile strength of concrete, splitting cracks may develop in the concrete surrounding the bar, resulting in the splitting failure mechanism. If sufficient resistance to splitting is provided by satisfactory confinement, the bond stress can reach the maximum bond strength, τ^* (Section CD). Depending on the ratio between concrete strength and shear strength of surface deformations, four different modes of bond failure can be identified as:

- *Shearing off part or all the surface deformations of the bar*: according to this failure mode, the bond strength of FRP bars appears to be governed either by the shear strength between successive layers of fibres or by the shear strength of bar deformations. Therefore, an increase in concrete strength will not provide higher bond strength. Furthermore, this type of bond failure will yield the highest possible bond resistance from a bar;
- *Concrete shear failure*: this mode of failure is similar to that of ribbed steel bars because failure occurs in the concrete, which crushes in front of bar deformations;
- *Combined mode*: for intermediate levels of concrete strength, a combined mode of the above failures is likely to develop;
- *Squeeze through*: Due to the low stiffness in the radial direction, the bar can ‘squeeze through’ the concrete. Bond resistance is provided by friction through wedging of the bar deformations on the surrounding concrete.

Once the bond strength has been reached, the bearing mechanism breaks down and the bond stress significantly decreases. The residual bond strength is mainly dependent on the frictional resistance, τ_r .

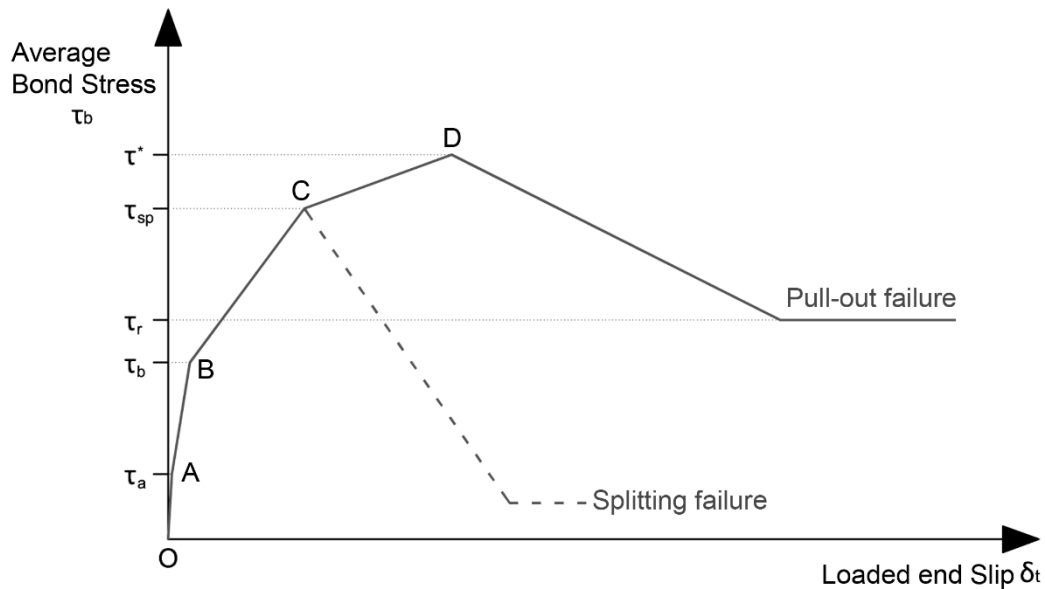


Figure 2.9 - Typical stages of a bond-slip relationship for deformed FRP bars [based on (CEB-FIP Report, 2000)]

As far as FRP reinforcement is concerned, it is worth mentioning the large variety of possible fibres intended for reinforcing the resin matrix. Thus, bond performance is also influenced by differences in the nature of the fibres (e.g. Aramid, Carbon, Glass, Hybrid, Basalt, etc.). Some of the results obtained for several types of FRP bars, with different surface treatments, under pull-out conditions are taken into account in this research for comparison with the tests here carried out.

2.3.5 Plain rebars behaviour under pull-out conditions

The interaction between different reinforcement material and concrete has been analysed in the previous paragraphs. As already mentioned, when plain or deformed bars are used, the failure mechanisms under pull-out condition significantly changes.

Nowadays, ribbed rebars are always employed in RC structures, thus, their bond behaviour with respect to concrete has attracted more attention than that of plain bars from a practical viewpoint. Moreover, as far as bond strength is concerned, ribbed rebars are characterised by much higher values than those typically exhibited by plain rebars. However, for some specific problems the necessity to study also the bond behaviour of plain rebars arises. In fact, a large number of existing RC buildings were constructed with plain reinforcing bars before the 1970s, and now many of them are in need of rehabilitation (Feldman and Bartlett, 2005), (Guohua Xing, Cheng Zhou, Tao Wu, 2015), (Verderame et

al., 2009). In addition, plain rebars are often used in precast concrete elements (Mo and Chan, 1996), thus their bond and anchorage in concrete needs to be understood. Another reason why plain rebars are taken into consideration when bond performance is investigated, is for comparison purposes with respect to ribbed bars.

The main mechanisms acting at the interface under pull-out conditions are chemical adhesion, friction and mechanical interlocking. It is commonly accepted that plain rebars cannot transfer bond forces by mechanical interlock due to the absence of lugs or other surface deformations (Feldman and Bartlett, 2005), (Guohua Xing, Cheng Zhou, TaoWu, 2015). Thus, researches on experimental bond behaviour between plain rebars and concrete usually neglect this phenomenon, assessing that bond is mostly transferred by adhesion and friction. The FIB bulletin n 10 (CEB-FIP Report, 2000) also reports that immediately after the chemical adhesion is lost, force transfer is provided by friction and is strongly affected by the transverse pressure and bar roughness. The ACI report on bond (ACI Committee 408, 2003) remarks that friction plays an important role for plain bars, with slip-induced friction resulting from transverse stresses at the bar surface caused by small variations in bar shape and surface roughness.

In the case of plain reinforcement, pull-out test results are expected to be more accurate for the assessment of the bond strength (Feldman and Bartlett, 2005). In fact, the pull-out test setup is usually characterised by the presence of a rigid plate which, in the case of ribbed bars, might lead to overestimate the bond strength. This is because the plate at the specimen base can induce an increase in lateral confinement which might prevent the splitting failure. As for plain rebars, instead, the splitting failure is unlikely to happen, thus the measured bond strength through pull-out tests can be considered much more reliable than that measured for ribbed rebars.

2.3.5.1 The role of surface roughness

Some studies ((Feldman and Bartlett, 2005), (Guohua Xing, Cheng Zhou, TaoWu, 2015)) and technical reports ((CEB-FIP Report, 2000), (ACI Committee 408, 2003)) remark the importance of the role of bar surface roughness on the bond performance. Particularly, Feldman et al. (Feldman and Bartlett, 2005) investigated the variability of bond strength for different surface roughness characteristics (sandblast treatments more or less heavy) by carrying out a large series of pull-out tests. Through these tests they found out that:

- 1) increases in bar roughness result in higher bond strengths and longer slip plateaus at maximum load;
- 2) the debonding between plain rebars and concrete is governed by two distinct bond mechanisms, i.e. adhesion before slip occurs, and wedging of small particles that break free from concrete upon slip.

Xing et al. (Guohua Xing, Cheng Zhou, TaoWu, 2015) also attributed a relevant role to the bar roughness, measuring the difference of bond strengths among plain smooth aluminium and plain, but rough, steel rebars. Fib bulletin (CEB-FIP Report, 2000) had already identified the wedging of stone particles mechanism as a main factor controlling bond for plain rebars and prestressing tendons for precast concrete. Then, ACI report (ACI

Committee 408, 2003) remarked that surface roughness is responsible for part of the frictional forces arising at the interface.

Other evidence of the roughness importance is provided by researches on bond performance of epoxy-coated bars. In fact, when an epoxy-coating is applied, surface roughness decreases, resulting in worse bond performances (Choi et al., 1991) than those typical for uncoated steel bars.

As far as non-metallic reinforcement is concerned, FRP bars with different surface characteristics have been tested in order to evaluate their pull-out behaviour. Some researches tend to neglect the mechanical action induced by surface roughness, and therefore consider bond solely dependent on the type of fibres and matrices (Nanni et al., 1995). Other studies, instead, observed that increases in surface roughness resulted in higher bond strengths and greater friction action after the loss of adhesion (Baena et al., 2009).

To conclude, it can be assessed that, despite the proven influence of the rebar surface roughness on bond capacity, its role on the interfacial mechanisms during the pull-out failure seems, however, to need further investigation.

2.3.6 Influence of the matrix nature on bond behaviour

The concrete physical and mechanical characteristics represent another factor influencing the bond behaviour at the reinforcement-matrix interface (CEB-FIP Report, 2000). The ACI report 408R-03 (ACI Committee 408, 2003) provides a comprehensive list of the concrete mechanical properties affecting the bond performance between concrete and steel reinforcement, as introduced in paragraph 2.3.3.1 of the present chapter. Concrete compressive and tensile strengths, its fracture toughness, and fresh state characteristics (e.g. workability and slump) have been found to influence the bond performance. Thus, it is clear how all these aspects change when different concrete mixes are concerned. A considerable amount of research has been focused on characterising the bond behaviour between reinforcement and several types of concrete matrices.

Xiao and Falkner (Xiao and Falkner, 2007) carried out a series of pull-out tests on specimens made of recycled aggregate concrete, considering deformed and plain steel reinforcing bars. Results of their experiments proved that the general shape of the bond-slip relationship between recycled aggregate concrete and steel rebars is very similar to the one for normal concrete and steel rebars. In terms of bond strength developed by plain rebars, they observed a decrease of 12% and 6% when recycled coarse aggregates were replaced with a percentage of 50% and 100%, respectively. No significant changes in bond strength values have been reported in the case of deformed bars. For the case of the same compressive strength, the bond strength between the recycled aggregate concrete and steel rebars has been found to be higher than the one developed by normal concrete and steel rebars (Xiao and Falkner, 2007). Other authors (Seara-Paz et al., 2014), instead, carried out experimental pull-out tests on recycled aggregate concrete specimens with different percentages of natural coarse aggregate replaced by recycled coarse aggregate (20, 50 and 100 %). They reported a decrease in the bond strength with the increase of recycled

aggregate content. It was thus deduced that the amount of recycled aggregate adversely affects bond performance.

The bond behaviour between steel rebars and fibre-reinforced concrete matrix has been also investigated in the literature (Harajli et al., 2002), (Annapoorna and Suresh, 2017). Harajli et al. (Harajli et al., 2002) conducted a series of experimental pull-out tests in order to evaluate the influence of fibre reinforcement on the bond performance. In their study, it was found that the improved splitting strength and the enhanced ductility typical of the fibre-reinforced concrete led to increase bond strength. Particularly, for fibre volume fraction equal to 2%, the bond strength increase was 33%. In the experiments carried out by Annapoorna et al. (Annapoorna and Suresh, 2017), instead, the bond strength did not significantly change, but FRC matrix improved the post cracking behaviour of the specimens.

When high strength concrete matrices are considered, the bond strength has been found to increase with the increase of concrete strength and of concrete age (Shen et al., 2016). Moreover, the increasing rate of the early-age bond strength is much higher than that related to the axial compressive strength (Shen et al., 2016).

Finally, the influence of lightweight aggregates on bond performance is taken into account. Due to the lower strength of the aggregate, lightweight concrete should have lower tensile strength, fracture energy, and local bearing capacity than normalweight concrete with the same compressive strength. As a result, the bond strength of rebars with respect to lightweight concrete has been found to be lower than that of bars embedded in normalweight concrete (ACI Committee 408, 2003). This trend was confirmed by the study conducted by Anwar Hossain (Anwar Hossain, 2008), which considered lightweight aggregates made of pumice. It was found that load-slip relationships of plain bars embedded in pumice lightweight concrete exhibited similar pre and post-peak responses to those of the specimens made of normal concrete. However, the bond strength values have been found to be lower in the case of pumice concrete, especially in the case of ribbed bars. Different lightweight aggregates were considered by Al-shannang and Charif (Al-shannang and Charif, 2017). They found that the values of bond strength in this case are comparable to those obtained using normal concrete. Recently, Trad et al. (Trad et al., 2018) pointed out that the literature review showed contrasting findings regarding the bond strength comparison between lightweight and normal concrete. In their study they identified a threshold of concrete density (i.e. 1600 kg/m³) above which there is no significant difference between concrete mixes with lightweight or normal aggregates in terms of bond strength.

2.4 Bond modelling

The vast amount of experimental data obtained from pull-out tests of rebars (especially steel ones) from concrete specimens, has laid the basis for the mathematical modelling of bond-slip laws. The FIB state-of-art report on bond (CEB-FIP Report, 2000) specifies that *“only by starting from basic properties and fundamental mechanisms (microlevel) can constitutive or behavioural laws be formulated in a consistent way (mesolevel), in order to*

be introduced into the analysis (macrolevel)”. Thus, the first and essential aspect to take into consideration is the local bond-slip relationship, which describes the interfacial interaction between the reinforcement and the matrix at the microlevel.

From the analytical point of view, a constitutive bond-slip relationship can be used to describe bond and introduced in the solution of problems such as the calculation of the development length. The CEB-FIP Model Code 2010 (fib, 2012a) reports the local bond-steel relationships for steel and FRP reinforcements, unifying the numerous models previously developed based on the wide database of pull-out test results.

2.4.1 Analytical formulation

The CEB-FIP Model code 2010 (fib, 2012a) provides analytical models for the description of the bond behaviour for both steel and FRP rebars. In fact, the differences among the two reinforcing materials, analysed in the previous paragraphs, lead to different mathematical descriptions. Values of bond strength are obtained by assuming a constant distribution of bond stresses along the bond length. This procedure has been widely accepted when dealing with steel reinforcement, because slip values at the loaded and unloaded ends are very similar, making reasonable to take an average uniform distribution of bond stresses. When FRP rebars are considered, instead, the value of the slip at the loaded end significantly differs from that at the unloaded end, meaning that the constant bond stress distribution assumption is not reliable (Achillides, 1998), (Muñoz, 2011).

Both of the cases are following considered, in order to understand how the analytical formulation can represent the difference highlighted.

2.4.1.1 Steel reinforcement

For monotonic loading the bond stresses between concrete and reinforcing bar for pull-out and splitting failures can be calculated as a function of the relative displacement (see Fig. 2.10), s , according to the following Eqs. (2.1)-(2.4):

$$\tau_b = \tau_{max}(s/s_1)^\alpha \quad \text{for } 0 \leq s \leq s_1 \quad (2.1)$$

$$\tau_b = \tau_{max} \quad \text{for } s_1 \leq s \leq s_2 \quad (2.2)$$

$$\tau_b = \tau_{max}(\tau_{max} - \tau_f) \frac{s-s_2}{s_3-s_2} \quad \text{for } s_2 \leq s \leq s_3 \quad (2.3)$$

$$\tau_f \quad \text{for } s_3 < s \quad (2.4)$$

where:

- s is the slip, i.e. the relative displacement between steel and concrete: $s = u_s - u_c$, with u_s representing the absolute displacements of the steel bar and u_c those of the concrete matrix;
- τ_{max} is the bond strength; and τ_f is the residual bond stress;
- $0 < \alpha \leq 1$ is a coefficient that controls the shape of first branch before the onset of debonding.

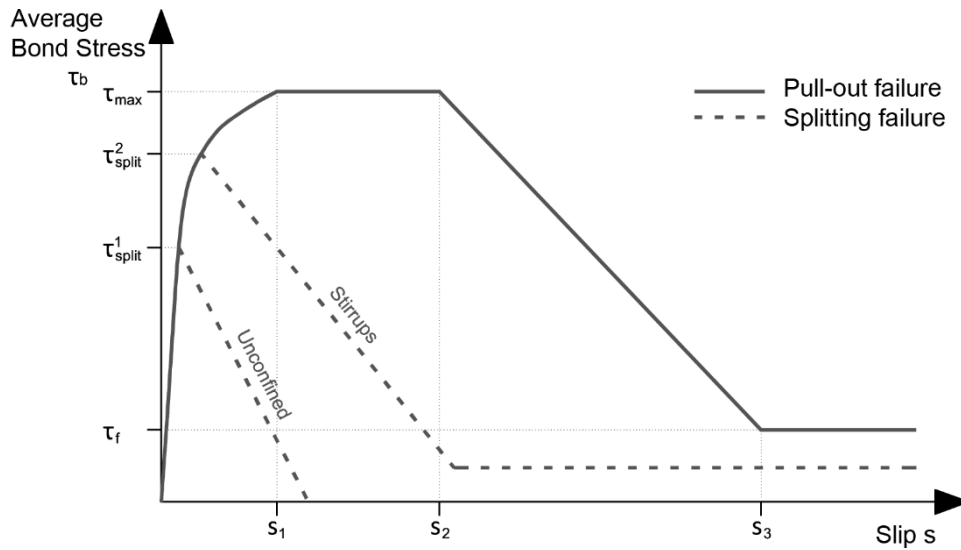


Figure 2.10 - Analytical bond-slip relationship for steel reinforcing bar-to-concrete interface

Depending on the type of failure (pull-out or splitting mechanism) and on confinement conditions, the CEB-FIP model code (fib, 2012a) provides the values of the parameters involved in the above equations (Eqs. (2.1) – (2.4)) for both ribbed and plain rebars (Table 6.1-1 and Table 6.1-2 of the CEB-FIP Model Code 2010 (fib, 2012a), respectively). It is worth mentioning that, according to the CEB-FIP model code 2010 (fib, 2012a), in the case of plain reinforcements $s_1=s_2=s_3$ and $\tau_{max}=\tau_f$. Therefore, the analytical law describing the bond-slip relationship in the case of plain reinforcement is represented by two branches: the first branch goes from zero up to the bond strength and the second branch is constant for growing slip. This means that, if parameter α is chosen equal to 1 (i.e. the relationship between s and τ_0 for $s < s_1$ is linear), the bond-slip law is an elastic-plastic model; while if α is chosen equal to 0, the final shape of the relation is represented by a rigid-plastic law. Values of α between 0 and 1 would result in parabolic-plastic laws.

2.4.1.2 Non-metallic reinforcement

‘Bond of non-metallic reinforcement’ is the term used in the CEB-FIP Model Code 2010 (fib, 2012a) to identify the interaction and transfer of forces between FRP reinforcement and concrete. Also in this case, the bond stresses between concrete and non-metallic reinforcing bars can be calculated as a function of the relative displacement s , according to Eqs. (2.5) and (2.6) (Fig. 2.11). The model reported in the CEB-FIP Model Code 2010 (fib, 2012a) is the one formulated by Cosenza et al. in (Cosenza et al., 1995).

$$\tau_b = \tau_m (s/s_m)^\alpha \quad \text{for } 0 \leq s \leq s_m \quad (2.5)$$

$$\tau_b = \tau_m - \tau_m p \frac{s-s_m}{s_m} \quad \text{for } s_m < s \leq s_u \quad (2.6)$$

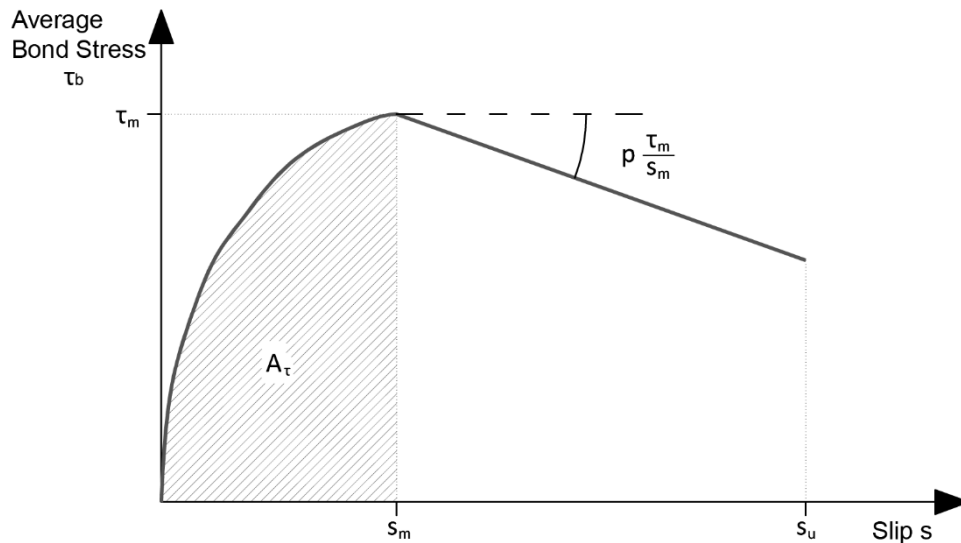


Figure 2.11 - Analytical bond-slip relationship for FRP reinforcing bar-to-concrete interface

For FRP reinforcing bars, the bond-slip relationship proposed by Cosenza et al. (Cosenza et al., 1995) is assumed to consist of two branches. The first branch, which goes from 0 up to the bond strength, τ_m , is described by a nonlinear ascending law characterised by the parameter α , whose value is often assumed equal to 0.25 (Cosenza et al., 1995). As for the second branch, a linear softening law describes the debonding and frictional stages.

2.4.2 Numerical modelling

The CEB-FIP report on ‘Bond of reinforcement in concrete’ (CEB-FIP Report, 2000) identifies the three main objectives of the bond modelling:

- 1) investigation of the bond behaviour at the local level in order to account for the resistant mechanisms, which are activated at the microscale (i.e. friction, bearing action, interface slip);
- 2) correlation between sectional behaviour and structural parameters (bottom and side concrete cover, bar diameter and free interspace, pull-out situations), in order to check and enhance the relatively simple equations required by structural design; and
- 3) assessment of the soundness and numerical efficiency of the bond stress-bar slip laws proposed in the literature to describe the bond behaviour at different scales.

To provide a general overview of the possibilities in numerical modelling of bond, some of the most used FE models are reported hereafter, referring to (CEB-FIP Report, 2000) for a detailed review.

2.4.2.1 Layer models

This approach exploits the consideration that bond-induced effects occur mostly in the concrete layer in proximity of the rebar. Thus, the common feature of the layer models

approach lies in the decomposition of the concrete cover in two regions. The region closer to the bar is intended for considering inelastic deformations and fracture, whereas the outer part of the concrete can be assumed undamaged. Table 2.2 summarises the main FE formulations of layer models developed so far.

Table 2.2 - Layer models review for bond modelling

Authors	Main model characteristics
Bresler and Bertero (Bresler and Bertero, 1968)	<ul style="list-style-type: none"> - Both the concrete layers have a linear-elastic behaviour, but the one closer to the bar is described through suitably tuned elastic constants; - The displacement field of the boundary layer represents the local slip at the bar-concrete interface.
Reinhardt et al. (Reinhardt et al., 1984)	<ul style="list-style-type: none"> - ‘Slip layer’ divided into torus-like elements, matching the shape of the ribs; - The slip layer is described by means of an elastic-plastic law in compression, and by an elastic-softening law in tension (linear softening).
Cox and Hermann (Cox and Hermann, 1992)	<ul style="list-style-type: none"> - Definition of a ‘process zone’ as a finite thickness region around the bar; - Where a 2D plasticity model relates the local slip and radial dilation to both the bond stress and the radial confinement stress.
Vervuurt and Van Mier (Vervuurt and Van Mier, 1995)	<ul style="list-style-type: none"> - Exploitation of the ‘lattice’ model for the description of the concrete layer closest to the bar.
G. Lilliu and Van Mier (Lilliu and van Mier, 2003)	<ul style="list-style-type: none"> - A 3D beam lattice model is used for simulating fracture processes in concrete, including bar-matrix debonding,

2.4.2.2 Fracture mechanics models

Fracture mechanics can be considered a branch of the solid mechanics’ theory in which the presence of cracks is assumed. It is aimed to find quantitative relations between the crack length, the material resistance to crack growth, and the stress at which the crack propagates up to cause structural failure (Anderson, 2012).

Since the splitting nature of bond failure, fracture mechanics can be used to study the problem of splitting concrete leading to the loss of bond in reinforced concrete members (Rots, 1989). Thus, the fracture mechanics approach usually addresses the typical splitting failure exhibited by ribbed bars sliding with respect to the surrounding concrete. The first studies analysing bond by means of fracture mechanics used its principles to model splitting concrete through secondary cracking, with no representation of longitudinal cracking ((Ingraffea et al., 1984), (Bazant and Sener, 1988), (Rots, 1989), (Gylltoft, 1989), etc.). Afterwards, other researchers took into consideration also the longitudinal cracking that occurs in flexural members leading to a significant loss of bond ((Choi et al., 1991), (Hadje-Ghaffari et al., 1994), etc.).

Some of the cited studies are summarised in Table 2.3, where the main characteristics of the proposed models based on the fracture mechanics approach, are reported.

Table 2.3 - Review of fracture mechanics approaches to bond modelling

Authors	Main model characteristics
Ingraffea et al. (Ingraffea et al., 1984)	<ul style="list-style-type: none"> - Nonlinear fracture mechanics and ‘crack nucleation and propagation code’ to model cracking discretely; - Description of crack formation, propagation and direction through the use of interface elements and the computation of the stress-intensity factor at increasing loads.
Rots (Rots, 1989)	<ul style="list-style-type: none"> - Smearred and discrete crack models including tensile softening; - Formation and propagation of cracks are governed by axisymmetry, while the crack pattern of longitudinal splitting is one of the input data.
Gylltoft (Gylltoft, 1989)	<ul style="list-style-type: none"> - Application of fracture mechanics to study bond failure in pull-out tests; - bond between a smooth bar and concrete while including constitutive relations for the fracture process zone in both the tangential and normal directions.
Choi et al. (Choi et al., 1991)	<ul style="list-style-type: none"> - Nonlinear fracture mechanics method in two steps: <ul style="list-style-type: none"> – First step: a 3D representation of concrete that splits along a predefined crack surface is used to determine the clamping force of the concrete on the steel as a function of lateral (splitting) displacement. – Second step: the results of the first step are used with interface link elements to model slipping of the bar.

2.4.2.3 Bond elements

Many formulations of finite elements specifically intended for modelling the bond-slip behaviour between steel reinforcing bars and concrete have been proposed in the literature. In fact, link, interface and contact elements have been used as a starting point to implement new bond elements describing the bond-slip relationship between reinforcing bars and concrete matrix. Ngo and Scordelis (Ngo and Scordelis, 1967) proposed a link element to connect one node of a concrete element to one node of an adjacent bar element. The link element has no physical dimensions, so two connected nodes have identical coordinates before slip occurs at the interface. For plane-stress problems, a link element consists of two springs, one parallel and one normal to the longitudinal axis of the reinforcing bar. Afterwards, Yankelevsky (Yankelevsky, 1985) formulated a one-dimensional finite element model, which is based on equilibrium and a local bond stress-slip law. Keuser and Mehlhorn reported in (Keuser and Mehlhorn, 1987) a review on the special contact elements proposed to model the bond-slip relationship between rebars and concrete. The main idea behind this approach is to ‘reduce’ bond to a contact problem, assuming for the concrete layer closest to the bar a negligible thickness compared to bar and matrix sizes. Contact elements allow for introducing a Mohr-Coulomb type friction law. More recently, Amleh and Ghosh (Amleh and Ghosh, 2006) developed a nonlinear 3D contact-based bond

element for modelling pull-out tests taking into consideration the corrosion action. Lundgren and Gylltoft (Lundgren and Gylltoft, 2000), instead, used an interface element with initial thickness equal to zero to input a new bond model based on the plasticity theory, able to account also for the splitting stresses arising into the concrete cover.

2.4.2.4 Damage mechanics approach

The main objective of continuum damage mechanics is to propose a continuum-mechanics based framework allowing to characterise, represent and model, at the macroscopic scale, the effects of distributed defects and their growth on the material behaviour (Kondo et al., 2007). Damage mechanics approach provides an alternative tool to the problem of bond modelling that does not require the introduction *a priori* of interface, contact or links elements. In this case, microcracking and, generally, nonlinearity of concrete surrounding the rebar need to be adequately taken into account (CEB-FIP Report, 2000). Pijauder-Cabot, Mazars et al. (Pijaudier-Cabot et al., 1991) developed a scalar damage model for concrete materials, where damage is represented by an isotropic scalar variable. Local and nonlocal versions of the model have been proposed.

Also damage models differentiating the normal and tangential (with respect to rebar development direction) damage factors have been formulated and used to simulate the bond behaviour at the steel-concrete interface (Soh et al., 1999).

A different numerical tool here taken into account for the bond modelling consists of Cohesive Zone Models (CZMs). A general description of the theory background for CZM and of the most adopted formulations, is provided in the next section. Particular attention has been given to the CZM formulations accounting for friction, due to the frictional component characterising the bond behaviour between reinforcement and concrete matrix.

2.5 Cohesive zone models

CZMs have become a popular numerical tool for modelling fracture in solids in FE-based analyses (Schwalbe et al., 2013). Since CZMs describe a separation, i.e. a failure phenomenon, between two surfaces previously perfectly bonded, they have been successfully used for the study of bond-slip behaviour in RC structures. Many examples of applications can be found in the literature ((Serpieri et al., 2014), (Raous and Ali Karray, 2009), (Ragueneau et al., 2006), etc.), describing pull-out tests of rebars from concrete matrices by means of CZMs in the framework of FE analysis. Actually, pull-out tests of steel rebars from concrete matrices have been also used as a benchmark to verify the efficiency of certain proposed CZMs in the mode II-dominant behaviour (Serpieri et al., 2014).

For these reasons, in the present work CZMs are employed to model the bond behaviour between reinforcement and concrete. Therefore, the main aspects of this approach are here reported, providing also the description of the most popular CZMs proposed in the literature so far.

2.5.1 The framework of Fracture Mechanics

In order to introduce the Cohesive Zone Modelling, it is necessary to recall some basic concepts of the Fracture Mechanics theory.

The fracture mechanics approach has three important variables: applied stress, flaw size, and fracture toughness, while traditional approach to structural design has two main variables: applied stress and yield or tensile strength. In the latter, a material is assumed to be adequate if its strength is greater than the external applied stress. The flaw size and fracture toughness replace strength as the relevant material property in fracture mechanics approach, whose role is to quantify the critical combinations of the three variables (Anderson, 2012). Fracture toughness can be seen as a measure of the resistance of a material to fracture, i.e. a measure of the ability of a material to resist crack propagation. In turn, it can be measured by two different parameters, namely critical strain energy release rate and critical stress intensity factor (SIF), depending on the adopted approach. The first possible approach is the *energy-balance approach*, which assumes that fracture occurs when the energy available for crack growth is high enough to overcome the resistance of the material. The energy-release rate, according to this approach, is the rate of change in potential energy with growing crack area for a linear elastic material. The second approach, instead, is the so-called *stress intensity approach*. It evaluates the stress state near the tip of a sharp crack, defining the critical stress intensity factor as fracture toughness, and it can be used for normal opening crack mode I and shear sliding modes II and III (K_I , K_{II} and K_{III}).

As long as the plastic crack tip zone remains within certain dimensions and the material behaviour can be considered linear-elastic, Linear Elastic Fracture Mechanics (LEFM) can be employed. Conversely, Non-Linear Elastic Fracture Mechanics (NLEFM) provides a different approach to the analysis of those cases where LEFM can no longer formulate suitable crack growth criteria.

2.5.1.1 Linear Elastic Fracture Mechanics

As far as LEFM is concerned, the critical strain energy release rate, G_c , is assumed to be equal to the fracture energy, G_f . LEFM lies its basis on two main concepts: (I) all energy dissipation is associated with the fracture process and (II) the deformation that occurs is linear elastic (Fischer-Cripps, 2007). The two approaches previously introduced in the framework of LEFM are briefly reported as follows.

The energy-balance criterion, proposed by Griffith (Roylance, 2001), assesses that two conditions are necessary for crack growth:

- i. The bonds at the crack tip must be stressed to the point of failure. The stress at the crack tip is a function of the stress concentration factor, which depends on the ratio of its radius of curvature to its length.
- ii. For an increment of crack extension (c), the amount of strain energy released (U_s) must be greater than or equal to that required for the surface energy of the two new crack faces (U_γ).

Mathematically, the second condition (ii) is expressed through Eq. (2.7).

$$\frac{dU_s}{dc} \geq \frac{dU_\gamma}{dc} \quad (2.7)$$

Thus, for a crack to extend, the rate of strain energy release per unit of crack extension must be at least equal to the rate of surface energy requirement. The strain energy released by introducing a double-ended crack of length $2c$ in an infinite plate of unit width under a uniformly applied stress σ_a (Fig. 2.12) is given by the following Eq. (2.8):

$$U_s = \frac{\pi\sigma_a^2 c^2}{E} \quad (2.8)$$

Eq. (2.9), instead, expresses the total surface energy, U_γ , for two surfaces of unit width and length $2c$.

$$U_\gamma = 4\gamma c \quad (2.9)$$

where γ is the fracture surface energy of the solid.

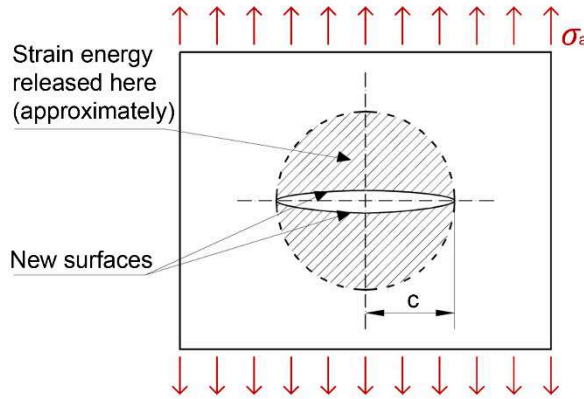


Figure 2.12 - Geometry and strain energy released of a double-ended crack of length $2c$ in an infinite plate of unit width under a uniformly applied stress σ_a

Therefore, by deriving Eq. (2.7) with respect to c and combining Eqs. (2.8) and (2.9), the following relation is obtained (Eq. (2.10)), which summarises the Griffith energy balance criterion for crack growth.

$$\frac{\pi\sigma_a^2 c}{E} \geq 2\gamma \quad (2.10)$$

The stress intensity factor criterion, instead, has been formulated by Irwin (Roylance, 2001). He demonstrated that the stress field $\sigma(r, \theta)$ in proximity of an infinitely sharp crack tip could be described mathematically through the following formula (Eq. 2.11):

$$\sigma(r, \theta) = \frac{K_I}{\sqrt{2\pi r}} \cos \frac{\theta}{2} \left(1 - \sin \frac{\theta}{2} \sin \frac{3\theta}{2} \right) \quad (2.11)$$

where the terms involving θ describe the distribution of the stress, while its magnitude is expressed through the definition of the so-called *stress intensity factor*, K_I , given by Eq. (2.12):

$$K_I = \sigma_a Y \sqrt{\pi c} \quad (2.12)$$

In Eq. (2.12), σ_a is the applied stress, Y represents a geometric factor and c is the crack half-length, as shown in Fig. 2.12. The stress intensity factor K_I can be defined as a combined ‘scale factor,’ which characterises the magnitude of the stress at some coordinates (r, θ) near the crack tip. Particularly, K_I is associated with tensile loading (i.e. Mode I), but stress intensity factors exist for other types of crack opening mode, namely Mode II and Mode III, referring to sliding (in-plane shear) and tearing (out-of-plane shear), respectively (Fig. 2.13). Also mixed modes may occur as a combination of any of the three basic modes.

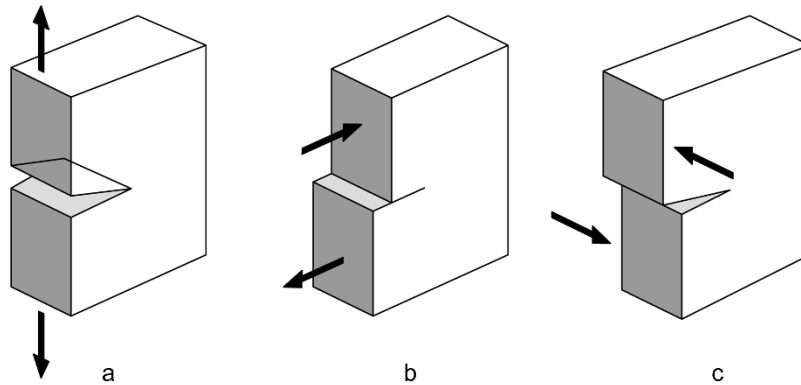


Figure 2.13 - Fracture Modes: (a) Mode I – opening; (b) Mode II – in plane-shear (sliding), and (c) Mode III – out-of-plane shear (tearing)

2.5.1.2 Non-Linear Elastic Fracture Mechanics

When the plastic zone is not sufficiently small compared to the specimen dimensions (i.e. large scale yielding) or the considered materials have inelastic stress-strain relations, concepts of Non-Linear Elastic Fracture Mechanics (NLEFM) or Elastic-Plastic Fracture Mechanics (EPFM) shall be applied to the study of the mechanics of fracture (Brocks et al., 2007). Essential parameters to establish the crack growth in the EPFM theory are:

- the *J-integral* formulated by (Cherepanov, 1967) and Rice (Rice, 1968) (or its analogue, C^* for creep crack growth, proposed by (Landes and Begley, 1976)); and
- *crack tip opening displacement (CTOD)*, δ , (Burdekin and Stone, 1966), (Dawes, 1985).

The *J-integral* is a line integral (path-independent) around the crack tip, which represents the rate of change of net potential energy with respect to crack advance (per unit thickness of crack front) for a nonlinear elastic solid. J can be considered as the energy flow into the crack tip, measuring the singularity strength at the crack tip for the case of elastic-plastic material response (Rice, 1968). Budiansky and Rice (Budiansky and Rice,

1973) also showed that the J -integral is identical to the energy release rate for a plane crack extension (Eq. (2.13)). Therefore, in the case of linear elastic materials, J is related to the stress intensity factors (K_I , K_{II} , K_{III}) through Eq. (2.14).

$$J = \mathcal{G} = -\frac{\partial U}{\partial A} \quad (2.13)$$

$$J = \mathcal{G}_I + \mathcal{G}_{II} + \mathcal{G}_{III} = \frac{1}{E'}(K_I^2 + K_{II}^2) + \frac{1}{2G}K_{III}^2 \quad (2.14)$$

where \mathcal{G} is the Griffith energy release rate, U the work of separation, A the crack area, E' the elastic modulus, and G the shear modulus.

The variation in crack tip opening displacement ($CTOD$), is the second essential parameter in the EPFM approach. It depends on the distance from the crack tip and its general expression is given by Eq. (2.15) (Shih, 1981).

$$CTOD = d_n \frac{J}{\sigma_y} \quad (2.15)$$

where J is the J -integral, d_n is a parameter depending on the hardening exponent of the material, and σ_y is the initial yield strength of the material.

In EPFM the $CTOD$ is a measure for the deformation at the crack tip, which can be compared to a critical value in a crack growth criterion. The critical value, which may depend on strain rate and/or temperature, is the value to be measured and can be seen as a measure of toughness.

2.5.1.3 Damage and fracture

To describe the failure process, two main approaches are available, namely the fracture mechanics (FM) approach, discussed above, and Continuum Damage Mechanics (CDM) theory (Mazars and Pijaudier-Cabot, 2001). While FM well describes the separation due to decohesion of two parts of a continuum body, CDM describes the local effects of microcracking through the evolution of the mechanical properties of the continuum (stiffness, anisotropy, permanent strain). Thus, CDM considers local approaches and micromechanical modelling of damage and fracture (Pineau, 2006). The general advantage, compared with classical fracture mechanics, is that, in principle, the parameters of the models are only material and not geometry dependent (Brocks et al., 2007).

The mechanics of damage is the study, through mechanical variables, of the mechanisms involved in the deterioration process when the materials are subjected to loading. At the microscale level, it corresponds to the accumulation of micro-stresses in the neighbourhood of defects or interfaces (Lemaitre, 1992). At the mesoscale level, instead, the concept of Representative Volume Element (RVE), introduced by Hill (Hill, 1963), Hashin (Hashin, 1963) and others, is usually exploited in order to express continuum quantities in terms of the parameters which characterise the microstructure and properties of the micro-constituents of the material neighbourhood (Nemat-Nasser and Hori, 1993). The discontinuous and discrete elements of damage are not considered within the RVE; rather their combined effects are lumped together through the use of a macroscopic internal variable (Luccioni and Oller, 2003).

The various types of damage at the micro-scale level (e.g. nucleation and growth of voids, cracks, micro-cracks, and other microscopic defects) can be described through a *damage variable* (or *tensor*), which represents the average material degradation (Voyiadjis and Kattan, 2008). Even though a rigorous description should employ a damage tensor to characterise the state of damage in materials, scalar variables are often used due to their simplicity.

Within the classical approach (Lemaitre, 1992), a very simple measure of the damage amplitude in a given plane is obtained by measuring the area of the intersection of all defects with that plane. Let consider a cubic RVE, whose side area is equal to dS . By naming ' dS_D ' the amount of area inside dS occupied by material discontinuities (e.g. cracks, voids, etc.), it is possible to define the (scalar) damage variable, D , through the following Eq. (2.16):

$$D = \frac{dS_D}{dS} \quad \text{With } 0 \leq D \leq 1 \quad (2.16)$$

In Eq. (2.16) dS_D represents the defects trace in the considered plane, thus the 'effective' area of that plane is equal to $dS - dS_D$.

For the undamaged material, $dS_D = 0$ and then $D = 0$. Since the damage is related to the growth of defects, D may grow from 0 to a critical value often taken in the literature equal to 1, which corresponds to a fully damaged material (effective area $dS - dS_D$ reduced to 0). In this case, it is reasonable referring to the effective stress given in Eq. (2.17), which considers the effective resistant area.

$$\tilde{\sigma} = \frac{F}{dS - dS_D} = \frac{F}{dS(1 - \frac{dS_D}{dS})} = \frac{F}{1 - D} \quad (2.17)$$

where F is the applied external force.

After this brief introduction on fracture mechanics and continuum damage mechanics theory, CZMs can be introduced, representing them an effective alternative approach to fracture-mechanics-based methods, not describing the fracture zone through idealised singular stresses, and being the materials parameters through which they are defined, independent of geometrical influence and mesh discretisation.

2.5.2 The cohesive zone model

A cohesive surface theory of fracture is a phenomenological continuum framework that is closely related to classical fracture mechanics. It addresses, however, a variety of issues that are difficult to address within a conventional fracture mechanics framework. Within this framework, the continuum is characterised by two constitutive relations; one is a volumetric constitutive law that relates stress and strain, while the other is a traction versus displacement jump relation across a cohesive surface. The cohesive constitutive relation embodies a description of the mechanical effects of the separation process as well as any dissipation associated with it (Needleman, 2013). It stems from the pioneering researches of Barenblatt (Barenblatt, 1962) and Dugdale (Dugdale, 1960), whose main characteristics are following discussed.

Barenblatt (Barenblatt, 1962) introduced a distribution of *cohesive forces* in the region ahead of a tensile crack (Figs. 2.14a and 2.14b). These cohesive forces represent a finite limit for the opening stresses (i.e. normal stresses), contrary to the infinite opening stresses of the linear elastic solution for a mathematically sharp crack. Two main hypotheses lied the basis for Barenblatt's theory: (1) the length over which the cohesive forces act is small compared to the crack size, which is particularly valid for brittle or quasi-brittle materials where deviations from linear elasticity is limited to a region near the crack tip; and (2) the distribution of the cohesive forces is identical for a given material and given external conditions.

Dugdale (Dugdale, 1960), instead, addressed the problem of steel sheets containing slits. Even though his aim concerned the direct calculation of the extent of the yielding zone ahead of the slit as a function of the applied load, the cohesive formulation was essentially the same as for fracture. Steel behaviour was idealised as elastic-plastic and yielding ahead of the crack tip was represented by a uniform tensile stress distribution (Fig. 2.14c). In both Barenblatt's and Dugdale's approaches, the size of the cohesive zone is determined as part of the solution, meaning that the extent of the cohesive zone is an output of the analysis (Needleman, 2013).

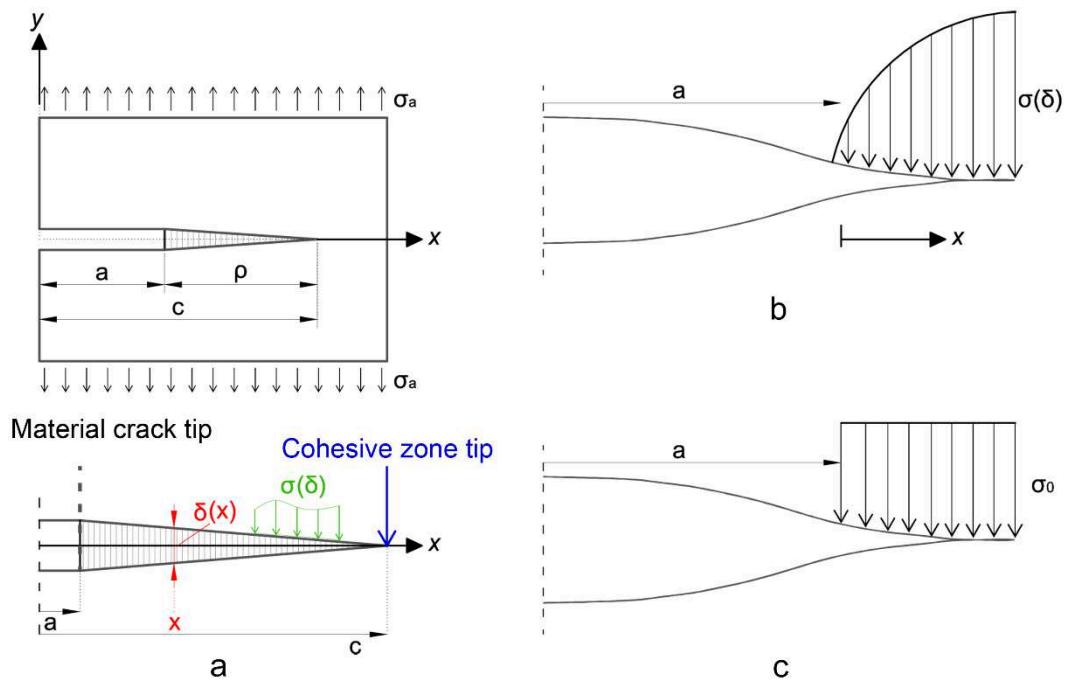


Figure 2.14 - a) Scheme of the cohesive zone ahead of a tensile crack; b) Barenblatt's crack model; and c) Dugdale's crack model

Another pioneering study concerning CZM is that proposed by Hillerborg et al. (Hillerborg et al., 1976). They introduced the so-called *fictitious crack model* in order to analyse crack formation and crack growth in concrete by means of fracture mechanics and

finite elements. Although the focus was on concrete fracture process, Hillerborg et al. (Hillerborg et al., 1976) provided a computational formulation of much wider application. In fact, by considering concrete a linear-elastic material and introducing the cohesive behaviour in correspondence of fracture zones, it was possible to extend the same formulation also to materials characterised by nonlinear and/or dissipative behaviours (Needleman, 2013).

Starting from these fundamental models, a considerable amount of cohesive zone models has been formulated. Some of them are recalled in Section 2.5.2.2, while the following section (Sec. 2.5.2.1) reports a general description of the cohesive zone model formulation in the framework of the FE analysis.

2.5.2.1 FE formulation of CZMs

Material separation is usually described by using *interface elements* in the framework of FE analysis. This means that in the cohesive zone modelling approach, damage does not involve the continuum elements representing the material, which, indeed, can have an arbitrary constitutive law. A different technique (i.e. the *strong discontinuity approach*) defines the cohesive elements within solid elements, which, thus, contain not only the damage of the structure but also its continuum properties (Brocks et al., 2007). A scheme of the implementation of the CZM in a FE model is represented in Fig. 2.15, where the idealised fracture process starting from a crack in the material (Fig. 2.15a) is related to the FE discretisation (Fig. 2.15b). According to the three fracture modes (Fig. 2.13), interface elements open when damage occurs, disconnecting the continuum solid elements. A traction-separation law (TSL) describes the whole fracture process (Fig. 2.15c reports a typical TSL).

A TSL is such that with increasing separation δ , the traction T (or σ) reaches a maximum, starts to decrease and eventually vanishes, allowing a complete decohesion. In local coordinate system the displacement jump is decomposed into normal (δ_n) and tangential (δ_t) components. Thus the corresponding tractions are T_n and T_t , respectively. When the normal or tangential component of the separation reaches a critical value, δ_{n0} or δ_{t0} (associated to the maximum normal T_{n0} or tangential T_{t0} traction, respectively), the continuum elements initially bonded, start to disconnect, until the complete decohesion which corresponds to the displacement values δ_{nc} or δ_{tc} , for opening or shear failure respectively.

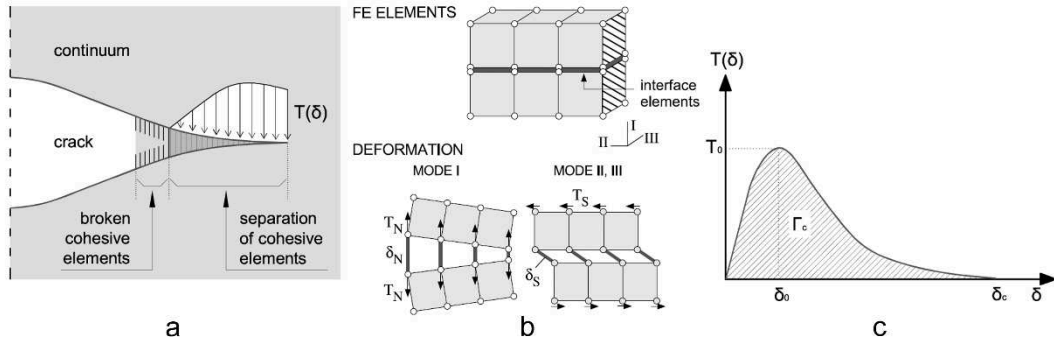


Figure 2.15 - a) Scheme of the cohesive zone [taken in (Cornec et al., 2003)]; b) FE implementation of CZM [taken in (Cornec et al., 2003)]; and c) typical traction-separation law (TSL) for describing the cohesive behaviour

The integration of the traction over separation, either in normal or in tangential direction, gives the energy dissipated by the cohesive elements, Γ_c (Fig. 2.15c), which can be obtained through the following Eq. (2.18):

$$\Gamma_c = \int_0^{\delta_c} T(\delta) d\delta \quad (2.18)$$

In the next section, a brief summary of the most popular laws (also called traction-separation laws, or decohesion laws) is reported, referring to ((Cornec et al., 2003), (Alfano, 2006), (Elices et al., 2002), (Chandra et al., 2002)) for a detailed review.

2.5.2.2 Traction-separation law

Since one-dimensional pure-mode response is the basic feature behind each cohesive model (Alfano, 2006), a first classification of the cohesive models is based on their pure-mode ‘shape’, i.e. the shape of the traction-separation law (TSL) in each mode. In the vast majority of CZMs, the traction-separation relations for the interfaces are such that with increasing interfacial separation, the traction across the interface reaches a maximum, then decreases and eventually vanishes permitting a complete decohesion (Chandra et al., 2002).

Another significant feature is related to the formulation, which can be either non-potential-based or potential-based (Park and Paulino, 2013). Some authors (Park and Paulino, 2013) claim that nonpotential-based CZMs cannot account for all possible separation paths, thus they do not guarantee consistency of the constitutive relationship under arbitrary mixed-mode conditions (Park and Paulino, 2013). However, nonpotential-based CZMs have been widely used in the literature, being suitable to describe numerous problems in a relative simple manner. As for potential-based models, a potential function characterises the fracture behaviour. Particularly, the cohesive tractions are obtained from the potential function, by deriving it with respect to the considered principal direction of the fracture surface.

Several CZMs are available in the literature. Some of the most popular are summarised in Table 2.4, where it is reported whether they are potential (P) or nonpotential (NP) -based and their characteristic TSL shapes.

Table 2.4 - Review of potential and nonpotential-based formulation of CZMs

CZM formulation	Reference	P / NP	TSL shape
Camacho and Ortiz	(Camacho and Ortiz, 1996)	NP	Purely decreasing (linear softening)
Ortiz and Pandolfi	(Ortiz and Pandolfi, 1999)	NP	Purely decreasing (linear softening)
Hilleborg et al.	(Hillerborg et al., 1976)	NP	Bilinear
Geubelle and Baylor	(Geubelle and Baylor, 1998)	NP	Bilinear
Alfano and Crisfield	(Alfano and Crisfield, 2001)	NP	Bilinear
Rice and Wang	(Rice and Wang, 1989)	NP	Exponential
Chandra et al.	(Chandra et al., 2002)	NP	Exponential
Xu and Needleman	(Xu and Needleman, 1994)	P	Exponential
Tvergaard and Hutchinson	(Tvergaard and Hutchinson, 1992)	NP	Trapezoidal
Allix et al.	(Allix et al., 1995)	NP	Linear-parabolic
Allix and Corigliano	(Allix and Corigliano, 1996)	NP	Linear-parabolic
Champaney and Valoroso	(Champaney and Valoroso, 2001)	NP	Linear-parabolic
Tvergaard	(Tvergaard, 1990)	NP	Polynomial
Park, Paulino and Roesler	(Park et al., 2009)	P	Polynomial

A brief description of the most widely used CZMs, reporting also the main parameters through which they are described, is following presented.

2.5.2.2.1 Dugdale and Barenblatt models

As previously introduced, Barenblatt ((Barenblatt, 1959), (Barenblatt, 1962)) and Dugdale (Dugdale, 1960) firstly introduced the concept of the CZM. The traction-separation laws representing their models are reported in Figs. 2.16a and 2.16b, respectively.

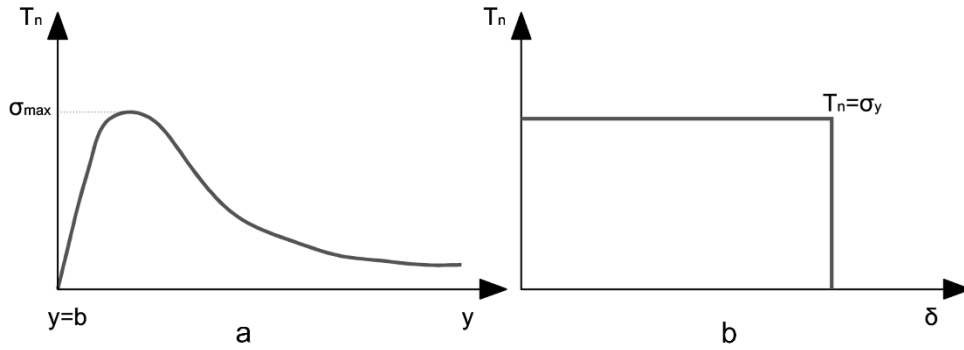


Figure 2.16 - TSL: a) Barenblatt's model; and b) Dugdale's model

Barenblatt's model is described through the definition of the parameter K , which represents the so-called 'modulus of cohesion' and is given by Eq. (2.19):

$$K = \int_0^d \frac{G(t)dt}{\sqrt{t}} \quad (2.19)$$

where:

- $G(t)$ is the intensity of the cohesive forces acting in the vicinity of the crack tip;
- t is the distance along the surface of the crack, reckoned along the normal to its contour;
- d is the width of the region in which the cohesive forces act.

By defining the tensile stress of separation for brittle materials, T_0 , and that of plastic deformation, T_1 , the parameter K is given by Eq. (2.20):

$$K = \sqrt{\frac{\pi E T_0}{1-\nu^2}} \quad \text{for brittle materials} \quad (2.20)$$

$$K = \sqrt{\frac{\pi E T}{1-\nu^2}} \quad \text{for ductile materials} \\ \text{with } T = T_0 + T_1$$

where E is the modulus of elasticity and ν the Poisson's ratio. Thus, it is possible to obtain the traction-separation law shown in Fig. 2.16a.

As for the Dugdale's model, the size of the inelastic zone, x , is obtained by equating the stress intensity factor, K_0 , due to T alone, with the stress intensity factor, K_i , due to σ_y alone. In particular, T is the tensile opening stress and σ_y is the yield strength of the material. By setting K_0 equal to K_i , x is given by Eq. (2.21):

$$x = L \sin^2 \left(\frac{\pi T}{4 \sigma_y} \right) \quad (2.21)$$

where L is the final yielded length of the crack and T can be derived in order to obtain the TSL shown in Fig. 2.16b.

2.5.2.2.2 Alfano and Crisfield nonpotential-based bilinear CZM

The CZM formulations proposed by Hilleborg et al. (Hilleborg et al., 1976); Geubelle and Baylor (Geubelle and Baylor, 1998); Crisfield and Alfano (Alfano and Crisfield, 2001) can be classified as bilinear, having a linear branch up to the cohesive strength characterised

by a finite stiffness, K_0 , followed by a linear softening until the cohesive traction, T , vanishes. In the following, only the model formulation by Alfano and Crisfield (Alfano and Crisfield, 2001) is reported.

For the uncoupled model the two bilinear, one-dimensional relationships (mode I and mode II) are described by the following analytical expressions (Eq. 2.22) and represented in Fig. 2.17.

$$T_i = \begin{cases} K_{0i} \delta_i & \text{if } (s_i[\delta_i])_{max} \leq \delta_{0i} \\ & \text{or } (i = 1 \text{ and } \delta_i < 0) \\ K_{0i} \delta_i \left[1 - \left(\frac{(s_i[\delta_i])_{max} - \delta_{0i}}{(s_i[\delta_i])_{max}} \right) \left(\frac{\delta_{ci}}{\delta_{ci} - \delta_{0i}} \right) \right] & \text{if } \delta_{0i} \leq (s_i[\delta_i])_{max} \leq \delta_{ci} \\ & \text{and } (i \neq 1 \text{ or } \delta_i \geq 0) \\ 0 & \text{if } (s_i[\delta_i])_{max} \geq \delta_{ci} \\ & \text{and } (i \neq 1 \text{ or } \delta_i \geq 0) \end{cases} \quad (2.22)$$

where:

- $(s_i[\delta_i])_{max}$ denotes the maximum value which has been attained by $s_i[\delta_i]$ (Eq. (2.23)). Note that τ represents a pseudo-time parameter within the range $\tau \in [0, t]$.

$$(s_i[\delta_i])_{max} = \max_{0 \leq \tau' \leq \tau} s_i[\delta_i(\tau')] \quad (2.23)$$

- the different behaviours in compression and tension with respect to mode I is accounted for to avoid penetration, introducing the following notation:

$$s_i[x] = \begin{cases} \langle x \rangle, & \text{if } i = 1 \text{ (mode I)} \\ |x|, & \text{if } i = 2 \text{ (mode II)} \end{cases} \quad (2.24)$$

where the symbol $\langle \cdot \rangle$ denotes the Mc Cauley brackets:

$$\langle x \rangle = \begin{cases} x, & x \geq 0 \\ 0, & x < 0 \end{cases}$$

- K_{0i} are penalty stiffness parameters;
- i stands for the fracture mode:
Mode I (opening): $i = 1 \equiv n$
Mode II (shear) : $i = 2 \equiv t$

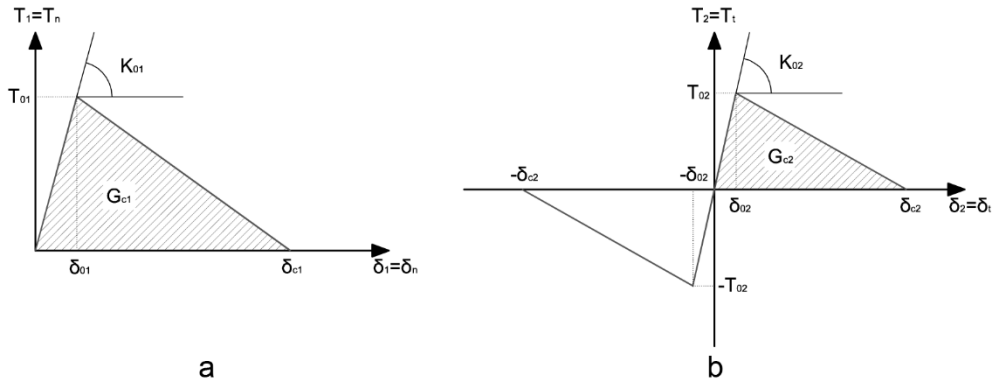


Figure 2.17 - Alfano and Crisfield model: a) mode I TSL; and b) mode II TSL

The energy release rate criterion according to LEFM theory, is indirectly used by equating the areas under the two TSLs of Fig. 2.17 to the critical energy release rates G_{c1} and G_{c2} , for mode I and II, respectively.

As far as the mixed mode is concerned, i.e. both opening and sliding modes are simultaneously taken into account, the total energy release rate is additively obtained by summing G_1 and G_2 , which are given in Eq. (2.25):

$$G_1 = \int_0^{\delta_1} T_1 d\delta_1 \quad G_2 = \int_0^{\delta_2} T_2 d\delta_2 \quad \Rightarrow \quad G = G_1 + G_2 \quad (2.25)$$

In the model of Alfano and Crisfield (Alfano and Crisfield, 2001) the problem of the determination of the mode ratio (i.e. G_i/G_{ci}) is addressed by using a constitutive model for the mixed-mode delamination (Mi et al., 1998) which fulfils the ellipse criterion of Eq. (2.26) under certain hypotheses and is based on parameter $\bar{\gamma}$, defined through Eqs. (2.27) and (2.28).

$$\left(\frac{G_1}{G_{c1}}\right)^{\alpha/2} + \left(\frac{G_2}{G_{c2}}\right)^{\alpha/2} = 1 \quad \text{with } \alpha: \text{ material parameter} \quad (2.26)$$

$$\bar{\gamma}(\tau) = \max_{0 \leq \tau' \leq \tau} \gamma(\tau') \quad (2.27)$$

$$\gamma(\tau') = \left[\left(\frac{(\delta_1(\tau'))}{\delta_{01}} \right) + \left(\frac{|\delta_2(\tau')|}{\delta_{02}} \right) \right]^{1/\alpha} - 1 \quad (2.28)$$

The constitutive relationship is then given by Eq. (2.29):

$$\mathbf{T}(\tau) = \begin{cases} \mathbf{K}\boldsymbol{\delta}(\tau) & \text{if } \bar{\gamma}(\tau) \leq 0 \\ [\mathbf{I} - \mathbf{D}(\tau)\mathbf{C}(\tau)\mathbf{K}\boldsymbol{\delta}(\tau)] & \text{if } \bar{\gamma}(\tau) > 0 \end{cases} \quad (2.29)$$

where:

- $\mathbf{K} = \text{diag}[K_i]$;
- \mathbf{I} is the identity matrix;
- $\mathbf{D}(\tau) = \text{diag}[d_i(\tau)]$, with $d_i(\tau) = \max\left\{1, \frac{\bar{\gamma}(\tau)}{1+\bar{\gamma}(\tau)} F_{ii}\right\}$, $F_{ii} = \frac{\delta_{ci}}{\delta_{ci} - \delta_{oi}}$;
- The matrix $\mathbf{C}(\tau)$ ensures that penetration is avoided and it is defined as follows:

$$\mathbf{C}(\tau) := \begin{bmatrix} h[\delta_1(\tau)] & 0 \\ 0 & 1 \end{bmatrix} \text{ with } h(x) = \begin{cases} 1 & \text{if } x \geq 0 \\ 0 & \text{if } x < 0 \end{cases}$$

Another fundamental assumption in the model proposed by Alfano and Crisfield (Alfano and Crisfield, 2001) is made in order to avoid that the complete debonding is not simultaneous for opening and sliding modes. The introduction of the parameter η , defined according to Eq. (2.30), allows for solving this problem.

$$\eta = 1 - \frac{\delta_{01}}{\delta_{c1}} = 1 - \frac{\delta_{02}}{\delta_{c2}} \quad (2.30)$$

2.5.2.2.3 Xu and Needleman potential-based exponential CZM

The formulation proposed by Xu and Needleman (Xu and Needleman, 1994) defines an exponential CZM through the introduction of a potential function at the interface, given by Eq. (2.31):

$$\phi(\Delta_n, \Delta_t) = \phi_n + \phi_n \exp\left(-\frac{\Delta_n}{\delta_n}\right) \left\{ \left[1 - r + \frac{\Delta_n}{\delta_n} \right] \left[\frac{1-q}{r-1} \right] - \left[q + \left(\frac{r-q}{r-1} \right) \frac{\Delta_n}{\delta_n} \right] \exp\left(-\frac{\Delta_t^2}{\delta_t^2}\right) \right\} \quad (2.31)$$

where:

- $q = \frac{\phi_t}{\phi_n}; r = \frac{\Delta_n^*}{\delta_n} \rightarrow$ coupling coefficients;
- $\phi_n, \phi_t \rightarrow$ work of normal and shear separation;
- $\Delta_n, \Delta_t \rightarrow$ normal and tangential displacement jumps;
- $\delta_n, \delta_t \rightarrow$ normal and tangential interface characteristic lengths;
- $\Delta_n^* \rightarrow$ value of Δ_n after complete shear separation takes place under the condition of normal tension being zero, $T_n = 0$.

The derivative of the potential function with respect to the normal separation leads to the normal cohesive traction (Eq. (2.32)) while its derivative with respect to the tangential separation results in the tangential cohesive traction (Eq. 2.33)).

$$T_n = -\left(\frac{\phi_n}{\delta_n}\right) \exp\left(-\frac{\Delta_n}{\delta_n}\right) \left\{ \left(\frac{\Delta_n}{\delta_n}\right) \exp\left(-\frac{\Delta_t^2}{\delta_t^2}\right) + \frac{1-q}{r-1} \left[1 - \exp\left(-\frac{\Delta_t^2}{\delta_t^2}\right) \right] \left[r - \frac{\Delta_n}{\delta_n} \right] \right\} \quad (2.32)$$

$$T_t = -\left(\frac{\phi_n}{\delta_n}\right) \left(2 \frac{\delta_n}{\delta_t} \right) \left(\frac{\Delta_t}{\delta_t} \right) \left\{ q + \left[\frac{r-q}{r-1} \right] \frac{\Delta_n}{\delta_n} \right\} \exp\left(-\frac{\Delta_n}{\delta_n}\right) \exp\left(-\frac{\Delta_t^2}{\delta_t^2}\right) \quad (2.33)$$

The works of normal and tangential separations are given by Eqs. (2.34) and (2.35):

$$\phi_n = \sigma_{max} e \delta_n \quad \text{with: } \sigma_{max} = T_{n,max} \quad (2.34)$$

$$\phi_t = \sqrt{\frac{e}{2}} \tau_{max} \delta_t \quad \text{with: } \tau_{max} = T_{t,max} \quad (2.35)$$

Fig. 2.18a shows the uncoupled mode I TSL (i.e. T_n law in function on Δ_n) obtained from Eq. (2.32) by considering $\Delta_t = 0$; whereas Fig. 2.18b provides the variation of T_t with respect to Δ_t and by assuming $\Delta_n = 0$ (uncoupled mode II TSL).

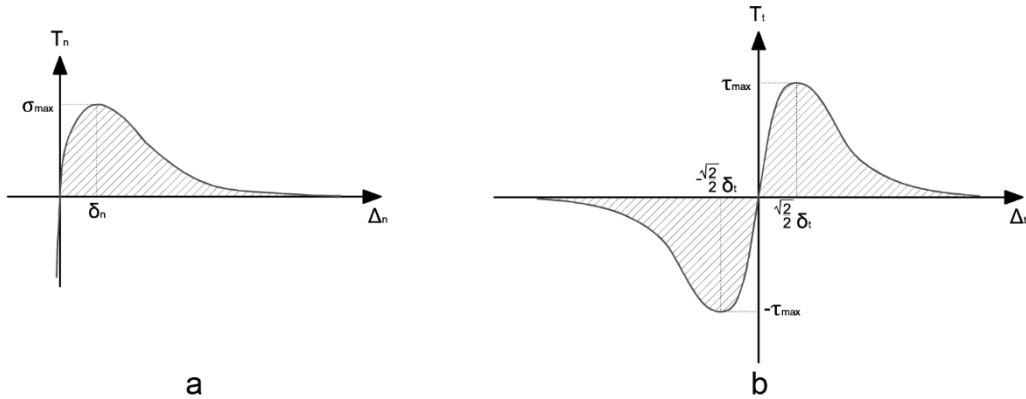


Figure 2.18 - Xu and Needleman model: a) TSL in mode I; and b) TSL in mode II

2.5.3 CZMs accounting for friction

For many engineering applications a non-negligible aspect is represented by the combination between the debonding process and friction, especially when interface models are applied to cementitious materials.

A simple way to combine friction and damage, proposed by Tvergaard in (Tvergaard, 1990), is to neglect friction as long as the interface damage is not complete and to introduce a friction law only when complete decohesion is attained. The behaviour of Tvergaard's interface debonding model is represented in Figs 2.19a and 2.19b. Particularly, from Fig. 2.19b, related to the tangential TSL, it is clear that a Coulomb-type friction law is introduced after the complete decohesion, i.e. when the tangential cohesive strength vanishes.

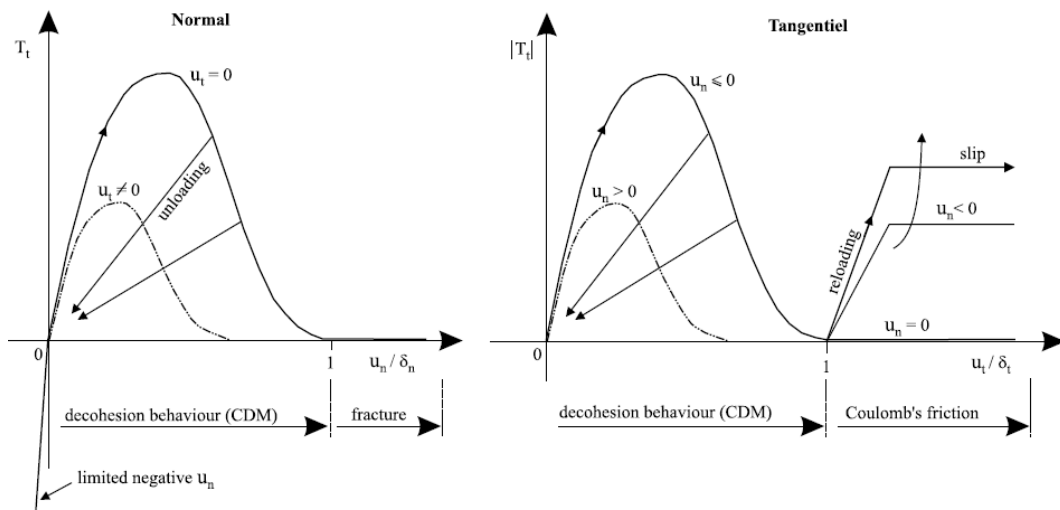


Figure 2.19 - Tvergaard's interface model accounting for friction: a) under normal loading; and b) under tangential loading [taken in (Tvergaard, 1990)]

Tvergaard's model lied the basis for the model subsequently proposed by Chaboche et al. (Chaboche et al., 1997). By following the main ideas of the Tvergaard's model, this model introduces additional terms that force a continuity and monotonicity in the tangential stiffness degradation between the decohesion behaviour and the Coulomb friction law that holds after complete separation, solving also some physical inconsistencies of the model presented by Tvergaard. Chaboche et al. model, also called 'plastic decohesion' model, considers an additive split of the tangential relative displacement (u_t) in an elastic and a plastic part, as shown in Eq. (2.36):

$$u_t = u_t^e + u_t^p \quad (2.36)$$

The normal traction, T_n , behaves according to Eq. (2.37), which is the same as in the Tvergaard model. In the ‘plastic decohesion’ model, instead, the tangential stress-displacement law is given by Eq. (2.38).

$$T_n = [EF(\lambda_{max})H(u_n) + KH(-u_n)] \frac{u_n}{\delta_n} \quad (2.37)$$

$$T_t = G \frac{u_t - u_t^p}{\delta_t} \quad (2.38)$$

where:

- $\lambda = 1 - \langle 1 - \sqrt{\left(\frac{u_n}{\delta_n}\right)^2 + \left(\frac{u_t}{\delta_t}\right)^2} \rangle$ → non-dimensioned parameter that plays role of a damage variable;
- F → function that describes the stiffness degradation;
- E and G → the initial stiffnesses respectively for normal and tangential conditions;
- H → the Heaviside function in order to specify the unilateral tension-compression contact condition;
- δ_n and δ_t → characteristic cohesive lengths (normal and tangential).

The Coulomb criterion (f), contrary to what happens in the Tvergaard model, is accounted for from the very beginning of the interfacial law, i.e. before complete decohesion (Fig. 2.20). The introduced friction term can be viewed as a kinematic hardening effect, with a decreasing hardening modulus as damage progresses. The expression of the Coulomb criterion is given in the following Eq. (2.39):

$$f = \left| T_t - \frac{GF(\lambda_{max})}{1-F(\lambda_{max})} \frac{u_t^p}{\delta_t} \right| - \mu \langle -T_n \rangle \quad (2.39)$$

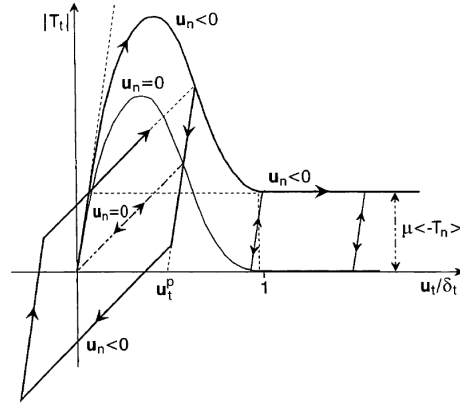


Figure 2.20 - Schematic behaviour of the Chaboche et al.'s model under tangential loading [taken in (Chaboche et al., 1997)]

The Chaboche et al.'s model has been formulated for the numerical simulation of non-linear interface behaviour in composite systems. As far as fibre debonding is concerned,

another interface model accounting for the combining effects of damage and friction has been proposed by Lin et al. (Lin et al., 2001).

The Lin et al.'s model is based on two uncoupled bilinear laws between the normal and tangential stress and the relative-displacement components, where an additional condition on the tangential stress accounts for friction. This condition imposes that the tangential stress must be lower than the modulus of the normal (compressive) stress multiplied by the friction coefficient.

Thus, starting from the rate-independent bilinear cohesive model proposed by Geubelle and Baylor (Geubelle and Baylor, 1998), Lin et al. modified the tangential law in order to account for frictional contact between the newly created fracture surfaces. The normal traction is given by the following Eq. (2.40):

$$T_n = \begin{cases} \frac{\sigma_{max}}{\delta_{max}} \delta_n & \text{For } \delta \leq \delta_{max} \\ \frac{\sigma_{max}}{\delta} \frac{1-\delta}{1-\delta_{max}} \delta_n & \text{For } \delta > \delta_{max} \end{cases} \quad (2.40)$$

As for the tangential traction, its expression depends on the value of the nondimensional normal displacement jump, δ_n . Thus, the expressions of T_t are given by the following Eqs. (2.41a) and (2.41b):

when $\delta_n > 0$:

$$T_t = \begin{cases} \frac{\sigma_{max} \Delta_n^c}{\delta_{max} \Delta_t^c} \delta_t & \text{For } \delta \leq \delta_{max} \\ \frac{\sigma_{max}}{\delta} \frac{1-\delta}{1-\delta_{max}} \frac{\Delta_n^c}{\Delta_t^c} \delta_t & \text{For } \delta > \delta_{max} \end{cases} \quad (2.41a)$$

when $\delta_n = 0$:

$$T_t = \begin{cases} \frac{\sigma_{max} \Delta_n^c}{\delta_{max} \Delta_t^c} \delta_t & \text{For } \delta \leq \delta_{max} \\ \frac{\sigma_{max}}{\delta} \frac{1-\delta}{1-\delta_{max}} \frac{\Delta_n^c}{\Delta_t^c} \delta_t & \text{For } \delta > \delta_{max} \\ \text{sign}(\Delta_t) \mu T_n & \text{For } |T_t| < \mu |T_n| \end{cases} \quad (2.41b)$$

where:

- $\delta_n = \frac{\Delta_n}{\Delta_n^c}$; $\delta_t = \frac{\Delta_t}{\Delta_t^c}$; $\delta = \sqrt{\delta_n^2 + \delta_t^2}$ → nondimensional normal, tangential and total displacement jumps;
- Δ_n^c and Δ_t^c → critical normal and tangential separations at which complete separation is assumed.

The uncoupled relationships for both normal and tangential tractions are reported in Figs. 2.21a and 2.20b, respectively.

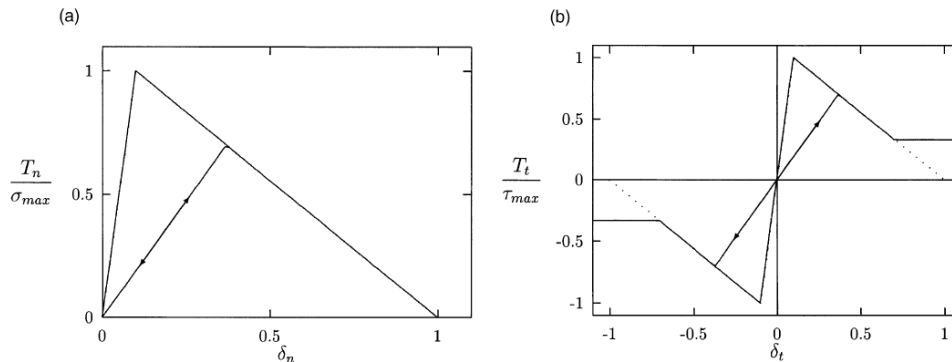


Figure 2.21 - Lin et al.'s model: a) uncoupled TSL in mode I; and b) uncoupled TSL in mode II accounting for friction [taken in (Lin et al., 2001)]

Another approach to introduce friction in a cohesive-zone model is based on nonassociative softening plasticity ((Lourenco, 1996), (Cocchetti et al., 2002), (Bolzon and Cocchetti, 2003), (Červenka et al., 1998)). In this framework, the interface formulations are generally characterised by an initial plastic yielding surface, which evolves according to a specific hardening/softening law, up to the Coulomb yielding surface, that allows to catch the residual frictional behaviour of the fully cracked material (Parrinello et al., 2009).

Several interface constitutive models have been formulated for different problems by using the nonassociative plasticity theory. As far as concrete is concerned, in (Carol et al., 2001) a hyperbolic initial yield locus has been used. (Cocchetti et al., 2002), adopted a piecewise linear yielding surface to model concrete dams; while for masonry walls, formulations of frictional-cohesive multidissipative models can be found in (Giambanco and Mroz, 2001) and (Oliveira and Lourenço, 2004).

Raous et al. (Raous et al., 1999), instead, formulated the so-called RCCM model, which has been later generalised by Del Piero and Raous (Del Piero and Raous, 2010). In this model, the adhesion is characterised by a state variable, β , which represents the intensity of adhesion and controls viscosity and Coulomb friction. As long as a reverse normal displacement is applied, the interface behaviour is elastic and the new value of the stiffness depends on the damage, which is evaluated by the intensity of adhesion. Unilateral conditions prevent any inter-penetration from occurring between the two edges of the interface. When a reverse tangential force is applied, the Coulomb threshold (i.e. the normal traction multiplied by the friction coefficient) has to be reached before reverse tangential sliding can occur (Raous et al., 2011). The normal and tangential laws described by the RCCM model are reported in Figs. 2.22a and 2.22b, respectively (Raous et al., 1999).

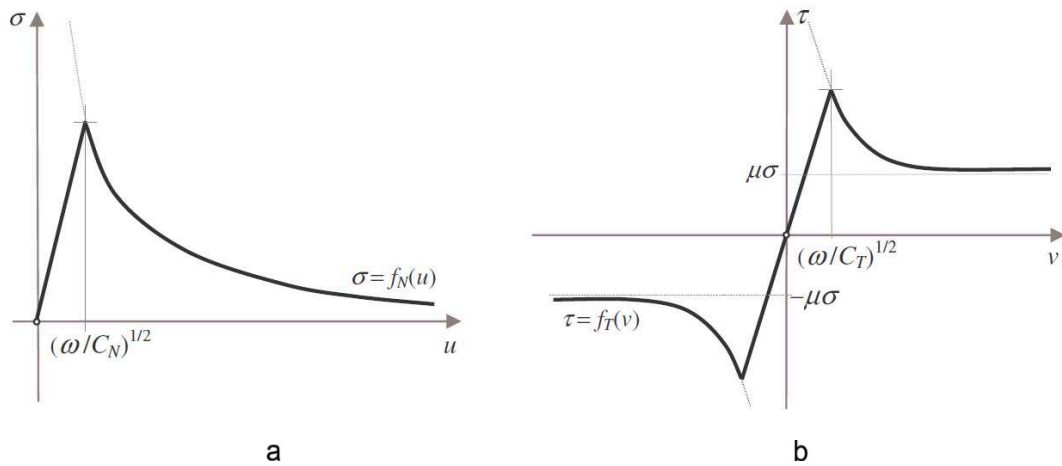


Figure 2.22 - RCCM model accounting for friction: a) TSL in mode I; and b) TSL in mode II [taken in (Raous et al., 1999)]

Further developments of this model have been presented in (Del Piero and Raous, 2010), where a unified model for adhesive interfaces with damage, viscosity and friction is formulated starting from the RCCM model (Raous et al., 1999). Fig. 2.23 represents the TSLs in mode I and II according to the model formulated by Del Piero and Raous (Del Piero and Raous, 2010).

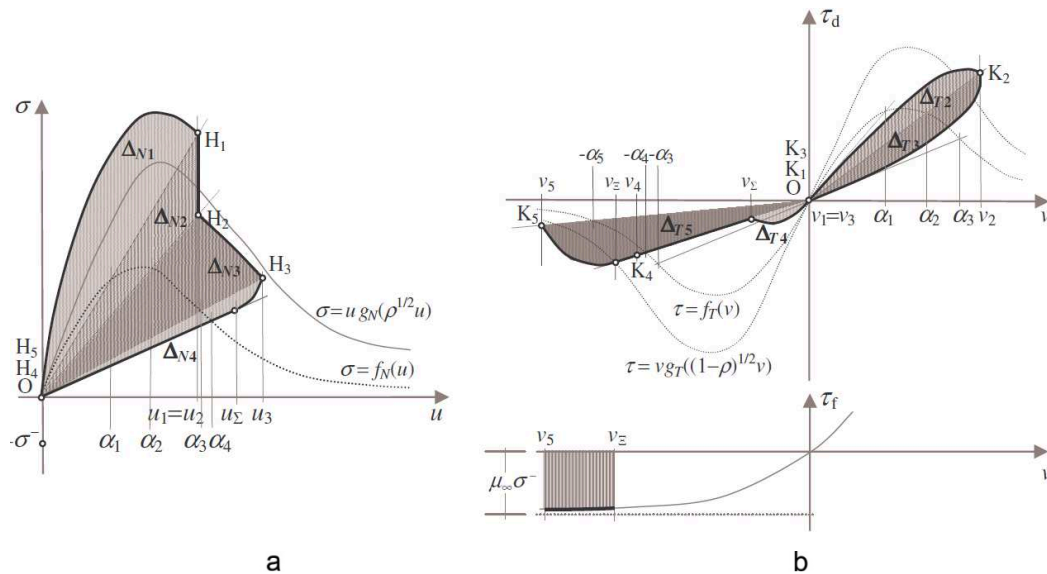


Figure 2.23 - Del Piero and Raous model accounting for friction and viscosity: a) TSL in mode I; and TSL in mode II [taken in (Del Piero and Raous, 2010)]

The different approach adopted by Alfano and Sacco (Alfano and Sacco, 2006) in their model considers a simplified micromechanical formulation in order to combine interface

damage and friction in a cohesive zone model. The main idea of this model is to consider a representative interface area (REA) at the micromechanical scale, which is assumed to be additively decomposed into an undamaged and a fully damaged part, with the damage parameter D being the relative measure of the damaged part. The undamaged part is described by a linear elastic behaviour, while the damaged one is governed by the Crisfield's damage evolution model (bilinear) (Alfano and Crisfield, 2001) with the introduction of the Coulomb-type friction law. Remarkably, this model does not require softening plasticity, because the gradual loss of cohesion is the natural outcome of the gradual evolution of the damage parameter D from zero to unity (Alfano and Sacco, 2006). A scheme of the REA composition is shown in Fig. 2.24, while the main constitutive relationships of the Alfano and Sacco model are given by Eqs. (2.42)-(2.50).

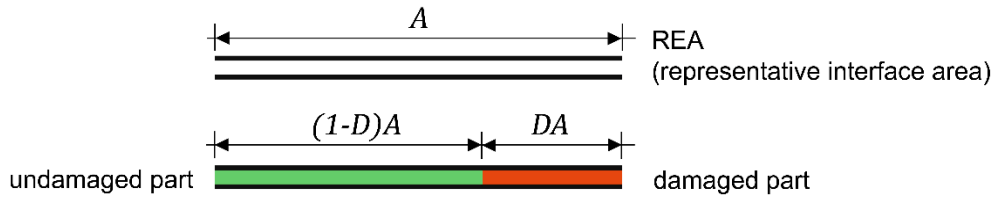


Figure 2.24 - Scheme of the bipartition of the REA into damaged and undamaged parts

The area of the REA, A , is additively portioned into an undamaged part, A_u , and a damaged part, A_d , as illustrated in the following Eq. (2.42):

$$A = A_u + A_d; A_u = (1 - D)A; A_d = DA \quad (2.42)$$

As for the kinematics aspect, the relative displacement, \mathbf{s} , is assumed to be constant over the entire REA (Eq. (2.43)). A further decomposition concerns the relative displacement in the damaged part, which is additively split into an elastic, \mathbf{s}^{de} , and an inelastic part, \mathbf{s}^{di} , as it is reported in Eq. (2.44). On the undamaged part, instead, the relative displacement is assumed to be totally elastic (Eq. (2.45)).

$$\mathbf{s}^u = \mathbf{s}^d = \mathbf{s} \quad (2.43)$$

$$\mathbf{s}^d = \mathbf{s}^{de} + \mathbf{s}^{di} \quad (2.44)$$

$$\mathbf{s}^u = \mathbf{s}^{ue} = \mathbf{s} \quad (2.45)$$

The interface stress is assumed to be constant on each part of the REA, and given by Eq. (2.46):

$$\boldsymbol{\sigma}^u = \mathbf{K}\mathbf{s} \quad \boldsymbol{\sigma}^d = \mathbf{H}(\mathbf{s} - \mathbf{s}^{di}) \quad (2.46)$$

where \mathbf{K} is a diagonal matrix which reports the stiffness values in all the fracture modes, and \mathbf{H} is the 'finite elastic stiffness' matrix (see (Alfano and Sacco, 2006) for the complete formulation).

Thus, the stress vector over the whole REA is defined as shown in Eq. (2.47):

$$\boldsymbol{\sigma} = (1 - D)\boldsymbol{\sigma}^u + D\boldsymbol{\sigma}^d \quad (2.47)$$

Each stress vector is additionally decomposed into the normal and the tangential components (i.e. σ and τ).

The Coulomb's type friction function, ϕ , in the model of Alfano and Sacco (Alfano and Sacco, 2006) is given by Eq. (2.48):

$$\phi(\boldsymbol{\sigma}^d) = \mu \langle \sigma^d \rangle_- + |\tau^d| = \mu \sigma^d + |\tau^d| \quad (2.48)$$

where μ is the friction coefficient.

Thus, the inelastic relative displacement s^{di} is governed by the nonassociative relationship given by Eq. (2.49):

$$\dot{s}^{di} = \dot{\lambda} \begin{bmatrix} 0 \\ \frac{\partial \phi}{\partial \tau^d} \end{bmatrix} = \dot{\lambda} \begin{bmatrix} 0 \\ \frac{\tau^d}{|\tau^d|} \end{bmatrix} \quad \text{with the Khun-Tucker conditions:} \quad (2.49)$$

$$\dot{\lambda} \geq 0 \quad \phi(\boldsymbol{\sigma}) \leq 0 \quad \lambda \dot{\phi}(\boldsymbol{\sigma}) = 0$$

The evolution law of the damage variable, D , is described by Eq. (2.50):

$$D = \max_{\text{history}} \tilde{D}; \quad \tilde{D} = \max \left\{ 0, \min \left\{ 1, \frac{1}{\eta} \left(\frac{\beta}{1+\beta} \right) \right\} \right\}; \quad 0 \leq D \leq 1 \quad (2.50)$$

where:

- $\frac{s_{01}}{s_{c1}} = \frac{s_{02}}{s_{c2}}$ → hypothesis made in the model that implies the proportionality of the elastic limit displacement (s_{0i} , where i stands for the fracture mode: '1' corresponds to the opening mode, and '2' to the sliding mode) and the displacement at complete debonding;
- $\eta = 1 - \frac{s_{01}}{s_{c1}} = 1 - \frac{s_{02}}{s_{c2}}$ → defined as 'ductility parameter';
- $\beta = \sqrt{\left(\frac{(s_1)_+}{s_{01}} \right)^2 + \left(\frac{s_2}{s_{02}} \right)^2} - 1$ → parameter that indicate that the response is linear elastic ($D = 0$) as long as $\beta \leq 0$

An example of the interface mechanical response with respect to the tangential direction (shear stress, τ , versus the sliding relative displacement, s_2 or δ_t) is reported in Fig. 2.25. It is possible to observe how friction modifies the response after the debonding process.

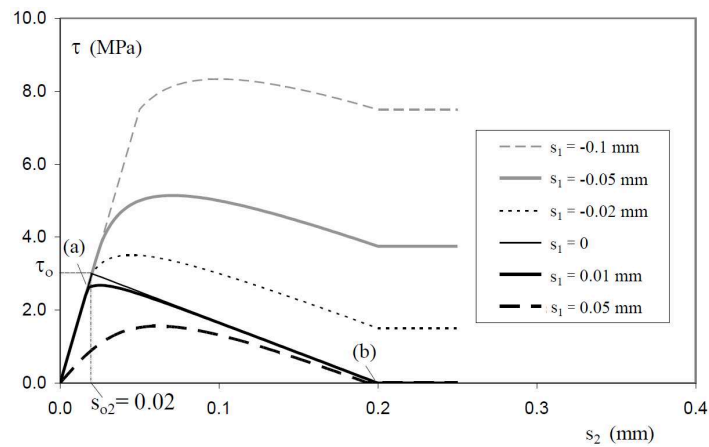


Figure 2.25 - Alfano and Sacco model accounting for friction: TSL in mode II [taken in (Alfano and Sacco, 2006)]

The model formulated by Alfano and Sacco in (Alfano and Sacco, 2006) has laid the basis for further developments able to account for the interlocking effect (Serpieri and Alfano model (Serpieri and Alfano, 2011)) and also for finite dilation and asperity degradation (Serpieri, Alfano and Sacco model (Serpieri et al., 2015)). In the first model (Serpieri and Alfano, 2011), the interlocking phenomenon has been simulated by modelling the smooth macro-interface (Fig. 2.26a) through the definition of a periodic pattern of a repeating unit (representative interface area RIA) at the microscale level (Fig. 2.26c). In this model, the RIA is constituted by a certain number, N_p , of elementary planes (hereafter called *microplanes*) which simulate the interface asperities. Each microplane is then governed by the combined cohesive-friction model by Alfano and Sacco (Alfano and Sacco, 2006).

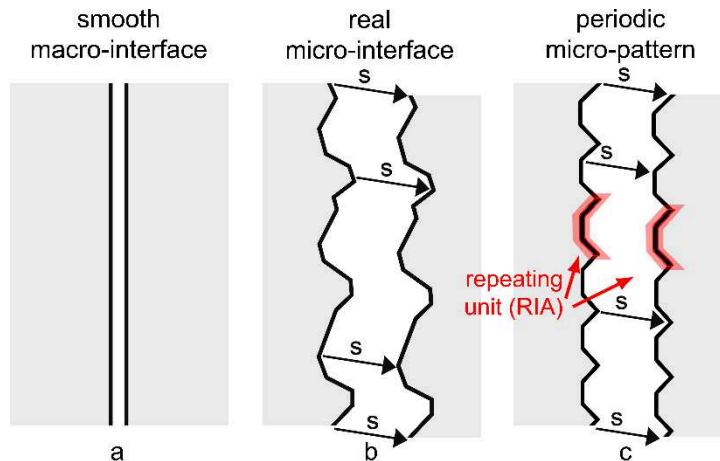


Figure 2.26 - Multiscale approach of the Serpieri and Alfano model (Serpieri and Alfano, 2011): a) smooth macro-interface; b) real micro-interface; and c) periodic micro-pattern of a repeating unit through which the interface is described

The enhancement introduced in the second model, hereafter called Multiplane Cohesive Zone Model (M-CZM) (Serpieri et al., 2015), instead, accounts for the finite depth of the aforementioned asperities by considering the progressive reduction in contact area between each couple of interfacing microplanes for increasing opening (macro-scale) relative-displacement.

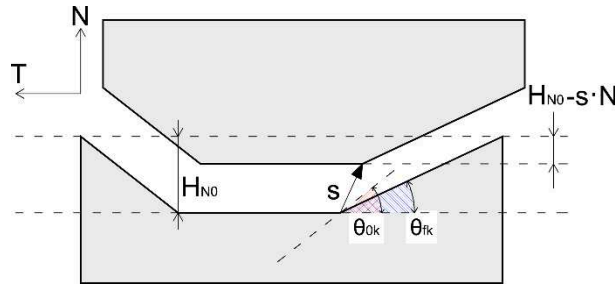


Figure 2.27 - Finite depth of the asperities in the M-CZM

The second novel aspect characterising the M-CZM concerns the progressive degradation of the interlocking effect, due to the rupture of the asperities and associated flattening of the fracture surface (Fig. 2.27). To account for this aspect, a progressive reduction of the inclination angles of the microplanes of the RIA is considered according to the exponential law reported in Eq. (2.51):

$$\theta_k = (\theta_{k0} - \theta_{kf}) e^{-\frac{\zeta_k}{\zeta_{k0}}} + \theta_{kf} \quad (2.51)$$

In Eq. (2.51), the current value of the microplanes inclination angle, θ_k is related to the frictional work, ζ_k , spent in sliding along the tangential direction of the k^{th} microplane, given by Eq. (2.52):

$$\zeta_k = \int_{\text{history}} \sigma_{kt} ds_{kf} \quad (2.52)$$

where θ_{k0} and θ_{kf} are the initial and final microplanes inclination angles, and ζ_{k0} is a characteristic energy value that controls the rate of degradation.

2.5.4 CZMs for description of bond-slip behaviour in RC structures

The cohesive modelling approach has been largely used to investigate the bond-slip behaviour between reinforcement and concrete. In this context, the introduction of friction in the model formulation allowed a better representation of the real behaviour exhibited by the steel-to-concrete interface during debonding.

The RCCM model formulated by Raous in (Raous et al., 1999), has been extended for describing the steel-concrete interfaces in reinforced concrete by using a variable friction coefficient (from a certain sliding value, $|u_t| = 0.3$ mm, onward) which simulates a ‘grinding phenomenon’ of the interface during the sliding (Raous and Ali Karray, 2009). This model has been used by the authors to simulate the experimental results obtained from a series of pull-out tests of steel bars from concrete matrices, obtaining good agreement between numerical and experimental curves. The main feature of this model concerns the decreasing

law which describes the friction coefficient for growing sliding at the interface. It is derived from the observation that, when sliding occurs, small particles are generated inside the interface giving birth to a grinding phenomenon that reduces the frictional action. The expression of the decreasing friction coefficient is given by Eq. (2.53):

$$\mu = \begin{cases} \mu_s & |u_t| \leq 0.3 \text{ mm} \\ \mu_d + (\mu_s - \mu_d) \frac{0.3 - |u_t|}{u_d} & |u_t| > 0.3 \text{ mm} \end{cases} \quad (2.53)$$

Ragueneau et al. (Ragueneau et al., 2006) formulated an inelastic constitutive model for a nondimensional zero-thickness joint finite element, which would represent the bond-slip phenomena between brittle cohesive materials and reinforcement. They developed a new 2D interface element, which takes into consideration the degeneration effects by introducing a strain-based constitutive model coupling hysteretic tangential behaviour and radial confinement effects on bonding phenomena. To this end, constitutive equations for bond model have been formulated within a 2D framework of continuum damage mechanics for brittle materials. The model couples contact and frictional sliding and captures mode II failure at the interface. The describing equations, in normal and tangential directions, are provided in Eqs. (2.54) and (2.55), respectively. Particularly, the normal and tangential stresses (σ_N and σ_τ) are derived from a thermodynamic potential, ψ (see (Ragueneau et al., 2006) for the potential equation), which is associated to the bond-interface element.

$$\sigma_N = (1 - d)(2\mu + \lambda)\varepsilon_N + d(2\mu + \lambda)(\varepsilon_N - \varepsilon_N^s) \quad (2.54)$$

$$\sigma_\tau = 2\mu(1 - d)\varepsilon_\tau + \sigma_\tau^s \quad ; \text{ with } \sigma_\tau^s = 2\mu d(\varepsilon_\tau - \varepsilon_\tau^s) \quad (2.55)$$

where:

- d → internal damage variable linked to cracking process, acting as a multiplier term that allows the coupling between cracking and frictional sliding;
- μ and λ → Lamé's coefficients correlating the strains tensor to the stresses one;
- $\boldsymbol{\varepsilon} = \begin{bmatrix} \varepsilon_N \\ \varepsilon_\tau \end{bmatrix}$ and $\boldsymbol{\sigma} = \begin{bmatrix} \sigma_N \\ \sigma_\tau \end{bmatrix}$ → strain and stress tensors;
- $\boldsymbol{\varepsilon}^s = \begin{bmatrix} \varepsilon_N^s \\ \varepsilon_\tau^s \end{bmatrix}$ and $\boldsymbol{\sigma}^s = \begin{bmatrix} \sigma_N^s \\ \sigma_\tau^s \end{bmatrix}$ → sliding strain and stress tensors.

The above formulation has been validated in (Ragueneau et al., 2006) by comparing numerical results to experimental pull-out curves, obtaining good agreement, especially due to the capability of the model to combine cracking and frictional sliding phenomena.

Other examples of the application of a CZM accounting for friction to the modelling of the bond-slip behaviour can be found in (Serpieri and Alfano, 2011) and (Serpieri et al., 2015b), where pull-out test results have been used to validate the proposed model. In (Serpieri and Alfano, 2011), the response of both plain and ribbed bars has been obtained

with the cohesive zone model proposed, finding out that the model is capable of well capturing the increasing effect of confining pressure on the strength and peak slip. However, the numerical results overestimated the strength and stiffness next to the peak values, probably due to the localised crushing and cracking phenomena within concrete which cannot be simulated by the modified Drucker–Prager model employed to simulate concrete behaviour. The prediction of the pull-out response obtained in (Serpieri et al., 2015b), demonstrated that the M-CZM captures all the qualitative aspects of the dissipative processes with satisfactory accuracy. In that case, only deformed bars have been taken into consideration, simulating the ribs with the asperities that characterise the M-CZM. Thus, the typical behaviour of ribbed bars under pull-out conditions could be well represented by adopting this model able to account for damage, friction, mechanical interlocking and dilatancy.

2.6 Reinforcement-to-concrete interface in fibre-reinforced concrete

The bond behaviour investigated so far concerns the traditional reinforcement in the forms of reinforcing bars. However, in the last decades alternative and/or supplementary ways have been introduced in order to enhance the RC structural performance. Particularly, the brittle nature of concrete and its weakness in resisting tensile stresses have been often addressed by adding fibres to the cementitious matrix. Fibre-reinforced composites, in fact, resist tensile forces through a composite action which relies on the force transmission mechanism between the matrix and the fibres. This mechanism is achieved through bond, defined as the shearing stress at the interface between the fibre and the surrounding matrix. Moreover, it is generally agreed that the increasing of the composite material toughness is mostly provided by the mechanism of fibre pull-out (Namur et al., 1991).

Thus, in the next paragraph, fibre-reinforced concrete (FRC) materials are introduced with particular regard to the bond behaviour between fibres and matrix, referring to (Bentur and Mindess, 2007) and (Brandt, 2008) for a detailed review on FRCs and to Chapter 6 and Chapter 7 of the present thesis for more specific concepts involving FRC characteristics.

2.6.1 Introduction to fibre-reinforced concrete

The addition of fibres to concrete mixtures is not a novel concept. Early patents on fibre-reinforced concrete date back to 1874 (A. Berard, USA) and fibres similar to those currently most widely used and employed were patented in 1927 (G. Martin, USA), 1939 (Zitkevic, Britain) and 1943 (G. Constantinesco, England), as reported by Namaan (Naaman, 1985) and (Beddar, 2002).

The presence of fibres is aimed to increase the material ductility in the post-peak range, since the well-known quasi-brittle behaviour of concrete. In fact, plain, unreinforced cementitious materials are characterised by low tensile strengths, and low tensile strain capacities (Bentur and Mindess, 2007). Historically, this lack in the tensile performance has been supplied by continuous reinforcing bars, which could be placed in the structure at the appropriate locations to withstand the imposed tensile and shear stresses. Conversely,

fibres are discontinuous and usually randomly distributed throughout the concrete matrix. Therefore, they are not as efficient as reinforcing bars in withstanding the tensile stresses. Thus, conventional reinforcing bars are used to increase the load-bearing capacity of concrete; fibres are more effective for crack control, since they tend to be more closely spaced than conventional reinforcing bars. This allows fibres to transfer tensile forces across cracks, reducing the width of cracks compared to unreinforced concrete and enhancing the post-cracking performance of the resultant composite material. An example of the typical FRC behaviour under tensile stresses is reported in the following Fig. 2.28, where the contribution of the fibres in the post-peak region is clearly visible.

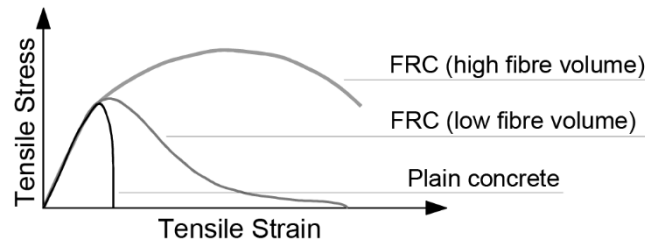


Figure 2.28 - Typical stress–strain curves for conventional and high performance FRC [after (ACI Committee 544, 1999)]

In general, the main factors governing the performance of fibre-reinforced concrete (FRC) depends on the:

- 1) the physical and mechanical properties of the fibres and their distribution and content;
- 2) the physical and mechanical properties of the concrete matrix;
- 3) the fibre-matrix interface bond properties.

A brief explanation of the factors affecting FRC performance is made here, referring to (Bentur and Mindess, 2007) for a complete discussion on the present topic.

2.6.1.1 Physical and mechanical properties of fibres and matrix

A wide range of fibres of different mechanical, physical and chemical properties have been considered and used for reinforcing concrete matrices (Bentur and Mindess, 2007). Fibres are usually classified in terms of material, length and aspect ratio (i.e. length to diameter ratio), geometrical configuration, orientation and distribution. Additionally, fibres of a specific material are usually characterised by a specific range of dimensions in terms of length, aspect ratio or by a preferable distribution pattern.

As far as fibres constituent materials are concerned, the literature provides a vast panorama. First distinctions concern metallic or non-metallic, natural or synthetic, inorganic or organic fibres.

Steel fibres are clearly ones of the most investigated, but recently several alternative materials have been proposed, especially with the aim to overcome the problem of corrosion.

Table 2.5 summarises some of the materials intended for realising reinforcing fibres, giving a synoptic view of the vast amount of data found in the literature for steel fibres ((Bentur and Mindess, 2007), (Błaszczński and Przybylska-Fałek, 2015)); glass fibres ((Chandramouli K. et al., 2010) (Ibrahim, 2016)); synthetic fibres (e.g. carbon (Chung, 2000), (Muley et al., 2015)), aramid ((Uchida et al., 2010), (Erdem et al., 2015)), acrylic (Mo et al., 2015), (Kumar and Ritu, 2015)), and others) (Cominoli et al., 2007), (Ludirdja and Young, 1992)); and natural fibres (Ardanuy et al., 2015).

Table 2.5 - Comparison among different materials used as fibre reinforcement for concrete

Fibre material	Physical form and length (length in mm)	Typical diameter (μm)	Typical vol.fraction (%)
Metallic			
Steel	Discrete/Short		
Stainless steel	12-60	5-1000	0.2-2.5
Glass			
E-glass	Discrete/short		
AR-glass	10-15	14	0.05-5
Synthetic			
Carbon	Discrete/short 5-6	7-15	0.25-1
Aramid	Discrete/short 3-4	14	0.5
Acrylic	Discrete/short 1-2	14-15	0.2-0.5
Nylon	Monofilament 12	9	0.2-0.5
Polyester	Monofilament 70-1000	50-500	~ 1
	Dispersible rovings 70-1000	5-15	~ 1
Polypropylene	Fibrillated 70-1000	15-100	
	Monofilament 70-1000	50-500	~ 1
Natural			
Cellulose – wood	Strands	variable	2-10
E.g.: pine, eucalyptus	(long fibres) 200-1000		
Cellulose – non-wood:			
- bast fibres (hemp, jute, kenaf, flax, ramie, etc.);	Staples/yarns (short fibres)		
- leaf fibres (sisal, henequen, pineapple, oil palm leaf fibres, banana, etc.),	50-100 Pulps (very short fibres)		

Fibre material	Physical form and length (length in mm)	Typical diameter (μm)	Typical vol. fraction (%)
- stalk fibres (straws – as rice, wheat and barley; reeds – as bamboo and grass – as esparto and elephant grass); - seed fibres (cotton, coir, and others)	1-10		

As it is possible to observe from Table 2.5, there are two main groups of fibre-reinforcing arrays in term of length: (i) continuous reinforcement in the form of long fibres which are incorporated in the matrix by techniques such as filament winding or by the lay-up of layers of fibre mats (Fig 2.29a and 2.29b); and (ii) discrete short fibres, usually less than 60 mm long, which are incorporated randomly in the matrix by methods such as spraying and mixing (Fig. 2.29cc) (Bentur and Mindess, 2007).

Noteworthy, the fibres orientation, distribution and content, strongly affect the mechanical performance of the FRC (Löfgren, 2005).

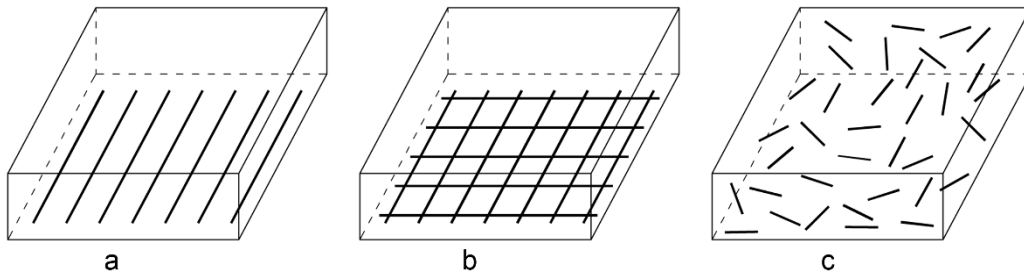


Figure 2.29 - Examples of fibre distribution and orientation: a) unidirectional in-plane distribution of continuous long fibres; b) bidirectional in-plane distribution of continuous long fibres; and c) random distribution of discrete short fibres

After the material characterisation, physical and chemical properties represent a further means of fibres classification (Naaman, 2003). Examples of physical and chemical properties are: density, surface roughness, chemical stability, non-reactivity with the cement matrix, fire resistance, etc.

The third relevant aspect that characterises a fibre, is represented by the mechanical properties, such as tensile strength, elastic modulus, stiffness, ductility, elongation to failure, surface adhesion properties, etc.

In terms of chemical/physical and mechanical properties, remarkable importance is assumed not just by the properties of the fibre itself, but by the properties of the fibre with respect to the concrete matrix. Naaman (Naaman, 2003) established some general relations between the properties of the fibres and matrix, which maximise the fibres effectiveness:

1. fibre tensile strength significantly higher than that of the matrix (2 to 3 orders of magnitude);
2. fibre-matrix bond strength preferably of the same order as or higher than the tensile strength of the matrix;

3. fibre elastic modulus in tension significantly higher than that of the matrix (at least 3 times);
 4. enough ductility so that the fibre does not fracture due to fibre abrasion or bending.
- In addition, the Poisson ratio and the coefficient of thermal expansion should be of the same order for both fibre and matrix. In fact, if the Poisson ratio is significantly larger than that of the matrix, debonding will occur due to lateral contraction of the fibre. However, this can be overcome by various methods such as surface deformation, fibre twisting, or mechanical anchorage. Additionally, it is important that the fibres are durable and can withstand the high alkaline environment of the concrete matrix (Löfgren, 2005). Once a fibre has been selected in terms of material and related physical and mechanical properties, an almost infinite combination of geometric properties related to its cross-sectional shape, length, diameter or equivalent diameter, and surface deformation can be selected (Naaman, 2003). The choice of the geometric configuration is affected by the fibre material and, in turn, strongly influences the mechanical performance of the resultant composite material. Further details on the fibre geometrical configuration are discussed in Chapter 6.

2.6.1.2 The fibre-matrix interface

Cementitious composites are characterised by an interfacial transition zone (ITZ) in proximity of the reinforcing inclusion, in which the microstructure of the paste matrix is considerably different from that of the bulk paste, away from the interface (Bentur and Mindess, 2007). The density and packing of the ITZ is influenced by several parameters, such as the size of the fibre in relation to the other constituents; the size and packing of the matrix material; the porosity of the matrix; and the surface roughness and chemistry of the fibre. Thus, several factors contribute to the complexity of the ITZ, whose properties affect especially the fibre-matrix bond, and the debonding process across the interface.

The stress transfer from reinforcement to concrete matrix can be described by dividing the process into two different situations, i.e. the stress transfer in the uncracked concrete and the stress transfer in the cracked concrete (post-cracking behaviour). During the early stages of loading, the nature of the interaction between the fibre and the matrix is elastic. In this phase the description of the stress field around the fibre can be satisfactorily described through the so-called *shear-lag theories* (Cox, 1952). Once the adhesion shear strength has been exceeded by the pull-out load, a debonded zone of a certain length is formed, and the shear stress distribution is uniform in this zone. Beyond the latter, the interfacial shear stress decreases, following the shear lag theory relationships. If debonding occurs prior to matrix cracking, slip occurs in the debonded zone, resulting in activation of the frictional resistance mechanism. However, the major effect of the fibres in FRC composites occurs in the post-cracking zone, when the *fibre bridging mechanism* (Li et al., 1993) takes place. The bridging action of the fibres across the cracks that have propagated in the brittle concrete matrix, mitigate the cracking formation process, improving the ductility of the composite and eventually preventing the fragile failure. While the stress-transfer mechanisms previously described control the stress-strain curve of the composite prior to cracking, the mechanisms involved in the post-cracking stage influence the ultimate strength and deformation properties of the FRC composite and its mode of failure. Fig. 2.30

summarises the post-cracking mechanisms acting during the post-cracking stage, i.e. matrix fracture and matrix spalling (or fragmentation), fibre-matrix interface debonding, post-debonding friction between fibre and matrix (fibre pull-out), fibre fracture, and fibre abrasion and plastic deformation (or yielding) of the fibre.

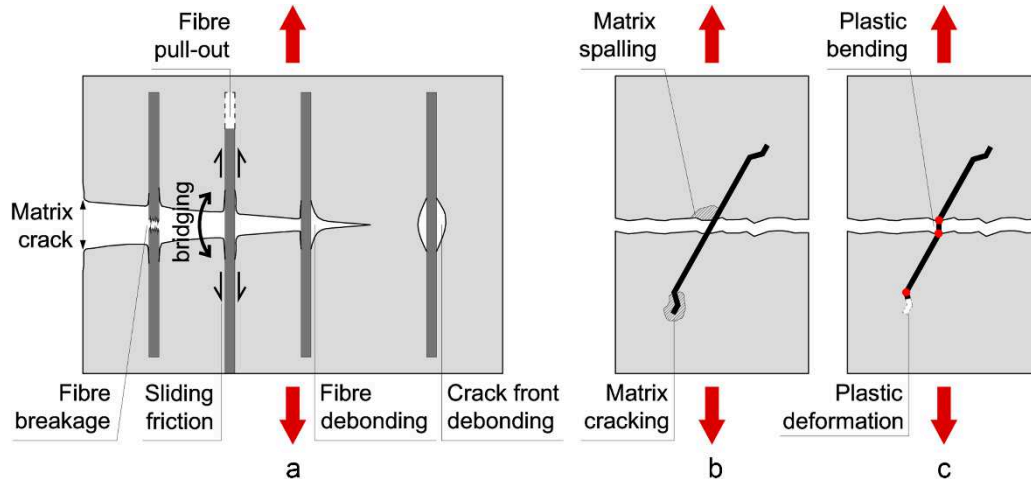


Figure 2.30 - a) Toughening effects and crack front debonding, the Cook-Gordon effect (Cook and Gordon, 1964), and debonding and sliding in the crack wake; b) matrix spalling and matrix cracking; c) plastic bending of inclined fibre during pull-out at the crack and at the end-anchor [based on (Löfgren, 2005)].

As it happens for reinforcing bars, the load transfer induced by the fibre which bridges the crack is usually assessed by single or multiple fibre pull-out tests. These tests provide the basis for predicting the overall behaviour of the composite in the post-cracking zone (Bentur and Mindess, 2007).

2.6.2 Fibre-matrix bond and pull-out mechanism

Naaman et al. (Naaman et al., 1989) identified the fibre-matrix bond mechanism as a major factor in composite material action, assessing that almost all the properties of a composite depend on the interfacial bond between fibres and matrix. As it happens in the case of rebars, the nature of bond in fibre reinforced cementitious composites is very complex because of the presence and the combined action of several mechanisms. In addition to the bond components identified for the bar-matrix interface, i.e. chemical adhesion, friction and mechanical interlocking, when fibres are concerned another mechanism has been found to have a role in the process: the fibre to fibre interlock, or entanglement. In fact, since many fibres are near each other, their interaction must be considered. As long as a single steel fibre is embedded in concrete and subjected to a direct tensile load (typical pull-out test), it behaves like a steel reinforcing bar in the same condition. When the presence of many other fibres is considered, instead, it should be taken into account the fibre entanglement, which, actually, modifies the behaviour of the whole composite (Naaman et al., 1989).

Fundamental information on the nature and strength of the interfacial bond between the fibre and the matrix in a FRC material is usually obtained using the single-fibre pull-out test. The latter simulates the stress distribution on the surface of a fibre normal to and bridging a matrix crack in a composite, as shown in Fig. 2.31. Certainly, the test is an approximation of the real situation, based on the assumption that the failure is due to matrix tensile fracture followed by fibre-matrix debonding and pull-out. Moreover, the combined effect provided by the presence of numerous fibres is not taken into account.

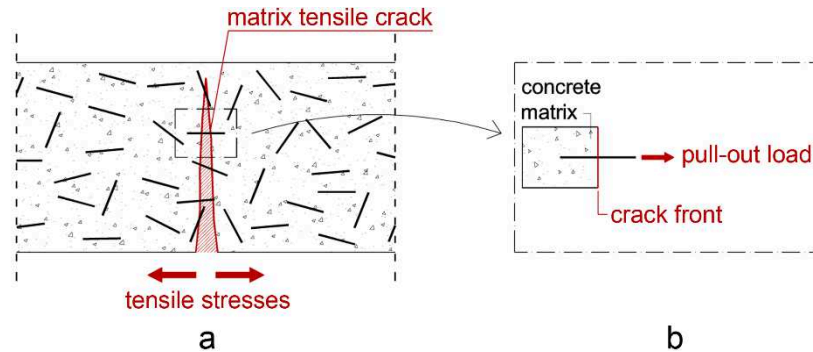


Figure 2.31 - a) Fibre normal to and bridging a matrix tensile crack in a real composite; and b) simulation of the real situation through single fibre pull-out test

Further considerations on the reliability of single fibre pull-out test are provided in Chapter 6, when the experimental results obtained here, are compared to the typical results presented in the literature.

2.6.3 Differences between reinforcing bars and fibres in terms of bond behaviour

Naaman et al. reported in (Naaman et al., 1989) that '*fibres feature a completely different behaviour than conventional reinforcement*'. Obviously, the main difference between traditional and fibre reinforcement lies in the fact that, unlike rebar, fibres are not continuous and near each other.

However, a single steel fibre embedded in concrete and subjected to a pull-out test, will behave like a steel reinforcing bar under the same condition. Thus, the bond behaviours of bars and fibres have some similarities, first of which are the main three mechanisms contributing to bond, i.e. chemical adhesion, friction, and mechanical interlocking.

2.6.4 Bond modelling for FRC

Since the main bond components between reinforcing bars and concrete have been recognised in the fibre-matrix bond behaviour, some of the modelling strategies presented in paragraph 2.4 of this chapter can be applied also to the study of the fibre-matrix relationship.

In particular, cohesive zone models have been largely applied to the study of interface debonding for FRC (Needleman, 2013). Moreover, for fibre pull-out processes, where the combination of separation and frictional sliding is crucial, a novel class of cohesive

constitutive models suitable for the analysis of material separation such as that related to cracks or delamination processes has been recently presented in (Mosler and Scheider, 2011).

A more detailed explanation of the CZMs applied to the study of fibre-matrix debonding is provided in Chapter 6 of the present thesis, where the relation between models and various fibre geometries is also taken into account on the basis of the experimental results obtained in the present research.

Chapter 3

Characterisation of the bond behaviour between concrete and titanium alloy bars through pull-out tests

In order to characterise the interface between titanium and concrete, a series of pull-out tests on titanium alloy bars from concrete specimens has been carried out. This chapter presents the mechanical properties of the materials, the specimens' preparation, the experimental set up, the testing procedure and the obtained results.

3.1 Pull-out test experimental methodology

Pull-out tests are commonly used to assess the bond behaviour between steel reinforcing bars and concrete, as discussed in paragraph 2.3.2 of Chapter 2. In the present work, in order to characterise the interface between titanium and concrete, the same procedure commonly adopted for steel reinforcing bars has been used, due to the metallic nature of the reinforcement. Thus, pull-out tests were carried out according to the standard RILEM RC6 (RILEM TC, 1983).

3.2 Materials

In this experimental work the titanium alloy Ti6Al4V, one of the most used titanium alloys, and two different concrete mixture are employed. The first one contains normal-weight aggregates, while the second one contains lightweight aggregates.

3.2.1 Concrete

Concerning concrete, two different mixtures were cast, i.e. normal (Normal-Weight Concrete, NWC) and lightweight aggregate concrete (Light-Weight Concrete, LWC). In particular, fine aggregate (maximum diameter, D_{max} , equal to 4 mm) consists of natural sand for both the mixtures, while coarse one ($D_{max}=15$ mm) consists of crushed gravel for NWC and expanded clay for LWC mixture. Details of the mix design for both the mixtures are reported in Table 3.1.

Table 3.1 - NWC and LWC concrete mixtures mix design

NWC mix			LWC mix		
		(kg/m ³)			(kg/m ³)
Water		184	Water		184
Cement CEM II A/L		335	Cement CEM II A/L		420
Fine aggregate (natural)	(0-4)	1010	Fine aggregate (natural)	(0-4)	785
Coarse aggregate	(4-15)	790	Coarse aggregate	(0-15)	340
Superplasticiser		2.7	Superplasticiser		3.4
			Air entraining admixture		2.6
Density		2325	Density		1735

The characterisation of the mechanical properties of the two mixtures, compression and indirect tensile tests have been carried out, according to the standard UNI-EN 12390, which provides indications for testing hardened concrete.

3.2.1.1 Compression test

Compression tests on NWC and LWC have been carried out following the European standard UNIEN 12390-3:2009 (UNIEN 12390-3:2009, 2009). For each batch of concrete mix, two control specimens (100x100x100 mm cubic specimens) were cast and cured for 28 days at a temperature of 20 ± 2 °C and a relative humidity of $60 \pm 5\%$. The control specimens' characteristics are summarised in the following Table 3.2.

Table 3.2 - Control specimens' characteristics - compression test

Specimen	Concrete mixture	Cast number	Dimension (mm x mm x mm)	Volume (mm ³)	Weight (kg)
1a	NWC	1	100 x 100 x 100	10 ⁶	2.375
1b	NWC	1	100 x 100 x 100	10 ⁶	2.335
2a	LWC	2	100 x 100 x 100	10 ⁶	1.685
2b	LWC	2	100 x 100 x 100	10 ⁶	1.665

Table 3.3, instead, reports the results of the compression tests for the NWC and LWC mixtures.

Table 3.3 - Mechanical properties of concrete: Compression test results

Specimen	Concrete Mixture	F (N)	A_c (mm ²)	f_c (MPa)	R_{cm} (MPa)
1a	NWC	381.29x10 ³	10 ⁴	38.13	42.2
1b	NWC	462.68x10 ³	10 ⁴	46.27	
2a	LWC	310.44x10 ³	10 ⁴	31.04	29.4
2b	LWC	277.06x10 ³	10 ⁴	27.71	

In Table 3.3, F is the maximum load achieved, in Newton, A_c is the cross-sectional area of the specimen, in square millimetres, and f_c is given by Eq. (3.1), according to the indications provided in (UNI EN 12390-3:2009, 2009):

$$f_c = \frac{F}{A_c} \quad (3.1)$$

The average cubic compressive strength is evaluated through Eq. (3.2):

$$R_{cm} = \frac{\sum_{i=1}^n f_{ci}}{n} \quad (3.2)$$

3.2.1.2 Indirect tensile test

The tensile strength of the two concrete mixtures has been evaluated following the standard UNI EN 12390-6:2010 (UNI EN 12390-6:2010, 2010). The control specimens' characteristics are reported in Table 3.4.

Table 3.4 - Control specimens' characteristics - indirect tensile test

Specimen	Concrete mixture	Cast number	Dimension (mm x mm x mm)	Volume (mm ³)	Weight (kg)
1c	NWC	1	100 x 100 x 100	10 ⁶	2.375
1d	NWC	1	100 x 100 x 100	10 ⁶	2.335
2c	LWC	2	100 x 100 x 100	10 ⁶	1.660
2d	LWC	2	100 x 100 x 100	10 ⁶	1.685

The tensile strength f_{ct} can be evaluated with Eq. (3.3):

$$f_{ct} = \frac{4F}{2d^2} \quad (3.3)$$

where F is the maximum load achieved during the test and d is the nominal dimension of the cross-section.

The results of the indirect tensile tests are summarised in the following Table 3.5, where F is the maximum load achieved during the test, d is the characteristic dimension of the cubic specimens, and f_{ct_m} is the average value of the tensile strength, f_{ct} , computed by applying Eq. (3.3).

Table 3.5 - Mechanical properties of concrete: Indirect Tensile test results

Specimen Label	Concrete Mixture	F (N)	d (mm)	f_{ct} (MPa)	f_{ct_m} (MPa)
1c	NWC	39.63x10 ³	100	1.98	1.9
1d	NWC	34.16x10 ³	100	1.71	
2c	LWC	30.40x10 ³	100	1.52	1.5
2d	LWC	29.70x10 ³	100	1.49	

3.2.2 Titanium alloy Ti6Al4V

The mechanical properties of titanium alloy bars have been evaluated through tensile tests according to the European standard UNI EN ISO 6892-1:2009 (UNI EN ISO 6892-1:2009, 2009) and compared to the ones declared by the manufacturer (TiFast S.r.l.). The standard UNI EN ISO 6892-1:2009 (UNI EN ISO 6892-1:2009, 2009) provides the tensile test method to adopt for metallic materials, thus it is suitable to assess the tensile strength of the titanium alloy specimens here considered.

Results of the tests conducted on two $\phi 8$ mm and two $\phi 16$ mm bars are reported in Table 3.6, while Table 3.7 reports the comparison with the characteristics provided by the manufacturer.

Table 3.6 - Mechanical properties of Titanium alloy: Tensile test results

Specimen	F_{max} (kN)	Δl_{Fmax} (mm)	$A_{sec,Ti}$ (mm ²)	$A_{g,t}$ (%)	σ_t (MPa)	$\sigma_{t,average}$ (MPa)
$\phi 8-1$	49.58	27.34	50.2655	12	986.41	962
$\phi 8-2$	47.15	31.73	50.2655	11	938.87	
$\phi 16-1$	193.72	34.84	201.0619	16	963.47	
$\phi 16-2$	192.91	28.32	201.0619	16	959.44	

In Table 3.6 the following notation has been adopted:

- F_{max} → maximum load achieved during the test;
- Δl_{Fmax} → displacement corresponding to the maximum load F_{max} ;
- $A_{sec,Ti}$ → cross-sectional area of the bar;
- $A_{g,t}$ → elongation (at percentage) at fracture;
- σ_t → tensile strength obtained through Eq. (3.4):

$$\sigma_t = \frac{F}{A_{sec,Ti}} \quad (3.4)$$

Table 3.7 - Properties of Ti6Al4V bars: manufacturer specifications and experimental results

Specifications provided by the manufacturer (TiFast S.r.l.)								Tensile Test Results	
D. ¹	Alloy	Surface finish	Surface roughness	Ult. ²	Yie. ³	Area red. ⁴	El. ⁵	Tensile strength (average)	Elastic Modulus (average)
(mm)			(μm)	(MPa)	(MPa)	(%)	(%)	(MPa)	(GPa)
8	Ti6Al4V	Peeled, Polished	<1.6	957	878	37	16	962.64	110
16	Ti6Al4V	Peeled, Polished	<1.6	980	923	52.3	16.3	961.45	90

¹ Bar diameter; ² Tensile ultimate strength; ³ Yield strength (offset 0.2%); ⁴ Reduction of area at ultimate strength; ⁵ Elongation

3.3 Specimen preparation and testing set-up

The pull-out specimens were prepared according to the standard RILEM RC 6 (RILEM TC, 1983). A 150 mm cubic mould was used to manufacture the pull-out specimens. The bond length, l_b , of the bars was made equal to five times the bar diameter, d_s , by using a plastic sleeve and the bars were placed so that they extend beyond the two sides of the specimens (see Fig. 3.1a). The concrete was cast with the Ti6Al4V bars in horizontal position inside the mould, in the middle of the specimen. After moulding, the specimens were transferred to a curing room for 24 h at a temperature of 20 ± 2 °C and a relative humidity of $60 \pm 5\%$. Thereafter, the concrete cubes were de-moulded and stored again under the same temperature and humidity conditions. The pull-out test setup is shown in Fig. 3.1b.

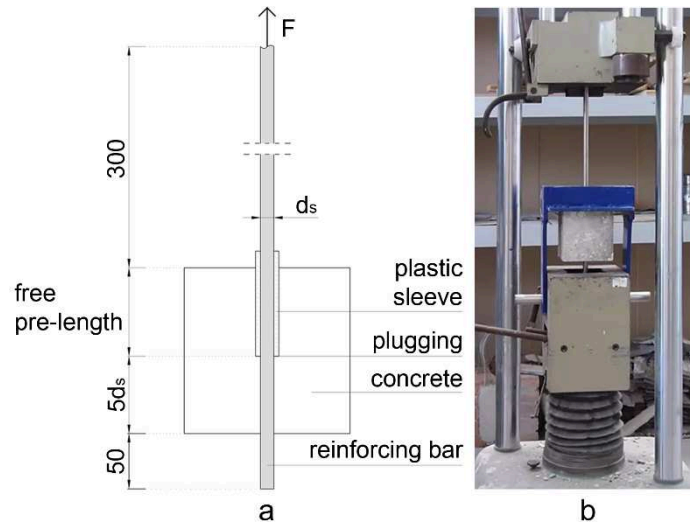


Figure 3.1 - a) Pull-out scheme; b) Pull-out test set-up

A total of eight specimens with the same characteristics two by two, were tested with the displacement control setting to track the post-peak behaviour. Fig. 3.2 shows the notation used to identify the pull-out specimens, while their characteristics are summarised in Table 3.8.

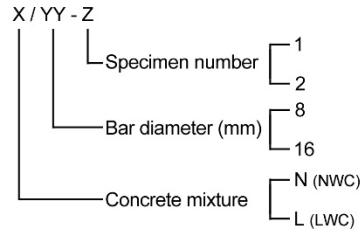


Figure 3.2 - Specimen identification

In order to better evaluate the properties of the Ti6Al4V-concrete interface, for one of each pair of identical specimens, the bar was not completely pulled out from the matrix and then the specimen was cut transversally. The cut position was chosen to capture both the matrix and the part of the bar not fully pulled out. Therefore, the cross-section obtained through this process could be observed with the Scanning Electron Microscope (SEM). Table 3.8 reports also which bar, for each pair of identical specimens, has been partially pulled-out to execute the cut. Details of the cut position, instead, are shown in Fig. 3.3.

Table 3.8 - Specimens for the pull-out test

Specimen	Concrete mixture	d_s	l_b	Fully/Partially pulled-out (F/P)
		(mm)	(mm)	
N/8-1	NWC	8	80	F
N/8-2	NWC	8	80	P
N/16-1	NWC	16	40	F
N16-2	NWC	16	40	P
L/8-1	LWC	8	80	F
L/8-2	LWC	8	80	P
L/16-1	LWC	16	40	F
L16-2	LWC	16	40	P

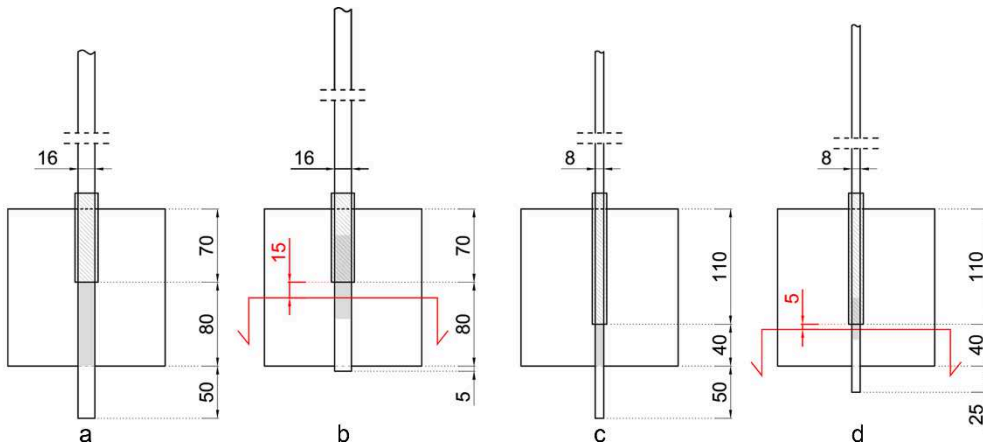


Figure 3.3 - $\phi 16$ mm bar specimens: a) initial configuration, b) final configuration with cut position; $\phi 8$ mm bar specimens: c) initial configuration, d) final configuration with cut position

3.4 Test results and discussion

The tensile force, F , measured in the test is transformed into bond stress, τ_{dm} , by Eq. (3.5), according to the standard RILEM RC 6 (RILEM TC, 1983):

$$\tau_{dm} = \frac{F}{\pi d_s l_b} \quad (3.5)$$

The bond strength, τ_{max} , is the maximum value reached by τ_{dm} , i.e. the one obtained by inserting in Eq. (3.9) the peak force F_{max} measured by the tests.

The experimental results obtained from the tests are summarised in Table 3.9, where f_{cm} is the mean value of the compressive strength for each concrete batch and the slip value of the loaded end at bond strength is indicated as s_{bs} . A normalised bond stress, τ_{dm}^* (Feldman and Bartlett, 2005), (Baena et al., 2009), with respect to the square root of concrete compressive strength has been also computed through Eq. (3.10) in order to compare the experimental results among the two types of concrete mixture. As a consequence, τ_{max}^* is the normalised bond strength corresponding to the bond strength τ_{max} . The expression of the normalised bond stress is given by the following Eq. (3.6):

$$\tau_{dm}^* = \frac{\tau_{dm}}{\sqrt{f_{cm}}} \quad (3.6)$$

The normalisation with respect to the square root of the compressive strength is commonly accepted for concrete with a compressive strength up to 55 MPa (ACI Committee 408, 2003). This is because the bond stress strictly dependent on the concrete tensile strength, which in turns is linearly related to the square root of the compressive strength (Neville, 2011).

Table 3.9 - Experimental pull-out test results

Specimen	f_{cm} (MPa)	F_{max} (kN)	τ_{max} (MPa)	S_{bs} (mm)	τ^*_{max} (MPa ^{0.5})
N/8-1	42.2	2.00	1.99	0.601	0.31
N/8-2 *	42.2	-	-	-	-
N/16-1	42.2	6.80	1.69	0.937	0.26
N/16-2	42.2	7.50	1.87	0.669	0.29
L/8-1	29.4	2.97	2.95	1.031	0.55
L/8-2	29.4	2.75	2.74	0.857	0.51
L/16-1	29.4	10.75	2.67	1.083	0.50
L/16-2	29.4	10.10	2.51	1.044	0.47

* Specimen N/8-2 failed the test for a sliding between the rebar end and the clamp device.

As it is possible to notice from Table 3.9, specimen N/8-2 failed the test due to sliding between the rebar and the clamp device, thus its response will not be taken into account.

3.4.1 Bond stress-slip relationship

Figs. 3.4-3.7 present the obtained bond stress-slip curves, reporting also the displacement threshold adopted to stop the test of the specimens intended for cutting. Fig. 3.4, which is related to the debonding of the Ti6Al4V $\phi 8$ mm bar from the NWC matrix, shows the response curve of specimen N/8-1 and the failure of the N/8-2 due to sliding between the bar and the clamp device of the testing machine.

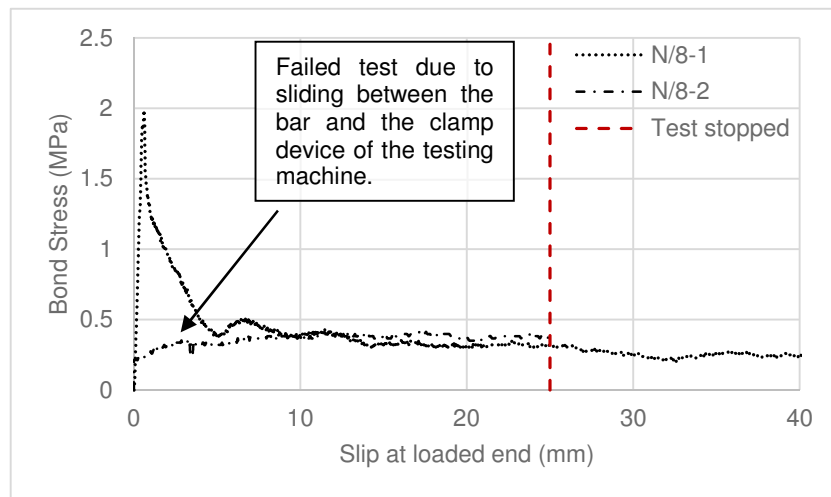


Figure 3.4 - Pull-out results: $\phi 8$ mm Ti6Al4V rebar from NWC specimen

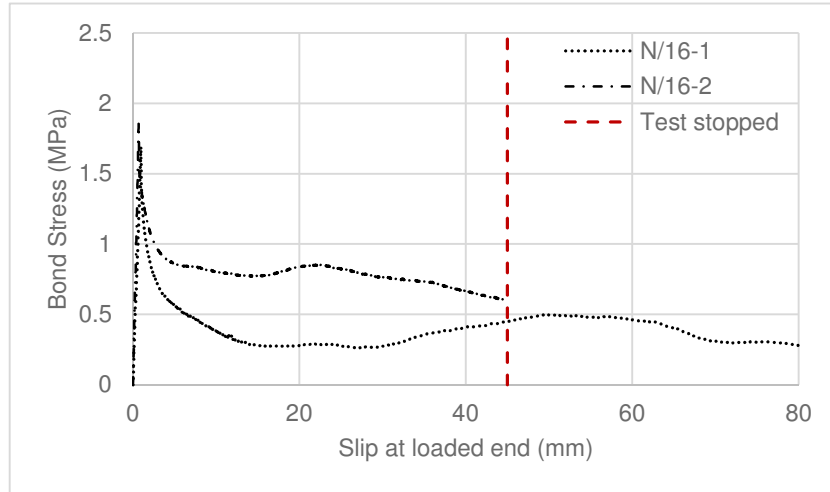


Figure 3.5 - Pull-out results: $\phi 16$ mm Ti6Al4V rebar from NWC specimen

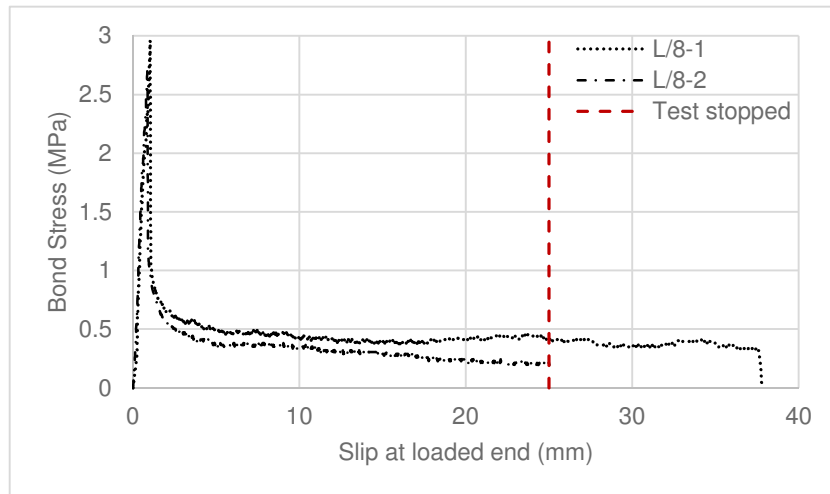


Figure 3.6 - Pull-out results: $\phi 8$ mm Ti6Al4V rebar from LWC specimen

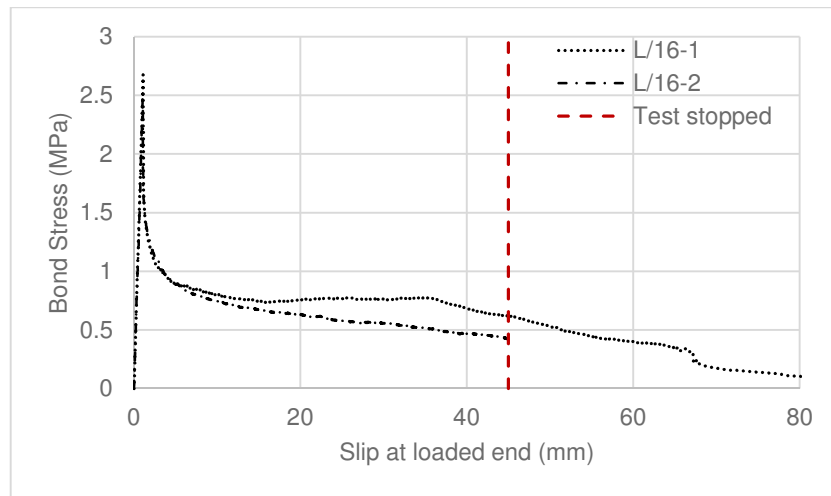


Figure 3.7 - Pull-out results: $\phi 16$ mm Ti6Al4V rebar from LWC specimen

All the bond-slip curves obtained from the experimental tests exhibit a pull-out failure characterised by an initial almost linear branch up to the pull-out force peak value (corresponding to the bond strength), followed by a sudden decrease in the stress that represents a significant adhesion reduction. Afterwards, the average bond stress shows a global declining trend without vanishing until the bar is fully pulled-out. The overall decay is gradual due to the presence of frictional shear and the simultaneous progressive reduction of embedded length. Despite this, the experimental curves show some local boosts (Fig. 3.8) in the bond stress during the post-peak phase. These local maximums could be explained by a rough fracture surface originated during the pull-out test, consisting of a sort of asperities at the interface, that would be responsible of the dilatant behaviour of the interface. Such behaviour might explain the local increases in the bond stress and also the significant post-peak residual stress, which does not vanish until the bar is completely pulled-out. Remarkably, this phenomenon is more appreciable in the case of NWC specimens.

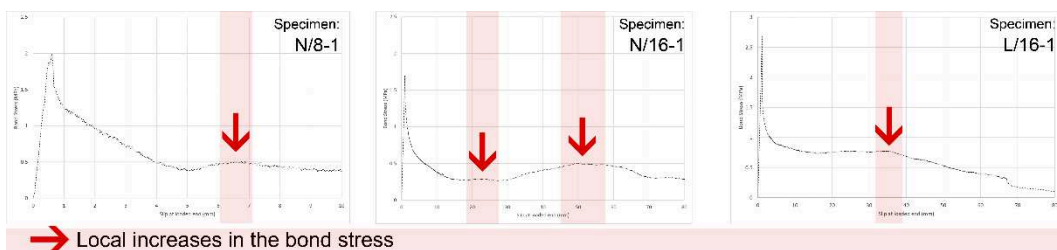


Figure 3.8 - Examples of local increases in the bond stress noticed in the experimental pull-out curve responses

To better understand the mechanisms acting at the interface during debonding and to establish the problem scale, in the next paragraph SEM observations carried out on cut specimens are presented.

3.4.2 SEM observations

In the present research, SEM observations are used as a tool to better investigate the properties of the broken Ti6Al4V-concrete interface. Thus, they are carried out on specimens cut after a sliding corresponding to about 55% of the bond length, namely 45 and 25 mm for $\phi 16$ and $\phi 8$ mm rebars respectively. A scheme of the cut position and the relative cross-section is reported in Fig. 3.9.

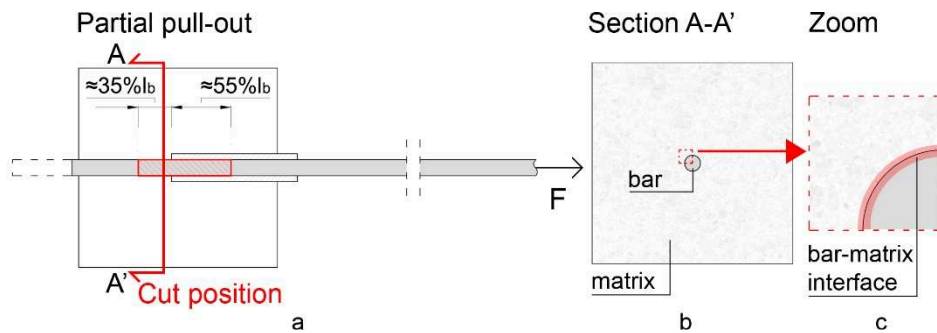


Figure 3.9 - a) Partial pull-out test and cut position; b) cross-section; c) bar-matrix interface intended for SEM observations

Considering that no data have been found in the literature concerning titanium-concrete interaction, SEM observations have been used first of all to assess whether the rebar material in the alkaline environment constituted by concrete, is able to create a chemical bond. In fact, some examples of SEM observations can be found in the literature to demonstrate the obtained value of bond strength between reinforcement and concrete from the chemical point of view. In the research of Franchi et al. (Franchi et al., 1999), SEM observations could provide a motivation for the increase in the bond strength for galvanised steel reinforcing bars pulled out from concrete specimens. They noted a densification of the concrete zone in proximity of the rebar interface, provided by the non-expansive products of the reaction between zinc and calcium hydroxide, i.e. zinc corrosion products, which penetrate into the concrete pores near the interface (Fratesi et al., 1990).

Moreover, SEM observations have been used to analyse the microstructure of interfaces in steel reinforced concrete by Horne et al. (Horne et al., 2007) and also to describe the interfacial transition zone between aggregates and cement paste by Diamond and Huang (Diamond and Huang, 2001). Thus, this instrument can provide a series of information which goes from the nature of the analysed materials to their dimensions and shapes. In fact, the second aspect here analysed concerns the establishment of the problem scale. As previously mentioned, experimental bond stress-slip relationships suggested the possibility of a dilatant behaviour of the interface during debonding due to the presence of the local

increases in the bond stress and to its significant residual value. Thus, SEM analyses have been mostly used to measure the interface expansion associated to the pull-out failure. The results of SEM observations for the specimens N/8-2, N/16-2, L/8-2, and L/16-2 are shown in the following Figs. 3.10-3.13.

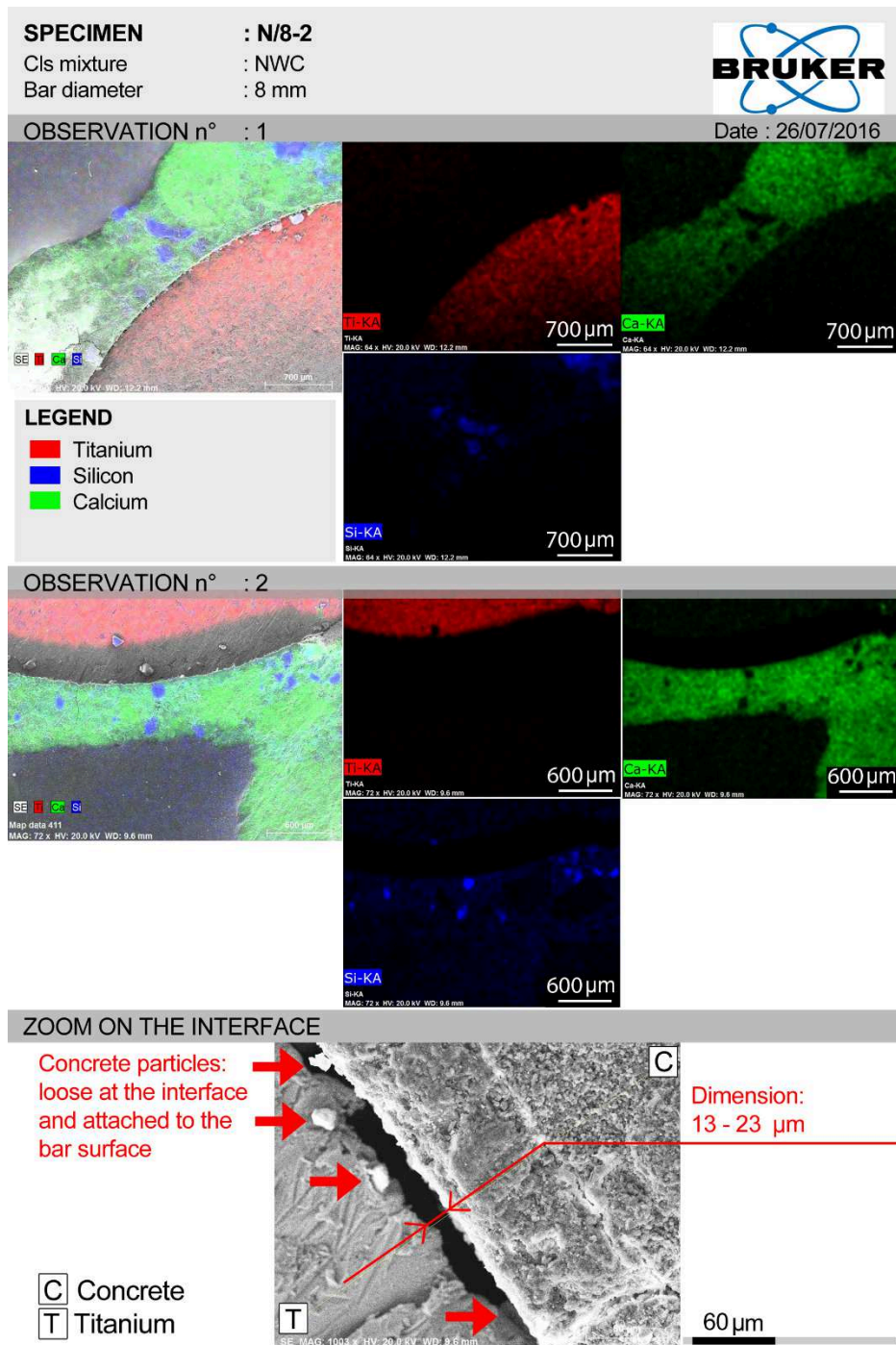


Figure 3.10 - SEM observation: specimen N/8-2

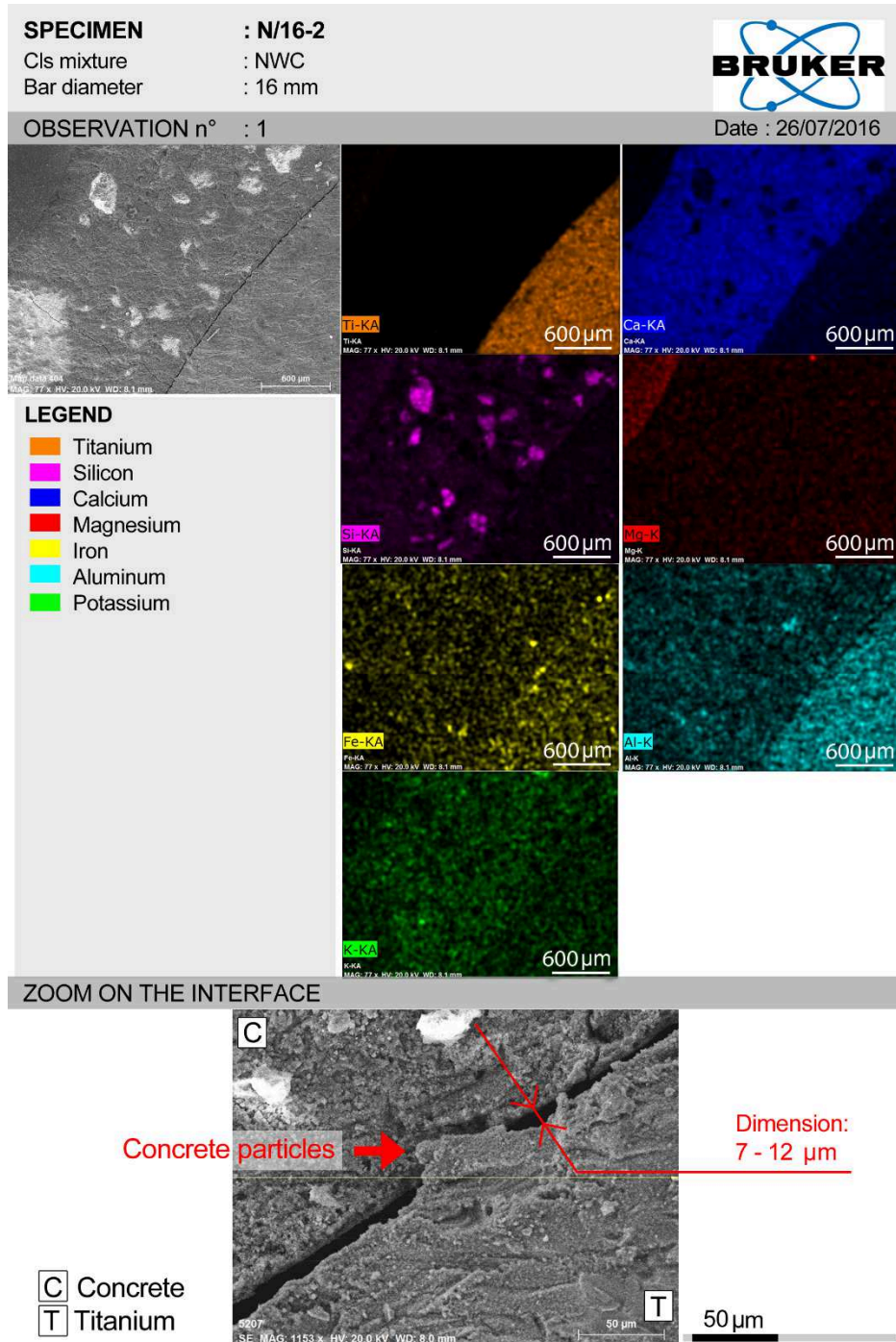


Figure 3.11 - SEM observation: specimen N/16-2

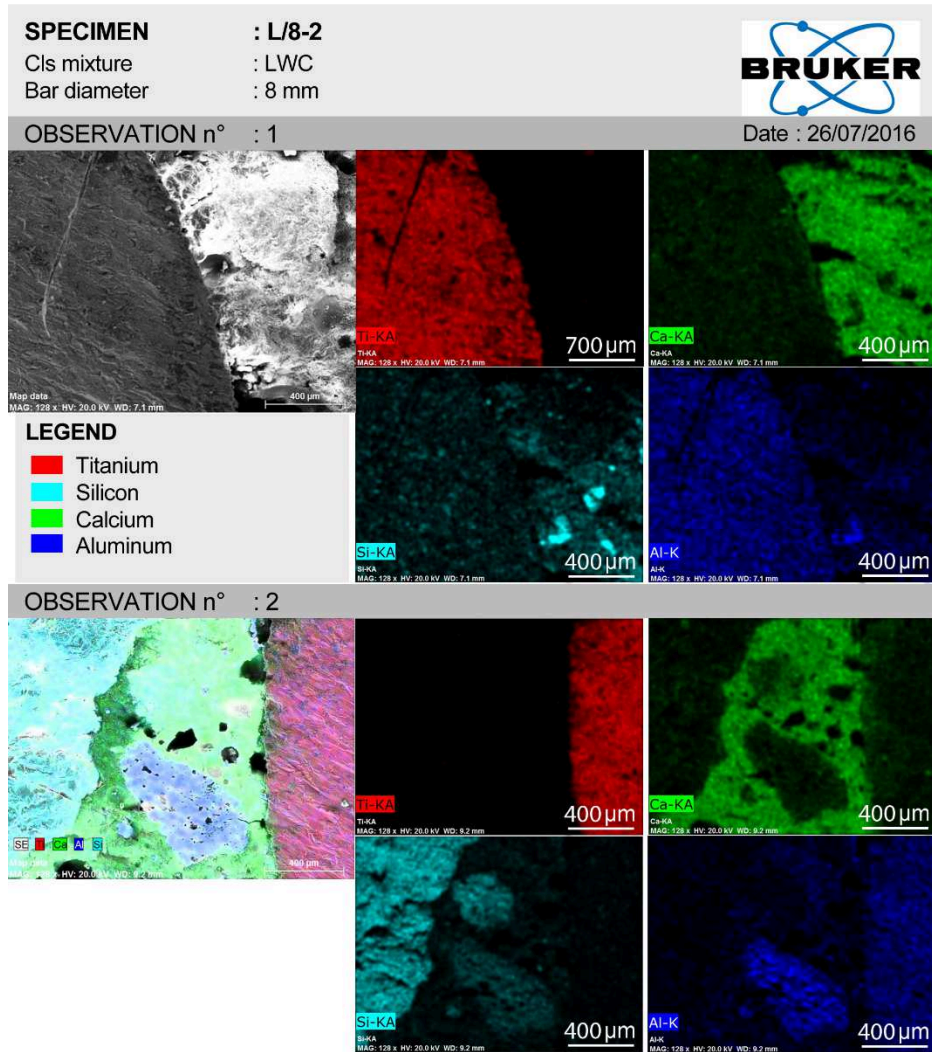


Figure 3.12 - SEM observation: specimen L/8-2

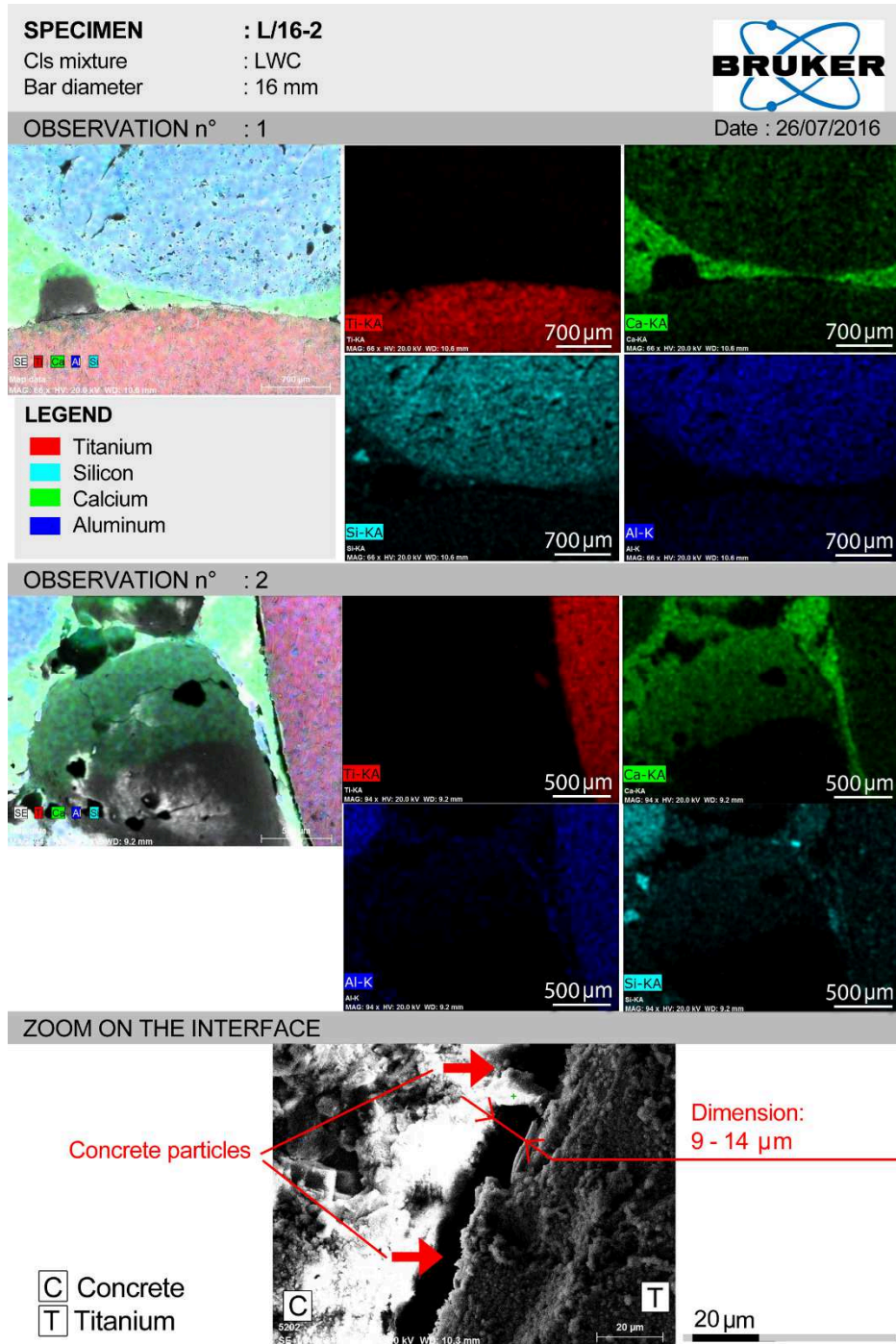


Figure 3.13 -SEM observation: specimen L/16-2

This thesis deals with the mechanical characterisation of the interface rather than with its chemical description. However, a first fundamental feature can be extracted from SEM observation, that is that no titanium alloy components and/or reaction products have been found into the pores of the concrete matrix. Moreover, no densification of the concrete ring surrounding the bars has been observed.

Nevertheless, SEM observations still provide useful information, such as the characteristic dimensions involved and the occurrence of features at the interface. Particularly, Figs. 3.14a summarise the information related to the occurrence of voids, concrete particles (loose at the interface and attached to the bar surface), aggregates adjacent to the interface, and microcracks. All these characteristics confirm the complexity of the bar-matrix interface, which essentially affects the bond performance. It is worth specifying that the term ‘concrete particles’ is here used in a general way to indicate the particles found at the interface consisting of matrix material. Thus, these particles can consist of cement paste, aggregates, or the combination of the two. A more detailed analysis is carried out in the following Section 3.4.3. Another important aspect highlighted by SEM observations is the separation occurring at the interface, visible when enlarging the the images (Fig. 3.14a). In fact by zooming on the interface, the presence of concrete particles attached to the bar surface and loose at the interface is even more appreciable, and it becomes possible also to measure the dilated interface. The range of dimensions measured for the analysed specimens goes from 7 to 23 μm , with average values around 10-15 μm . This information allows for assessing that when a plain bar is subjected to pull-out from a concrete matrix, the interface breaks not only due to the relative sliding between the two surfaces, but also a normal separation occurs. These observations give hints to hypothesise that the bar surface roughness (order of 1-2 μm) is able to originate a more complex and inhomogeneous surface consisting of the proper bar surface and residual matrix material attached to it. This ‘new surface’ is rougher than that of the bar, having a sort of asperities irregularly distributed along the bar. When the bar is forced to slide inside the concrete channel, the ‘new’ rougher surface induces stresses to the surrounding concrete, resulting in a dilated interface (order of 10-15 μm). This mechanism could be assimilated to the one governing the pull-out of ribbed bars, i.e. interlocking, but it occurs at the microscale level, thus the involved stresses are much lower. This ‘*microscale interlocking*’ might explain also the features presented by the bond-slip relationships, where the bond stresses were significant up to the complete pull-out of the bar (i.e. slip almost equal to the bond length). Moreover, the local increases in the bond stress observed in the bond-slip relationships would be motivated by the irregular distribution of the asperities on the bar surface. In fact, the complexity of the concrete microstructure affects the adhesion between the matrix and the bar, allowing the creation of the asperities in an inhomogeneous manner. For example, voids or aggregates adjacent to the interface prevent the formation of a proper adhesion zone, which results in a weaker bond.

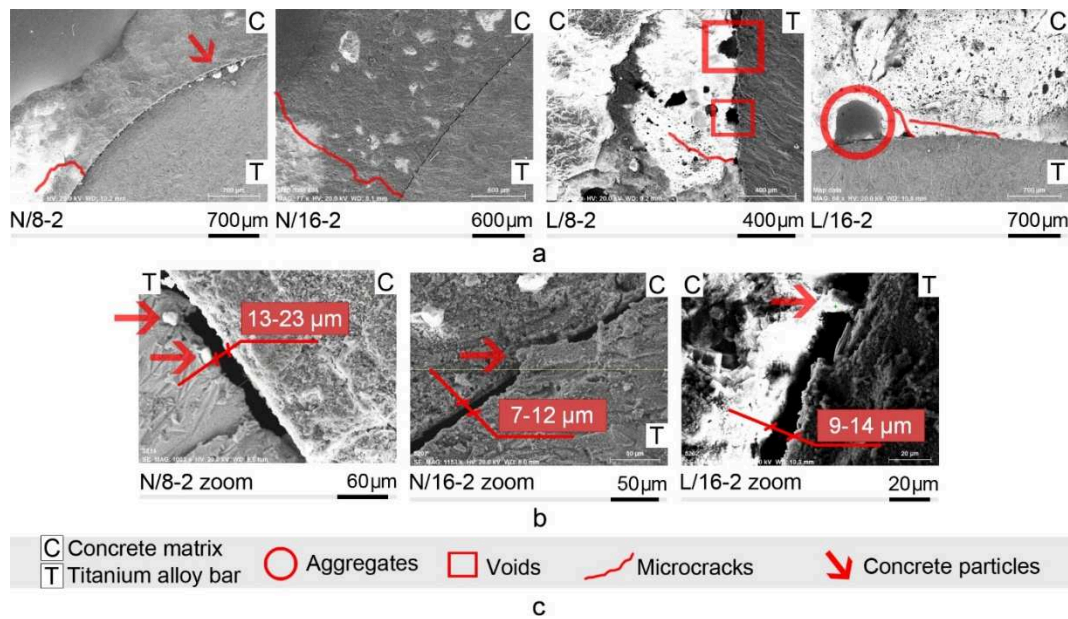


Figure 3.14 - SEM observations: a) Bar-matrix interfaces of N/8-2, N/16-2, L/8-2 and L/16-2 specimens with indication of the main features; b) Zoom on the interface of N/8-2, N/16-2 and L/16-2 specimens with the indication of the interface measures; c) Legend

To confirm the hypotheses made here, additional investigation on rebar surface is reported in the next paragraph, where the influence of concrete mixture is evaluated also through means of microscopic analysis of the pulled out rebars.

3.4.3 Influence of concrete mixtures

Two different concrete mixtures, i.e. NWC and LWC, have been tested in the present study. Despite the fact that the measured compressive strength of LWC is significantly lower (29 MPa) than that of NWC (42 MPa), the mean bond strength value resulted from the tests on LWC is higher than that on NWC specimens. In particular, by comparing the normalised bond strength values, it emerges that the average is $0.51 \text{ MPa}^{0.5}$ for LWC while NWC specimens achieve an average value of $0.29 \text{ MPa}^{0.5}$. A possible explanation for this peculiar and non-negligible phenomenon could refer to the grains distribution of the types of the aggregates used, because the other mixture components are the same and the maximum aggregate diameter is fixed. The difference between the two investigated batches consists in the nature of the coarse aggregate phase, i.e. normal-weight crushed gravel and light-weight expanded clay ones, but the developed bond strength does not seem to depend on the chemical bond between rebars and aggregates as much as that between rebars and cement. In fact, as remarked by Angst et al. (Angst et al., 2017) for the case of steel rebars, the concrete part of the interface zone can be assumed similar to the interfacial transition zone between cement paste and aggregate particles. In other words, it is reasonable to assume that the reinforcement is mostly in contact with the cement phase of the concrete

matrix and not with the aggregates. This suggests that other phenomena depending more on the aggregates physical distribution than on their chemical nature, affect the bond-slip behaviour at the interface.

By observing the specimen rupture surfaces from the indirect tensile tests of the two studied mixtures (Fig. 3.15a), it can be noticed that the LWC fracture surface (Fig. 3.15c) appears more homogeneous than that of NWC (Fig. 3.15b) in terms of voids, honeycombs and especially aggregates spatial distribution.

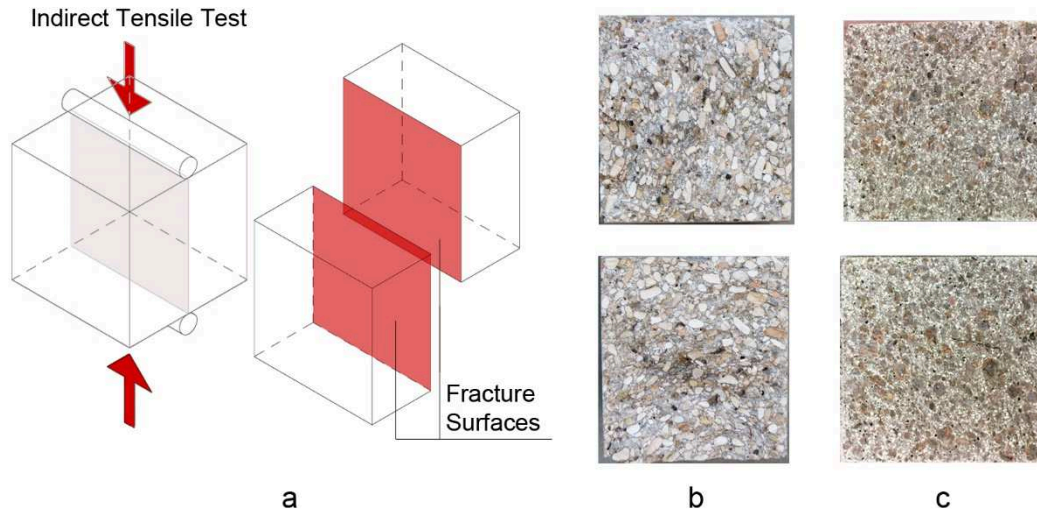


Figure 3.15 - Indirect tensile test fracture surface: a) scheme; b) NWC; c) LWC

A similar indication is provided by both the visual and microscopic analyses of the pulled-out Ti6Al4V rebars from the concrete matrices. Fig. 3.16 shows the rebar portion that was bonded to the matrix. The presence of residual matrix materials on the rebar surface, for both the mixtures tested, supports the hypothesis of the interface dilatancy hypothesised by observing the bond stress-slip relationships (Par. 2.3.1).

Concerning NWC (Figs. 3.16a and 3.16b), the rebar shows some distinct spots, while in the case of LWC (Figs. 3.16c and 3.16d) the rebar surface exhibits a sort of microfilm of residual material relatively uniform. On one hand, this aspect seems to affect the bond strength value, which is higher when adhesion regularly involves a larger surface (LWC case). On the other hand, it can be responsible for the local boosts of the softening branch of bond stress-slip responses in the case of NWC, when adhesion is restricted to discrete areas.

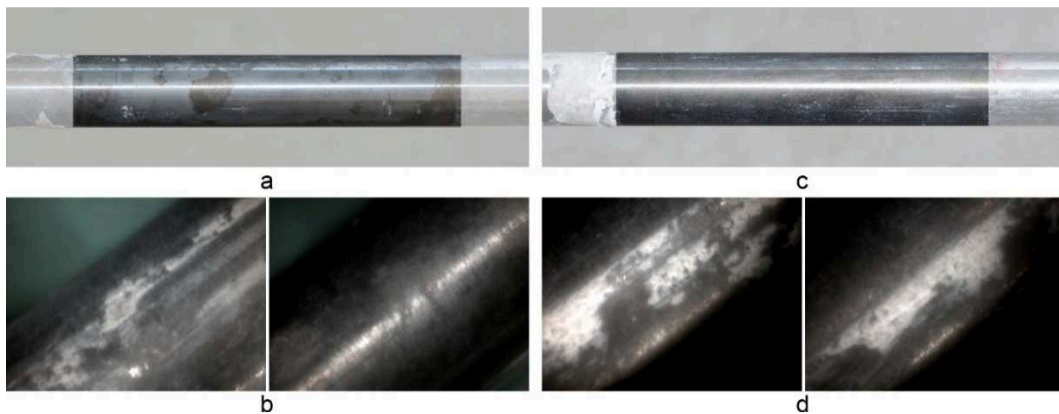


Figure 3.16 - a) Visual and b) Microscopic Analysis of Ti6Al4V bars pulled out from NWC specimens; c) Visual and d) Microscopic Analysis of Ti6Al4V bars pulled out from LWC specimens

3.4.4 Comparison with other reinforcement materials

In this paragraph the attention is focused on bond strength values obtained from the pull-out test by comparing normalised bond strength values of the Ti6Al4V-concrete interface with those reported in the literature for plain rebars of different materials. A considerable amount of data is available with regard to pull-out tests, but just those obtained under similar conditions are taken into account, even if some parameters related to the bar surface (e.g. roughness, treatment, finish) are not always available. At this preliminary step it has been considered essential to assess whether Ti6Al4V-concrete bond performance is comparable to that of other materials used as concrete reinforcement. Data found in the literature are compared to the mean values of the normalised bond strengths obtained from the pull-out tests, which are equal to 0.29 and 0.51 MPa^{0.5} for NWC and LWC respectively.

Reference values for the bond strength in the case of plain steel rebars can be found in (Feldman and Bartlett, 2005), where the influence of various parameters, e.g. surface roughness, bar embedded length, concrete compressive strength, on the bond strength are investigated. Table 3.10 reports the results obtained in (Feldman and Bartlett, 2005) for plain steel rebars differing only for surface treatment and concrete strength. Data for plain steel rebars bond-slip behaviour from different type of concrete mixtures can be found also in (Anwar Hossain, 2008). In Table 3.10 only those related to normal-weight concrete are reported. In (Mo and Chan, 1996) it is possible to find the comparison between plain steel rebars and plain galvanized steel ones, i.e. zinc-coated. Other authors presented comparisons between ribbed and plain steel rebars and plain aluminium ones (Guohua Xing, Cheng Zhou, TaoWu, 2015). Results reported in (Ertzibengoa et al., 2012) concerning comparisons between steel round rebars and flat (square cross-section) stainless steel ones have also been considered. For different types of FRP (e.g. Aramid, Glass, Carbon, Hybrid Fibre Reinforced Polymer) reinforcements, a vast amount of results is available in the literature ((Antonietta Aiello et al., 2007), (Achillides and Pilakoutas, 2004), (Baena et al., 2009)). Table 3.10 shows only some of those, with particular attention to several rebar surface characteristics that have been tested, e.g. fine or coarse sandblast

treatments, roughness increments. Finally, also some experimental data found in (Chung et al., 2008), (Jorge et al., 2012), and (Cairns et al., 2006) and concerning bond strength values of corroded steel rebars, are considered in order to understand the influence of the corrosion phenomenon on bond performance. Due to the formation of corrosion products, the resistant cross-section of the rebar reduces progressively while its volume increases, leading to the appearance of splitting stresses in the concrete cover. The same corrosion products tend to fill matrix voids and honeycombs, increasing its density and resulting, at first, in higher bond strength values, as discussed in Chapter 2. However, as it is shown in (Chung et al., 2008) and (Jorge et al., 2012), with respect to the pull-out behaviour of ribbed rebars, the cracking phenomenon induced by the presence of ribs tends to be even worse when the so-called Corrosion Level (CL) increases, eventually leading to a reduction of the bond strength. In the case of plain rebars, instead, splitting cracks usually do not form during the debonding process. This fact results in an even more significant increase of the bond strength induced by corrosion. Despite this, as noted by Cairns et al. (Cairns et al., 2006), the volumetric expansion due to oxides formation creates tensile hoops strains in the concrete surrounding the bar, and eventually leads to longitudinal cracking of the concrete cover. Thus, also in this case the cracking formation process becomes responsible for the progressive loss of bond strength. Moreover, they found out that the layer of corrosion products is mechanically weak and could reduce the interface friction action, weakening the bond. The last two rows of Table 3.10 report some of the experimental results presented in (Jorge et al., 2012) for plain rebars, showing the initial increment of bond strength.

Table 3.10 presents several examples of bond strength values (τ_{max}) and normalised ones (τ^*_{max}) with respect to concrete strength (f_{cm}) for different rebar materials, plain (P) rebar surface characteristics (possible textures or treatments, roughness, R_y), bond lengths (l_b), and cross-section geometrical details (bar diameter d_s for round bars or sides dimension $a \times b$ for rectangular cross-section bars). The same data are reported in Fig. 3.17, where the normalised bond strengths collected in the literature are compared with those measured here for the Ti6Al4V bars.

Table 3.10 - Bond strength values comparison for plain rebars

REF.	Rebar material	Plain rebar - - Surface texture	R_y	τ_{max}	d_s	a	b	l_b	f_{cm}	τ^*_{max}
			(μm)	(MPa)	(mm)	(mm)	(mm)	(mm)	(MPa)	(MPa ^{0.5})
	Steel	P - smooth	3.1	1.21	16			192	14.4	0.32
(Feldman and Bartlett, 2005)	Steel	P - smooth	3.1	1.79	16			192	44	0.27
	Steel	P - sandblast	11.3	2.28	16			192	9	0.76
	Steel	P - heavy sandblast	24.7	3.10	16			192	15	0.80

REF.	Rebar material	Plain rebar - - Surface texture	R_y	τ_{max}	d_s	a	b	l_b	f_{cm}	τ^*_{max}
(Anwar Hossain, 2008)	Steel	P		1.84	10			125	31.3	0.33
(Mo and Chan, 1996)	Steel	P		2.76	12.7			120	27	0.53
	Zinc-coated steel	P		0.92	12.7			120	27	0.18
(Ertzibengoa et al., 2012)	Steel	P	13.2	5.26	10			50	61.3	0.67
	Stainless Steel	P	0.4	1.49		4	20	50	59.8	0.19
	Stainless Steel	P	3.0	1.79		4	20	50	59.8	0.23
(Guohua Xing, Cheng Zhou, TaoWu, 2015)	Steel	P		2.22	16			115	40.8	0.35
	Aluminium Alloy	P		0.23	16			115	40.8	0.04
(Antonietta Aiello et al., 2007)	CFRP	Coarse sanded		3.99	8			64.7	52.73	0.55
	CFRP	Fine sanded		2.74	8			40	46.82	0.40
	GFRP	Coarse sanded		3.89	8			55	52.73	0.54
	GFRP	Fine sanded		3.38	8			52.5	52.73	0.47
	Steel	Smooth		1.10	12			60	30.53	0.20
(Achillides and Pilakoutas, 2004)	GFRP	P - Rough		12.50	13.5			81	49	1.79
	GFRP	P - Medium Rough		5.30	10.5			60	41	0.83
	GFRP	P - Smooth		1.20	16			80	45	0.18
	CFRP	P - Rough		11.80	13.5			81	46	1.74
	CFRP	P - Rough		14.00	8			48	41	2.19
	AFRP	P - Rough		10.10	13.5			81	45	1.51
	AFRP	P - Rough		5.40		8	8	81	45	0.80
Hybrid FRP	P - Smooth		1.30	8			81	45	0.19	
(Jorge et al., 2012)	Steel	P		3.40	12			80	49.6	0.48
	Corroded Steel	P		5.50	12			80	49.6	0.78

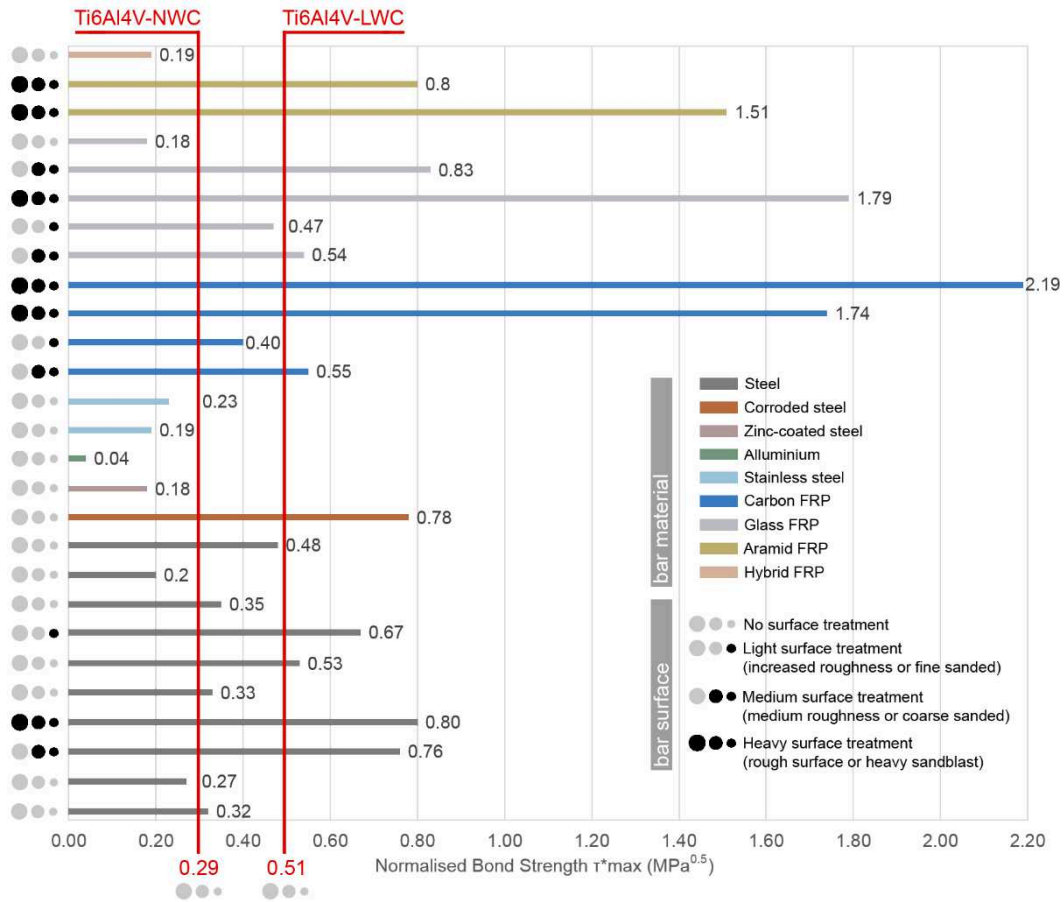


Figure 3.17 - Bond Strength comparison for Plain rebars

For the sake of completeness, some experimental results found in the literature and concerning pull-out tests of ribbed rebars are also considered ((Guohua Xing, Cheng Zhou, TaoWu, 2015), (Antonietta Aiello et al., 2007), (Chung et al., 2008), (Jorge et al., 2012)). Table 3.11 reports some of them, demonstrating that normalised bond strength values in the case of steel plain rebars are about 20-30% of those related to ribbed rebars (around 0.4-0.5 $MPa^{0.5}$ for plain rebars and around 2-3 $MPa^{0.5}$ for ribbed ones). This means that studying the pull-out behaviour of plain rebars can be very useful to better understand the pure pull-out failure mechanism, which represents a considerable percentage of the bond strength and would be overshadowed by the massive mechanical interlocking phenomenon induced by ribs.

Table 3.11 - Bond strength values comparison for ribbed rebars

REF.	Rebar Material	Ribbed rebar	R_y (μm)	τ_{max} (MPa)	d_s (mm)	l_b (mm)	f_{cm} (MPa)	τ^*_{max} ($\text{MPa}^{0.5}$)
(Guohua Xing, Cheng Zhou, TaoWu, 2015)	Steel	R		20.33	16	115	48.5	2.92
(Antonietta Aiello et al., 2007)	GFRP	R		14.16	12.7	72.5	52.73	1.95
	Steel	R		8.52	13.3	66.5	30.53	1.54
(Chung et al., 2008)	Steel (CL=0%)	R		14.70	13	37.1	28.3	2.76
	Corroded Steel (CL=2%)	R		15.6	13	38.4	28.3	2.93
	Corroded Steel (CL=5%)	R		10.50	13	36.6	28.3	1.97
(Jorge et al., 2012)	Steel	R		12.10	12	80	49.6	1.72
	Corroded Steel	R		11.80	12	80	49.6	1.68

By comparing normalised bond strength values obtained for Ti6Al4V rebars and those found in the literature (Table 3.10 and Fig. 3.17), it is possible to observe that they are comparable for most of the cases where plain rebars of different materials are used. In particular, for plain steel rebars with a surface roughness higher ($3.1 \mu\text{m}$) than that of tested Ti6Al4V ones ($1.6 \mu\text{m}$), normalised bond strength is almost the same in the case of Ti6Al4V-NWC interface, i.e. $0.20 \div 0.35$ and $0.29 \text{ MPa}^{0.5}$ for Ti6Al4V-NWC. As for Ti6Al4V-LWC interface, instead, the normalised bond strength is $0.51 \text{ MPa}^{0.5}$, which is higher than that developed between plain steel rebars without surface treatments. When sandblast treatments are applied to steel rebars, and thus the surface roughness is sensibly increased, the normalised bond strength significantly grows up to values around $0.8 \text{ MPa}^{0.5}$. Conversely, plain smooth zinc-coated steel reinforcements exhibit lower values of normalised bond strength ($0.18 \text{ MPa}^{0.5}$) with respect to those resulting from the tests on Ti6Al4V. The same condition can be noticed for stainless steel ($0.19 \text{ MPa}^{0.5}$ for $R_y=0.4 \mu\text{m}$ and $0.23 \text{ MPa}^{0.5}$ for $R_y=3.0 \mu\text{m}$), plain aluminium ($0.04 \text{ MPa}^{0.5}$), and smooth GFRP ($0.18 \text{ MPa}^{0.5}$) rebars. Also in the case of different type of FRP reinforcements, when roughness is augmented by applying surface treatments, the normalised bond strength meaningfully increases up to values around $2\text{-}2.5 \text{ MPa}^{0.5}$. Finally, bond strengths for plain rebars pulled out from a cement-based repair mortar (composed by cementitious grout, sand, synthetic resin, silica fume and polyamide fibres) corroded and non-corroded, are reported. In this case, the initial bond strength increase induced by corrosion is remarkable, i.e. from 0.48 to $0.78 \text{ MPa}^{0.5}$. These last data cannot be directly compared with those obtained in the present work, being the former obtained for a different type of matrix specifically designed for bond improvement and corrosion reduction. However, they are able to outline a sort of general trend for the bond behaviour under increasing corrosion action, which is also noticeable from Table 3.11 for ribbed rebars. Even if, at first, corrosion leads to a non-

negligible increase of bond strength (especially for plain rebars), eventually it always adversely influences the overall bond performance between rebar and matrix, due to the cracking formation process that it induces. This constitutes the main reason why other corrosion resistant materials have been largely investigated as possible reinforcement for concrete structures.

In this context, the possibility to use titanium alloy could play an important role as it exhibits an outstanding corrosion resistance (Donachie, 2000) and, as demonstrated in this experimental work, a bond strength value with respect to concrete comparable with that of steel (plain rebars with even higher surface roughness), higher than that of stainless steel (plain flat rebars also when surface roughness is increased) and sensibly greater than that of FRP (plain smooth rebars).

3.5 Concluding remarks after experimental testing

The main results obtained from the experimental pull-out tests on Ti6Al4V reinforcing bars from NWC and LWC are summarised below:

- bond-slip relationships for all the considered combinations of rebar diameter and concrete matrix are characterised by the typical pull-out curve shape, which is the results of the micromechanisms acting at the interface;
- although plain bars are considered, all the bond-slip relationships exhibited a significant residual pull-out load (i.e. bond stress) and some local boosts during the post-peak phase of the pull-out response;
- SEM and microscope analyses highlighted two main aspects: (i) the presence of residual concrete material attached to the bar surface portion previously embedded into the concrete matrix; and (ii) the dilation of the interface after a slip value equal to 55% of the bond length;
- the Ti6Al4V-NWC interface has a significantly lower bond strength, normalised with respect to the square root of concrete compressive strength, than that exhibited by the Ti6Al4V-LWC interface, i.e. 0.29 vs. 0.51 MPa^{0.5};
- the fracture surface of NWC obtained from the indirect tensile tests appears much more inhomogeneous than that of LWC in terms of aggregates and voids spatial distribution;
- despite the differences between the bond strengths of Ti6Al4V-NWC and Ti6Al4V-LWC interfaces, their values have been found to be similar or even higher than those found in the literature for more traditional materials used as reinforcement when plain bars are considered.

From the analysis of this experimental evidence, some hypotheses can be formulated in order to explain the behaviour shown by the Ti6Al4V-concrete interface under pull-out conditions. They are summarised below:

- for plain rebars pulled out from a concrete matrix, the surface roughness plays an important role because it activates an interlocking mechanism at microscopic level;
- as a consequence of surface roughness, Ti6Al4V-concrete interface exhibits a frictional dilatant behaviour, responsible for the noticeable residual load capacity shown by all the tests carried out;
- matrix homogeneity in terms of aggregates spatial distribution promotes the development of higher bond strengths at the interface with the rebar.

To verify these hypotheses and filter out the actual micro-mechanisms affecting the macroscopic response of the rebar-concrete debonding process, finite element analysis is employed and presented in the next Chapters 4 and 5.

Chapter 4

Finite Element Modelling of the pull-out behaviour between titanium bars and concrete

Pull-out test results can be seen as the macroscopic response of the rebar-matrix debonding process occurring at a lower scale. To better evaluate the interfacial micromechanisms having a role in that process, Finite Element (FE) analysis can be employed, as long as the numerical model incorporates sufficient aspects of such micromechanics. To this end, several CZMs have been used.

This chapter contains the description of the numerical models and the comparison of the results obtained by simulating the debonding process through different CZM formulations available in the literature.

4.1 Description of the numerical model

The numerical analyses have been carried out with the finite-element code ANSYS R16 (© ANSYS, 2015). Due to the symmetry of the pull-out problem, a 2D axisymmetric model is employed in the analyses, even if the specimens used in test were cubic. This is because experimental evidence confirms that the specimen edges do not give any contribution when specimens are large enough and the failure is provided by a pure pull-out mechanism (Lundgren, 2005).

Concrete and titanium are discretised by fully integrated 8-node axisymmetric elements, while 6-node quadratic interface elements are used in correspondence of the bar-matrix interface. In its proximity a mesh refinement has been applied, so that elements close to the interface are six times smaller than those on the free edge of the concrete matrix. Moreover, a ‘match control’ (© ANSYS, 2015) matches the mesh of the two surfaces in contact, i.e. the bar and matrix sides of the interface. The interface length is equal to five times the bar diameter, which corresponds to 40 and 80 mm respectively for the $\phi 8$ and $\phi 16$ mm rebars

studied with the present model. Geometry (Fig. 4.1a), interface details and boundary conditions (Fig. 4.1b), and mesh discretisation (Fig. 4.1c) of the pull-out FE model are reported in Fig. 4.1 for the model with bars having the diameter equal to 8 mm. As for the models with 16 mm bars, the geometry, interface details, and mesh discretisation are shown in Fig. 4.2a, Fig. 4.2b and Fig 4.2c respectively.

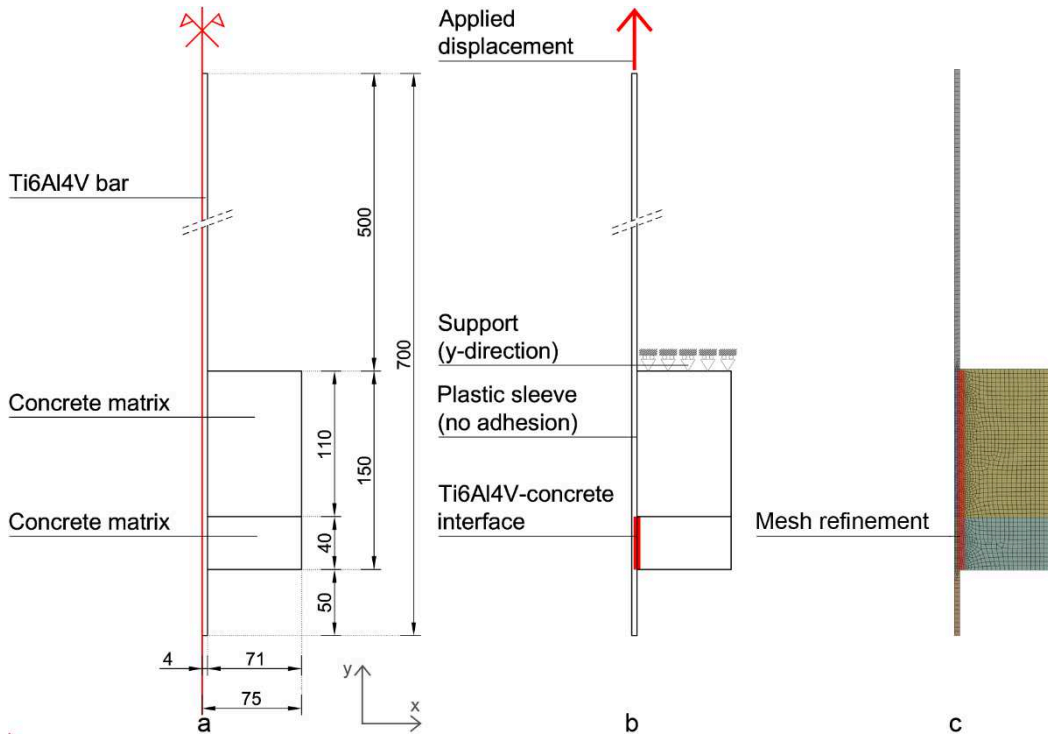


Figure 4.1 - FE model of the specimens with 8 mm bar diameter: a) Geometry; b) Interface details and boundary conditions; and c) Mesh discretisation

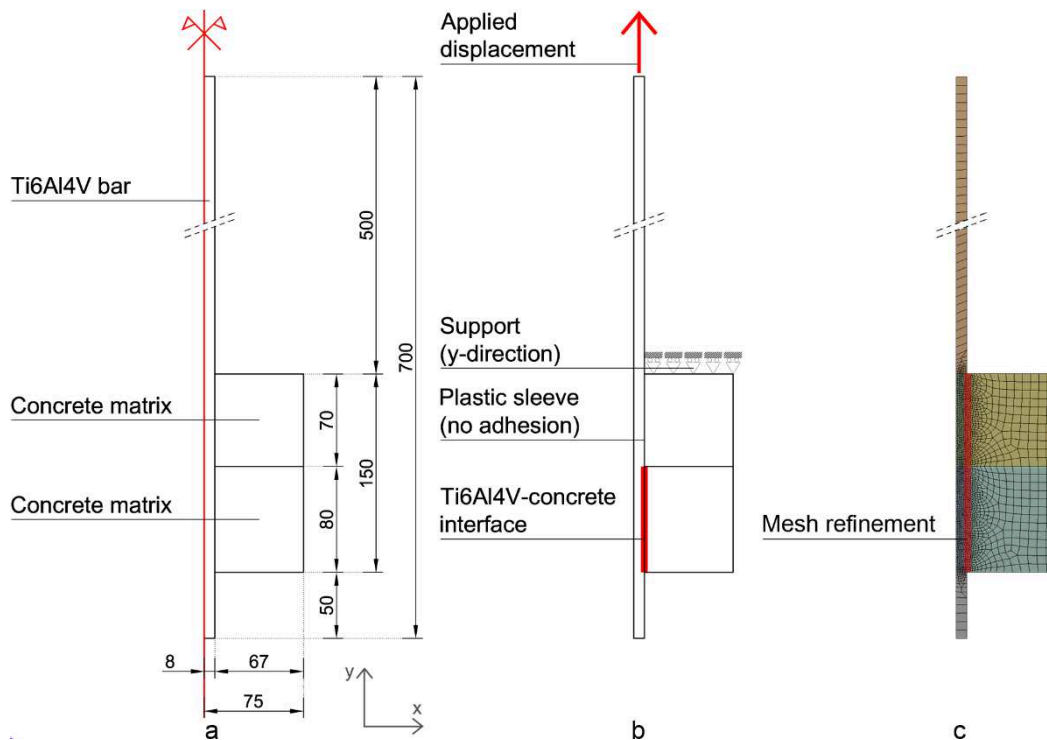


Figure 4.2 - FE model of the specimens with 16 mm bar diameter: a) Geometry; b) Interface details and boundary conditions; and c) Mesh discretisation

4.1.1 Material models

The bulk material properties are reported in Table 4.1 and have been derived from compressive and indirect tensile tests on concrete (NWC and LWC) and tensile tests on Ti6Al4V bars (see Chapter 3). Both concrete and titanium alloy have been modelled through a linear-elastic behaviour, since the stresses in the pull-out tests give negligible damage and plasticity effects (Lundgren, 2005).

Table 4.1 - Material properties for the FE analysis

	Isotropic Elasticity			Compressive Yield Strength	Tensile Yield Strength	Compressive Ultimate Strength	Tensile Ultimate Strength
	Density	Young's Modulus	Poisson's Ratio				
	(kg/m ³)	(MPa)	(-)	(MPa)	(MPa)	(MPa)	(MPa)
NWC	2325	33885	0.18	-	-	42	1.8
LWC	1735	30400	0.18	-	-	29	1.5
Ti6Al4V	4500	100000	0.36	920	920	-	962

4.1.2 Interface model

In order to include fracture in the model, it is firstly necessary to adopt the appropriate elements to discretise the interface. As previously mentioned, 6-nodes quadratic interface elements are used in correspondence of the bar-matrix interface. For these elements, the interfacial separation is defined as the displacement jump, δ , between the adjacent interface surfaces, as given by Eq. (4.1):

$$\delta = u^{TOP} - u^{BOTTOM} = \text{interfacial separation} \quad (4.1)$$

The definition of the separation is based on local element coordinate system, as it is shown in Fig. 4.3. The normal of the interface is denoted as local direction \mathbf{n} , and the local tangential direction is denoted as \mathbf{t} . Thus, the normal and tangential displacement components are given by the following Eqs. (4.2) and (4.3), respectively:

$$\delta_N = \mathbf{n} \cdot \delta \quad \text{normal separation} \quad (4.2)$$

$$\delta_T = \mathbf{t} \cdot \delta \quad \text{tangential (shear) separation} \quad (4.3)$$

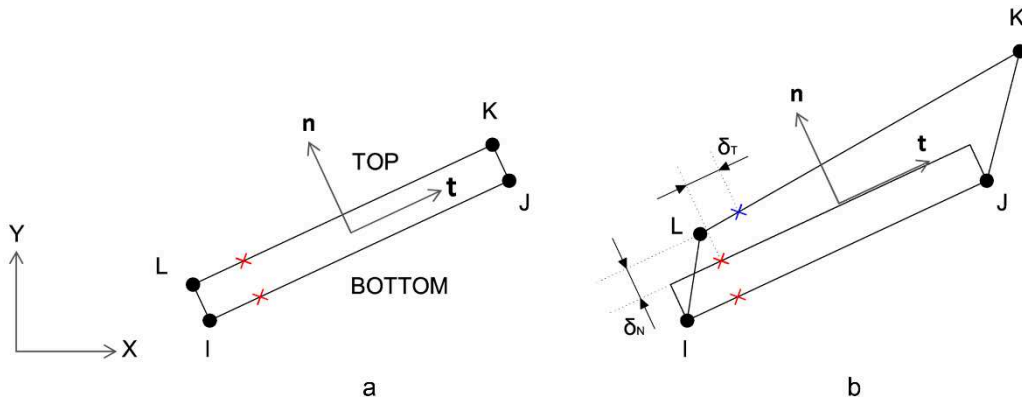


Figure 4.3 - Scheme of the interface: a) initial configuration; and b) deformed configuration

4.1.2.1 Interface delamination

In order to consider failure criteria for the interface, the ‘interface delamination’ feature has to be included into the analysis. To this end, the Cohesive Zone Model (CZM) method has been adopted in the present work, since it represents a computer and cost effective method to represent the interfacial failure in composite materials, as explained in paragraph 2.5 of Chapter 2.

Two of the most widely used CZM formulations, i.e. exponential (Fig. 4.4a) and bilinear (Fig. 4.4b), have been here employed in order to (i) understand their advantages and limitations, and (ii) verify if it is possible to describe the Ti6Al4V bar-to-concrete debonding process.

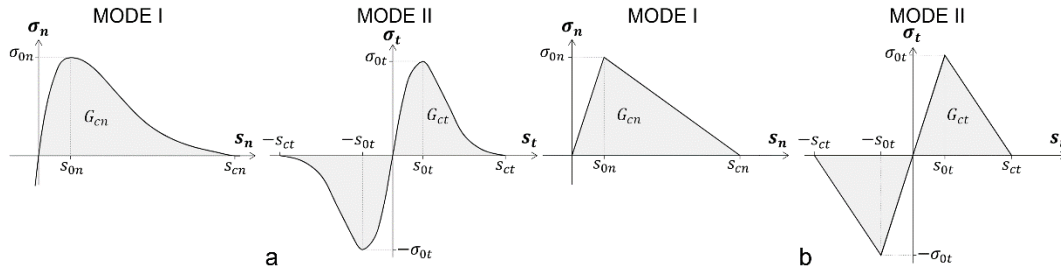


Figure 4.4 - a) Mode I and Mode II Exponential CZM laws; b) Mode I and Mode II Bilinear CZM laws

ANSYS R16 (© ANSYS, 2015) provides the formulation of Alfano and Crisfield (Alfano and Crisfield, 2001) for the bilinear CZM and that proposed by Xu and Needleman (Xu and Needleman, 1994) for the exponential law. These models are directly applicable to the elements used in proximity of the bar-matrix interface. Starting from these ‘simple’ models, it is possible to calibrate the parameters that describe debonding for each fracture mode (mode I – normal; mode II – tangential), i.e. critical energy release rate G_c , maximum cohesive traction σ_0 , displacement jump at maximum cohesive traction (s_0) and at complete debonding (s_c). It is worth underlining that in the case of the pull-out mechanism, fracture is governed by a mode II fracture behaviour, being the shear forces and the subsequent relative sliding the main responsible for the interface failure. The values extracted from the experimental testing are reported in Table 4.2 for both NWC and LWC. Nevertheless, some formulations of the CZM do not involve directly these parameters and further considerations are needed and discussed in the next paragraphs.

Table 4.2 - Experimental interface delamination parameters for Mode II dominated fracture behaviour

Property	Unit	Value	
		NWC	LWC
Maximum Tangential Traction	σ_{0t} (MPa)	1.85	2.80
Tangential Displacement at Maximum Tangential Traction	s_{0t} (mm)	0.45	0.64
Tangential Displacement Jump at Complete Debonding	s_{ct} (mm)	1.00	1.07

4.1.3.1.1 Xu and Needleman model

The model proposed by Xu and Needleman in (Xu and Needleman, 1994) has been generally described in Section 2.5.2.2.3. By adapting the general model to the present problem, it is possible to assume the coupling coefficients r and q equal to 0 and 1, respectively. Therefore, the work of separation is assumed equal in both normal and tangential direction. With the previous hypothesis, the function of the surface potential is given by Eq. (4.4), and its derivatives with respect to normal and tangential directions provide the normal and tangential cohesive tractions, respectively (Eqs. (4.5) and (4.6)).

$$\phi(\delta) = e\sigma_{N,max}\bar{\delta}_N \left[1 - (1 + \Delta_N)e^{-\Delta_N}e^{-\Delta_T^2} \right] \quad (4.4)$$

$$T_N = \frac{\partial \phi(\delta)}{\partial \delta_N} = e \sigma_{N,max} \Delta_N e^{-\Delta_N} e^{-\Delta_T^2} \quad (4.5)$$

$$T_T = \frac{\partial \phi(\delta)}{\partial \delta_T} = 2e \sigma_{N,max} \frac{\overline{\delta_N}}{\overline{\delta_T}} \Delta_T (1 + \Delta_N) e^{-\Delta_N} e^{-\Delta_T^2} \quad (4.6)$$

where:

- $\phi(\delta)$ → surface potential;
- $\sigma_{N,max}$ → maximum normal traction at the interface;
- $\overline{\delta_N}$ → normal separation across the interface where the maximum normal traction is attained with $\delta_T = 0$;
- $\overline{\delta_T}$ → shear separation where the maximum shear traction is attained at $\delta_T = \frac{\sqrt{2}}{2} \overline{\delta_T}$;
- $\Delta_N = \delta_N / \overline{\delta_N}$ → normalised normal separation across the interface;
- $\Delta_T = \delta_T / \overline{\delta_T}$ → normalised tangential separation across the interface;

As it is possible to observe from the above constitutive relations for the exponential formulation of the CZM, the indication of a mode II dominant behaviour for the interface delamination is not direct. Thus, the values presented in Table 4.2 cannot be inserted as input into the model, whereas the parameters need to be identified in order to fit the experimental curves. Table 4.3 reports the identified parameters for the exponential formulation of the CZM.

Table 4.3 - Parameter values for Exponential CZM

Property	Model parameter	Unit	Value	
			NWC	LWC
Maximum normal traction	$\sigma_{N,max}$	(MPa)	6.00	12.00
Normal separation across the interface	$\overline{\delta_N}$	(mm)	0.10	0.10
Shear separation at maximum shear traction	$\frac{\sqrt{2}}{2} \overline{\delta_T}$	(mm)	0.80	1.05

4.1.3.1.2 Alfano and Crisfield model

Paragraph 2.5.2.2.2 of Chapter 2 describes the general model proposed by Alfano and Crisfield (Alfano and Crisfield, 2001) for a bilinear CZM. In ANSYS R16 (© ANSYS, 2015), it is possible to indicate a mode II dominated fracture behaviour, by inputting a negative value of the maximum normal traction. In particular, the mode II dominated behaviour assumes that the separation of the material interfaces is dominated by the displacement jump tangent to the interface. Thus, the following equations describe the specialisation for a mode II dominated fracture behaviour of the general bilinear model described in Section 2.5.2.2.2. The tangential cohesive traction, T_T , is given by Eq. (4.7):

$$T_T = K_T \delta_T (1 - D_T) \quad (4.7)$$

where:

- K_T → tangential cohesive stiffness ($T_{T,max}/\delta_T^*$);
- $T_{T,max}$ → maximum tangential cohesive traction ($\sigma_{T,max}$);
- δ_T^* → tangential displacement jump at maximum tangential cohesive traction;
- δ_T^c → tangential displacement jump at the completion of debonding;
- α → ratio δ_T^* to δ_T^c ;
- δ_T^{max} → maximum tangential displacement jump attained in deformation history:
 $\max \delta_T(\tau')$, where $0 \leq \tau' \leq \tau$
- D_T → damage parameter associated with Mode II/III dominated bilinear cohesive law, defined as:

$$D_T = \begin{cases} 0 & \delta_T^{max} \leq \delta_T^* \\ \left(\frac{\delta_T^{max} - \delta_T^*}{\delta_T^{max}} \right) \left(\frac{\delta_T^c - \delta_T^*}{\delta_T^c} \right) & \delta_T^* < \delta_T^{max} \leq \delta_T^c \\ 1 & \delta_T^{max} > \delta_T^c \end{cases}$$

For Mode II dominated cohesive law, the normal cohesive traction, T_N , and the normal displacement jump behaviour are assumed to follow the tangential cohesive traction and tangential displacement jump behaviour, according to Eq. (4.8):

$$T_N = K_N \delta_N (1 - D_T) \quad (4.8)$$

where:

- K_N → normal cohesive stiffness ($T_{N,max}/\delta_N^*$);
- $T_{N,max}$ → maximum tangential cohesive traction (to indicate the Mode II dominated behaviour $T_{N,max} = -\sigma_{N,max}$);
- δ_N^* → normal displacement jump at maximum normal cohesive traction;
- δ_T^c → normal displacement jump at the completion of debonding.

For the mode II behaviour, the parameter values adopted for the analyses (i.e. the maximum tangential traction, the tangential displacement jump at the completion of debonding, and the ratio between the tangential displacement at maximum tangential traction and that at the completion of debonding) have been derived from those obtained experimentally, whereas those parameters related to mode I have been identified in order to fit the experimental curves and by adopting the conventional negative value for the maximum normal traction. For both NWC and LWC, the input parameter values for the bilinear CZM are reported in Table 4.4.

Table 4.4 - Parameter values for Bilinear CZM

Property	Model parameter	Unit	Value	
			NWC	LWC
Maximum Normal Traction	$\sigma_{N,max}$	(MPa)	-1.00	-1.00
Normal Displacement Jump at the Completion of Debonding	δ_N^c	(mm)	1E-4	1E-4
Maximum Tangential Traction	$\sigma_{T,max}$	(MPa)	1.85	2.80
Tangential Displacement Jump at the Completion of Debonding	δ_T^c	(mm)	1.00	1.07
Ratio	$\frac{\delta_N^*}{\delta_N^c} = \frac{\delta_T^*}{\delta_T^c}$	(-)	0.45	0.64
Non-Dimensional Weighting Parameter	β	(MPa)	1E-4	1E-4

4.1.3 Analysis settings

Quasistatic nonlinear incremental analyses have been performed by applying a prescribed displacement in the y -direction at the top of the bar in two load steps. In particular, for the pull-out of $\phi 8$ mm rebars, the prescribed final displacement is 12.5 mm, while for the $\phi 16$ mm ones, the displacement is equal to 25 mm. The first load step (0-5 mm) has been divided in 500 substeps, with constant prescribed displacement increment of 0.01 mm in each substep, in order to obtain a more precise and detailed curve in the linear and post-peak regions of the system response. In the second load step instead (5-12.5 and 5-25 mm for $\phi 8$ and $\phi 16$ rebars, respectively), the displacement increment in each substep is 0.1 mm (Fig. 4.5). Table 4.5 summarises the analysis settings.

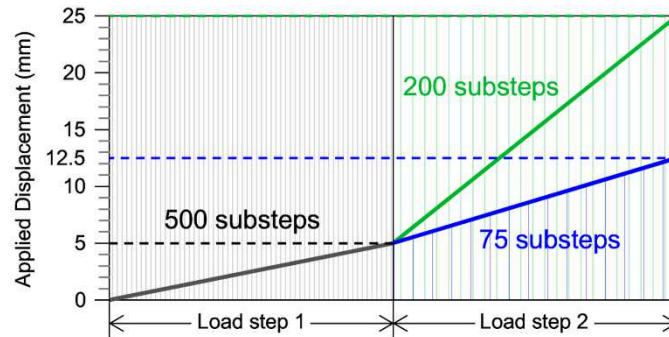
Figure 4.5 - Applied displacement in two substeps for the models with $\phi 8$ and $\phi 16$ bars

Table 4.5 - Analysis settings

Bar diameter	Total prescribed displacement	Applied displacement within Loadstep 1	Applied displacement within Loadstep 2	Substeps of Loadstep 1	Substeps of Loadstep 2
(mm)	(mm)	(mm-mm)	(mm-mm)	(-)	(-)
8	12.5	0-5	5-12.5	500	200
16	25	0-5	5-25	500	75

Noteworthy, it has been considered sufficient to study the behaviour up to a slip value equal to about 30% of the interface length because, after that value, the experimental curves show a gradual decreasing that is mostly due to the reduction of the embedment length. Moreover, the attention is focused on the crucial mechanisms involved in the debonding process, i.e. adhesion, interlocking and friction, which can be already captured for prescribed displacements considerably lower than the bond length.

4.2 Results with exponential and bilinear CZMs

By applying the bilinear and exponential CZMs for the simulation of the interface fracture, load-displacement curves have been obtained for the two types of concrete mixture (NWC and LWC) and the two bar diameters considered ($\phi 8$ and $\phi 16$ mm). The comparison between numerical and experimental curves is reported in the following Figs. 4.6-4.11.

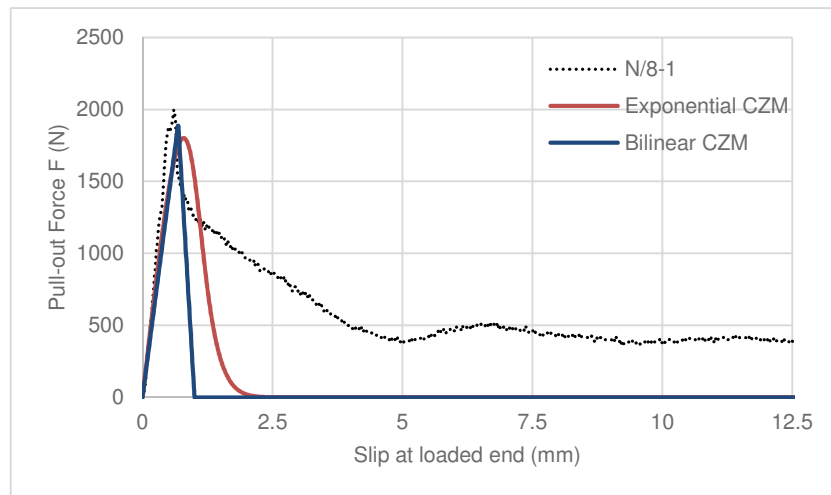


Figure 4.6 - $\phi 8$ mm rebars pull-out from NWC specimens: Comparison between Bilinear (Alfano and Crisfield, 2001) and Exponential (Xu and Needleman, 1994) CZMs and experimental curves

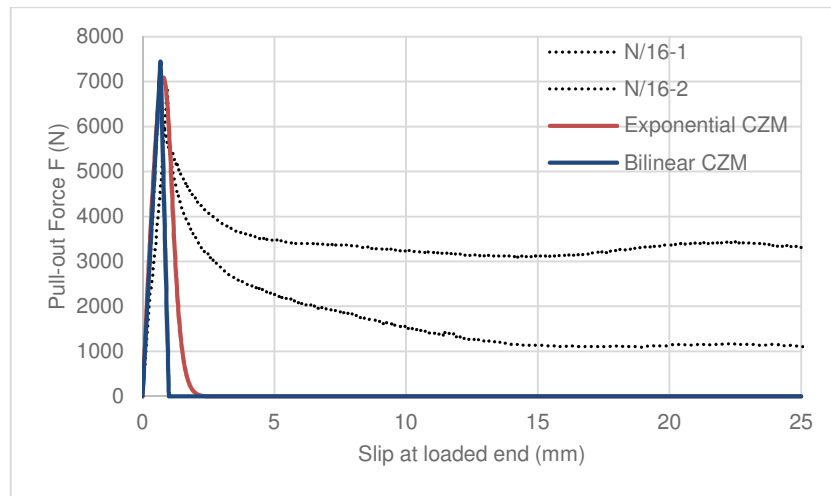


Figure 4.7 - $\phi 16$ mm rebars pull-out from NWC specimens: Comparison between Bilinear (Alfano and Crisfield, 2001) and Exponential (Xu and Needleman, 1994) CZMs and experimental curves

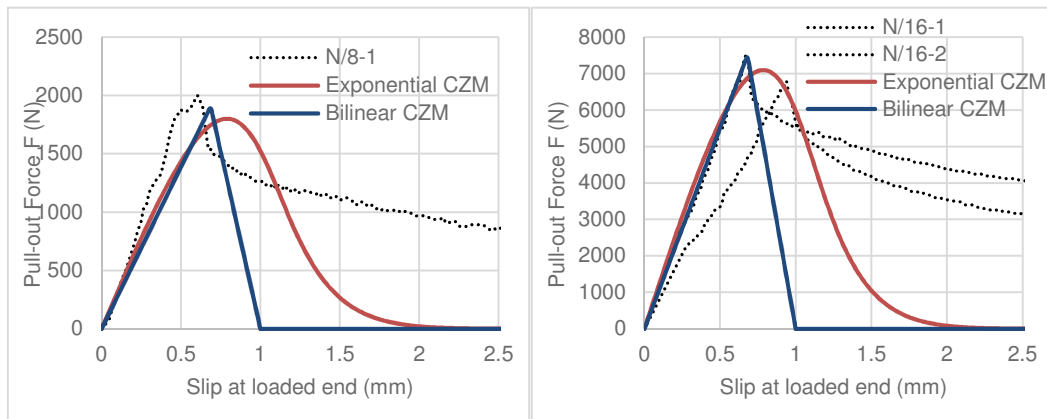


Figure 4.8 - $\phi 8$ and 16 mm rebars pull-out from NWC specimens, zoom on the elastic branch: Comparison between Bilinear (Alfano and Crisfield, 2001) and Exponential (Xu and Needleman, 1994) CZMs and experimental curves

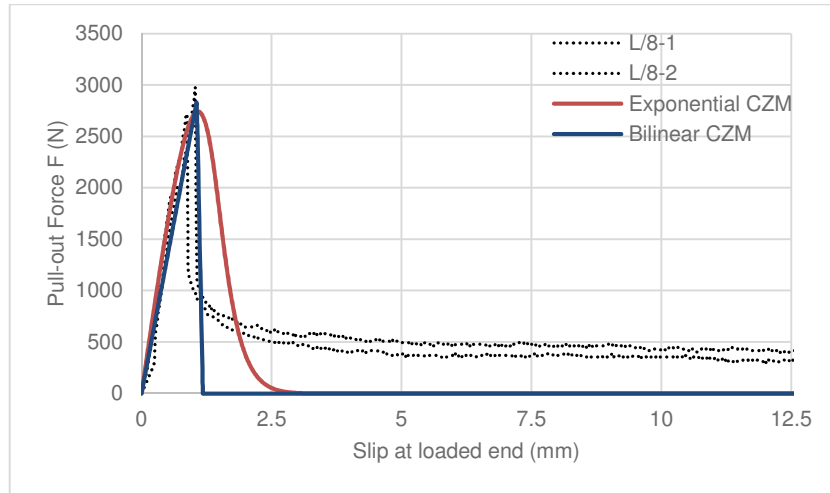


Figure 4.9 - $\phi 8$ mm rebar pull-out from LWC specimens: Comparison between Bilinear (Alfano and Crisfield, 2001) and Exponential (Xu and Needleman, 1994) CZMs and experimental curves

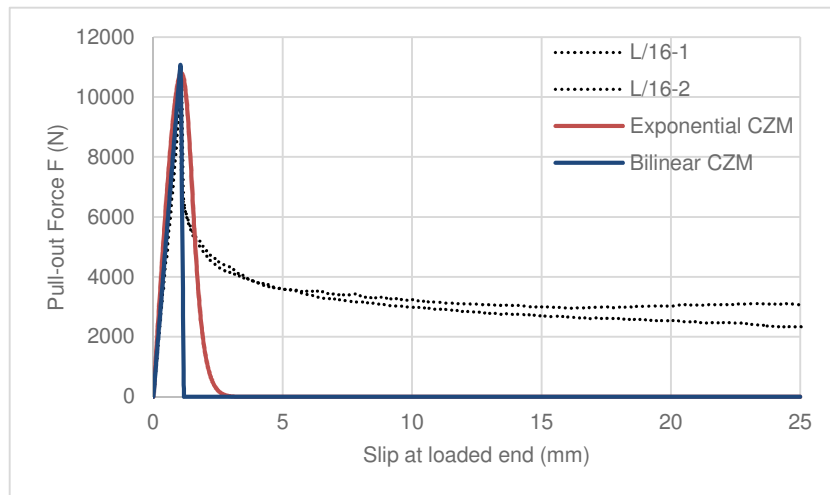


Figure 4.10 - $\phi 16$ mm rebar pull-out from LWC specimens: Comparison between Bilinear (Alfano and Crisfield, 2001) and Exponential (Xu and Needleman, 1994) CZMs and experimental curves

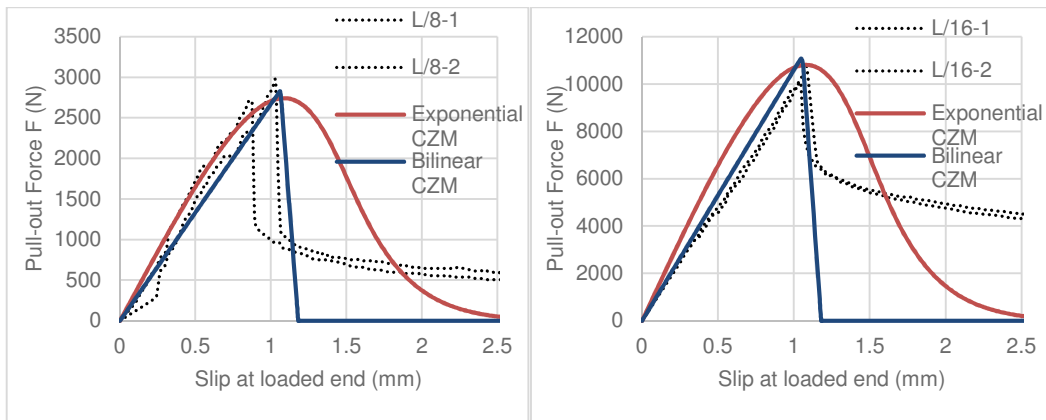


Figure 4.11 - $\phi 8$ and 16 mm rebar pull-out from LWC specimens, zoom on the elastic branch: Comparison between Bilinear (Alfano and Crisfield, 2001) and Exponential (Xu and Needleman, 1994) CZMs and experimental curves

Figs. 4.6-4.11 show that the two cohesive zone models used, i.e. the bilinear and exponential formulations, can well capture the behaviour of the response curve within the elastic and immediate post-peak ranges. Especially in the case of the Alfano and Crisfield (bilinear) model (Alfano and Crisfield, 2001), the first part of the softening curve corresponding to the post-peak sudden drop can be well represented by the numerical curves (Figs. 4.8 and 4.11). However, both of the models are unable to capture the residual force obtained from all the experimental curves. This residual force has a significant value, being a non-negligible percentage (around 35% on average) of the peak one.

In order to not disregard this significant part of the load capacity, a different CZM has been considered, where the contribution of friction is accounted for. The following paragraph reports the results obtained with the CZM combining damage and friction proposed by Alfano and Sacco (Alfano and Sacco, 2006).

4.3 CZM accounting for friction

Among the models accounting for friction available in the literature and presented in Section 2.5.2.3 of the present thesis, the model proposed by Alfano and Sacco (Alfano and Sacco, 2006) has been chosen in order to verify if the contribution of friction is capable of capturing the residual pull-out force value shown by all the experimental curves.

4.3.1 Model formulation

As mentioned in Section 2.5.3, the main idea behind the model introduced by Alfano and Sacco (Alfano and Sacco, 2006) is to decompose the representative element area (REA) into a damaged and an undamaged parts. Then, the model proposed by Alfano and Crisfield (Alfano and Crisfield, 2001) is implemented on the damaged part of the REA, while the behaviour of the undamaged portion is considered linear-elastic.

A brief recall of the model is summarised in the following Eqs. (4.9) and (4.10):

$$\begin{cases} \sigma = (1 - D)K_1 s_1 + D\sigma_d \\ \tau = (1 - D)K_2 s_2 + D\tau_d \end{cases} \quad (4.9)$$

with:

$$\sigma_d = [1 - h(s_1)]K_1 s_1 ; \quad \tau_d = K_2(s_2 - s_2^{di}) ; \quad \dot{s}_2^{di} = \dot{\lambda} \frac{\tau_d}{|\tau_d|} \quad (4.10)$$

$$\mu\sigma_d + |\tau_d| \leq 0 ; \quad \dot{\lambda} < 0 ; \quad \dot{\lambda}(\mu\sigma_d + |\tau_d|) = 0$$

where:

- σ and τ → Normal and tangential components of the stress $\boldsymbol{\sigma}$;
- D → Damage variable as defined in Eq. (2.50) (Section 2.5.3);
- K_1 and K_2 → Normal and tangential stiffnesses. Particularly, K_2 accounts for the elasticity of crack interfaces interacting through asperities;
- s_1 and s_2 → Normal and tangential components of the relative displacement vector \mathbf{s} ;
- $h(x)$ → Heaviside function: $h(x) = \begin{cases} 1 & \text{if } x \geq 0 \\ 0 & \text{if } x < 0 \end{cases}$
- \dot{s}_2^{di} → Derivative of the tangential component of the inelastic part of the relative displacement in the damaged part;
- $\dot{\lambda}$ → Coefficient introduced through the Khun-Tacker conditions, and such that:
 $\dot{\lambda} \geq 0; \phi(\boldsymbol{\sigma}) \leq 0; \dot{\lambda}\phi(\boldsymbol{\sigma}) = 0$
- μ → Friction coefficient.

4.3.2 Model implementation in the FE code ANSYS R16

The model proposed by Alfano and Sacco (Alfano and Sacco, 2006) has been implemented in the software ANSYS R16 through a user-subroutine, by following the algorithm presented in (Alfano and Sacco, 2006). The subroutine requests writing in FORTRAN programming language.

It is worth remarking that the model formulation in terms of interface relationship is non-holonomic, thus the response with one or more interfaces described by such law turns out to be path-dependent (Alfano and Sacco, 2006). However, in the present case a quasi-static nonlinear incremental analysis has been performed, which is divided into a finite number of steps and, within each of them, a step-wise holonomic law is introduced.

In the framework of the FE analysis, the inelastic relative displacement \mathbf{s}^{di} and the damage variable, D , represent the history variables of the model. Their values are thus updated at each step, starting from an initial value, which is initialised at the beginning of the analysis, so that it is known. Another model feature is the ‘relative displacement driven’ formulation, which implies that at each step the equations have to be solved for the unknown variable represented by the stress vector, $\boldsymbol{\sigma}$.

4.3.3 Results with CZM accounting for friction

The input parameter for the CZM accounting for friction proposed by Alfano and Sacco (Alfano and Sacco, 2006) are reported in Table 4.6. In the first instance the same fracture energy and the same maximum cohesive traction for both modes I and II have been adopted. As a matter of fact, this has been found to be not influent in the overall system response, which is not able to represent the experimental behaviour due to the impossibility to represent the residual pull-out force plateau.

Table 4.6 - Input parameters for the CZM accounting for friction proposed by Alfano and Sacco (Alfano and Sacco, 2006)

Parameter	Unit	Expression	Description	Value adopted in the analysis	
				NWC	LWC
G_{cn}	(kJ/m ²)	$G_{cn} = \frac{1}{2} \sigma_{0n} s_{cn}$	Fracture Energy Mode I (Normal)	0.925	2.50
G_{ct}	(kJ/m ²)	$G_{ct} = \frac{1}{2} \sigma_{0t} s_{ct}$	Fracture Energy Mode II (Tangential)	0.925	2.50
σ_{0n}	(MPa)		Maximum Cohesive Traction Mode I (Normal)	1.85	2.80
σ_{0t}	(MPa)		Maximum Cohesive Traction Mode II (Tangential)	1.85	2.80
η	(-)	$\eta = 1 - \frac{s_{0n}}{s_{cn}} = 1 - \frac{s_{0t}}{s_{ct}}$	Coefficient that controls the ratio between the displacement at the completion of debonding and its value at maximum cohesive traction	0.55	0.40
μ	(-)		Friction Coefficient	0.5	0.5

The results of the analyses are reported in the following Figs. 4.12-4.15.

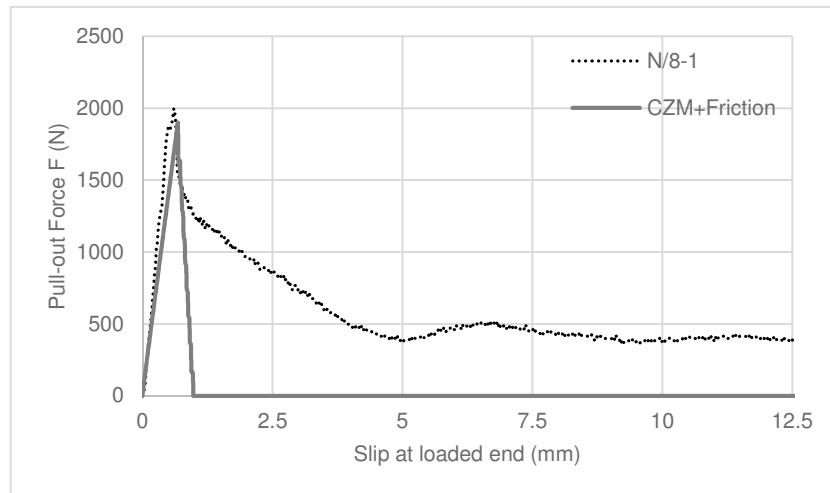


Figure 4.12 - $\phi 8$ mm rebar pull-out from NWC specimens: Comparison between CZM accounting for friction (Alfano and Sacco, 2006) and experimental curves

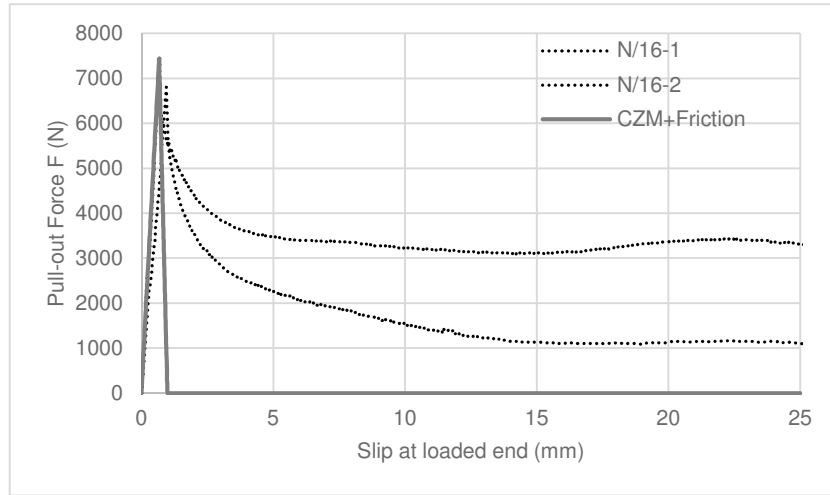


Figure 4.13 - $\phi 16$ mm rebars pull-out from NWC specimens: Comparison between CZM accounting for friction (Alfano and Sacco, 2006) and experimental curves

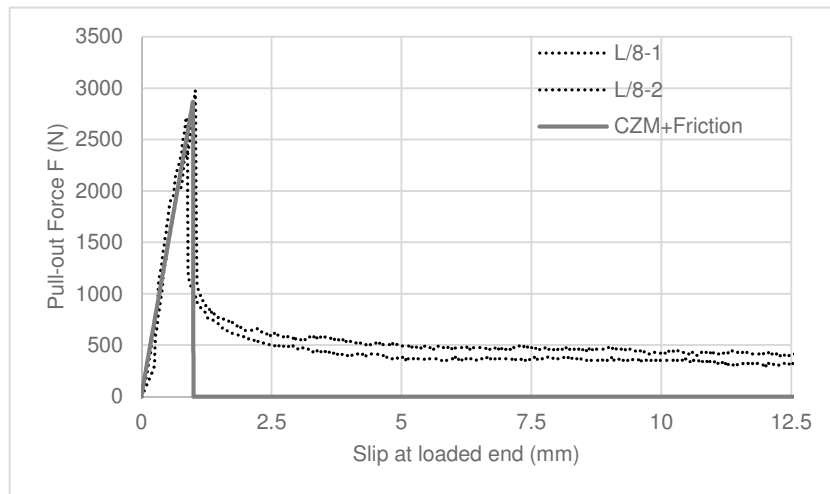


Figure 4.14 - $\phi 8$ mm rebars pull-out from LWC specimens: Comparison between CZM accounting for friction (Alfano and Sacco, 2006) and experimental curves

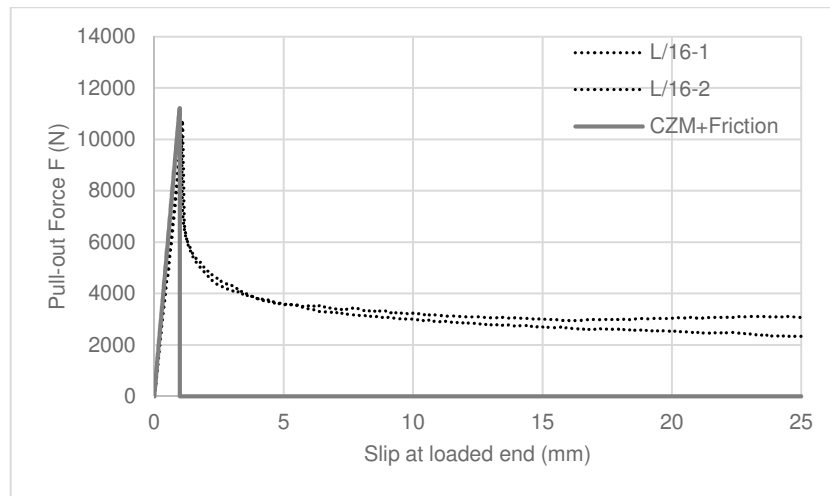


Figure 4.15 - $\phi 16$ mm rebars pull-out from LWC specimens: Comparison between CZM accounting for friction (Alfano and Sacco, 2006) and experimental curves

The model proposed by Alfano and Sacco (Alfano and Sacco, 2006), which includes friction, does not capture the residual post-peak force, as it happens with the two models considered above, i.e. exponential and bilinear formulations.

By taking for example the model concerning the pull-out of $\phi 16$ mm bars from NWC, the stress evolution along the interface is shown in Fig. 4.16. Particularly, Fig. 4.16a shows the portions of bar and matrix on which normal stresses are computed. Figs. 4.16b-4.16e show the evolution over time (i.e. at different substeps) of the values of the direct stress both on the portions A and B, previously identified, and along the interface. Negative values of the normal stress correspond to compression, whereas positive ones are traction stresses. Along the interface the maximum absolute value reached by the compressive stress is equal to 0.16795 MPa at substep 66 (Fig. 4.16-d). However, at this stage, the interface is still not debonded, thus the adhesion is not completely lost. Fig. 4.16e, instead, represents a post-debonding phase, where friction should give its most significant contribution. This does not happen because the compressive stress is almost equal to zero. Therefore, friction does not play any role in this model during the post-debonding phase.

Chapter 4 – Finite Element Modelling of the pull-out behaviour between titanium bars and concrete

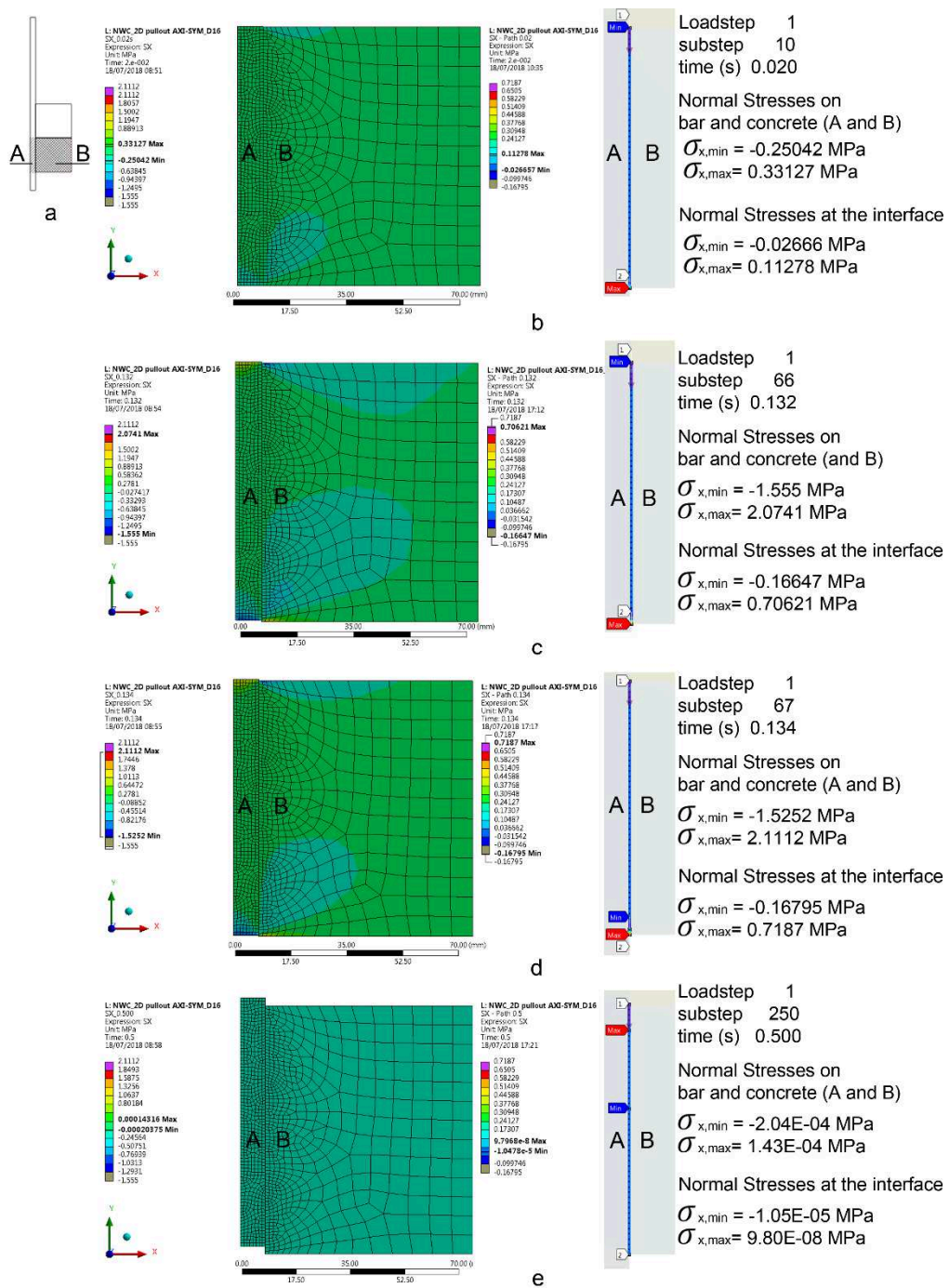


Figure 4.16 - a) scheme of the interface; evolution of the normal stress on bar and matrix portions and along the interface: b) substep 10; c) substep 66; d) substep 67; and e) substep 250

The behaviour showed by the model with the frictional-cohesive interface was expected to happen, since the Poisson's coefficient of titanium is higher than that of concrete (i.e. $\nu_t=0.36$ and $\nu_c=0.18$, respectively). Thus, when the interface is allowed to debond, the lateral deformation (x -direction) of the bar subjected to the tensile pull-out load causes a further detachment with respect to the matrix surface. This, does not allow the compressive stresses and, therefore, the frictional forces to develop. Therefore, it results that at the beginning, when the interface is bonded, the normal (x -direction) strain distributions of the bar (ϵ_{xt}) and the matrix (ϵ_{xc}) can be assumed equal except for some local effects near the upper bond end (Fig. 4.17a). On the contrary, during debonding the bar normal strains exceed those of the matrix, enhancing the separation of the two surfaces (Fig. 4.17b).

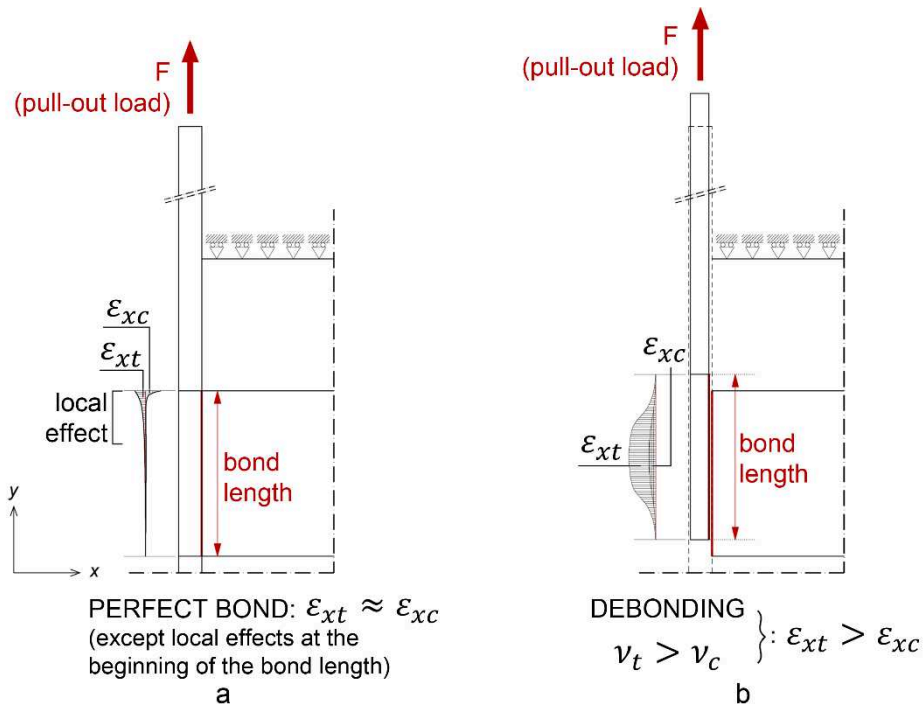


Figure 4.17 - a) bar and matrix strain distribution along the interface during the bonding stage; and b) bar and matrix strain distribution along the interface during the debonding stage

An initial perfectly bonded interface can be obtained by supposing a purely linear softening CZM (Fig. 4.18a). In this case the transversal (x -direction) deformations, and as a consequence the strain distributions, of the bar and the matrix at the interface are the same (Fig. 4.18b), except for the local effects at the upper end of the bond length. The bar and matrix strain distributions near the bond end, in fact, have been found to be different even when a perfectly bonded interface is considered (Mimura et al., 2011). In real structures, this effect is usually negligible due to the development length of the rebars. On the contrary, when pull-out tests are performed, the bond length is not long enough to disregard the differences in the strain distribution. This phenomenon is more evident when an initial

imperfect bond (i.e. the stiffness of the elastic-linear branch of the CZM is finite) is adopted (Fig. 4.19a). In this case, deformations and strains of the bar and the matrix are significantly different even when the interface is still bonded (Fig. 4.19b).

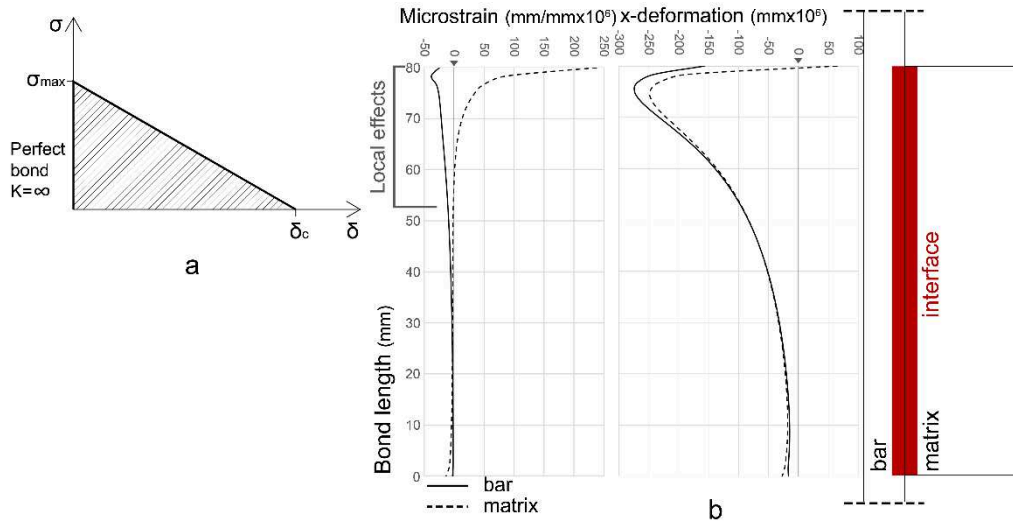


Figure 4.18 - a) Purely linear softening CZM: a perfect bond at the beginning of the analysis; b) bar and matrix normal strain and directional deformation distributions along the interface during the bonding stage

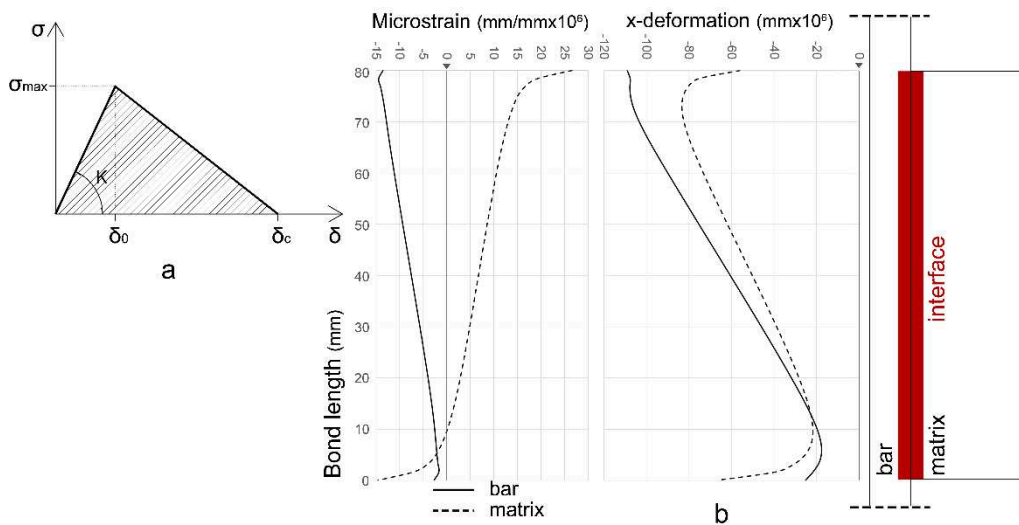


Figure 4.19 - a) Bilinear softening CZM with finite stiffness at the linear-elastic branch; b) bar and matrix normal strain and directional deformation distributions along the interface during the bonding stage

4.3.4 Further validation

In order to demonstrate the validity of the results obtained with the CZM accounting for friction proposed by Alfano and Sacco (Alfano and Sacco, 2006), an analysis with an applied lateral pressure is carried out. In this manner, it is possible to appreciate contribution provided by friction. Only the results for the $\phi 16\text{mm}$ rebar in NWC specimen is reported, since the other specimens provided same qualitative results. Fig. 4.20 shows the model adopted for the analysis with the new set of boundary conditions, while Fig. 4.21 shows the obtained pull-out force-slip curves for a normal lateral pressure equal to 100 MPa.

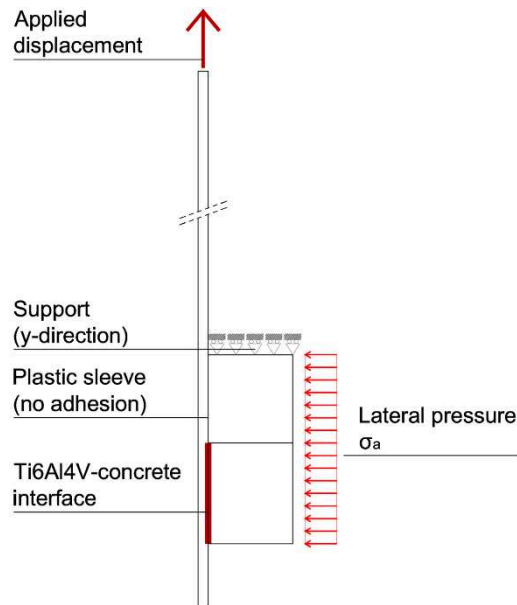


Figure 4.20 - FE model of the specimens with 16 mm bar diameter and the applied lateral pressure σ_a

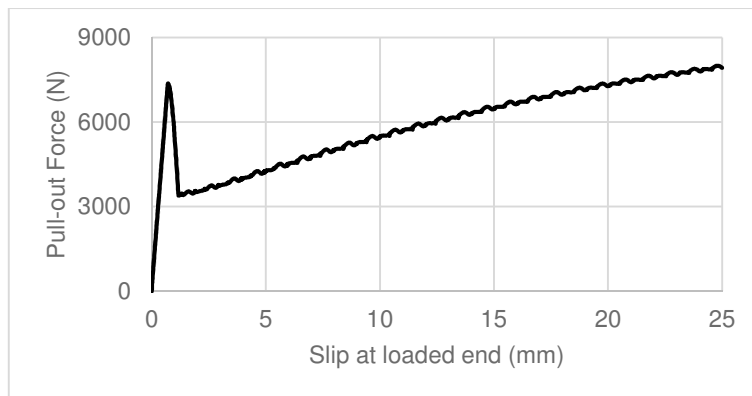


Figure 4.21 - Pull-out curve response (up to 5 mm of slip) of $\phi 16\text{ mm}$ titanium alloy rebar from NWC specimen, with a CZM accounting for friction and a constant lateral pressure $\sigma_a = 100\text{ MPa}$

4.4 Concluding remarks

In this chapter several formulations of existing cohesive zone models have been employed in order to make a first estimation of the fracture parameters values, even if the experimental results could not be completely represented using exponential, bilinear and frictional CZMs. However, it has been found that the exponential model proposed by Xu and Needleman (Xu and Needleman, 1994) is capable of capturing the experimental bond strength and the stiffness of the first part of the curve, which corresponds to an almost linear branch up to the bond strength. The bilinear model proposed by Alfano and Crisfield (Alfano and Crisfield, 2001), instead, not only well represents the linear behaviour and the value of the bond strength, but also captures the initial stiffness of the decreasing branch, i.e. the pull-out force drop corresponding to a significant loss of adhesion. Finally, by using the model proposed by Alfano and Sacco (Alfano and Sacco, 2006), which combines damage and friction, the post-peak significant residual force is still not described by the numerical model. This is because, without an additional lateral pressure, the test set-up and the differences in the bar and matrix Poisson's coefficients do not promote the development of compressive stresses at the interface. What the model allows to better understand, in fact, is that, actually, traction stresses originated at the interface during the pull-out failure mechanism.

In order to understand the physics behind the whole phenomenon, further analyses with other CZM formulations are presented in the next chapter. On one hand, a cohesive model accounting for a frictional coefficient, formulated by starting from the Alfano and Crisfield bilinear model (Alfano and Crisfield, 2001) has been proposed. On the other hand, the model presented by Serpieri, Alfano and Sacco in (Serpieri et al., 2015a) and accounting not just for damage and friction but also for mechanical interlocking and dilatancy, has been employed to verify if these micro-mechanisms had a role during the pull-out tests carried out herein. Moreover, this model has been modified and extended.

Chapter 5

New cohesive models for the characterisation of the interface between plain Ti6Al4V bars and concrete

This chapter presents the numerical results obtained by employing the FE models described in Chapter 4, where other CZMs, with respect to those previously used, are implemented. In particular, a first formulation is derived from the model formulated by Alfano and Crisfield (Alfano and Crisfield, 2001) and considers the frictional mechanism by adding an exponential branch to the bilinear law. The second formulation, instead, concerns the implementation in the FE code of the CZM accounting for damage, friction, mechanical interlocking and dilatancy proposed by Serpieri, Alfano and Sacco in (Serpieri et al., 2015a), hereafter called M-CZM to indicate the multiplane approach. Moreover, in this chapter, an extension to this model is proposed. With the extended CZM, sensitivity analyses, identification and validation of the FE model representing the pull-out tests, are carried out. It is worth remarking that in the present research, the FE analysis has been used as a tool to better understand the mechanisms involved in the debonding process between plain titanium bars and concrete. In fact, the micro-mechanics based formulation of the model by Serpieri, Alfano and Sacco (Serpieri et al., 2015a) allows for describing the actual micro-mechanisms governing the pull-out failure.

5.1 A new CZM derived from the Alfano and Crisfield bilinear model

By observing the experimental curves presented in Chapter 2, a phenomenological model can be formulated in order to describe the curve entirely. A simple modification in the formulation of the Alfano and Crisfield bilinear model (Alfano and Crisfield, 2001)

allows to consider the tangential traction T_t not vanishing after the complete debonding, but decreasing slowly according to an exponential law. As a consequence, the model needs more input parameters that can be identified only by carrying out experimental tests.

The modified model formulation is presented in Eqs. (5.1) and (5.2), while the difference between the original and the modified models is represented in Fig. 5.1. It is worth noting that the modified law is necessary only for the mode II fracture behaviour, i.e. the tangential cohesive law, being the normal opening mode not affected by the frictional behaviour. In fact, the exponential branch added in this formulation is aimed to represent the frictional effect on the cohesive behaviour by considering a first tangential stress ($c_1 + c_2$), simulating the residual value of the cohesive traction after the sudden post-peak loss of adhesion, and a final residual tangential stress (c_1) asymptotically approached with growing slip. The rate of the decreasing law between these two tangential stresses is controlled by the parameter α , whose value belongs to the interval $[0,1]$.

The tangential cohesive traction, T_t , is given by Eq. (5.1), while the expression of the damage variable, D_t , is provided by Eq. (5.2):

$$T_t = K_t \delta_t (1 - D_t) \quad (5.1)$$

$$D_t = \begin{cases} 0 & \text{if } \delta_t^{max} \leq \delta_t^* \\ \left(\frac{\delta_t^{max} - \delta_t^*}{\delta_t^{max}} \right) \left(\frac{\delta_t^c}{\delta_t^c - \delta_t^*} \right) \left(1 - \frac{c_1 + c_2}{K_t \delta_t^{max}} \right) & \text{if } \delta_t^* \leq \delta_t^{max} \leq \delta_t^c \\ 1 - \frac{c_2 + c_1 e^{-\alpha(\delta_t^{max} - \delta_t^c)}}{K_t \delta_t^{max}} & \text{if } \delta_t^{max} < \delta_t^c \end{cases} \quad (5.2)$$

where the newly introduced parameters are:

- c_1 → value of the bond stress immediately after the post-peak drop;
- c_2 → final residual value of the bond stress;
- α → parameter between 0 and 1 through which the rate of the decreasing exponential branch is defined.

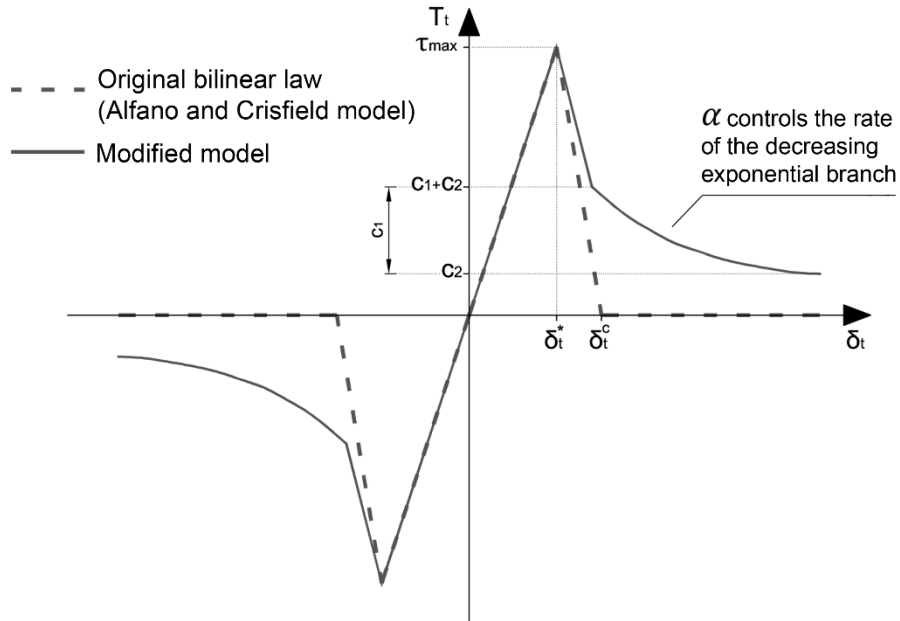


Figure 5.1 - Alfano and Crisfield Bilinear CZM vs Modified law (tangential law)

5.1.1 Results with the modified Alfano and Crisfield model

The input data are summarised in Table 5.1 for all the analysed cases, i.e. for the two bar diameters investigated ($\phi 8$ and $\phi 16$ mm) and the two concrete batches (NWC and LWC). The fracture parameters are the same as those identified for the Alfano and Crisfield bilinear model (paragraph 4.1.3.1.2 of Chapter 4), while the values of the parameters c_1 , c_2 , and α are chosen in order to fit the experimental curves for each case.

The comparison between numerical and experimental results is reported in Figs. 5.2-5.5. Noteworthy, the models here employed are the same used before, i.e. those described in Chapter 4 and represented in Fig. 4.1 of the same chapter.

Table 5.1 - Input parameters for the modified Alfano and Crisfield model

Parameter	Unit	NWC		LWC	
		$\phi 8$	$\phi 16$	$\phi 8$	$\phi 16$
τ_{max}	(MPa)	1.85	1.85	2.80	2.80
$G_{c,t}$	(kJ/m ²)	0.925	0.925	1.50	1.50
δ_t^c	(mm)	1.00	1.00	1.07	1.07
δ_t^*/δ_t^c	(-)	0.60	0.45	0.6	0.6
c_1	(MPa)	0.635	0.735	0.635	0.735
c_2	(MPa)	0.365	0.60	0.365	0.60
α	(-)	0.50	0.50	0.50	0.50

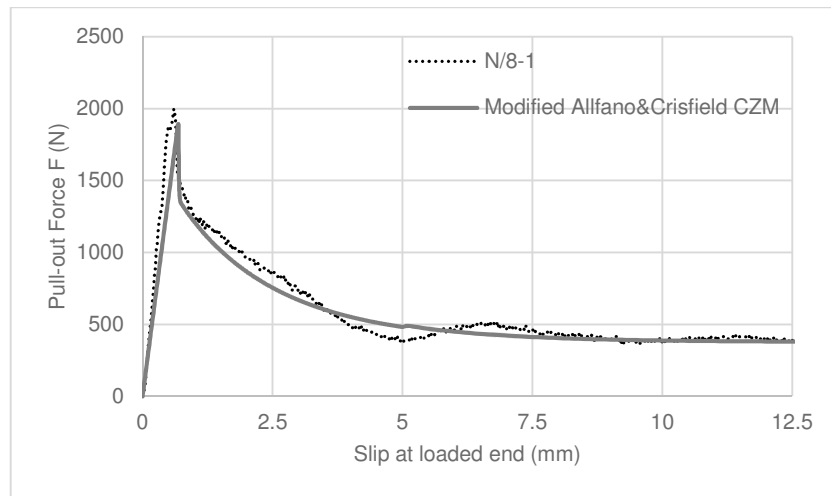


Figure 5.2 - $\phi 8$ mm rebars pull-out from NWC specimens: Comparison between Modified Alfano and Crisfield CZM and experimental curves

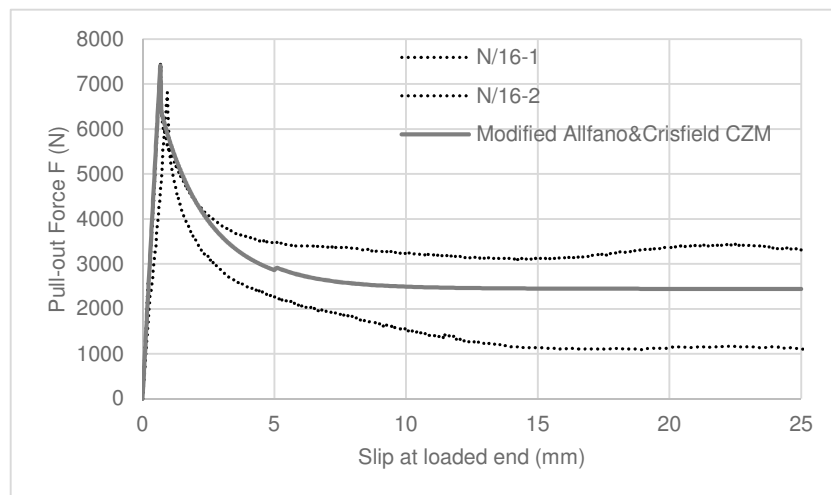


Figure 5.3 - $\phi 16$ mm rebars pull-out from NWC specimens: Comparison between Modified Alfano and Crisfield CZM and experimental curves

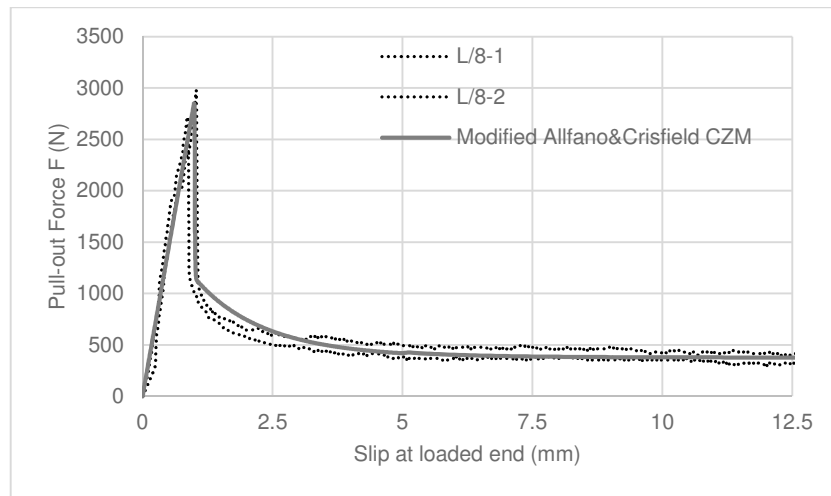


Figure 5.4 - $\phi 8$ mm rebar pull-out from LWC specimens: Comparison between Modified Alfano and Crisfield CZM and experimental curves

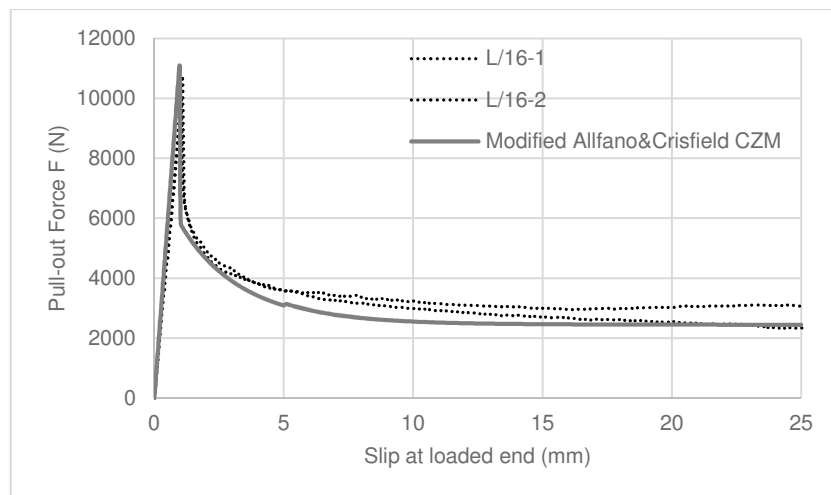


Figure 5.5 - $\phi 16$ mm rebar pull-out from LWC specimens: Comparison between Modified Alfano and Crisfield CZM and experimental curves

By implementing the modified Alfano and Crisfield CZM in the FE model, the agreement between experimental and numerical curves appears very good. However, the approach adopted for modelling the post-peak phase is not the results of a physical description of the mechanisms acting at the interface. It can be seen as the representation of the interfacial frictional behaviour, but it is not derived from a friction-based model. In order to overcome the limitations of this kind of approach, which is strongly phenomenological, in the next paragraph a micro-mechanics based formulation of the CZM is employed. In this way, the actual mechanisms acting at the interface can be considered,

and thus a physics-based description of the behaviour obtained from the experimental tests is provided.

5.2 M-CZM and ‘enhanced degrading M-CZM’

To simulate the post-peak response exhibited by the pull-out test curves, but also to support some of the hypotheses made to explain such behaviour (see section 3.5), the frictional cohesive-zone model proposed by Serpieri, Alfano and Sacco in (Serpieri et al., 2015a) has been employed and partially extended, as explained below. The original cohesive model is called M-CZM, to indicate the multiplane approach adopted by Serpieri, Alfano and Sacco (Serpieri et al., 2015a) and accounts for damage, friction, dilatancy, and interlocking. The M-CZM has been implemented in a user-subroutine (USERCZM) in the FE code ANSYS R16 (© ANSYS, 2015). A description of the model is made here, referring to (Serpieri et al., 2015a) for more details.

5.2.1 Original M-CZM

The key points of the M-CZM (Serpieri et al., 2015a) are summarised in this section. Some of the main aspects were already present in the model formulated by Serpieri and Alfano (Serpieri and Alfano, 2011). Moreover, the bipartition of the elementary interface area into a damage and undamaged parts and the combination between damage and friction of the model proposed by Alfano and Sacco (Alfano and Sacco, 2006) are also fundamental features of the present model.

The notation reported in Fig. 5.6 is assumed. In a pre-defined interface Γ , a crack can initiate and propagate, and the displacement field is allowed to be discontinued.

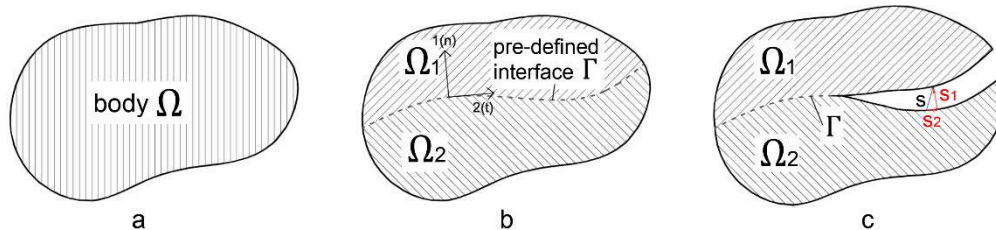


Figure 5.6 - a) body without interface; b) interface model in the initial (undeformed) configuration; and c) interface model in the deformed configuration

The first key point of the M-CZM is the multiscale approach, which allows for the description of the smooth macro interface through a periodic micro-pattern with a repeating unit, RIA, made of a certain number of microplanes, as shown in Fig. 5.7. Thus, an approximation of the actual geometry of the asperities is taken into account at the microscale level.

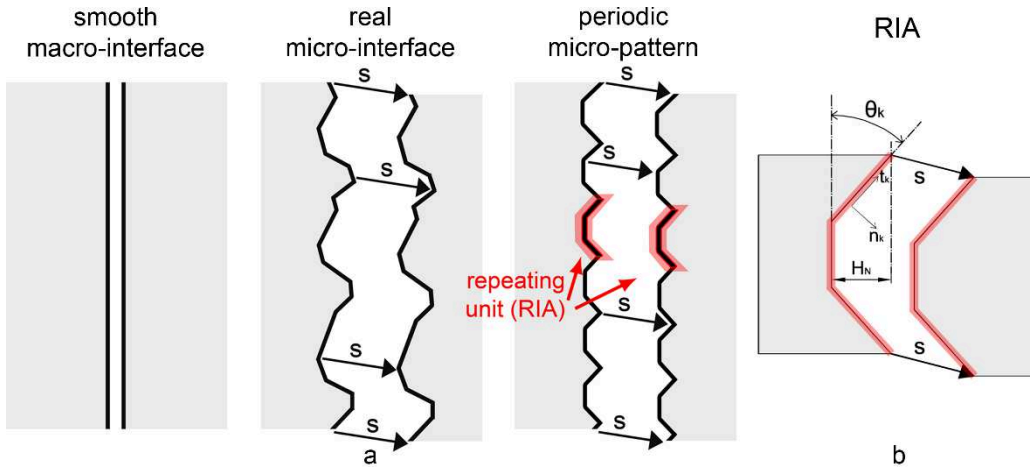


Figure 5.7 - a) the multiscale approach for describing the smooth macro-interface through a periodic pattern of RIA; and b) RIA scheme

It is worth noting that this model allows for placing the interface elements along the smooth macro-interface, without the necessity to capture the asperities details by the spatial FE discretisation. At first, the number of elementary planes (also called ‘microplanes’) N_p constituting the RIA is assumed equal to 3. However, in order to verify the influence of the microplanes number, some analyses have been performed by using a RIA made of 5 microplanes. Fig. 5.7b shows the unique relative-displacement vector, \mathbf{s} , which defines the only deformation occurring at the interface within the RIA. In fact, the stiffness of the asperities is considered infinite, and, thus, they do not undergo any deformations. On each k^{th} microplane, the macro-scale relative-displacement vector is decomposed into mode I and mode II components, s_n and s_t respectively, depending on the microplane inclination angle θ_k . The local components s_n and s_t are computed accounting for elastic damage and friction using the model developed by Alfano and Sacco (Alfano and Sacco, 2006). The thermodynamic consistency is assured by adopting the same fracture energy in modes I and II (Serpieri et al., 2015b). In this way it is possible to use a single damage variable, D_k , on each microplane, which evolves according to an associated-type damage law. The cohesive law relating the relative displacement vector \mathbf{s} to the interface stress $\boldsymbol{\sigma}$ is determined by solving the microscale problem for the RIA at each integration point of each interface element of the macroscale model, linking the two scales.

5.2.1.1 Formulation of the interface constitutive law

According to (Serpieri and Alfano, 2011), Eq. (5.3) relates the free energy per unit area, Ψ , to the free energies associated with each microplane, Ψ_k by means of weight coefficients γ_k .

$$\Psi = \sum_{k=1}^{N_p} \gamma_k \Psi_k \quad (5.3)$$

Denoting by A_p the overall area of the RIA, and by A_k the effective area of the k^{th} microplane, the total area of all microplanes, A , is given by Eq. (5.4):

$$A = \sum_{k=1}^{N_p} A_k \quad (5.4)$$

The coefficient γ_k is then defined as reported in Eq. (5.5):

$$\gamma_k = \frac{A_k}{A_p} = \hat{\gamma}_k \frac{A}{A_p} \quad (5.5)$$

where $\hat{\gamma}_k = \frac{A_k}{A}$ is the effective area fraction of each microplane

If A_{pk} is the projection of A_k onto the average interface plane, the total projected area, A_p , is expressed by Eq. (5.6):

$$A_p = \sum_{k=1}^{N_p} A_{pk} \quad (5.6)$$

By combining equations (5.4) and (5.5), the final expression of the total area of all microplanes, A , is given by Eq. (5.7):

$$A = A \sum_{k=1}^{N_p} \hat{\gamma}_k \Rightarrow \sum_{k=1}^{N_p} \hat{\gamma}_k = 1 \quad (5.7)$$

The free energy per unit area on each microplane, Ψ_k , is given by the sum of the elastic energy on the undamaged and damaged parts of such a microplane, denoted by Ψ_k^u and Ψ_k^d , respectively (Serpieri and Alfano, 2011). Ψ_k is expressed by Eq. (5.8):

$$\Psi_k = (1 - D_k)\Psi_k^u + D_k\Psi_k^d \quad (5.8)$$

where Ψ_k^u and Ψ_k^d are given by Eqs. (5.9) and (5.10), respectively:

$$\Psi_k^u = \frac{1}{2}(K_n s_{kn}^2 + K_t s_{kt}^2) \quad (5.9)$$

$$\Psi_k^d = \frac{1}{2}[K_n \langle s_{kn} \rangle_-^2 + K_t (s_{kt} - s_{kf})^2] \quad (5.10)$$

where:

- s_{kn} and s_{kt} → relative displacement components in local modes I and II w.r.t. the local microplane reference system;
- $\langle s_{kn} \rangle_-$ → negative part of the normal component of the relative displacement vector, i.e. $\langle s_{kn} \rangle_- = (s_{kn} - |s_{kn}|)/2$;
- K_n and K_t → elastic stiffnesses in modes I and II introduced in the form of penalty stiffness factors that must be not too high to avoid hill-conditioning (Alfano and Crisfield, 2001);
- s_{kf} → frictional slip on each microplane.

The local relative-displacement components s_{kn} and s_{kt} are related to the global ones, s_N and s_T through the relation expressed in Eq. (5.11):

$$\begin{bmatrix} s_{kn} \\ s_{kt} \end{bmatrix} = \mathbf{R}_k \begin{bmatrix} s_N \\ s_T \end{bmatrix} = \begin{bmatrix} \cos \theta_k & \sin \theta_k \\ -\sin \theta_k & \cos \theta_k \end{bmatrix} \begin{bmatrix} s_N \\ s_T \end{bmatrix} \quad (5.11)$$

where \mathbf{R}_k represents a rotation matrix.

Being the macroscopic stress the derivative of the free energy per unit area with respect to the relative-displacement vector, Eq. (5.3) leads to the expression of the stress tensor, $\boldsymbol{\sigma}$, given by Eq. (5.12):

$$\boldsymbol{\sigma} = \frac{\partial \Psi}{\partial \mathbf{s}} = \sum_{k=1}^{N_p} \gamma_k \boldsymbol{\sigma}_k \quad \text{where} \quad \boldsymbol{\sigma}_k = \frac{\partial \Psi_k}{\partial \mathbf{s}} \quad (5.12)$$

On the k^{th} microplane, stress is in turn divided into damaged and undamaged parts, as shown in Eq. (5.13):

$$\boldsymbol{\sigma}_k = \frac{\partial \Psi_k}{\partial \mathbf{s}_k} = (1 - D_k) \boldsymbol{\sigma}_k^u + D_k \boldsymbol{\sigma}_k^d \quad \text{with:} \quad \boldsymbol{\sigma}_k^u = \frac{\partial \Psi_k^u}{\partial \mathbf{s}_k} \quad \text{and} \quad \boldsymbol{\sigma}_k^d = \frac{\partial \Psi_k^d}{\partial \mathbf{s}_k} \quad (5.13)$$

By referring to the local microplane reference system (\mathbf{n}_k - \mathbf{t}_k), the normal and tangential local stress components, σ_{kn} and σ_{kt} , are given by Eq. (5.14):

$$\sigma_{kn} = \frac{\partial \Psi_k}{\partial s_{kn}} \quad \sigma_{kt} = \frac{\partial \Psi_k}{\partial s_{kt}} \quad (5.14)$$

By combining equations (5.8), (5.9), (5.10) and (5.14), it results:

$$\begin{bmatrix} \sigma_{kn} \\ \sigma_{kt} \end{bmatrix} = (1 - D_k) \begin{bmatrix} K_n s_{kn} \\ K_t s_{kt} \end{bmatrix} + D_k \begin{bmatrix} K_n (s_{kn})_- \\ K_t (s_{kt} - s_{kf}) \end{bmatrix} \quad (5.15)$$

The model of Alfano and Sacco (Alfano and Sacco, 2006), combining damage and friction, accounts for uncoupled evolution of the damage variable D_k and of the tangential frictional slip, s_{kf} . The damage variable, D_k , evolution is defined so as to produce a linear decreasing traction-relative displacement law in pure modes I and II. The hypothesis behind this damage model, originally proposed in (Alfano and Crisfield, 2001), assumes that for modes I and II the interface is characterised by a unique ‘ductility parameter’ η , given in Eq. (5.16):

$$\eta = 1 - \frac{s_{0n}}{s_{cn}} = 1 - \frac{s_{0t}}{s_{ct}} \quad (5.16)$$

being s_{0n} and s_{0t} the relative-displacement values at the onset of damage in modes I and II, respectively, and s_{cn} and s_{ct} those corresponding at the completely loss of cohesion.

Given the peak stresses in modes I and II, σ_{0n} and σ_{0t} , the relative fracture energies, G_{cn} and G_{ct} , are simply obtained from Eq. (5.17), with the further condition $G_{cn} = G_{ct}$, which guarantees the thermodynamic consistency (Serpieri et al., 2015b).

$$G_{cn} = \frac{1}{2} \sigma_{0n} s_{cn} \quad G_{ct} = \frac{1}{2} \sigma_{0t} s_{ct} \quad (5.17)$$

The damage evolution is given by the following law expressed by Eq. (5.18):

$$D_k = \max \left\{ 0, \min \left\{ 1, \frac{\beta_k}{\eta(1-\beta_k)} \right\} \right\} \quad \text{where} \quad \beta_k = \max_{\text{history}} \sqrt{\left(\frac{(s_{kn})_-}{s_{0n}} \right)^2 + \left(\frac{s_{kt}}{s_{0t}} \right)^2} \quad (5.18)$$

The set of governing equations is completed by those that describe the evolution of the history parameter s_{kf} , which represents the frictional slip. It enters the model in the form of nonassociative plasticity and it accounts for inelastic sliding on the k^{th} microplane, acting only in tangential direction. With reference to the k^{th} microplane, a Coulomb-like function (ϕ_k) with no cohesion and characterised by a friction coefficient μ , is introduced in the model (Serpieri and Alfano, 2011) through the following Eq. (5.19):

$$\begin{aligned}\phi_k(\boldsymbol{\sigma}_k^d) &= \mu \langle \sigma_{kn}^d \rangle_- + |\sigma_{kt}^d| \Rightarrow \phi_k(s_{kn}, s_{kt}, s_{kf}) = \\ &= \mu K_n \langle s_{kn} \rangle_- + |K_t (s_{kt} - s_{kf})|\end{aligned}\quad (5.19)$$

Frictional slip is obtained by introducing a slip function $g(\boldsymbol{\sigma}_k^d)$ and assuming that:

$$\dot{s}_{kf} = \lambda \frac{\partial g}{\partial \sigma_k^d} \quad (5.20)$$

where g is the slip potential and λ is the slip multiplier analogous to the plastic multiplier introduced in elastoplasticity (Simo and Hughes, 1998). In order to address a pure frictional effect with no dilatancy contributed by individual microplanes, the following slip potential, $g(\boldsymbol{\sigma}_k^d)$, is considered (Eq. (5.21)):

$$g(\boldsymbol{\sigma}_k^d) = \hat{g}(\sigma_{kt}^d) = |\sigma_{kt}^d| \quad (5.21)$$

It is worth noting that the dilatant effect is given by the combined interaction among the N_p microplanes constituting the RIA and not by the governing law of each individual elementary plane.

The slip potential (5.21) provides an entirely tangential flow rule, given by Eq. (5.22):

$$\dot{s}_{kf} = \dot{\lambda}_k \frac{\partial \hat{g}}{\partial \sigma_{kt}^d} = \dot{\lambda}_k \text{sign}(\sigma_{kt}^d) \quad \text{Note that: } \dot{\mathbf{s}}_{kf} = \begin{bmatrix} 0 \\ \dot{s}_{kf} \end{bmatrix} \quad (5.22)$$

which is completed by the additional Khun–Tucker conditions, expressed through Eq. (5.23):

$$\dot{\lambda}_k \geq 0 \quad \phi_k(\boldsymbol{\sigma}_k^d) = \phi_k(s_{kn}, s_{kt}, s_{kf}) \leq 0 \quad \dot{\lambda}_k \phi_k(s_{kn}, s_{kt}, s_{kf}) = 0 \quad (5.23)$$

The new aspects introduced in the model presented in (Serpieri et al., 2015a) with respect to the previous model formulated by Serpieri and Alfano in (Serpieri and Alfano, 2011) concerns:

- 1) the finite depth of the asperities; and
- 2) the progressive interlocking degradation.

The main laws able to account for these aspects are presented in the next subsections.

5.2.1.1.1 Modelling of the finite depth of the asperities

In order to account for the finite depth of the asperities, the idea introduced by Serpieri et al. (Serpieri et al., 2015a) is to describe equilibrium no longer referring to the initial system geometry, but to its current deformed configuration, determined by the displacement vector \mathbf{s} . Thus, for the k^{th} microplane of the RIA with $\theta_k \neq 0$, the potential area in contact, A_k , in the deformed configuration is given by Eq. (5.24):

$$A_k = \left\langle \frac{H_N - (\mathbf{s} \cdot \mathbf{n})_+}{\sin \theta_k} \right\rangle_+ = \left\langle \frac{H_N - (s_N)_+}{\sin \theta_k} \right\rangle_+ = A_{0k} \left\langle 1 - \left\langle \frac{s_N}{H_N} \right\rangle_+ \right\rangle_+ \quad (5.24)$$

where H_N is the total height of the asperities (Fig. 5.7b) and A_{0k} is the initial microplane area, in turn, given by the following Eq. (5.25):

$$A_{0k} = \frac{H_N}{\sin \theta_k} \quad (5.25)$$

Thus, the area fraction, γ_k , considering the current contact area of the k^{th} microplane, becomes:

$$\gamma_k = \frac{A_k}{A_p} = \frac{A_{0k}}{A_p} \left\langle 1 - \left\langle \frac{s_N}{H_N} \right\rangle_+ \right\rangle_+ = \gamma_{0k} \mathcal{A}_g \left(\frac{s_N}{H_N} \right) \quad \text{where } \mathcal{A}_g = \langle 1 - \langle x \rangle \rangle \quad (5.26)$$

5.2.1.1.2 Modelling of interlocking degradation

The progressive interlocking reduction originated in the k^{th} microplane due to the asperities degradation is addressed by an exponential law that relates the current value of the microplane inclination angle, θ_k , to the frictional work, ζ_k , spent in sliding along the local tangential direction (\mathbf{t}_k) since the beginning of the analysis. Eq. (5.27) gives the value of θ_k , while the frictional work, ζ_k , is given by Eq. (5.28):

$$\theta_k = (\theta_{k0} - \theta_{kf}) e^{-\zeta_k / \zeta_{k0}} + \theta_{kf} \quad (5.27)$$

$$\zeta_k = \int_{\text{history}} \sigma_{kt} ds_{kf} \quad (5.28)$$

where:

- θ_{k0} → initial inclination angle of the k^{th} microplane, i.e. at the beginning of the analysis;
- θ_{kf} → final inclination angle of the k^{th} microplane, i.e. value asymptotically approached when ζ_k tends to infinity;
- ζ_{k0} → characteristic energy value controlling the rate of degradation.

In this model the variation of area fractions induced by change in θ_k are neglected, and parameters $\hat{\gamma}_{0k}$ are kept constant.

5.2.2 Enhanced degrading M-CZM

The model presented in (Serpieri et al., 2015a) considers the asperities degradation by updating the current value of the microplanes inclination angle θ_k . However, the depth of the asperities H_N is kept constant during the analysis. At each step the reduction in the contact area is taken into account by subtracting the normal component of the macro-displacement ($\mathbf{s} \cdot \mathbf{N} = s_N$) from the value of H_N , which is always equal to the initial one (Figs. 5.8a and 5.8b). The modified M-CZM is hereafter referred to as *enhanced degrading M-CZM*.

The first modification here proposed consists of considering the asperities depth not constant during the analysis, but varying according to the microplanes inclination angle degradation. Therefore, the degradation of the asperities is enhanced in this model.

For the microplanes characterised by the condition $\theta_k \neq 0$, and by assuming an initial asperities depth associated to the k^{th} microplane (H_{N0k}), the current value of H_{Nk} is given by Eq. (5.29):

$$H_{Nk} = H_{N0k} \frac{\tan \theta_k}{\tan \theta_{k0}} \quad (5.29)$$

Eq. (5.29) provides, at each step, the current value of the asperities depth, which is then used to compute the reduction in contact area as in the M-CZM formulation (Fig. 5.8c).

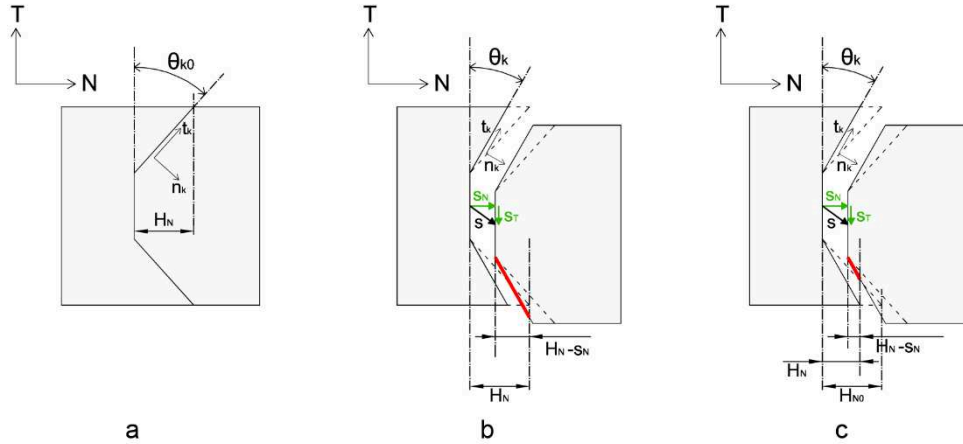


Figure 5.8 - a) RIA initial configuration; RIA deformed configuration: b) reduction in contact area depending on the opening displacement with H_N kept constant; and c) H_N is updated according to θ_k degradation law and then the reduction in contact area is computed

The M-CZM assumes three microplanes, each of them with the same area fraction equal to 1/3 (Fig. 5.9a). With reference to the case of the same microplanes number ($N_p=3$), the enhanced degrading M-CZM, instead, considers different area fractions (γ_k) for the microplanes (Fig. 5.9b), thus enhancing the flexibility of the model and especially giving the opportunity to attribute more or less ‘importance’ to the inclined microplanes (Figs. 5.9c and 5.9d, respectively).

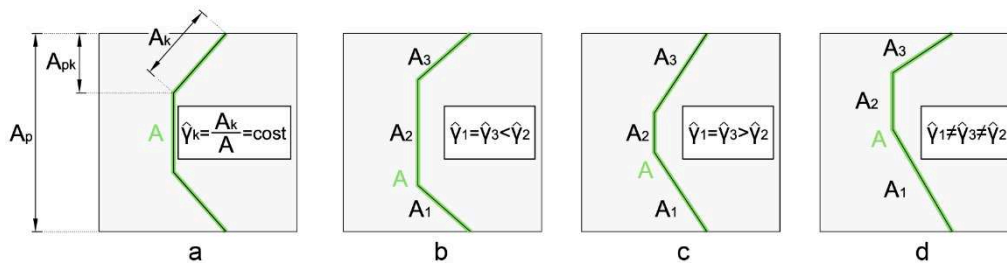


Figure 5.9 - a) M-CZM with constant area fractions among the microplanes; e) b) higher area fraction for the horizontal microplane; c) higher area fractions for the inclined microplanes; and d) different area fractions among the microplanes

The enhanced degrading M-CZM has been implemented in a user-subroutine (USERCZM) in the FE code ANSYS R16 (© ANSYS, 2015). The models employed (Figs. 4.1 and 4.2), the analysis settings and the bulk material properties the are those already shown in Chapter 4.

A scheme of the RIA with the three microplanes here adopted is presented in Fig. 5.10a. However, in order to understand the influence of the microplanes number, N_p , a RIA consisting of five microplanes (Fig. 5.10b) has also been considered.

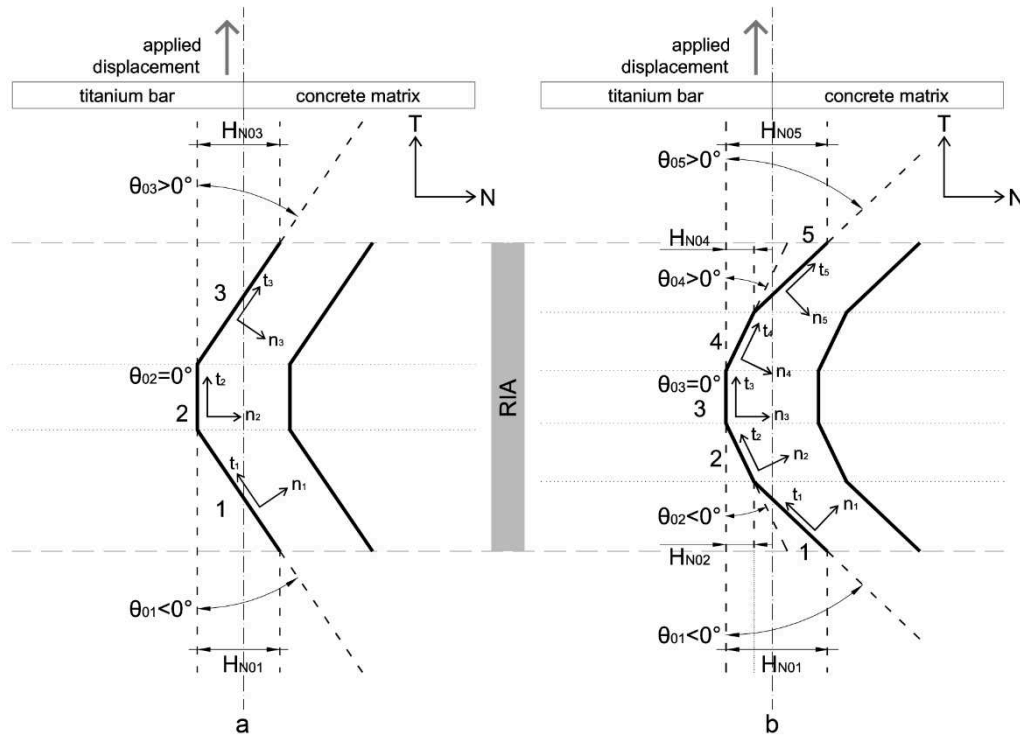


Figure 5.10 - RIA scheme: a) 3 microplanes; and b) five microplanes

Table 5.2 summarises all the parameters involved in the enhanced degrading M-CZM model, with their description and expression where needed.

Table 5.2 - Input parameters for the enhanced degrading M-CZM

Parameter	Unit	Expression	Description
G_{cn}	(kJ/m ²)	$G_{cn} = \frac{1}{2} \sigma_{0n} s_{cn}$	Fracture Energy Mode I (Normal)
G_{ct}	(kJ/m ²)	$G_{ct} = \frac{1}{2} \sigma_{0t} s_{ct}$	Fracture Energy Mode II (Tangential)
σ_{0n}	(MPa)		Maximum Cohesive Traction Mode I (Normal)

Parameter	Unit	Expression	Description
σ_{0t}	(MPa)		Maximum Cohesive Traction Mode II (Tangential)
η	(-)	$\eta = 1 - \frac{s_{0n}}{s_{cn}} = 1 - \frac{s_{0t}}{s_{ct}}$	Coefficient that controls the ratio between the displacement at complete debonding and its value at maximum cohesive traction
μ	(-)		Friction Coefficient
$\hat{\gamma}_{0k}$	(%)		Initial area fraction of the k^{th} microplane
θ_{0k}	(deg)		Initial inclination angle of the k^{th} microplane
θ_{fk}	(deg)		Final inclination angle of the k^{th} microplane
ζ_{0k}	(kJ/m ²)		Characteristic energy value controlling the rate of degradation on the k^{th} microplane
H_{N0k}	(mm)		Initial depth of asperities on the k^{th} microplane

5.3 Numerical results and discussion

The results of the numerical analyses are reported in this section. First of all, a typical response curve obtained by employing the enhanced degrading M-CZM in correspondence of the bar-matrix interface, is presented in order to:

- understand if the enhanced degrading M-CZM is able to describe the progressive failure of the interface under pull-out conditions, and how it works;
- verify which micro-mechanisms, among those included in the enhanced degrading M-CZM, have an actual role during the interface failure;
- understand how the interfacial micro-mechanisms affect the overall system response;
- compare the results obtained by using (i) a CZM that does not consider a micro-patterned interface, (ii) the M-CZM original formulation; and (iii) the enhanced degrading M-CZM.

For these scopes, one of the analysed case (i.e. the model with $\phi 16$ mm bar embedded in NWC) is taken as reference and an initial set of values for the model parameters is chosen (Table 5.4). Initially, a three-portioned RIA scheme is assumed (3 microplanes, according Fig. 5.10a), with each microplane having the same area fraction equal to 1/3. As for the proper fracture parameters (i.e. fracture energy, maximum cohesive traction and ratio of slip at maximum cohesive traction to slip at complete debonding), the parameters identified by using the bilinear CZM formulated by Alfano and Crisfield (Alfano and Crisfield, 2001) are employed (see Chapter 3). Notice that, with the enhanced degrading M-CZM, it is possible to take the same fracture energy (G_c) and the same maximum cohesive traction (σ_0) for both modes I and II (Serpieri et al., 2015b). This is because the increase of total energy dissipated per unit of new cracked energy with increase in mode II/mode I ratio is the result of the interplay between damage, friction and geometry of the asperities. In other

words, the larger the mode II/mode I ratio, the more is the energy dissipated through friction which is added to that dissipated due to loss of cohesion.

Table 5.3 - Initial set of enhanced degrading M-CZM input parameters

Parameter	Unit	Value	Comments
G_c	(kJ/m ²)	0.925	The values of these parameters are derived from the analyses carried out by employing the bilinear CZM (Alfano and Crisfield, 2001)
σ_0	(MPa)	1.85	
η	(-)	0.55	
μ	(-)	0.50	A typical value of the static friction coefficient for steel-concrete interface varies between 0.57 and 0.70 (Rabbat and Russell, 1985). A lower value is initially employed for the titanium-concrete interface.
$\hat{\gamma}_{01} = \hat{\gamma}_{02} = \hat{\gamma}_{03}$	(%)	33.33	Same area for all the microplanes.
θ_{01}	(deg)	-40	The symmetry between microplanes 1 and 3 is kept in terms of inclination angles and characteristic energy value. Microplane 2 is parallel to the interface.
θ_{f1}	(deg)	-2	
ζ_{01}	(kJ/m ²)	3.35	
θ_{02}	(deg)	0	The final microplanes inclination angle is equal to 2°, thus this means that the interface is not completely flattered at the end of the analysis.
θ_{f2}	(deg)	0	
ζ_{02}	(kJ/m ²)	0	
θ_{03}	(deg)	40	The initial depth of asperities is assumed equal for all the microplanes.
θ_{f3}	(deg)	-2	
ζ_{03}	(kJ/m ²)	3.35	
$H_{N01} = H_{N02} = H_{N03}$	(mm)	0.010	

5.3.1 Characteristics of pull-out response with the enhanced degrading M-CZM

Fig. 5.11 reports the numerical response curve obtained by using the FE model of Fig. 4.2 of Chapter 4 of the present thesis, and applying the enhanced degrading M-CZM with the parameter values of Table 5.3.

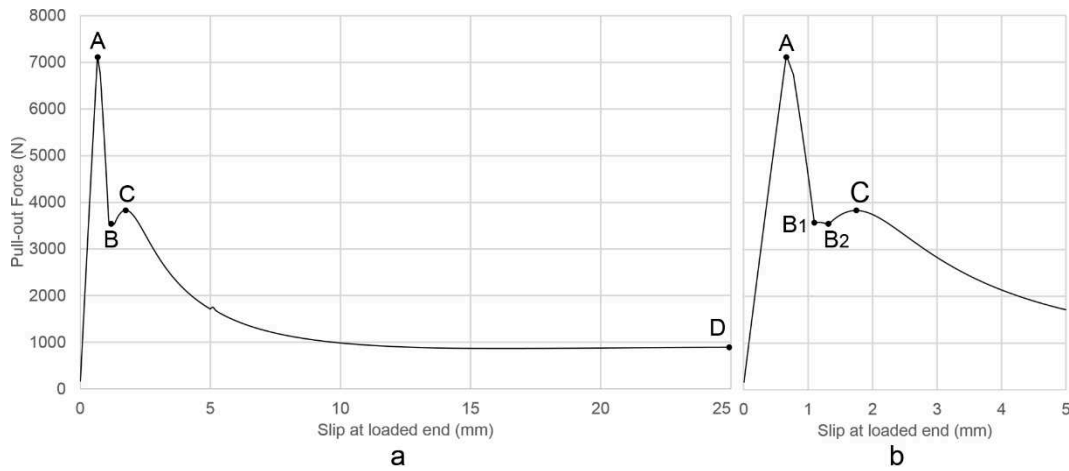


Figure 5.11 - Typical pull-out curve obtained by employing the enhanced degrading M-CZM: a) whole curve; and b) enlargement on the first 5 mm of slip

From Fig. 5.11a it is possible to observe the characteristic shape that assumes the pull-out response curve by employing the enhanced degrading M-CZM. The curve is characterised by an initial linear branch up to the maximum pull-out load (point A), which is followed by an immediate drop down to a first residual value (point B). Then, the pull-out force increases again and reaches a second local maximum (point C) and, afterwards, it gradually decreases approaching the final residual value (point D). When enlarging the graph (Fig. 5.11b), it is possible to recognise two distinct points in proximity of point B, namely B1 and B2. In order to understand how the damage evolves on the three microplanes, the damage variable, D_k (Eq. (5.18)), trend has been tracked, by computing its value in the most significant substeps. The substeps belonging to the main two loadsteps in which the analysis has been subdivided (see Fig. 4.5 of Chapter 4), are identified in Fig. 5.12. The evolution of the damage variable during the analysis is provided in Fig. 5.13.



Figure 5.12 - Identification of the most significant substeps

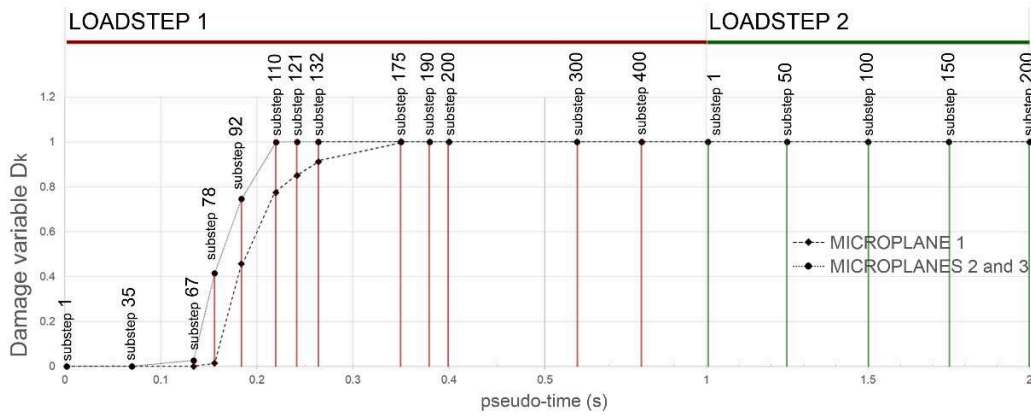


Figure 5.13 - Damage variable trend on the three microplanes

A scheme of the progressive loss of adhesion on the three microplanes, associated with the damage evolution, is reported in Fig. 5.14. At the beginning, there is complete adhesion at the interface (Fig. 5.14a). Then, the force drop after the peak (substep 110) corresponds to the breakage of the microplanes 2 and 3 (Fig. 5.14b). At this stage, in fact, D_k reaches the maximum value (i.e. 1) for microplanes 2 and 3 ($D_2=D_3=1$), but there still is adhesion on microplane 1 (i.e. $D_1 < 1$) (Fig. 5.13). This promotes a new increasing in the pull-out force until a second maximum (substep 175), which can be either local or global. At substep 175, adhesion is lost also on microplane 1 (Fig. 5.14c), thus the pull-out force starts to decrease gradually and D_1 reaches the maximum value 1 also on microplane 1.

During the loadstep 2, the interface is fully damaged (i.e. $D_k=1$ on all the microplanes). Thus, at this stage the pull-out force gradual decreasing depends only on the degradation of the inclination angle and the asperities depth of microplane 1. The evolutions of the

inclination angle (θ_1) and the asperities depth (H_{N1}) on microplane 1, are reported in Fig. 5.15a and 5.15b, respectively.

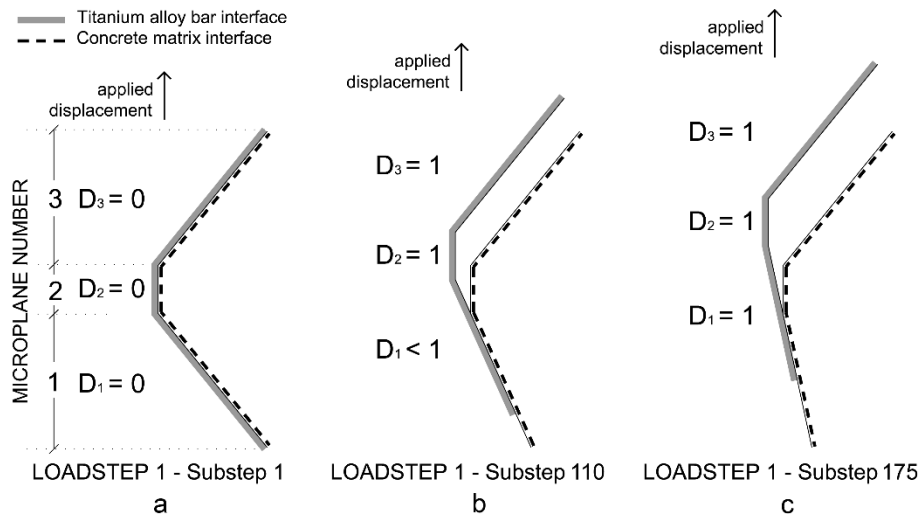


Figure 5.14 - Progressive loss of adhesion on the RIA microplanes during loadstep 1: a) substep 1; b) substep 110; and c) substep 175

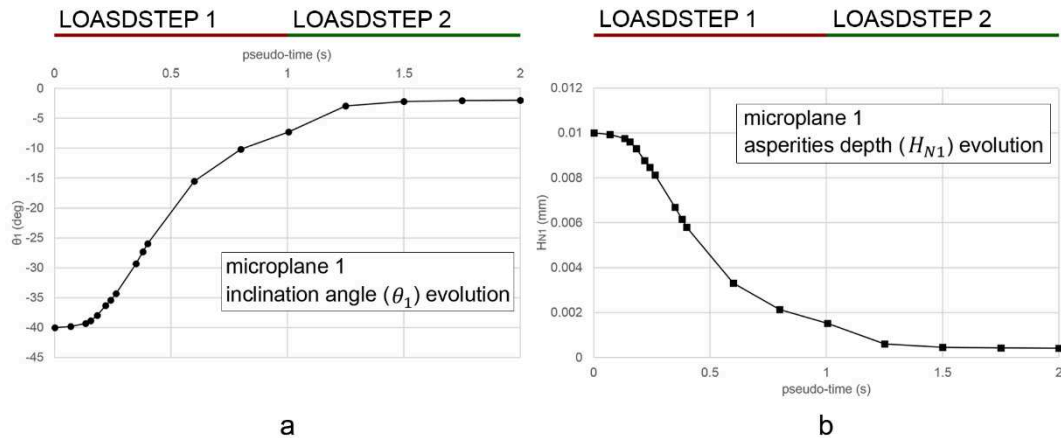


Figure 5.15 - Evolution of: a) inclination angle (θ_1); and b) asperities depth (H_{N1}) on microplane 1 during loadsteps 1 and 2

The decomposition of each point of the interface into a certain number of microplanes allows for the simulation of the fracture process in a progressive way. This seems to be consistent with the experimental curves obtained from the tests, suggesting that the interface fracture is a gradual process that does not involve simultaneously the whole interface and makes the pull-out force to decrease slowly to a residual value.

The importance of the multiplane approach is demonstrated in the next paragraph, where the results obtained by employing the enhanced degrading M-CZM and the same model without the multiplane description of the interface, are compared.

5.3.2 Influence of the multiplane-structure of the interface

The influence of the multiplane structure of the interface is investigated in this paragraph, in order to verify how this kind of approach leads to a better description of the interface failure under pull-out conditions. Fig. 5.16 shows the comparison between the response curves obtained by employing the enhanced degrading M-CZM with the input parameter values reported in Table 5.3, the same model without the microplane-structure of the interface (i.e. where the inclination angles of all the microplanes are equal to zero) and with the other parameter values fixed, and the experimental pull-out curve of the specimen N/16-2 (see Chapter 3).

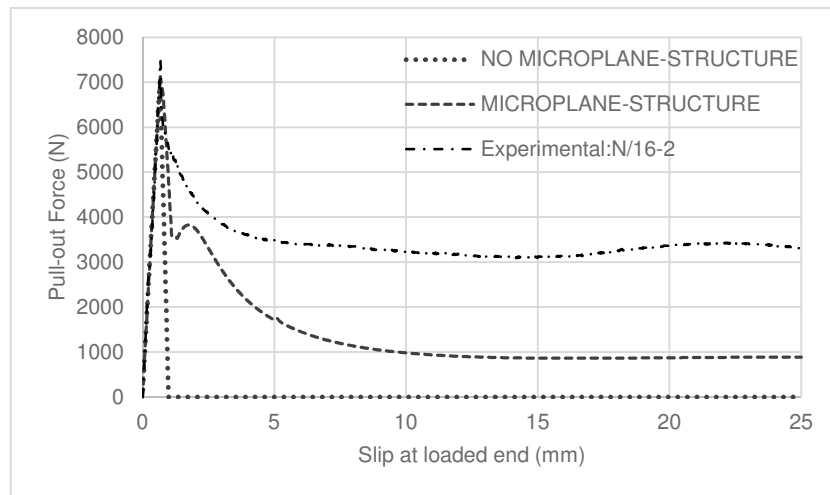


Figure 5.16 - Influence of the microplane-structured interface

Under pull-out conditions, without a lateral pressure and in the case of plain rebars, the normal stresses at the interface are almost equal to zero. Thus, frictional forces cannot develop and this does not represent the experimental results here obtained. The microplane-structure of the interface allows for describing the irregular interface originated during pull-out due to the bar roughness and the residual concrete material locally attached to the bar surface. This dilatancy effect is captured only by introducing the elementary planes. Moreover, their presence guarantees for a gradual decreasing of the pull-out force, which has been actually observed in the experiments and can be explained by the combination between the progressive reduction of the embedment length and the rupture of the asperities due to the forced sliding of the bar inside the concrete channel.

To reach a satisfactory agreement between the numerical and experimental curves, it is necessary to carry out an identification procedure to estimate the most suitable values of the model parameters. This will be done in the forthcoming paragraphs, while in the next

one a comparison between the response curves obtained by describing the interface failure with the M-CZM proposed in (Serpieri et al., 2015a) and the enhanced degrading M-CZM, is made in order to evaluate the contribution provided by the further degradation process here proposed.

5.3.3 Contribution of the degradation of the asperities depth

In this paragraph the comparison between the response curves obtained by using the M-CZM formulated by Serpieri et al. in (Serpieri et al., 2015a) and the enhanced degrading M-CZM here proposed, is presented. The values of the parameters are those summarized in Table 5.3 for both the models.

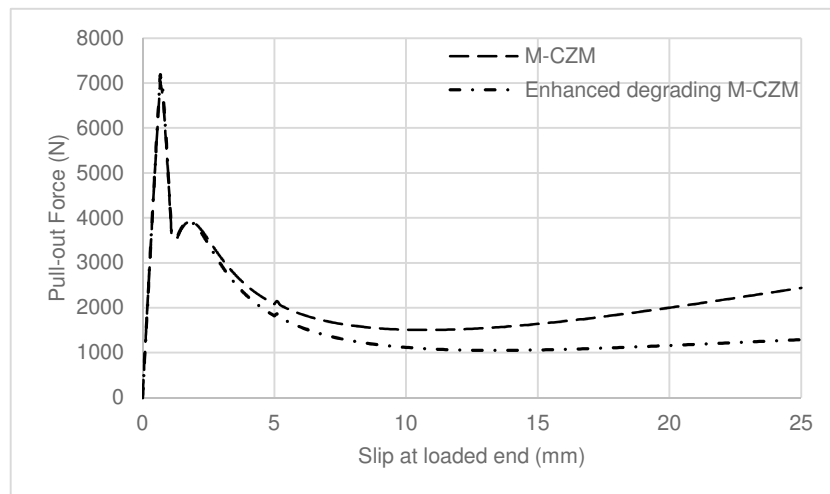


Figure 5.17 - Comparison between the response curves obtained by using the M-CZM (Serpieri et al., 2015a) and the enhanced degrading M-CZM

From Fig. 5.17 it is possible to see how the degradation of the asperities depth introduced in the enhanced degrading M-CZM affects the pull-out curve response. Without considering the further degradation process, the pull-out force tends to increase with growing slip. This is actually correct from the numerical point of view, because the micromechanics-based CZM does not update the pairing of contact surfaces on the interface in the deformed configuration. Therefore, when the interface length is progressively reduced (i.e. for growing values of the slip), the numerical model cannot account for the reduction of the bond length. However, when the degradation of the asperities depth is considered, according with the microplanes inclination angle degradation, the flatter of the fracture surface is better captured and the effect of the interface length reduction is less significant, even though it is still present.

To account for the interface length progressive reduction when numerical and experimental curves are compared, the final numerical reaction force F is scaled through Eq. (5.30).

$$F = F_{measured} \frac{\text{interface length} - \text{current slip}}{\text{interface length}} \quad (5.30)$$

5.3.4 Sensitivity analysis and identification

Several sensitivity analyses were performed to evaluate the influence that each model parameter has on the overall system response. Particularly, sensitivity to the microplanes number, N_p , constituting the RIA and to the area fraction of each microplane, $\hat{\nu}_{0k}$, is preliminary analysed to establish the RIA characteristics to adopt for the subsequent analyses. For these analyses, only the results concerning the model with $\phi 16$ mm bar embedded in NWC are reported. Once a suitable RIA scheme has been assumed, sensitivity to the remaining model parameters is checked. After each analysis, the most suitable value for the investigated parameter is chosen in order to fit the experimental curves, for the models with $\phi 16$ mm bars embedded in both NWC and LWC. Thus, the identification procedure is carried out simultaneously with each sensitivity analysis. The values of the parameters obtained from the identification procedure are then introduced in the FE models with $\phi 8$ mm rebars, and the resulting numerical responses are compared with the experimental ones. This phase represents the validation of the enhanced degrading M-CZM, which generalises its application.

Sensitivity analyses and identification involve those parameters mostly affecting the post-peak response. In fact, concerning the linear and the immediate post-peak branches, with the bilinear CZM (Alfano and Crisfield, 2001) it was already possible to capture the maximum cohesive traction and the correspondent slip value. The calibration of these parameters, the fracture energy and the ratio between the slip at maximum traction and the slip at the complete debonding has led to the values summarised in Table 5.4, for NWC and LWC respectively.

Table 5.4 - Fixed input parameters for the enhanced degrading M-CZM

Parameter	Unit	Value	
		NWC	LWC
G_{cn}	(kJ/m ²)	0.925	1.50
G_{ct}	(kJ/m ²)	0.925	1.50
σ_{0n}	(MPa)	1.85	2.80
σ_{0t}	(MPa)	1.85	2.80
η	(-)	0.55	0.40

In all the following analyses the response of the interface model is evaluated in terms of pull-out force-slip curves and compared to the obtained experimental results. The parameters reported in Table 5.4 are kept constant, while the other parameters involved in the model have been varied to understand their contribution.

5.3.4.1 Preliminary sensitivity analyses

The influence of the RIA microplanes number and of the area fraction assigned to each microplane is here checked through two preliminary sensitivity analyses. To this end, the model with $\phi 16$ mm bar embedded in NWC is taken as example. Thus, the fixed parameters

in this case are summarised in the third column of Table 5.4, while the values of the other model parameters are specified for each analysis.

5.3.4.1.1 Sensitivity to the microplanes number

Two analyses are performed considering three and five microplanes constituting the RIA, as shown in Figs. 5.10a and 5.10b, respectively. In order to evaluate only the influence of the microplanes number (N_p), the area fraction of each microplane is equal to 1/3 and 1/5 for the 3- and 5-microplanes RIA. Moreover, since the microplanes discretisation of the RIA is an approximation of the real interface, it has been considered reasonable to keep the symmetry in terms of microplanes inclination angles. Thus, for each RIA scheme, i.e. 3 and 5 microplanes, the inclined microplanes are symmetric with respect to the horizontal plane (see Fig. 5.10).

The fixed values of the model parameters related to the NWC (third column of Table 5.4) are adopted for the analysis, while the values of the other variable parameters involved in analysis are summarised in Table 5.5, for a RIA consisting of 3 and 5 microplanes, respectively. The obtained response curves are presented in Fig. 5.18.

Table 5.5 - Enhanced degrading M-CZM input parameters for sensitivity analysis to N_p

3 microplanes			5 microplanes		
Parameter	Unit	Value	Parameter	Unit	Value
θ_{01}	(deg)	-40	θ_{01}	(deg)	-40
θ_{f1}	(deg)	0	θ_{f1}	(deg)	0
ζ_{01}	(kJ/m ²)	3.35	ζ_{01}	(kJ/m ²)	3.35
H_{N01}	(mm)	0.015	H_{N01}	(mm)	0.015
θ_{02}	(deg)	0	θ_{02}	(deg)	-20
θ_{f2}	(deg)	0	θ_{f2}	(deg)	0
ζ_{02}	(kJ/m ²)	0	ζ_{02}	(kJ/m ²)	3.35
H_{N02}	(mm)	0	H_{N02}	(mm)	0.015
θ_{03}	(deg)	40	θ_{03}	(deg)	0
θ_{f3}	(deg)	0	θ_{f3}	(deg)	0
ζ_{03}	(kJ/m ²)	3.35	ζ_{03}	(kJ/m ²)	0
H_{N03}	(mm)	0.015	H_{N03}	(mm)	0
			θ_{04}	(deg)	20
			θ_{f4}	(deg)	0
			ζ_{04}	(kJ/m ²)	3.35
			H_{N04}	(mm)	0.015
			θ_{05}	(deg)	40
			θ_{f5}	(deg)	0
			ζ_{05}	(kJ/m ²)	3.35
			H_{N05}	(mm)	0.015

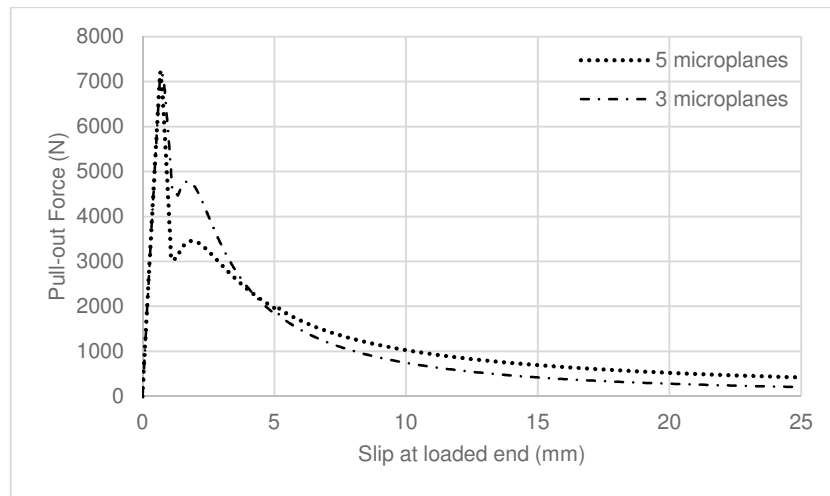


Figure 5.18 - Sensitivity to N_p : pull-out curves for the model with $\phi 16$ mm and NWC obtained by using a RIA consisting of 3 and 5 microplanes

By considering a RIA consisting of 5 microplanes, the first linear branch and the peak force of the response curve match the case of the 3 microplanes RIA. The immediate post-peak residual force and the second local maximum characterising the curve response shape, instead, are significantly lower than those obtained by adopting 3 microplanes. However, the curve shapes are very similar, being both of them characterised by a linear branch up to the maximum pull-out load, a sudden drop down to a residual value, a new increasing up to a local maximum and, afterward, a decreasing branch.

For this reason, it has been chosen to adopt a 3 microplanes RIA, which allows for a smaller number of input variables. This means that a three-portioned RIA is sufficiently accurate to describe the pull-out mechanism, while maintaining a reduced number of input parameters. Therefore, a RIA constituted by three microplanes has been adopted for all the following sensitivity analyses.

5.2.3.1.2 Sensitivity to the microplanes area fractions

In order to verify the influence of the area fractions of the microplanes into the final response curve, three cases have been analysed: the first one considers the same area fraction for each microplane, in the second case the area of the horizontal elementary plane is higher than that corresponding to each inclined plane, and, finally, the third case analyses a RIA in which the inclined microplanes have greater area fractions than that attributed to the plane parallel to the interface (i.e. microplane 2). The area fractions corresponding to the inclined microplanes are equal, in order to maintain the symmetry with respect to the horizontal microplane. The input parameter values are summarised in the third column of Table 5.4 (fixed parameter values for NWC) and in the following Table 5.6, and the results concerning the model with the $\phi 16$ mm bar embedded in NWC are reported in Fig. 5.19.

Table 5.6 - Enhanced degrading M-CZM input parameters for sensitivity analysis to $\hat{\gamma}_{0k}$

Parameter	Unit	Value			
θ_{01}	(deg)	-40			
θ_{f1}	(deg)	0			
ζ_{01}	(kJ/m ²)	3.35			
H_{N01}	(mm)	0.015			
			Case 1	Case 2	Case 3
$\hat{\gamma}_{01}$	(%)	33.33	33.33	7.5	42.5
θ_{02}	(deg)	0			
θ_{f2}	(deg)	0			
ζ_{02}	(kJ/m ²)	0			
H_{N02}	(mm)	0			
			Case 1	Case 2	Case 3
$\hat{\gamma}_{02}$	(%)	33.33	33.33	85	15
θ_{03}	(deg)	40			
θ_{f3}	(deg)	0			
ζ_{03}	(kJ/m ²)	3.35			
H_{N03}	(mm)	0.015			
			Case 1	Case 2	Case 3
$\hat{\gamma}_{03}$	(%)	33.33	33.33	7.5	42.5

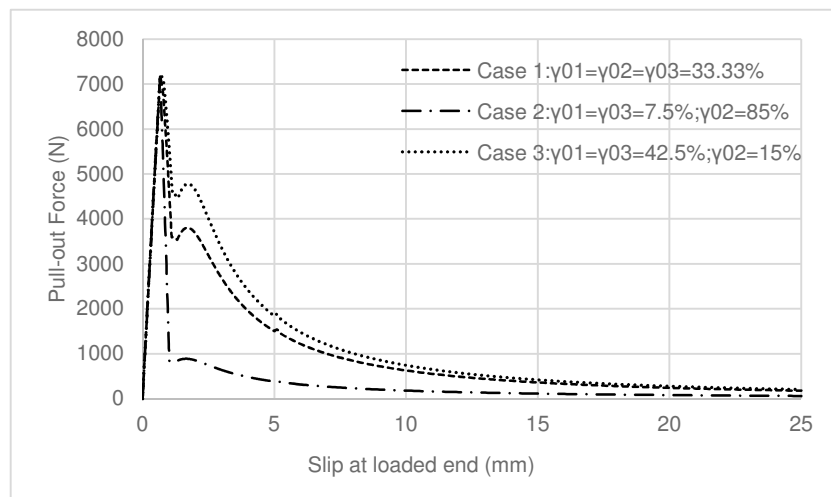


Figure 5.19 - Sensitivity to $\hat{\gamma}_{0k}$: pull-out curves for the model with $\phi 16$ mm and NWC obtained by using three combination of area fractions

By varying the area fractions of the three microplanes, it is possible to obtain different response curves especially in terms of residual pull-out force value immediately after the post-peak drop. When the inclined microplanes occupy, in total, 85% of the RIA area (i.e. case 3), the pull-out force after the drop is the highest among the analysed cases. This allows for obtaining a sufficiently high residual force without increasing too much the

initial inclination angles of the microplanes, thus case 2 represents the area fractions combination chosen for all the following analyses.

In all the following sensitivity and identification analyses, a RIA consisting of three microplanes, characterised by a smaller area fraction for the horizontal plane ($\hat{\gamma}_{02}=15\%$) and higher area fractions for the inclined microplanes ($\hat{\gamma}_{01}=\hat{\gamma}_{03}=42.5\%$), is adopted.

5.3.4.2 Sensitivity to initial microplanes inclination angle and identification

In this paragraph, the attention has been focused on the influence of the initial inclination angle of the microplanes, considering the final one equal to zero. In particular, the angle that has been varied is $\theta_{01}=-\theta_{03}$, while $\theta_{02}=0$. For this reason, in this section the variation parameter is called θ_0 , which corresponds to the modulus of θ_{01} and θ_{03} . Table 5.4 summarises the values of the fixed parameters for NWC and LWC, while the following Table 5.7 reports the values of the other input parameters adopted for the sensitivity analysis to θ_0 . Figs. 5.11a and 5.11b show the response curves for NWC and LWC, respectively.

Table 5.7 - Enhanced degrading M-CZM input parameters for sensitivity analysis to θ_0

Parameter	Unit	Value	
		NWC	LWC
θ_{01}	(deg)	VARIABLE	VARIABLE
θ_{f1}	(deg)	0	0
ζ_{01}	(kJ/ m ²)	3.35	3.35
H_{N01}	(mm)	0.015	0.015
θ_{02}	(deg)	0	0
θ_{f2}	(deg)	0	0
ζ_{02}	(kJ/ m ²)	0	0
H_{N02}	(mm)	0.015	0.015
θ_{03}	(deg)	VARIABLE	VARIABLE
θ_{f3}	(deg)	0	0
ζ_{03}	(kJ/ m ²)	3.35	3.35
H_{N03}	(mm)	0.015	0.015
μ	(-)	0.50	0.50

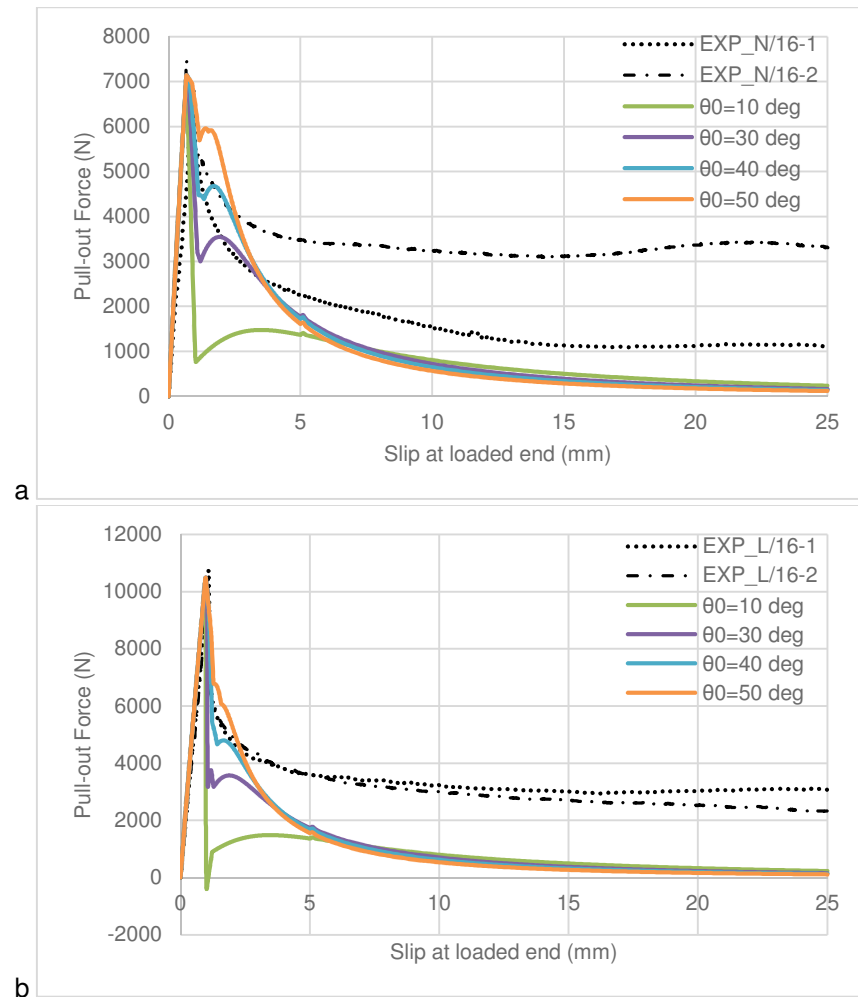


Figure 5.20 - Sensitivity to θ_0 : a) NWC; b) LWC

From Fig. 5.20 it is possible to observe that θ_0 influences the residual pull-out force value after the sudden drop caused by the partial loss of adhesion. Starting from this value the pull-out force tends to increase again, reaching a local maximum and, afterwards it decreases according to the exponential degradation law for θ_k and tends to zero. This aspect, which is expected by taking $\theta_f=0$, clearly does not represent the real system behaviour, which exhibits a significant residual value of the pull-out force.

For both NWC (Fig. 5.20a) and LWC (Fig. 5.20b) the most suitable initial microplane inclination angle value is 50 deg. Thus this value has been adopted for the following analyses. It will be shown later how better correlation with the shape of the experimental curve can be obtained by calibrating the parameter ζ_{0k} corresponding to the characteristic energy value.

5.3.4.3 Sensitivity to final microplanes inclination angle and identification

The parameter here considered in the sensitivity analysis is the final microplanes inclination angle. Also in this case the angle that has been varied is $\theta_{f1} = -\theta_{f3}$, whose modulus is referred to as θ_f , while $\theta_{f2} = 0$. Table 5.4 reports the enhanced degrading M-CZM fixed input parameters and Table 5.8 summarises those for the sensitivity analysis to θ_f . Figs. 5.21a and 5.21b show the related results for NWC and LWC, respectively.

Table 5.8 - Enhanced degrading M-CZM input parameters for sensitivity analysis to θ_f

Parameter	Unit	Value	
		NWC	LWC
θ_{01}	(deg)	-50	-50
θ_{f1}	(deg)	VARIABLE	VARIABLE
ζ_{01}	(kJ/ m ²)	3.35	3.35
H_{N01}	(mm)	0.015	0.015
θ_{02}	(deg)	0	0
θ_{f2}	(deg)	0	0
ζ_{02}	(kJ/ m ²)	0	0
H_{N02}	(mm)	0.015	0.015
θ_{03}	(deg)	50	50
θ_{f3}	(deg)	VARIABLE	VARIABLE
ζ_{03}	(kJ/ m ²)	3.35	3.35
H_{N03}	(mm)	0.015	0.015
μ	(-)	0.50	0.50

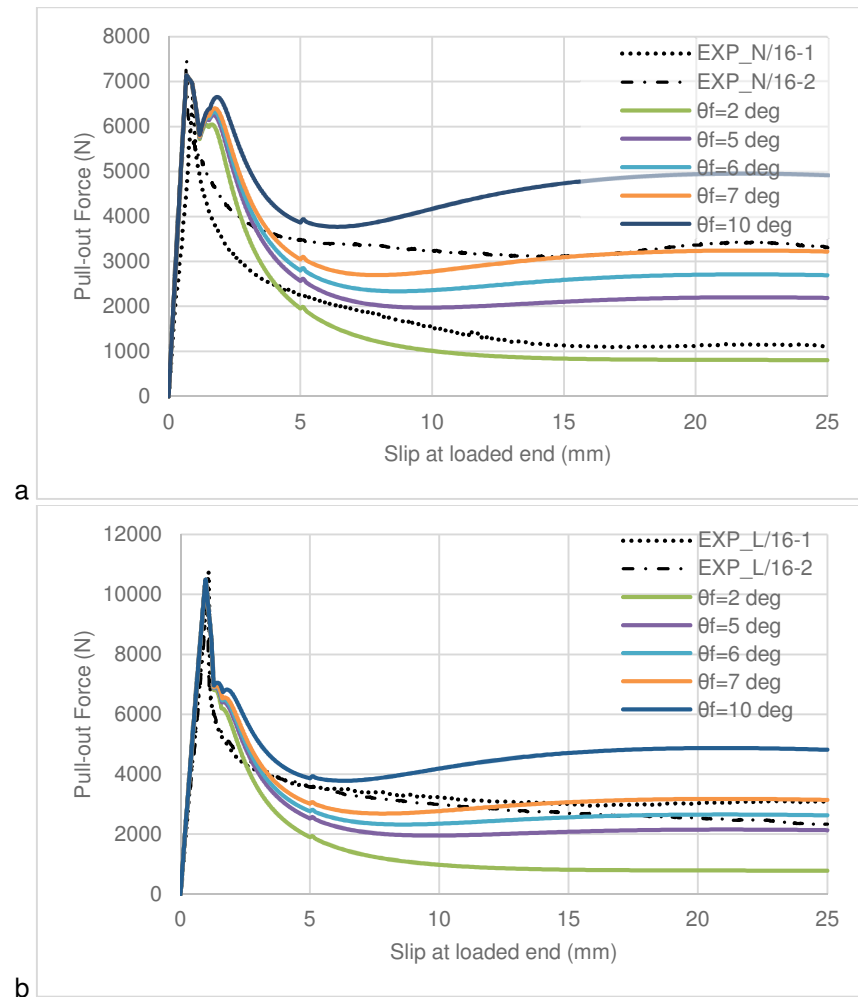


Figure 5.21 - Sensitivity to θ_f : a) NWC; b) LWC

By keeping fixed the initial microplane inclination angle and varying the final one, FE analyses provide the results presented in Fig. 5.21. It is possible to notice that θ_f variation affects mostly the system response starting from the second local maximum. For growing θ_f , the pull-out force value tends to be higher, making possible to identify the final inclination angle that better matches the residual pull-out force value obtained from the experimental investigation.

Fig. 5.21a shows the results obtained for NWC, where a θ_f value of about 5 deg seems to be a good compromise among the two experimental curves, which actually exhibit a significant scatter. In the case of LWC (Fig. 5.21b) the final microplane inclination angle value that better represent the experimental curves is around 6 deg. These values are thus adopted for the following analyses.

5.3.4.4 Sensitivity to characteristic energy value and identification

The influence of the characteristic energy value ζ_0 is investigated in this paragraph. Afterwards, its value for NWC and LWC is found through the identification procedure. In Tables 5.4 and Table 5.9 the enhanced degrading M-CZM input parameters for the sensitivity analysis to ζ_0 are summarised, while its results are shown in Figs. 5.22a and 5.22b for NWC and LWC.

Table 5.9 - Enhanced degrading M-CZM input parameters for sensitivity analysis to ζ_0

Parameter	Unit	Value	
		NWC	LWC
θ_{01}	(deg)	-50	-50
θ_{f1}	(deg)	-5	-6
ζ_{01}	(kJ/m ²)	VARIABLE	VARIABLE
H_{N01}	(mm)	0.015	0.015
θ_{02}	(deg)	0	0
θ_{f2}	(deg)	0	0
ζ_{02}	(kJ/m ²)	0	0
H_{N02}	(mm)	0.015	0.015
θ_{03}	(deg)	50	50
θ_{f3}	(deg)	5	6
ζ_{02}	(kJ/m ²)	VARIABLE	VARIABLE
H_{N03}	(mm)	0.015	0.015
μ	(-)	0.50	0.50

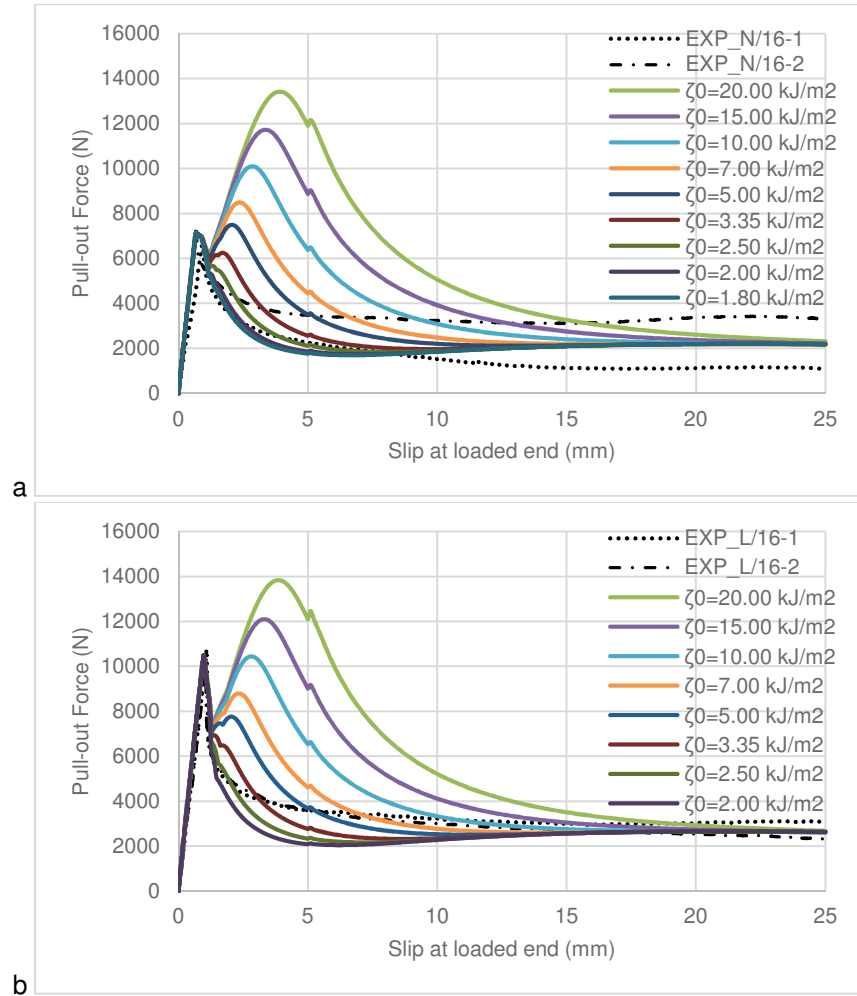


Figure 5.22 - Sensitivity to ζ_0 : a) NWC; b) LWC

The parameter ζ_0 strongly influences the shape of the system response curve in the post-peak area. From Fig. 5.22, it is possible to observe that for higher values of ζ_0 , after the post-peak drop, the pull-out force increases dramatically up to a second local (or global) maximum. This appears to be consistent with the physical meaning of ζ_0 which represents the energy value through which the RIA microplanes degrade. The higher the parameter ζ_0 is, the more energy is associated to the fracture of the RIA microplanes, resulting in response curves characterised by ‘bumps’ in correspondence of the fracture of each microplane. In fact, as it is underlined in Figs. 5.13 and 5.14, the pull-out force drop corresponds to the rupture ($D_2=D_3=1$) of the second and third microplanes, while the second local maximum and the following decrease is associated to the failure of the first

microplane ($D_1=1$). For greater values of ζ_0 the microplanes needs higher values of the pull-out force to fail.

Conversely, the experimental suggest that the interface failure is a gradual process that does not involve simultaneously the whole interface and makes the pull-out force decrease slowly to a residual value. In the numerical models, for both NWC and LWC, this can be represented through the parameter ζ_0 , whose value is identified in order to match the curve shape. In particular, for NWC (Fig. 5.22a) $\zeta_0=1.80$ kJ/m², while for LWC (Fig. 5.22b) $\zeta_0=2.50$ kJ/m².

5.3.4.5 Sensitivity to asperities depth and identification

The parameter whose influence has been investigated in this paragraph, is the initial asperities depth H_{N0} . The enhanced degrading M-CZM accounts for its degradation consistently with the microplane inclination angle decreasing law, thus the input parameter H_{N0} refers to its initial value. Figs. 5.23a and 5.23b present the results of the sensitivity analysis to H_{N0} for NWC and LWC, which has been carried out by adopting the enhanced degrading M-CZM parameters values collected in Tables 5.4 and 5.10.

Table 5.10 - Enhanced degrading M-CZM input parameters for sensitivity analysis to H_{N0}

Parameter	Unit	Value	
		NWC	LWC
θ_{01}	(deg)	-50	-50
θ_{f1}	(deg)	-5	-6
ζ_{01}	(kJ/m ²)	1.80	2.50
H_{N01}	(mm)	VARIABLE	VARIABLE
θ_{02}	(deg)	0	0
θ_{f2}	(deg)	0	0
ζ_{02}	(kJ/m ²)	0	0
H_{N02}	(mm)	VARIABLE	VARIABLE
θ_{03}	(deg)	50	50
θ_{f3}	(deg)	5	6
ζ_{03}	(kJ/m ²)	1.80	2.50
H_{N03}	(mm)	VARIABLE	VARIABLE
μ	(-)	0.50	0.50

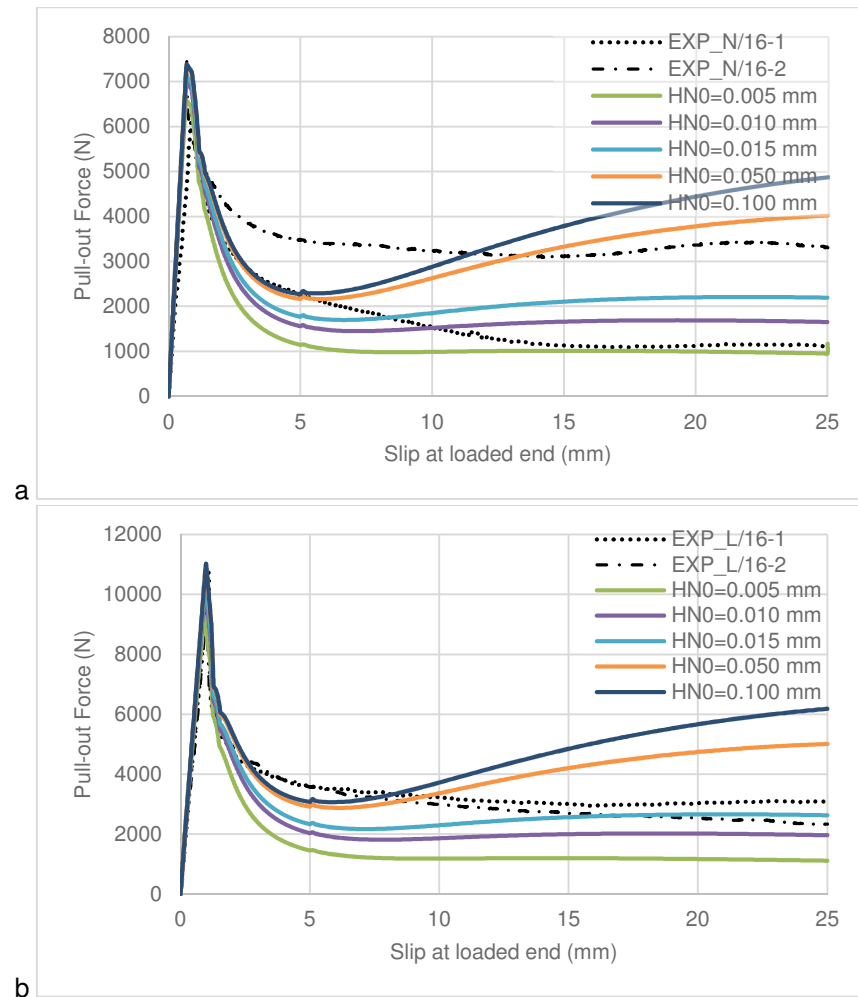


Figure 5.23 - Sensitivity to H_{N0} : a) NWC; b) LWC

Fig. 5.23 shows that the initial asperities depth slightly influences the force peak value in the linear branch, while it affects more significantly the final part of the curve. If H_{N0} is sufficiently high, it is possible to observe that the pull-out force starts to increase with growing slip values. Conversely, the experimental curves show a gradual decreasing trend of the pull-out force after the post-peak zone. This appears to be consistent with lower values of H_{N0} , which, moreover, are of the same magnitude of those observed with SEM analyses in Chapter 3 (i.e. 10-15 μm). In fact, from SEM analyses, it has been observed that after a slip equal to almost 55% of the bond length, the interface was dilated and the range of dimension was around 10-15 μm on average. The dilation of the interface can be attributed to the presence of some concrete material attached to the surface of the bar, which in turn, is caused by the bar roughness. Thus, the latter activates a sort of mechanical interlocking at the microscale level which is incremented by the presence of concrete

particles on the bar surface. These particles can be seen as asperities, which, under pull-out conditions, undergo rupture due to the forced sliding inside the concrete channel.

In this context, SEM analyses can be seen as a valid tool to measure the ‘scale’ of the problem, meaning that they provide information about the range of dimensions of the dilated interface and about the magnitude of the combination of surface roughness and residual concrete material attached to the bar surface, represented by the asperities depth investigated in this paragraph.

5.3.4.6 Sensitivity to friction coefficient and identification

The last parameter investigated is the friction coefficient, μ . Tables 5.4 and 5.11 collect the input values of the enhanced degrading M-CZM parameters used for this sensitivity analysis, whose results are reported in Figs. 5.24a and 5.24b for NWC and LWC, respectively.

Table 5.11 - Enhanced degrading M-CZM input parameters for sensitivity analysis to μ

Parameter	Unit	Value	
		NWC	LWC
θ_{01}	(deg)	-50	-50
θ_{f1}	(deg)	-5	-6
ζ_{01}	(kJ/m ²)	1.80	2.50
H_{N01}	(mm)	0.015	0.015
θ_{02}	(deg)	0	0
θ_{f2}	(deg)	0	0
ζ_{02}	(kJ/m ²)	0	0
H_{N02}	(mm)	VARIABLE	VARIABLE
θ_{03}	(deg)	50	50
θ_{f3}	(deg)	5	6
ζ_{03}	(kJ/m ²)	1.80	2.50
H_{N03}	(mm)	0.015	0.015
μ	(-)	0.50	0.50

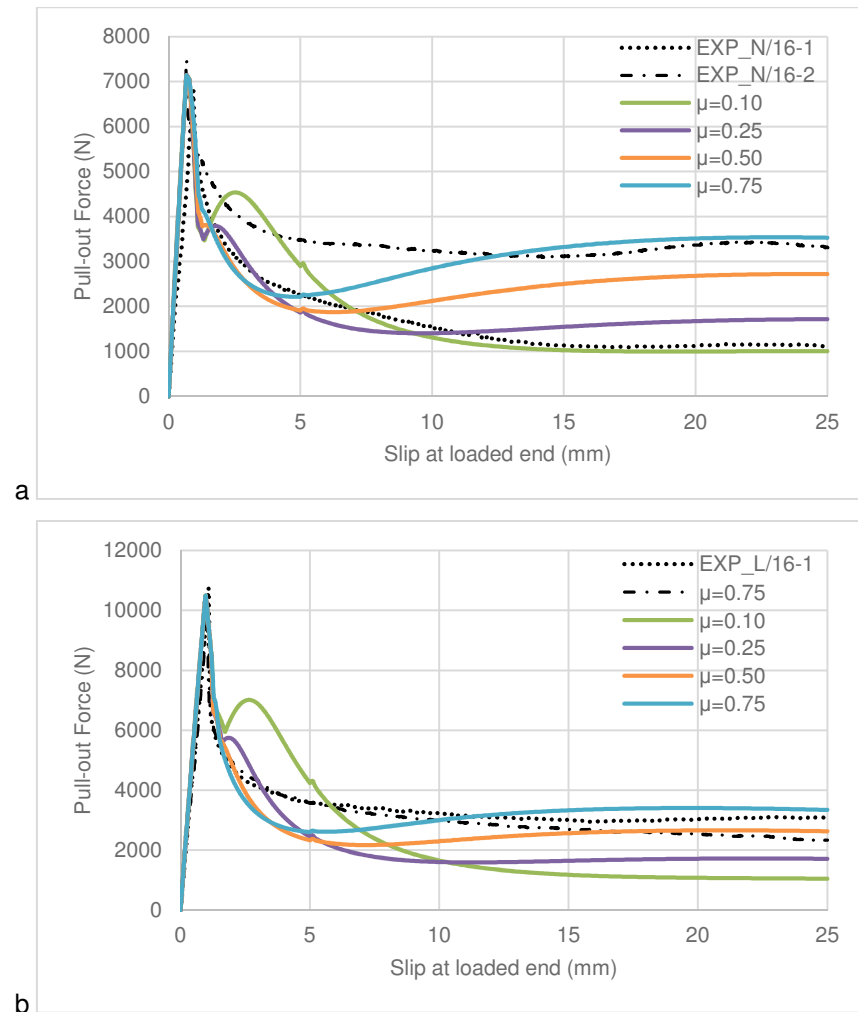


Figure 5.24 - Sensitivity to μ : a) NWC; b) LWC

The value of the friction coefficient, μ , obviously affects mostly the pull-out response after the post-peak drop. For lower values (i.e. $\mu=0.10$ and $\mu=0.25$) the pull-out force exhibits the typical bumps explained for the sensitivity analysis to ζ_0 , while its final residual value is lower than that experimentally measured. On the contrary, when higher values of the friction coefficient are chosen (i.e. $\mu=0.5$ and $\mu=0.75$), the shape of the response curve is similar to the experimental curves and the final pull-out force value matches those measured with the tests. Thus, the most suitable value for the friction coefficient, for both NWC and LWC, is 0.50. Even though no data have been found in the literature concerning the friction coefficient between titanium alloys and concrete, a friction coefficient of 0.50 seems to be a reasonable value since typical values of the friction coefficient for steel-to-concrete interface vary between 0.57 and 0.70 (Rabbat and Russell,

1985). Even though in this case the metallic surface is not made of steel, the comparison between bond strength of plain steel bars-to-concrete and plain Ti6Al4V bars-to-concrete resulted in similar values, and thus similar friction coefficients among the two interfaces can be hypothesised.

5.3.4.7 Results of the identification procedure

The identification procedure has been carried out simultaneously with the sensitivity analyses. This is because, after each sensitivity analysis, the most suitable and representative value has been identified and adopted for the following analyses. The results of this process are summarised in Table 5.12, where the final values of the enhanced degrading M-CZM parameters are reported. Then, Figs. 5.25 and 5.26 show the comparison between numerical and experimental curves for the $\phi 16$ mm rebars in the cases of NWC and LWC respectively.

Table 5.12 - Final values of enhanced degrading M-CZM input parameters after identification procedure

Parameter	Unit	Value	
		NWC	LWC
G_c	(kJ/m ²)	0.925	1.50
σ_0	(MPa)	1.85	2.80
η	(-)	0.55	0.40
θ_{01}	(deg)	-50	-50
θ_{f1}	(deg)	-5	-6
ζ_{01}	(m ² /kJ)	1.80	2.50
H_{N01}	(mm)	0.015	0.015
θ_{02}	(deg)	0	0
θ_{f2}	(deg)	0	0
ζ_{02}	(m ² /kJ)	0	0
H_{N02}	(mm)	0.015	0.015
θ_{03}	(deg)	50	50
θ_{f3}	(deg)	5	6
ζ_{03}	(m ² /kJ)	1.80	2.50
H_{N03}	(mm)	0.015	0.015
μ	(-)	0.50	0.50

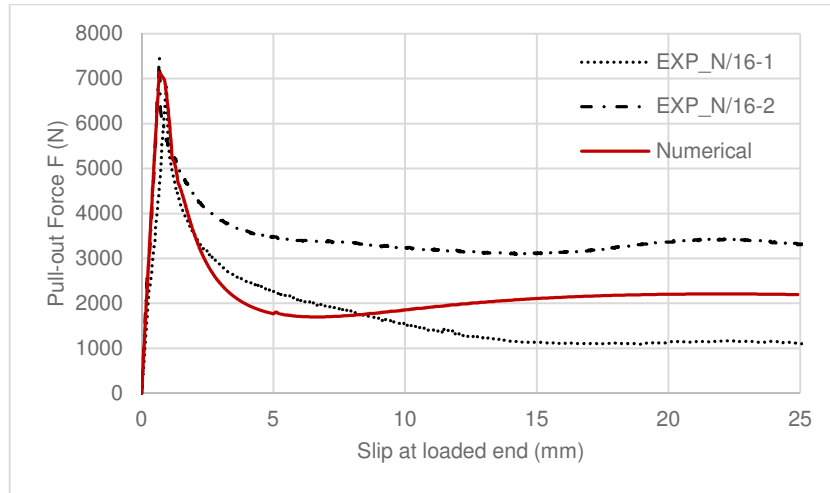


Figure 5.25 - Numerical-experimental comparison: $\phi 16$ rebar, NWC

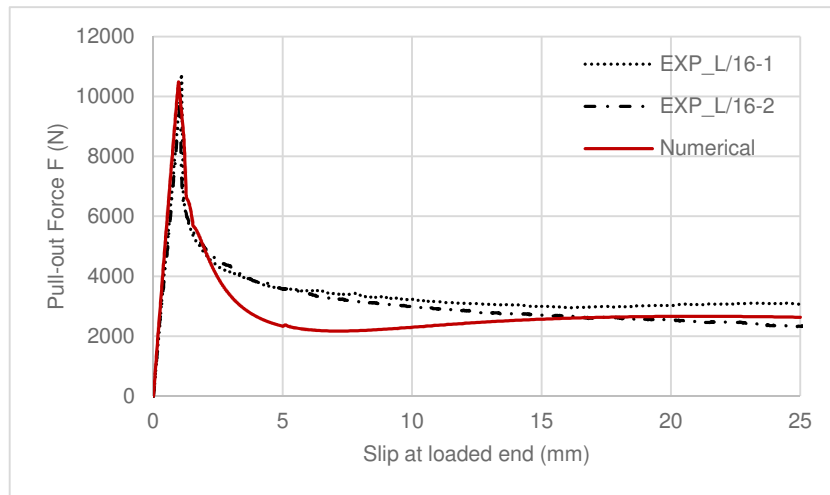


Figure 5.26 - Numerical-experimental comparison: $\phi 16$ rebar, LWC

Figs. 5.25 and 5.26 demonstrate that the enhanced degrading M-CZM is able to overcome the biggest limitation shown by the bilinear and exponential cohesive models, namely the impossibility to capture the residual force at the end of the post-peak branch. Instead, the shape of the post-peak curve is well captured by using this cohesive model able to account for damage, friction, mechanical interlocking and dilatancy. In addition, the introduction in the model of the asperities depth degradation made it possible to avoid the increasing trend of the pull-out force with growing slip values. Although numerical and experimental curves do not achieve a perfect agreement by using the enhanced degrading M-CZM, it is worth underlining that pull-out tests usually exhibit a significant scatter,

especially in terms of residual force value. This makes it more important to capture and reproduce the physics behind the phenomenon than the precise force values, and, in this respect, the introduced enhanced degrading M-CZM provided good results.

5.3.4.8 Validation

After the sensitivity analyses conducted to identify model parameters giving good correlation for pull-out tests conducted on $\phi 16$ mm rebars, the validation of the enhanced degrading M-CZM is carried out by performing FE analyses, using the same parameters (reported in Table 5.12), for the cases of $\phi 8$ mm rebar with both NWC and LWC matrices (Figs. 5.27 and 5.28).

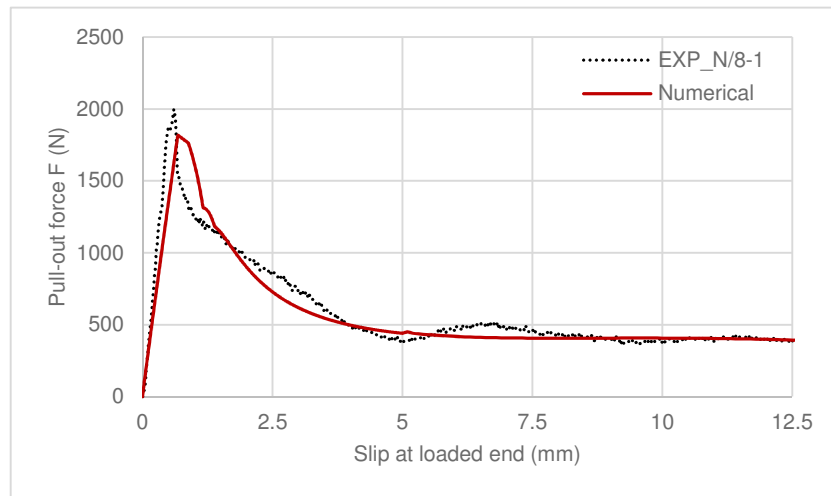


Figure 5.27 - Numerical-experimental comparison: $\phi 8$ rebar, NWC

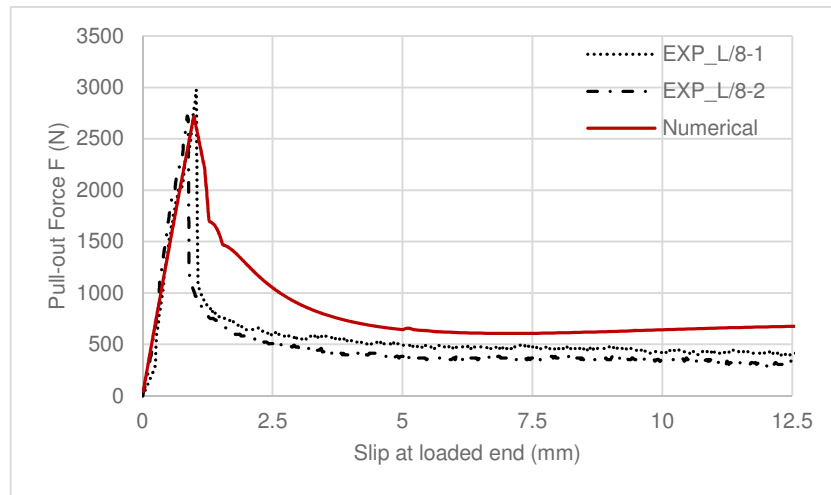


Figure 5.28 - Numerical-experimental comparison: $\phi 8$ rebar, LWC

Figs. 27 and 28 show good agreement between numerical and experimental curves, confirming the general validity of the proposed cohesive model. In other words, once the parameters are identified for a certain concrete batch, they can be introduced in a different model, leading to reasonable force-slip response curves. However, how it is possible to observe from Fig. 5.28, in the case of LWC the numerical model overestimates the pull-out load capacity especially in the region immediately after the peak. The result presented in Fig. 5.28 is obtained by inserting the same parameters values identified for the case of the $\phi 16$ mm bar pull-out, but probably in this case the exact experimental curve would be obtained by adopting a lower characteristic energy value.

5.3.5 Stress distribution along the interface

For the sake of completeness, the stress distribution along the interface is analysed in this section. Both normal and tangential stresses evolutions during the pull-out simulations carried out by using the enhanced degrading M-CZM are tracked in order to understand how the introduction of the multiplane structure of the interface affects the results. For brevity, just the results concerning the model simulating the $\phi 16$ mm bar embedded in NWC is reported, being the qualitative behaviour the same for all the other analysed cases (i.e. $\phi 16$ mm bar pull-out from LWC and $\phi 8$ mm bar pull-out from NWC and LWC). Since the performed numerical analyses are quasi-static, normal and tangential stresses (σ_x and τ_{xy} , respectively) have been computed in correspondence of some critical substeps identified from the overall pull-out force-slip response curve, as shown in Fig. 5.29.



Figure 5.29 - Substep identification for computing stress distributions at the interface

For the identified substeps, the evolution along the interface of the normal and tangential stresses (σ_x and τ_{xy} , respectively) is reported in Fig. 5.30. It is worth noting that the compressive stress (i.e. $-\sigma_x$) at the interface is equal to zero until the interface is bonded (up to substep 87), while its modulus increases as the slip grows (i.e. debonding and

frictional stages). This allows frictional forces to develop. The maximum compressive stress is, in fact, reached at the end of the analysis (i.e. substep 200). As for the normal stress distribution along the interface, its maximum values are reached at the beginning of the bond length (lower end), as shown in Fig. 5.30 and 5.31. The tangential stress evolution during the analysis, instead, demonstrates that the maximum value is achieved at substep 68, which corresponds to the pull-out force peak. Afterwards, the tangential stress decreases by remaining almost constant along the interface until substep 100 (i.e. slip equal to 15 mm). At this step, in fact, the tangential stress distribution along the interface exhibits higher values (in modulus) at the beginning of the bond length (lower end), as shown in Fig. 5.30 and 5.32c.

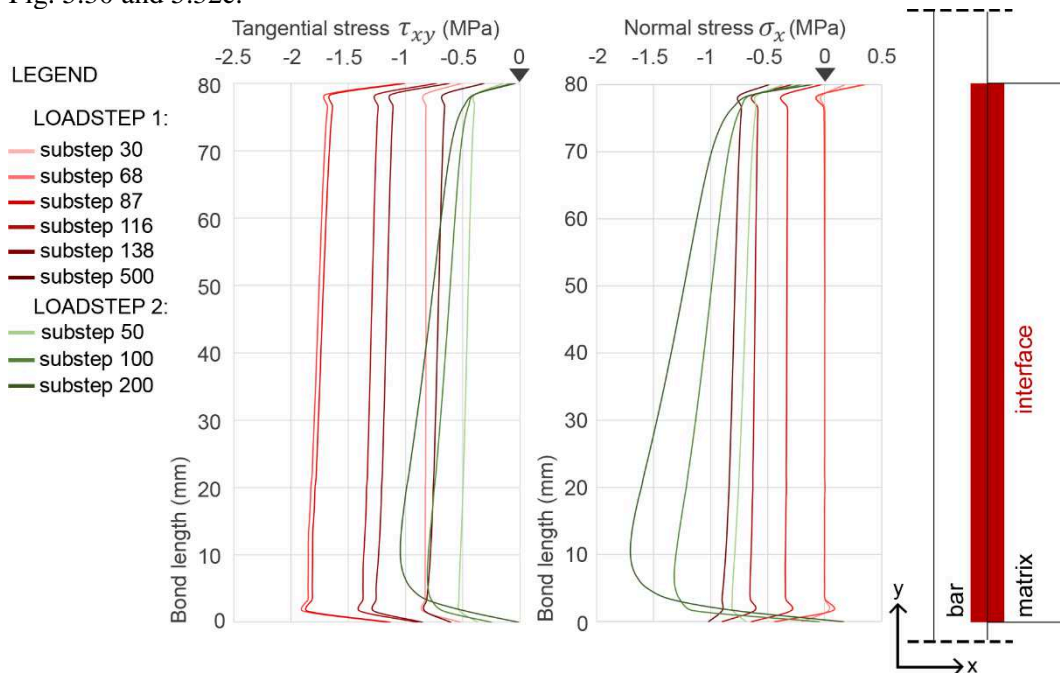


Figure 5.30 - Normal (σ_x) and tangential (τ_{xy}) stress distributions along the interface at different substeps

Figs 5.31 and 5.32 report the normal and tangential stress distributions on the bar and matrix portions involved in the debonding process. For each stress distribution three situations are shown, corresponding to substeps 30 (bonding phase) and 68 (pull-out force peak) of loadstep 1, and to substep 100 (post-debonding/frictional phase) of loadstep 2.

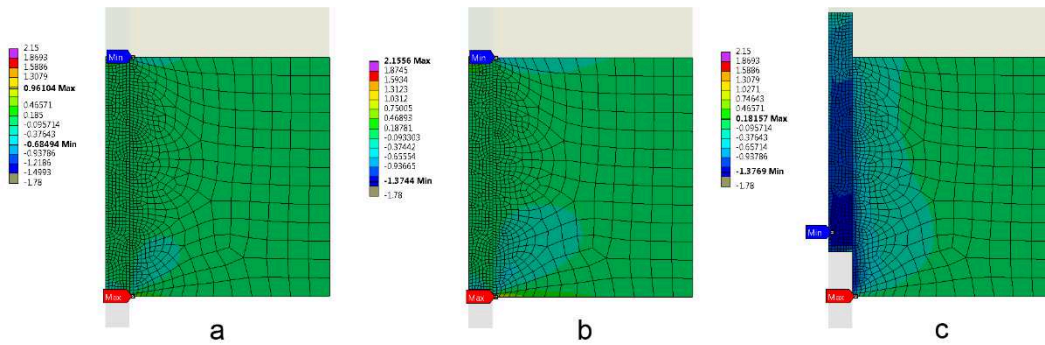


Figure 5.31 - Normal stress evolution: a) Loadstep 1 - substep 30 (bonding phase); b) Loadstep 1 - substep 68 (pull-out force peak); and c) Loadstep 2 - substep 100 (post-debonding/frictional phase)

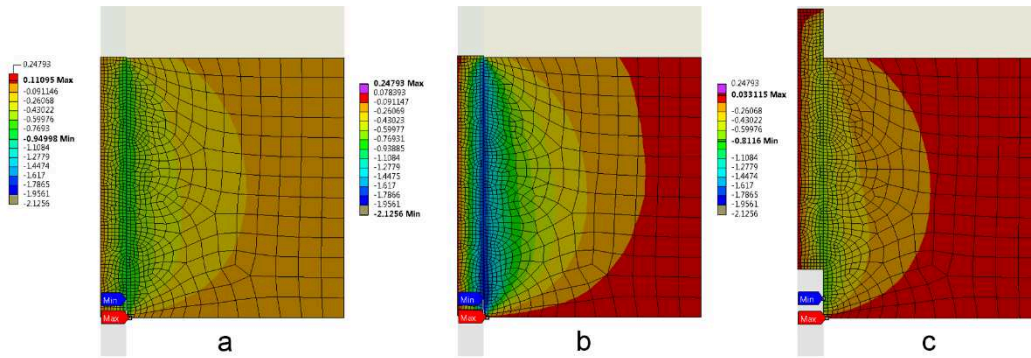


Figure 5.32 - Tangential stress evolution: a) Loadstep 1 - substep 30 (bonding phase); b) Loadstep 1 - substep 68 (pull-out force peak); and c) Loadstep 2 - substep 100 (post-debonding/frictional phase)

5.4 Concluding remarks

In this chapter two different CZM formulations have been used to simulate the experimental results obtained from the pull-out tests. The first model, i.e. the modified Alfano and Crisfield CZM, is deduced from the experimental curves and it consists of a linear branch up to the maximum cohesive traction, a linear softening immediately after the peak until reaching a first residual cohesive traction, and an exponential softening branch down to the final value of the residual cohesive traction. By employing this CZM, the numerical and experimental curves match very well. However, the main drawback of this model is that its formulation is not based on *a priori* physical considerations, thus its range of validity is expected to be narrower than that of the M-CZM. In addition, the values of the model parameters are strictly depending on the particular situation that the model is simulating.

The second model here adopted is an extension of the M-CZM formulated by Serpieri et al. in (Serpieri et al., 2015a), here called ‘enhanced degrading M-CZM’. It is based on a multiplane-structured RIA in which the CZM formulation of Alfano and Sacco (Alfano and

Sacco, 2006) accounting for damage and friction is implemented. The presence of the inclined microplanes allow for accounting mechanical interlocking and dilatancy. Moreover, the microplanes and asperities degradation describes the flatter process of the interface. With this model, able to simulate the pull-out conditions, several sensitivity analyses have been carried out, followed by an identification procedure in order to identify the values of the parameter that best fit the experimental curves in the case of the pull-out of $\phi 16$ mm bars from both NWC and LWC. Afterwards, the exact same parameters values have been adopted for the models simulating the pull-out of $\phi 8$ mm bars from NWC and LWC specimens. In this case, good agreement has been obtained, validating and generalising the enhancing degrading M-CZM.

Chapter 6

Single fibre pull-out tests of straight and hooked-end Ti6Al4V fibres

The interfacial behaviour between titanium alloy reinforcement and concrete, with particular regard to LWC, is here further investigated by carrying out experimental tests on titanium alloy fibres and LWC. Since the well-known importance of the stress transfer mechanism in fibre-reinforced composites, single fibre pull-out tests are carried out focusing on the differences and analogies between the bond behaviour of bars and straight fibres, and on the mechanisms coming in when different geometrical configurations of the fibres are taken into account. The differences in the behaviour of bars and straight fibres under pull-out conditions is further investigated by means of the FE analysis, in which the enhanced degrading M-CZM is used to simulate the reinforcement-matrix debonding. The values of the enhanced degrading M-CZM input parameters better representing the single fibre pull-out curves turned out to be consistent with their physical meaning discussed in Chapter 5. Thus, a further validation of the model is here obtained.

6.1 Introduction to the single fibre pull-out test

The single fibre pull-out test is often used to assess the effectiveness of a fibre in transferring the stress to the surrounding matrix (Cunha et al., 2010). As it happens in the case of the bar pull-out test, the fibre slip is monitored as a function of the applied load on the reinforcement, which, in this case, is constituted by the fibre (Naaman and Najm, 1991), (Banthia and Trottier, 1994), (Li and Chan, 1994).

6.1.1 Relevance of the test results

Establishing the correlation between the single fibre pull-out test results and the fibre behaviour in a real composite, represents a very complex task. Over decades some authors concluded that the single fibre pull-out test data could not be correlated to the behaviour of

a fibre in the composite materials (Hughes and Fattuhi, 1975), (Maage, 1977). However, single fibre pull-out tests are conducted to optimise the fibre and matrix characteristics, understand the fibre-matrix interfacial properties, and to study the behaviour of the whole composite material (Banthia and Trottier, 1994), (Cunha et al., 2010).

Thus, understanding the behaviour of the single titanium alloy fibre pulled-out from a concrete matrix can be considered a fundamental step toward the possibility to combine titanium and concrete in a fibre reinforced concrete composite material.

6.1.2 Test configurations

The experimental research carried out in the past highlighted two main groups of pull-out test configurations, i.e. single-sided and double-sided specimens. Among the first group, Fig. 6.1a shows the configuration employed for example by Grünewald (Grunewald, 2004), Markovic (Markovic, 2006), Caggiano et al. (Caggiano et al., 2015). Fig. 6.1b, instead, represents the test set-up of pull-out tests on single-sided specimens used by Naaman and Najm (Naaman and Najm, 1991); whereas Li and Chan (Li and Chan, 1994) employed the configuration shown in Fig. 6.1c. Several authors carried out pull-out tests on double-sided specimens (Fig. 6.1d), i.e. Naaman and Shah (Naaman and Shah, 1976), Banthia and Trottier (Banthia and Trottier, 1994), Robins et al. (Robins et al., 2002), and Abdulle and Xiao (Abdulle and Xiao, 2014).

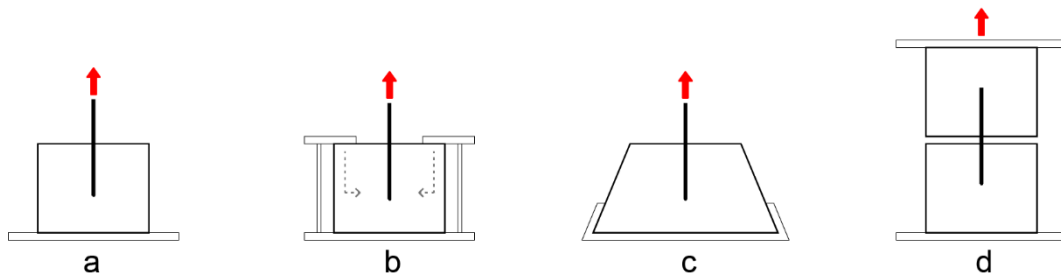


Figure 6.1 - Pull-out test configurations: a), b) and c) single-sided specimens; d) double-sided specimens








6.1.3 Pull-out test typical results

A source of complexity for the micromechanical behaviour of fibre reinforced cementitious composites is represented by the presence and combined action of several mechanisms of bond (Cunha et al., 2010). According to Naaman and Najm (Naaman and Najm, 1991), the main mechanisms acting at the fibre-matrix interface during the fibre pull-out are adhesion, friction, and mechanical interlocking. Thus, the same mechanisms identified for the bar-matrix debonding process are recognised in the case of the fibre pull-out. When straight, smooth fibres are employed, the main contributions to bond are provided by chemical adhesion and friction, whereas mechanical interlocking plays a role especially for deformed fibres.

In contrast to the limited possibilities of deforming a reinforcing bar, fibres can assume a wide range of geometries as well as numerous surface deformations aimed at improving

the bond between them and the surrounding matrix. Moreover, the fibre cross-section can be round, flat, triangular, etc. Some examples of the most widely adopted fibre configurations are provided in Table 6.1, according to the classification presented by Naaman in (Naaman, 2003) and recently revised by Cunha et al. (Cunha et al., 2010).

Table 6.1 - Most used steel fibre profiles

Longitudinal profile		Cross-section	Example in the literature
	Smooth	Round, Flat, Any shape	(Alwan et al., 1991)
	Indented, Corrugated, Roughened surface	Round, Flat, Any shape	(Chanvillard and Aitcin, 1996)
	Crimped	Round, Flat, Any shape	(Banthia and Trottier, 1994) (Banthia and Sappakittipakorn, 2007) (Alwan et al., 1999)
	Hooked-end	Round	(Robins et al., 2002) (Abdallah et al., 2016b) (Abdallah and Fan, 2017)
	Paddled-end	Round, Flat	(Hamoush et al., 2010)
	Polygonal twisted	Polygonal - Triangular, - Rectangular	(Naaman, 2003) (Lee and Kighuta, 2017)
	Spiral	Round	(Hao and Hao, 2017) (Hao et al., 2014)

The smooth straight and the hooked-end steel fibres are taken as examples in order to analyse the typical pull-out response curves. The comparison between them, in fact, is able to provide a clear explanation of the different mechanisms acting at the fibre-matrix interface under pull-out conditions.

The pull-out behaviour of a smooth straight fibre is generally described by three phases, namely the bonded state, the debonding phase and the frictional phase (Naaman et al., 1991), as shown in Fig. 6.2a. Initially the fibre is bonded to the concrete matrix by means of an interfacial bond, which transfers the pull-out stress from the fibre to the surrounding concrete up to the maximum bond stress, i.e. the bond strength τ_{max} . Once the bond strength is reached, the bond stress starts to decrease, originating the debonding phase which corresponds to the interface progressive failure. Once the debonding is complete, frictional stresses remain the only means of force transfer until the full pull-out of the fibre (Naaman et al., 1991), (Bentur and Mindess, 2007). When the fibre is straight, the

mechanism can be assimilated to that analysed in the case of the bar pull-out (Chapters 2 and 3), even if some differences have been found due to the size of the fibre with respect to bars (Bažant and Desmorat, 1994).

When deformed geometric configurations (e.g. hooked-end (Alwan et al., 1999), (Van Gysel, 1999), crimped, spiral (Hao and Hao, 2017), etc.) are taken into account, instead, the pull-out response curve is characterised by a different mechanism in the immediate post-peak phase, which results from the plastic deformation of the fibre (Löfgren, 2005). In particular, Fig. 6.2b shows the typical case of a hooked-end fibre under pull-out load (Alwan et al., 1999). The maximum load reached is usually higher than that developed by a straight fibre under pull-out conditions and also the shape of the bond-slip curve is different. In fact, the mechanical contribution given by the hook corresponds to the energy required to straighten the fibre. Thus, the plastic deformation of the fibre is responsible for the higher energy dissipated in this process with respect to the straight fibre. The amount of slip at the peak and until the end-hook has been straightened depends on the geometry of the fibre, as well as the shape of the bond-slip curve in the immediate post-peak area (Löfgren, 2005).

Fig. 6.2c shows the contribution of the hook with respect to a straight end fibre, in terms of bond-slip response curve.

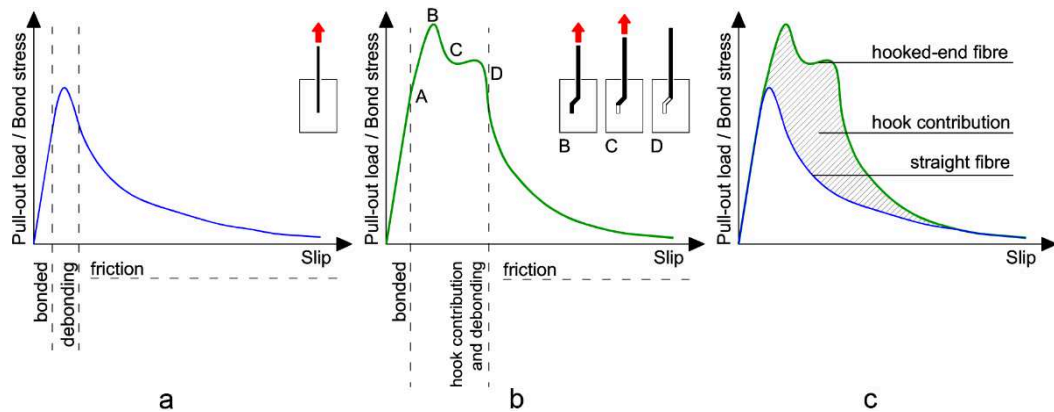


Figure 6.2 - Typical bond-slip response curve of: a) straight fibre; and b) hooked-end fibre; c) comparison between straight and hooked-end fibre in terms of bond-slip response curve

6.2 Experimental single fibre pull-out test

The second experimental series of tests carried out in this thesis concerns the single fibre pull-out. In fact, the fibre-matrix interface plays an important role in controlling the macroscopic mechanical properties of fibre composites (Sørensen and Lilholt, 2016), as much as the bar-matrix interface influences the RC structural response. Thus, the characterisation of the fibre-matrix bond behaviour represents a necessary step towards the possibility to design a composite materials made of lightweight concrete and titanium fibres.

To this end, a series of single fibre pull-out tests is carried out, testing not just the untraditional material used for the reinforcement but also two different geometrical configurations of the fibres. This allows for comparing the contribution of a mechanical anchorage (provided by the hook at the end of the fibre) with respect to the straight fibre configuration. As previously discussed, the hook geometry thoroughly affects the post-crack behaviour of fibres in structural elements (Shafaei et al., 2017).

6.2.1 Materials

The materials employed in this experimental work are lightweight concrete (LWC) for the matrix and the titanium alloy Ti6Al4V for the fibres. The mix design adopted for the LWC cast is reported in Table 6.2.

Table 6. 2 - LWC mix design

LWC mix		(kg/m ³)
Water		188
Cement CEM II A/L 42.5R		460
Fine aggregate (natural sand)	(0-4 mm)	585
Coarse aggregate (Expanded Clay)	(0-15 mm)	470
Superplasticiser		4.6
Density (theoretical)		1708

The mechanical properties of the employed materials have been established by performing compression and indirect tensile tests regarding the concrete batch, while for the titanium wires the characteristics provided by the manufacturer have been adopted. The results are summarised in Tables 6.3 and 6.4 for concrete and titanium wires, respectively.

Table 6.3 - Mechanical properties of LWC

	UNI EN 12390-3:2009	UNI EN 12390-6:2010	
	Average compressive strength	Average tensile strength	
Measured density	f_{cm}	f_{tm}	
(kg/m ³)	(MPa)	(MPa)	
LWC	1900	49	1.22

It is worth underlying that the measured density is higher than the theoretical value derived from the mix design. However, consistently with this result the average compressive strength is much higher than that expected (49 MPa vs. 40 MPa). This happened because the water content of the lightweight aggregate is difficult to measure precisely and, in this case, it had been underestimated, eventually leading to higher density. Nevertheless, the concrete can be still considered ‘lightweight’, being its density equal to 1900 kg/m³, which lies within the range identified by the report ACI 213R-03 (ACI Committee 213, 2003) to consider structural concrete ‘lightweight’ (1400-2100 kg/m³). Moreover, as far as bond strength is concerned, the resulting values are related to the

concrete compressive strength to obtain normalised values comparable among different concrete matrices, thus the results here obtained do not lose significance and generality.

Regarding titanium wires, instead, the mechanical properties provided by the manufacturer are summarised in Table 6.4. The material has been provided in the form of wires of 1.2 mm of diameter and a length equal to 910 mm. Thereafter, fibres have been created by cutting and deforming (for the hooked-end configuration) the titanium alloy wires.

Table 6.4 - Mechanical properties of the titanium wires (provided by the manufacturer)

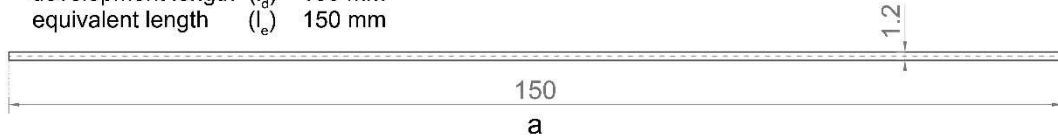
Diameter	Length	Material	Yield strength	Elongation
ϕ	l		f_{ty}	
(mm)	(mm)		(MPa)	(%)
1.2	910	Ti6Al4V (Titanium Grade 5)	820	6

6.2.2 Geometrical configuration of the fibres

In this work it has been chosen to realise hooked-end fibres. Although other shapes are considered equally or more performant (e.g. twisted (Naaman, 2003), spiral (Hao et al., 2014), etc.), the realisation process of hooked-end fibres is relatively simple and, in the present case, it maximises the number of fibres from the titanium wires available. Moreover, if the whole FRC material is concerned, three-dimensional configurations like the spiral one may intertwine during the cast, preventing the fibre-matrix adherence, which is essential to create an efficient composite material. However, the hook shape chosen in this work is not the most traditional one, presenting a further bend at the fibre ends. Examples of double-bended hooks can be found in the literature (Abdallah et al., 2016b), (Abdallah and Fan, 2017), (Shafaei et al., 2017). In order to estimate the contribution of the hook at the end of the fibres, also straight fibres have been tested. The geometric details of both straight and deformed fibres are reported in Figs. 6.3a and 6.3b, respectively. Noteworthy, for the pull-out test in the case of hooked-end fibres, just one end has been bended, being the other one intended for clamping the fibre to the testing machine.

STRAIGHT FIBRE (S)

diameter	(Φ)	1.2 mm
development length	(l_d)	150 mm
equivalent length	(l_e)	150 mm



HOOKED-END FIBRE (HE)

diameter	(Φ)	1.2 mm
development length	(l_d)	151.56 mm
equivalent length	(l_e)	150 mm

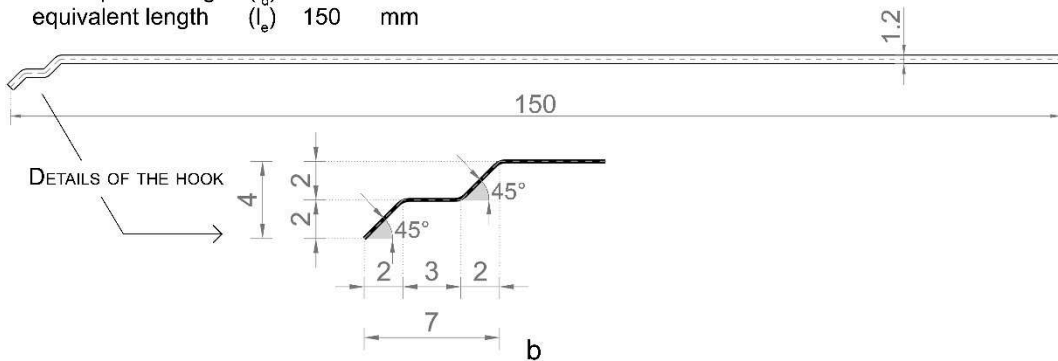


Figure 6.3 - Geometric details of: a) smooth straight; and b) hooked-end Ti6Al4V fibres

6.2.3 Specimen preparation and test set-up

Thirty cylindrical specimens have been realised (Fig. 6.4), with the titanium alloy fibre positioned in the middle of the specimen and with an embedded length equal to 45 mm. Fig. 6.5 reports the geometrical details of the specimens, while the test set-up is shown in Figs. 6.6 and 6.7. A metallic frame (Lancioni et al., 2017) (Fig. 6.7b) has been used to support the specimen and anchor it to the testing machine. Tests were performed using a testing machine with a load bearing capacity of 5 kN (Fig. 6.7a) with the displacement control setting and a test rate equal to 1 mm/min. Strain gauges positioned as shown in Fig. 6.6a were employed in order to measure the possible deformation of the Ti6Al4V fibre.



Figure 6.4 - Cast of the specimens

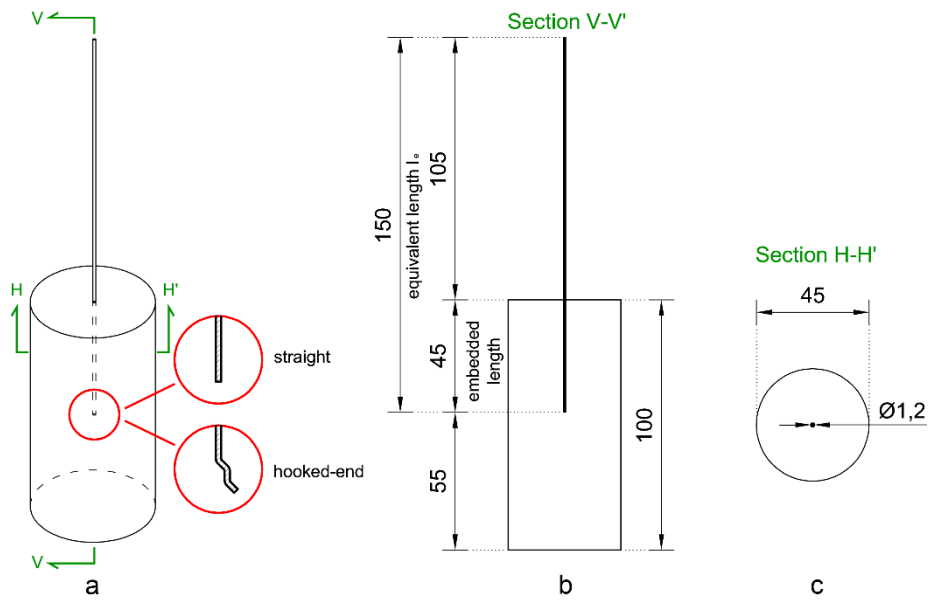


Figure 6.5 - Geometrical details of the specimens for the single fibre pull-out test: a) perspective view; b) longitudinal cross-section (Section V-V'); and c) transversal cross-section (Section H-H')

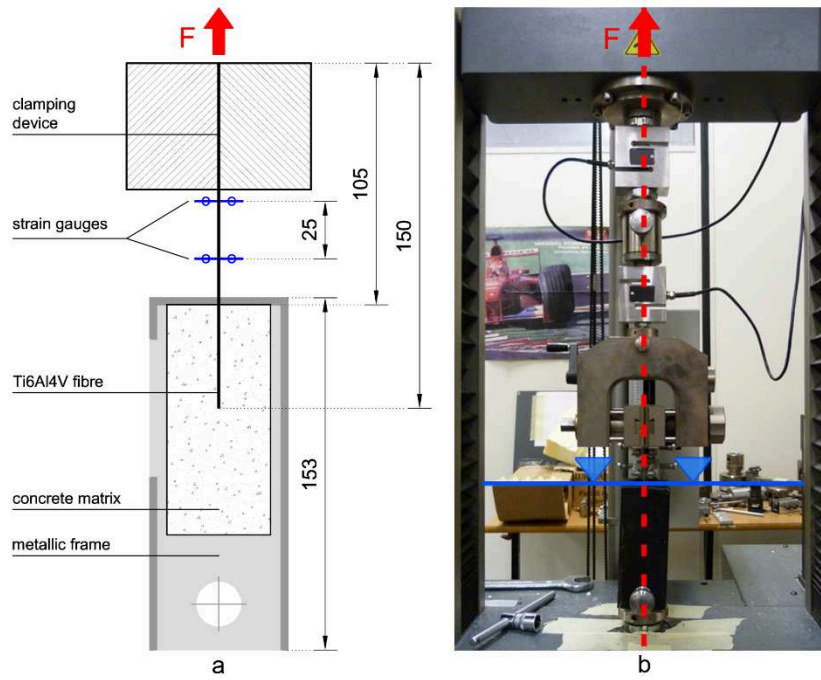


Figure 6.6 - Pull-out test set-up: a) scheme of the test; b) execution of the test

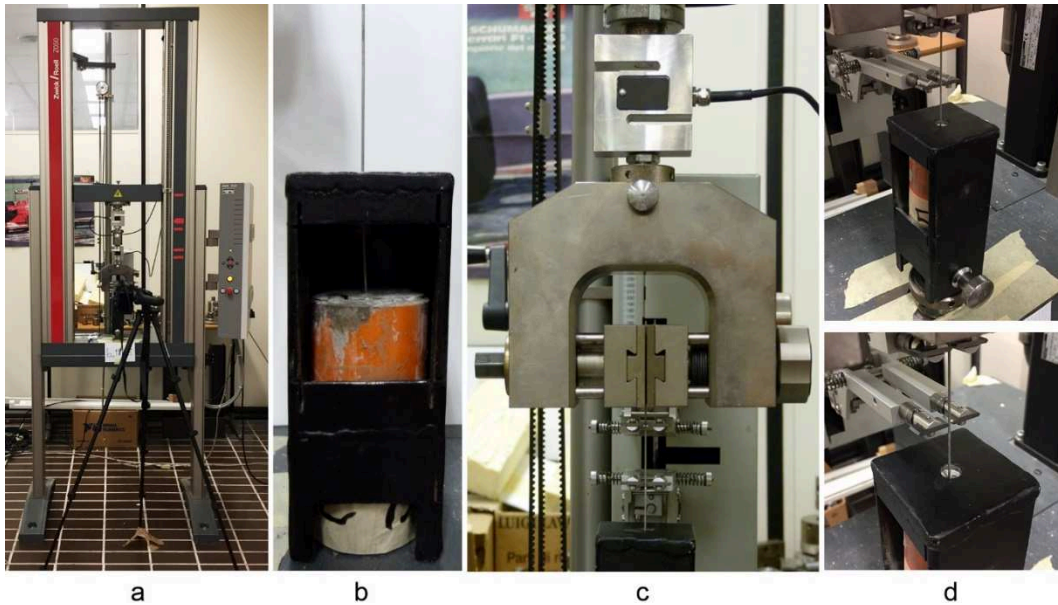


Figure 6.7 - Pull-out test details: a) testing machine; b) metallic frame; c) clamping device; and d) strain gauges

6.2.4 Experimental results

The results of the single fibre pull-out tests are summarised in Table 6.5, where the identification of the specimens is as shown in Fig. 6.8. As in the case of the bar pull-out test, the maximum measured force F_{max} is transformed into bond strength, τ_{max} by Eq. (6.1):

$$\tau_{max} = \frac{F_{max}}{\pi d_s l_b} \quad (6.1)$$

where d_s is the fibre diameter and l_b is the bond length.

The displacement at bond strength in Table 6.5 is reported as s_{bS} . The normalised value of the bond strength, τ^*_{max} , with respect to concrete compressive strength (f_{cm}), given by Eq. (6.2), is also reported in Table 6.5.

$$\tau^*_{max} = \frac{\tau_{max}}{\sqrt{f_{cm}}} \quad (6.2)$$

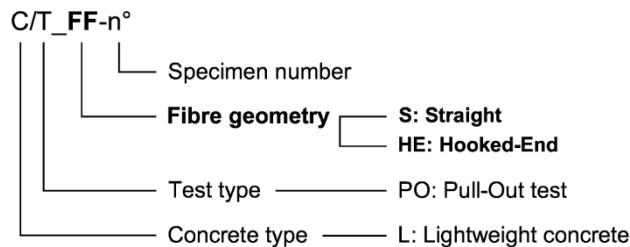


Figure 6.8 - Specimen identification

Table 6.5 - Single fibre pull-out test results

Specimen	F_{max}	τ_{max}	τ_{max}^*	s_{bs}	Fibre strain at F_{max}	Max fibre strain
					$\varepsilon_f^{F_{max}}$	$\varepsilon_{f,max}$
	(N)	(MPa)	(MPa ^{0.5})	(mm)	(mm/mm)	(mm/mm)
L/PO_S-1	594.19	3.50	0.50	0.76	-*	-*
L/PO_S-2	331.33	1.95	0.28	0.42	0.0042	0.34
L/PO_S-3	324.09	1.91	0.27	0.36	0.0031	0.58
L/PO_S-4	616.78	3.64	0.52	0.87	0.0059	0.89
L/PO_S-5	426.94	2.52	0.36	0.48	0.0040	0.40
L/PO_S-6	387.02	2.28	0.33	0.97	0.0035	0.85
L/PO_S-7	545.07	3.21	0.46	1.10	0.0051	0.76
L/PO_S-8	326.98	1.93	0.28	0.37	0.0029	0.07
L/PO_S-9	250.92	1.48	0.21	0.46	0.0024	0.60
L/PO_S-10	517.58	3.05	0.44	0.97	0.0045	0.82
L/PO_S-11	223.26	1.32	0.19	0.40	0.0014	0.81
L/PO_S-12	334.01	1.97	0.28	0.52	0.0038	0.54
L/PO_S-13	440.97	2.60	0.37	0.43	0.0041	0.89
L/PO_S-14	495.85	2.92	0.42	0.52	0.0065	0.88
L/PO_S-15	349.32	2.06	0.29	0.33	0.0065	0.89
L/PO_HE-1	929.58	5.48	0.78	2.57	0.014	0.68
L/PO_HE-2	725.39	4.28	0.61	1.66	0.008	0.82
L/PO_HE-3	992.13	5.85	0.84	3.18	0.019	0.80
L/PO_HE-4	752.07	4.43	0.63	1.50	0.008	0.52
L/PO_HE-5	866.31	5.11	0.73	3.38	0.011	0.77
L/PO_HE-6	895.78	5.28	0.75	1.99	0.012	0.61
L/PO_HE-7	845.80	4.99	0.71	3.42	0.010	0.85
L/PO_HE-8	877.16	5.17	0.74	2.59	0.011	0.69
L/PO_HE-9	937.52	5.53	0.79	4.51	0.017	0.89
L/PO_HE-10	749.77	4.42	0.63	2.41	0.007	0.50
L/PO_HE-11	990.03	5.84	0.83	2.78	0.019	0.75
L/PO_HE-12	1065.08	6.28	0.90	4.07	0.029	0.82
L/PO_HE-13	41.61	0.25	0.04	0.19	0.006	0.72
L/PO_HE-14	554.27	3.27	0.47	2.02	0.006	0.85
L/PO_HE-15	832.52	4.91	0.70	1.85	0.010	0.86

*failed measurement

6.2.4.1 Bond stress-slip relationships

Results of the single fibre pull-out test consist of bond stress-slip relationships (τ_{dm} - s), as in the case of the bar pull-out test presented in Chapter 3. The relationships obtained from the tests are reported in the following Figs. 6.9-6.12. Particularly, Fig. 6.9 shows the results obtained for the straight fibres, whereas Fig. 6.11 reports the bond-slip relationships resulting from the pull-out tests of the hooked-end fibres. Figs. 6.10 and 6.12 show the same relationships by enlarging the graphs on the first 5 and 10 mm of slip for two fibre shapes here considered, respectively.

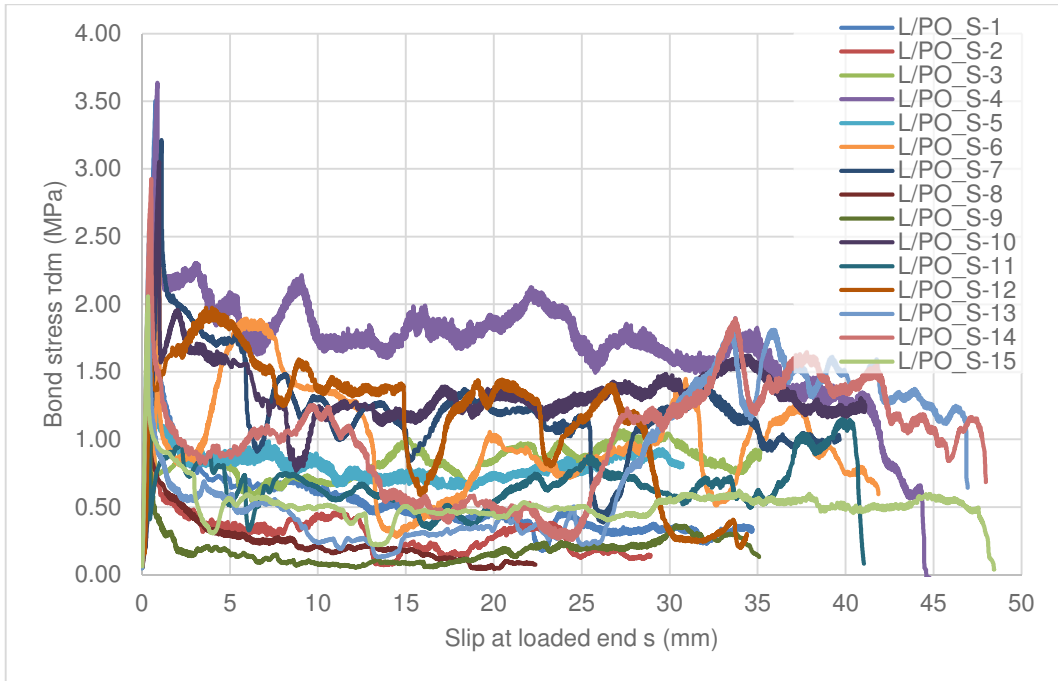


Figure 6.9 - Single fibre pull-out test results: Straight fibre

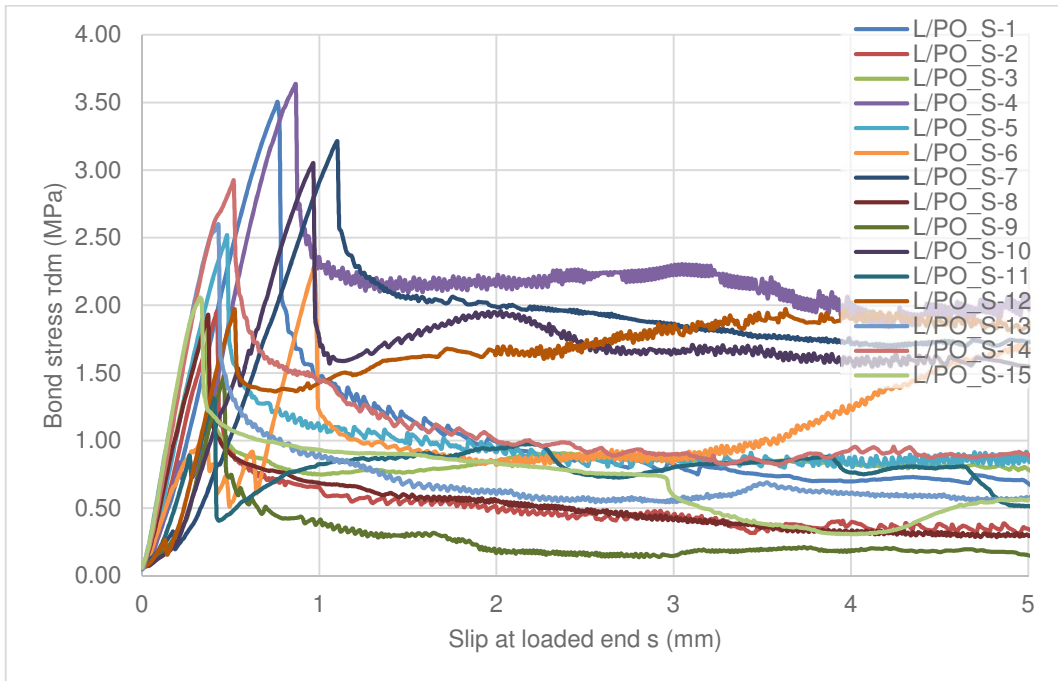


Figure 6.10 - Zoom on the first 5 mm of slip of the single fibre pull-out test results: Straight fibre

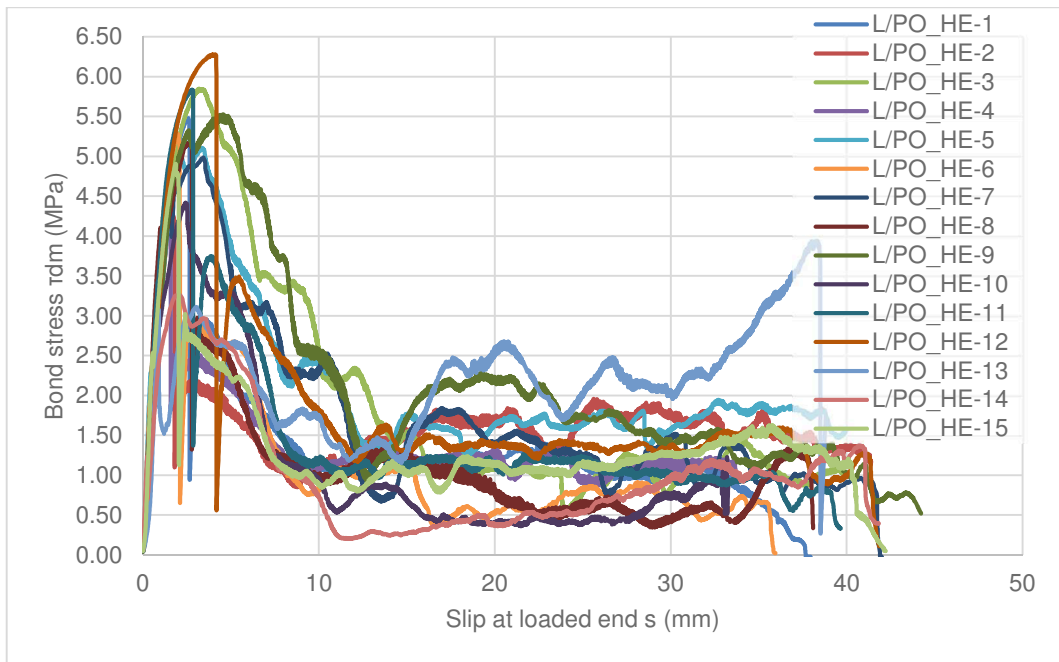


Figure 6.11 - Single fibre pull-out test results: Hooked-end fibre

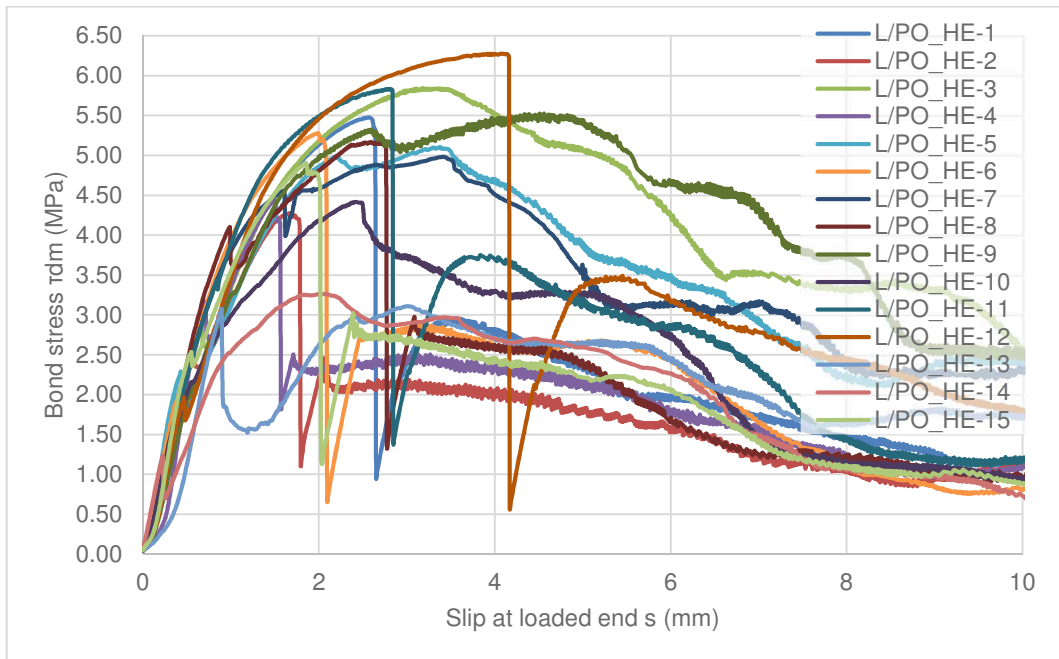


Figure 6.12 - Zoom on the first 10 mm of slip of the single fibre pull-out test results: Hooked-end fibre

6.2.4.2 Influence of fibre geometry

The comparison between straight and hooked-end configurations of the fibre shape highlights that the average bond strength in the first case (2.42 MPa) is significantly lower than that developed in the second case (4.74 MPa). Moreover, it occurs for a slip value which is equal to 0.60 mm on average for straight fibres and 2.54 mm on average for hooked-end fibres. Thus, the increase in the pull-out energy, i.e. the area under the bond-slip relationship, is remarkable when the fibre geometry is switched from a straight configuration to a deformed one.

The hook contribution is due to the plastic deformation of the fibre, which occurs before the fibre is pulled-out from the matrix. Fig. 6.13 shows the hooked-end fibres pulled-out, which lose their shape during the tests, being straightened and plastically deformed.



Figure 6.13 - Hooked-end fibres after pull-out test

In terms of bond-slip relationship the hook contribution can be clearly seen in Fig. 6.14, where two bond-slip response curves representative of the results obtained herein, i.e. L/PO_S-5 and L/PO_HE-5, are compared.

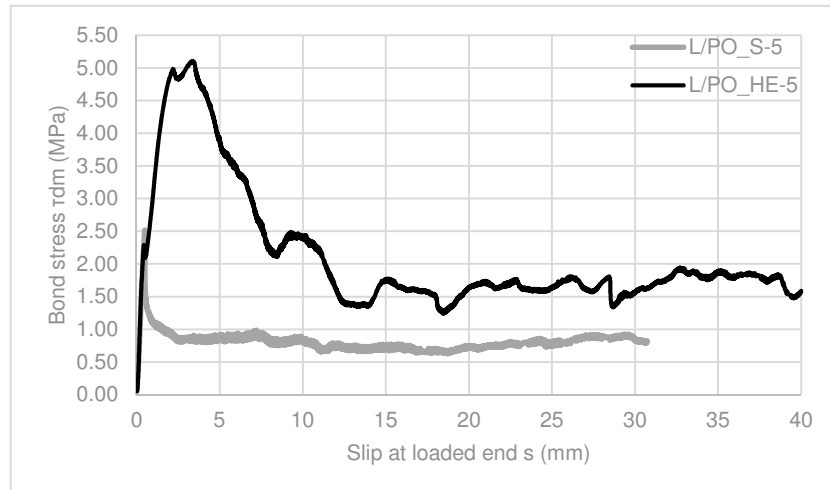


Figure 6.14 - Bond-slip response curve comparison between straight and hooked-end fibres

By focusing the attention on the first millimetres of slip (Fig. 6.15), it can be observed that for the straight fibres (Fig. 6.15a) the significant loss of adhesion, translated in the bond stress immediate drop, occurs for a slip equal to 0.48 mm (L/PO_S-5 specimen). As for the hooked-end fibres (Fig. 6.15b), the first decrease in the bond stress happens for a slip value equal to 0.42 mm (L/PO_HE-5), which is similar to the slip value correspondent to the bond strength in the case of the straight fibres. Moreover, the bond stress values are similar. Thus, in the case of hooked-end fibres, the first drop of bond stress is similar to that observed for straight fibres in terms of bond stress and slip values and correspond to the partial loss of chemical adhesion. As observed by Alawan et al. (Alwan et al., 1999) and Abdallah et al. (Abdallah et al., 2017), this step corresponds to full debonding of the fibre with respect to the surrounding matrix. Once the fibre is debonded, a significant role is played by the plastic deformation of the hook, which depends on the geometric characteristics of the fibres. In the present case the fibre has three bends at each end, thus the resultant curve does not present the typical shape shown in Fig. 6.2. In fact, the pull-out of a 'traditional' hooked-end fibre (i.e. with two bends per end) is characterised by the progressive mobilisation end entrance of the first plastic hinge (PH1) into the straight part of the channel. Further straightening under PH2 results in a slight increase in pull-out load (Fig. 6.16a). Once both PH1 and PH2 have straightened the fibre, the pull-out load needs only to overcome frictional resistance, as it happens for a straight fibre (Abdallah et al., 2018). In the present case, instead, three plastic hinges originated in correspondence of the three curvatures (Fig. 6.16b), resulting in slightly different shapes in the bond-slip response curves, higher bond strength and greater total energy needed to deform the hook. An experimental comparison among different types of hooks for hooked-end fibres has been recently carried by Abdallah and Fan in (Abdallah and Fan, 2017), where the pull-out response curves of fibres with two, three and four bends is quantified.

A representation of the fibre strengthening process, with the progressive plastic deformation of the hook, for the significant steps of the bond-slip curve is provided in Fig. 6.15b.

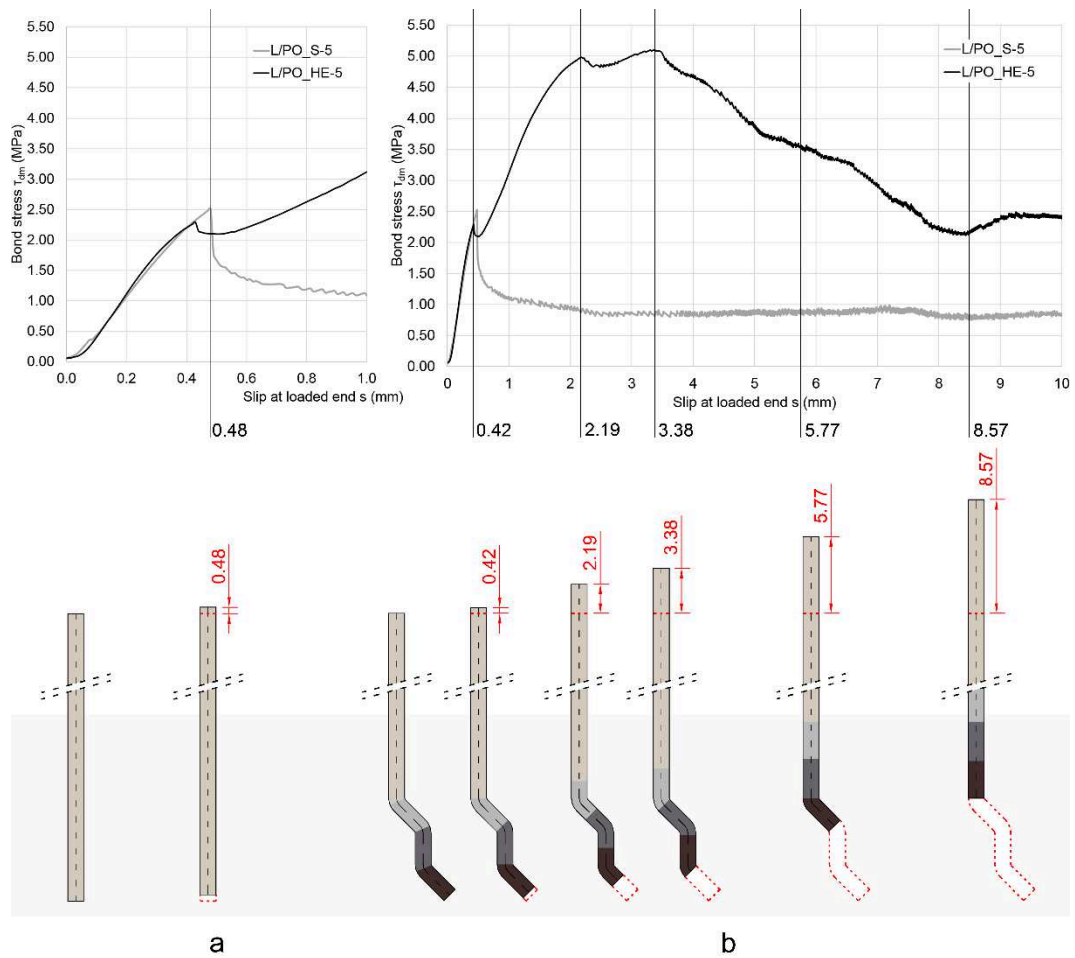


Figure 6.15 - Fibre pull-out mechanism: a) rigid sliding of straight fibres; and b) plastic deformation (strengthening) of the hook of hooked-end fibres

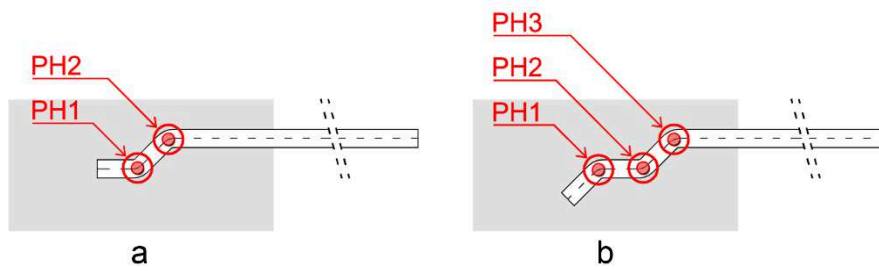


Figure 6.16 - Plastic hinges: a) hooked-end fibre with two curvatures; and b) hooked-end fibre with three curvature

The hook plasticisation provides a typical response curve shape that has been obtained also in the present experiments for specimens L/PO_HE-3, -5, -7, -9, -10, -13, and -14 (Fig.

6.17a). As for the remaining specimens (L/PO_HE-1, -2, -4, -6, -8, -11, -12, and -15), instead, another curve shape can be observed (Fig. 6.17b). In this case, the load has a sudden drop after the peak, and the pull-out behaviour afterwards resembles that of a straight fibre. As noted by Naaman et al. (Naaman et al., 1989), this behaviour is due to the hook rupture inside the matrix before straightening. Thus, in this case the hook contribution provides less pull-out energy than that observed for plastic deformation.

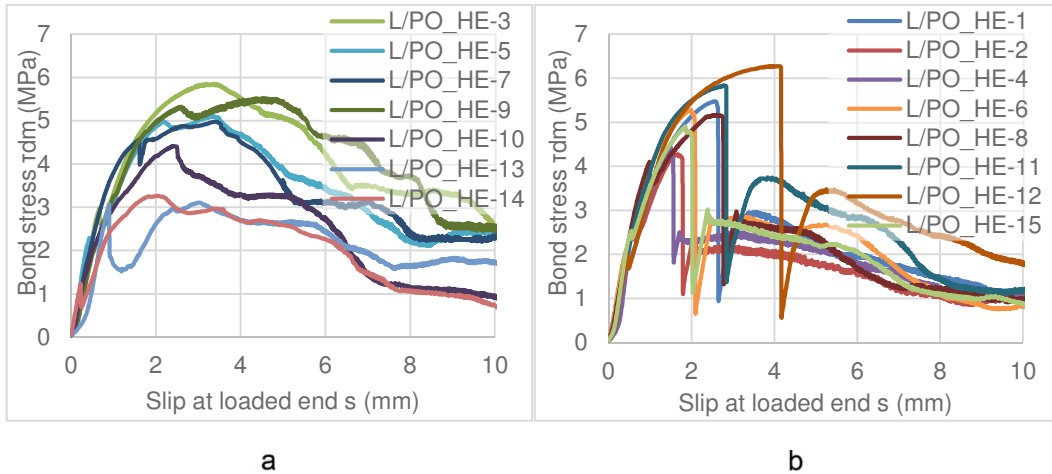


Figure 6.17 - Comparison between pull-out response curves of hooked-end fibres: a) hook plastic deformation response; and b) hook rupture response

From Fig. 6.18, it is possible to notice the difference between a plastically deformed hook and a broken one. The fibres took as example are those pulled-out from specimens L/P-O_HE-7 and L/PO_HE-6, respectively.



Figure 6.18 - a) plastically deformed hook (specimen L/PO_HE-7); and b) broken hook (specimen L/PO_HE-6)

6.2.4.3 Hook contribution

In order to quantify the hook contribution, and thus the main mechanical component of bond, the average pull-out energy (E_{p-o}) has been computed for hooked-end and straight fibres, respectively. Results of the comparison are reported in the following Table 6.6. It is

worth noting that the pull-out energy has been computed until a slip value equal to 20 mm in order to neglect some local increases in the bond stress exhibited by some response curves related to the hooked-end fibres. Moreover, as discussed in paragraph 6.2.4.2, the hook contribution appears to greatly increase the bond stress until the fibre is completely straightened. This, in the present experimental work, happens for slip values lower than 20 mm.

Table 6.6 - Hook contribution

Fibre series		Average τ_{max} (MPa)	Average E_{p-o} (kJ)
Straight	(S)	2.42	2508
Hooked-end	(HE)	4.74	5256
Hook contribution		+ 95.5%	+ 109.5%

6.2.4.4 Experimental scattering and curve averaging procedure

A significant aspect arisen from the tests carried out, is represented by the scattering of the results, both for straight and hooked-end fibres.

As far as hooked-end fibres are concerned, the scattering of the results can be attributed to differences in the straightening process of the hook. In fact, as recently noted by Abdallah and Fan (Abdallah et al., 2018), even when no further plastic deformation of the hook can occur, some experimental curves exhibit a residual load increase at the last stage of the pull-out response. If the hook is not completely straightened, its sliding inside the concrete channel requires increasing forces to advance. The non-complete straightening of the fibre leads to some geometrical irregularities, which contribute to increase friction with respect to the matrix channel and thus (Soetens et al., 2013), (Isla et al., 2015). This phenomenon is, of course, difficult to happen always in the same way, thus the resultant curves can vary significantly. The consequent local crushing of the matrix due to the hook deformation, is another scattering source, being strictly depending on each particular case.

However, this does not seem to be the only reason why pull-out responses present scattering of the results. In fact, also straight fibres pull-out responses often differ notably. One of the causes can lie on the fact the fibres may be inclined with respect to the load direction. Bond-slip relationships have been found to vary significantly with the fibre inclination angle (Lee et al., 2010), (Cunha, 2010) (Isla et al., 2015), (Zhang and Yu, 2016), (Cao and Yu, 2018). Particularly, the fibre inclination has an influence on the post-peak load and the energy absorption capacity (Isla et al., 2015).

In the present experimental study, fibres are theoretically aligned to the load direction (i.e. crack plane), but some deviations from the vertical direction may occurred during the cast, resulting in slightly inclined fibres that, eventually, led to differences in the pull-out response.

Finally, it is worth mentioning the heterogeneous nature of the concrete matrix. Fibres in the concrete mixture act as a separate phase surrounded by an additional interfacial transition zone (ITZ) with different mechanical properties and microstructure compared to

the bulk matrix (Zacharda et al., 2017). However, their position with respect to the other phases of the matrix (i.e. fine and coarse aggregates, cement, voids, etc.) can vary significantly. Moreover, the fibre can encounter different occurrences during its sliding inside the concrete channel, that may affect its pull-out response behaviour. A study on the influence of concrete heterogeneity on the steel fibres pull-out behaviour has been recently carried out in (Cox, 2015), resulting in the observation of an overall increase in pull-out force and spread in pull-out experimental curves for those cases in which aggregates are adjacent to the fibres.

To conclude, the scattering of pull-out test results originates from several aspects that influence the complex process of bond developing and subsequent debonding. Since one representative curve is usually needed to estimate the general behaviour and/or numerically reproduce the experimental results, the curve averaging procedure presented by Naaman et al. (Naaman et al., 1989) has been often adopted in the literature (Cunha et al., 2010), (Isla et al., 2015), (Abdallah and Fan, 2017). The criterion proposed by Naaman et al. (Naaman et al., 1989) suggests to take the peak pull-out load equal to the average of the peak pull-out loads recorded for the individual pull-out tests. For the pre-peak branch, the slip axis is divided into a given number of equal intervals and for each of them the corresponding pull-out load is evaluated. The average of these loads at each interval is computed, and taken as the average load at the corresponding end slip interval based on the peak point of the average curve. The same procedure is applied to the descending (post-peak) branch of the average curve.

By following the procedure proposed by Naaman et al. (Naaman et al., 1989) and assuming the slip interval equal to 0.05 mm for the pre-peak branch and equal to 1 mm for the post-peak branch, for the experiments here carried out, Fig. 6.19a represents the average curve of the series of tests on straight fibres, whereas Fig. 6.19b reports the representative curve for the series of tests on hooked-end fibres.

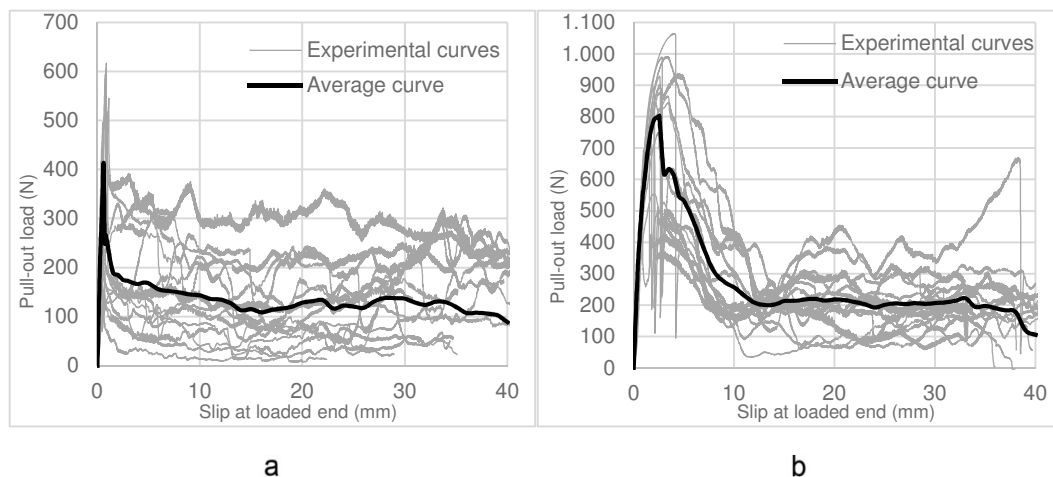


Figure 6.19 - Average curve: a) straight fibres series; and b) hooked-end fibres series

6.3 Comparison between bar and fibre pull-out tests

The results obtained from the bar pull-out tests presented in Chapter 3 and those extracted from the single fibre pull-out tests are here compared in terms of shape of the response curve and bond strength. The comparison is made among the specimens with $\phi 8$ and $\phi 16$ mm bars embedded in LWC with regard to the bar pull-out tests, and the series of pull-out tests on straight fibres from LWC. In this way, the main difference is represented by the reinforcement diameter. Fig. 6.20 shows the average response curve for each group of specimens, i.e. L/PO_B16, L/PO_B8, and L/PO_S1.2. The related results are reported in Table 6.7.

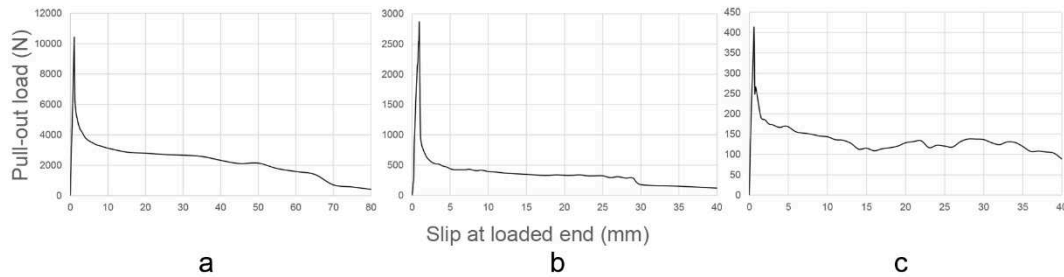


Figure 6.20 - Pull-out Load-slip average curves: a) $\phi 16$ mm bar in LWC specimens (L/PO_B16); b) $\phi 8$ mm bar in LWC specimens (L/PO_B8); and c) $\phi 1.2$ mm fibres in LWC specimens (L/PO_S1.2)

Table 6.7 - Comparison between bar and fibre pull-out tests

Group of specimens	Type of reinforcement	Diameter (mm)	Bond length (mm)	F_{max} (N)	τ_{max} (MPa)	f_{cm} (MPa)	τ_{max}^* (MPa ^{0.5})	S_{bs} (mm)
L/PO_B16	bar	8	40	2846.15	2.59	29.4	0.48	1.06
L/PO_B8	bar	16	80	10404.70	2.84	29.4	0.53	0.94
L/PO_S1.2	fibre	1.2	45	410.95	2.42	49	0.35	0.60

In terms of pull-out responses, the curve shapes demonstrate that the mechanisms acting at the interface are the same for bars and fibres under pull-out conditions. All the curves, in fact, are characterised by the linear bonding phase up to the bond strength, followed by the drop corresponding to a significant loss of adhesion, and afterwards by a decreasing softening branch that makes the pull-out force to decrease down to a residual value until the reinforcement is completely pulled out, i.e. the interface length is equal to zero. Although the matrix is always made of LWC, the average compressive strength for the specimens intended for single fibre pull-out tests resulted much higher than that measured for the concrete matrices in the case of bar pull-out. Thus, even if the measured bond strength values computed for the three groups of specimens analysed are similar (i.e. 2.59, 2.84, and 2.42 MPa for L/PO_B16, L/PO_B8, and L/PO_S1.2, respectively), when they are referred to the concrete compressive strength, the resultant normalised values for bars are higher than that measured for fibres (~ 0.51 vs. 0.35 MPa^{0.5}). As far as the bar pull-out tests are concerned, the behaviours exhibited by $\phi 16$ and $\phi 8$ bars follow the trend

highlighted by Bazant et al. in (Bazant and Sener, 1988) and (Bažant and Desmorat, 1994), i.e. the bond strength is higher when smaller diameters are employed. When the reinforcement is reduced to a fibre, instead, the bond strength in the tests carried out does not increase. This appears to be in contrast to what observed by Bazant et al. (Bažant and Desmorat, 1994), but it should be remarked that the pull-out conditions for the single fibre pull-out tests were different to those adopted for the bar pull-out tests. Thus, the size effect theorised by Bazant et al. ((Bazant and Sener, 1988), (Bažant and Desmorat, 1994)) does not apply to the present case when fibres are employed. Despite this, the analogies observed among the behaviours of bars and fibres need a further investigation. To this end, in the following paragraphs, after a brief introduction on the single fibre pull-out models, FE simulations of single fibre pull-out tests are carried out starting from the models adopted for the bar pull-out models described in Chapter 5.

6.4 Modelling of the single fibre pull-out behaviour: a review on straight and hooked end fibres

The prediction of the fibre pull-out behaviour by employing analytical or numerical models has been largely addressed in the literature. A first classification is based on the fibre geometrical configuration. In fact, models suitable for straight fibres are not always able to describe the pull-out behaviour of deformed fibres, since the behaviour of hooked-end fibres is thoroughly governed by the mechanical anchorage (Cunha, 2010). Therefore, a brief summary on the basis of modelling for straight and hooked-end fibre under pull-out conditions is made in the next paragraphs, while the numerical simulation of the tests carried out in the present thesis is carried out in the forthcoming paragraph 6.5.

6.3.1 Models for straight fibres

Lawrence (Lawrence, 1972) proposed one of the first pull-out model relating the shear stress distribution along the fibre to the matrix and fibre elastic properties and assuming constant friction along the failed interface (Cunha, 2010). This model laid the basis for further enhancements proposed by Gopalaratnam and Shah (Gopalaratnam and Shah, 1987). Their model assumes an initial elastic transfer of the interfacial shear stresses, which shifts progressively to a frictional interaction when debonding takes place. The model proposed by Wang et al. (Wang et al., 1988), instead, considers only frictional bond, without the elastic stress transfer at the beginning of the pull-out.

The model proposed by Naaman et al. (Naaman et al., 1991) for the pull-out behaviour of straight fibres, employs an idealised stress-slip relationship. Linear elasticity prevails until the bond shear strength at the interface is reached. In correspondence of the bond strength it is assumed a complete failure of the bond and, by incrementing further the slip, a dynamic frictional condition takes place under a constant frictional shear stress. Thus, the entire pull-out force-slip response of a straight fibre may be separated into three stages, i.e. (i) linear-elastic stage, where the fibre length is assumed to be perfectly bonded to the matrix; (ii) partial debonding stage, where, beyond the pull-out strength, a part of the fibre is still fully bonded to the matrix while the remaining part is debonded; and (iii) fully

debonded and frictional pull-out stage, characterised by the complete debonding of the fibre from the matrix and by the pull-out force decrease governed by friction. Naaman et al. (Naaman et al., 1991), observed also that for large slip the frictional stress decays with an exponential law with growing slip.

The previous models can be classified among the ‘*stress-based models*’, which assume that debonding occurs when the interfacial shear stress exceeds the shear strength. However, the pull-out problem can be described also by ‘*fracture-based models*’ by treating the debonding zone as an interfacial crack. The condition for the debonding propagation is such that an adequate fracture energy must be supplied (Stang et al., 1990).

6.3.2 Models for hooked-end fibres

Among the deformed fibre, the models predicting the pull-out behaviour of hooked-end fibres are here briefly discussed, since they are employed also in the present experimental work.

In the field of the hooked-end fibres two main approaches for modelling the pull-out behaviour have been theorised in the past: the first uses the equations of static force and moment equilibrium in a friction pulley analogue (Alwan et al., 1999); and the second one adopts the principle of virtual work (Chanvillard, 1999). Both of the theories admit static and dynamic friction respectively for static elastic loading and for dynamic slip beyond the elastic limit (Abdallah et al., 2018).

The model proposed by Alwan et al. (Alwan et al., 1999) accounts for the mechanical anchorage contribution provided by the fibre hook as a friction pulley analogue. The pull-out load versus slip curve is similar to that of a straight fibre up to the load value corresponding to the complete debonding, i.e. the pull-out strength in the case of the straight fibre. Therefore, the mechanical bond provided by the hook is considered as a function of the work needed to straighten the fibre during pull-out, i.e. the work of the two plastic hinges corresponding to the two bends at the fibre end. Thus, in order to predict the full pull-out response a two-step process is needed: the first step considers the pull-out load increase provided by the plastic hinges, whereas the second step adds the frictional action to the hinges work. An enhancement of this model has been recently proposed by Abdallah and Fan (Abdallah et al., 2016a) by considering a polynomial function enabling a continuous pull-out versus slip curve.

As for the virtual work-based model proposed by Chanvillard (Chanvillard, 1999), it applies the virtual work principle to each release of the anchorage provided by the hooked-end fibre.

6.3.3 Numerical implementation

The fibre pull-out process has been described in detail and analytically formulated by Naaman et al. (Naaman et al., 1991) as a process consisting of three main stages, i.e. bond phase, debonding phase and frictional stage. The implementation of models describing the fibre pull-out in the framework of numerical analysis has been largely addressed in the literature. As discussed in Chapter 2 of the present thesis, many approaches are possible when FE analysis is employed to describe the pull-out process (e.g. fracture mechanics

approach, damage mechanics theory, cohesive zone modelling, etc.). Among others, CZMs have been here taken into account and an enhanced multiplane cohesive model has been formulated to describe the bar pull-out phenomenon. A further application of this model to the case of the single fibre pull-out process is carried out in the next paragraph.

6.5 Finite element analysis of single fibre pull-out tests

The FE simulation of the single fibre pull-out tests is carried out by employing the enhanced degrading M-CZM formulation presented in Chapter 5. This provides a further validation of the model, whose range of applicability is investigated with respect to the debonding process of a single fibre embedded in a concrete matrix. The attention has been focused on the series of specimens having straight fibres. The considerations made for the bar pull-out problems concerning the symmetry and the usage of a 2D axisymmetric modelling approach apply also to the present case. However, the values of the enhanced degrading M-CZM parameters that better represent the experimental results are different to those identified for bars. An analysis of these differences is made here in order to verify if they are consistent with the physics of the phenomenon.

6.5.1 Finite element simulation of straight single fibre pull-out test

Fig. 6.21 shows the FE model employed for the analysis, with the geometrical details (Fig. 6.21a), the boundary conditions (Fig. 6.21b), and the mesh discretisation (Fig. 6.21c) adopted.

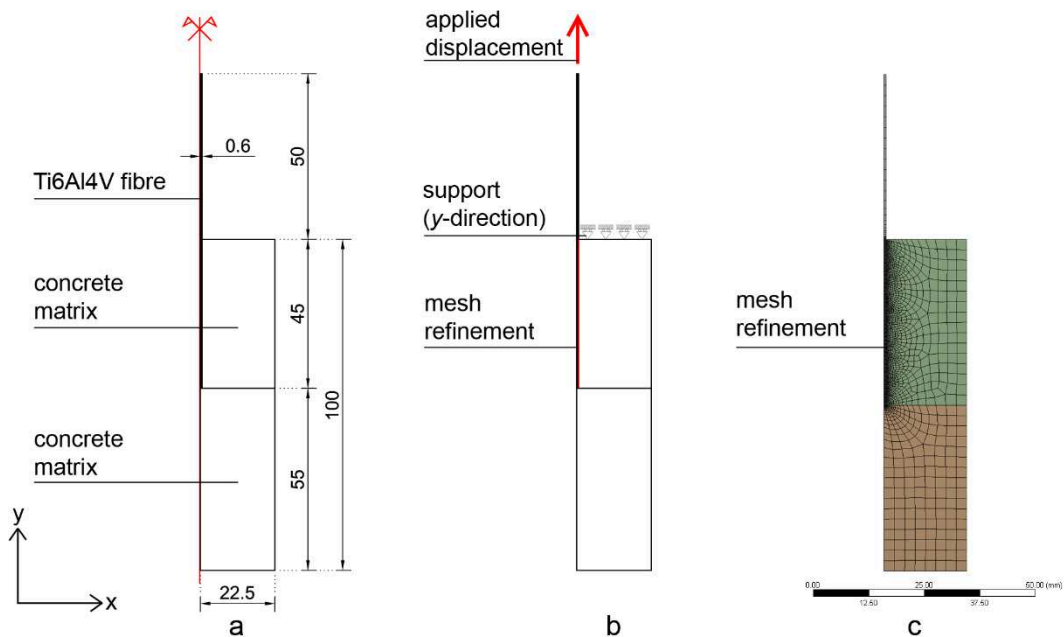


Figure 6.21 - 2D axisymmetric FE model of the single straight fibre pull-out tests: a) geometry, b) boundary conditions; and c) mesh discretisation

As for the material models adopted, the titanium alloy and concrete have been modelled through linear-elastic behaviour, as in the case of the bar pull-out models. The bulk material properties are reported in Table 6.8.

Table 6.8 - Material properties for the FE analysis

	Isotropic elasticity					
	Density	Young's modulus	Poisson's ratio	Tensile Yield Strength	Compressive Ultimate Strength	Tensile Ultimate Strength
	(kg/m ³)	(MPa)	(-)	(MPa)	(MPa)	(MPa)
LWC	1900	30400	0.18	(-)	49	1.22
Ti6Al4V	4500	100000	0.36	820	(-)	857

The enhanced degrading M-CZM has been adopted for modelling the interface debonding. The most suitable values of the model parameters have been identified starting from those identified for the bar pull-out test simulations. The resulting parameters values are reported in Table 6.9.

Table 6.9 - Enhanced degrading M-CZM input parameters for the single fibre pull-out test FE simulation

Parameter	Unit	Value
G_c	(kJ/m ²)	0.726
σ_0	(MPa)	2.42
η	(-)	0.25
θ_{01}	(deg)	-50
θ_{f1}	(deg)	-13
ζ_{01}	(m ² /kJ)	1.70
H_{N01}	(mm)	0.002
θ_{02}	(deg)	0
θ_{f2}	(deg)	0
ζ_{02}	(m ² /kJ)	0
H_{N02}	(mm)	0.002
θ_{03}	(deg)	50
θ_{f3}	(deg)	13
ζ_{03}	(m ² /kJ)	1.70
H_{N03}	(mm)	0.002
μ	(-)	0.50

The comparison between the numerical curve and the experimental average curve obtained from the experimental tests is reported in the following Fig. 6.22. By following the same procedure adopted for the bar pull-out simulations, the analysis is carried out up to a slip equal to 12.5 mm, which represents about the 30% of the bond length.

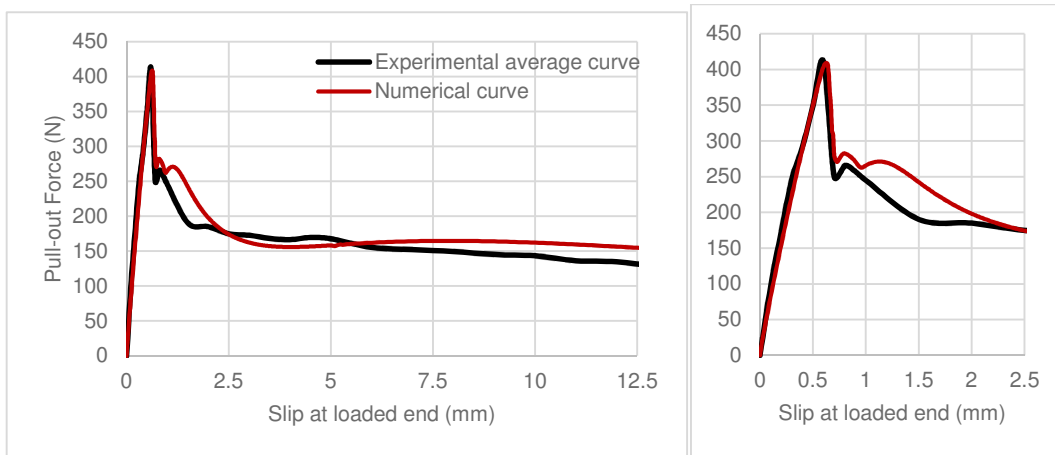


Figure 6.22 - Comparison between the experimental average curve and the numerical curve obtained with the enhanced degrading M-CZM: curve until a slip equal to 12.5 mm; and zoom on the first 2.5 mm of slip

From Fig. 6.22 it is possible to observe that the enhanced degrading M-CZM is able to capture the experimental behaviour with good approximation. As for the linear behaviour and the immediate drop of the pull-out force, the numerical model replicates almost perfectly the experimental results. In the post-peak range, instead, some discrepancies between experiments and simulation can be observed. However, from the qualitative point of view, it can be assessed that, by employing the enhanced degrading M-CZM, the FE model is able to capture the main features of the experimental curve. In fact, the second local maximum in the pull-out force and the following softening characterising the test responses are present in the numerical curves. This result has been obtained by adopting the parameters values reported in Table 6.9. With reference to the values identified for the bar pull-out tests, the changes in the parameters values for the single pull-out simulations, regard:

- the fracture parameters (G_c , σ_0 , and η): their values are extracted from the experimental results. This means that it was not possible to adopt the same fracture parameters adopted for the bar pull-out simulations. Besides, this appears to be consistent with the size effects usually characterising the pull-out responses and, mostly, with the fact that different set-up has been adopted for the tests;
- the characteristic energy value ($\zeta_0 = \zeta_{01} = \zeta_{03}$): this value was equal to 2.50 kJ/m² for LWC and to 1.80 kJ/m² for NWC in the case of bar pull-out models. In the single fibre pull-out tests the concrete batch was LWC but, as previously reported, it exhibited different mechanical properties from the LWC realised for the bar pull-out tests, i.e. higher density (from 1735 to 1900 kg/m³) and higher compressive strength (from 29 to 49 MPa). Thus, the lower ζ_0 that had to be adopted for the single fibre pull-out simulations does not surprise and, moreover, it appears consistent with the trend observed, that is higher density and compressive strength lead to lower characteristic energy value;

- the initial asperities depth ($H_{N0} = H_{N1} = H_{N3}$): from the considerations made in Chapter 5, it has been observed a relation between the dimension of the dilated interface, measured with SEM, and the value of H_{N0} . Particularly, for bar pull-out tests the identified value of H_{N0} was equal to 10-15 μm . In the fibre pull-out simulations, instead, the most suitable value of H_{N0} is equal to 2 μm . If H_{N0} is actually able to represent the asperities originated from the adhesion between the reinforcement and concrete (i.e. the concrete material attached to the surface of the reinforcement that creates a new irregular interface), it appears reasonable that for fibres the value of H_{N0} is lower. This is because the reinforcement surface is much less extended than that of bars and, thus, the asperities that might originate from the reinforcement-matrix adhesion should be smaller;
- the final value of the microplane inclination angle ($\theta_f = \theta_{f1} = -\theta_{f3}$): in this case the value adopted for the bar pull-out simulations (with reference to LWC) was lower than that suitable for representing the fibre pull-out response (i.e. from 6 deg to 13 deg). The value of θ_f is related to the residual pull-out force in the softening phase of the curve response, and, in the enhanced degrading M-CZM it is the result of the microplanes degradation. The fact that a lower value of θ_f better represents the case of fibre with respect to bar pull-out simulations, can be attributed to a reduced capacity to break the asperities. In fact, if the asperities are less deep for fibres than for bars (i.e. lower values of H_{N0}), it is also reasonable to assume that the microplanes degradation process is weaker than that hypothesised for bar debonding. Thus, starting from the same initial microplanes inclination angle ($\theta_0=50$ deg) necessary leads to different final microplanes inclination angles ($\theta_f=6$ deg for bars and $\theta_f=13$ deg for fibres).

Chapter 7

Titanium Alloy-Fibre Reinforced Lightweight Concrete: a preliminary experimental study

In this chapter, a preliminary study on the possibility to conceive a fibre reinforced concrete with titanium alloy fibres is carried out. The experimental tests here presented are aimed to measure the performance of a lightweight titanium alloy-FRC, thus LWC mixture is adopted for the matrix, whereas two different alloys of titanium are used to realise the reinforcing fibres. The fracture toughness of the resultant material, i.e. Titanium Fibre Reinforced Lightweight Concrete (here called ‘TiFRC’ for the sake of brevity), has been measured through three-point bending tests on standardised specimens and through a flexural test on a full-scale beam. Since the metallic nature of titanium alloy fibres, steel-fibre reinforced concrete (SFRC) is taken as reference for the typical values of fibre percentage in the mixture, and for the standards to adopt to carry out the tests. Moreover, the effects induced by fibres corrosion on SFRC performance are discussed, because they represent the main reason why alternative materials for fibres have been investigated in the literature and proposed in the present thesis.

7.1 Some concepts on steel fibre reinforced concrete

Since titanium is a metallic material, in this paragraph particular attention is focused on steel fibre reinforced concrete (SFRC) in terms of typical geometrical configurations and volume fractions of fibres; and mechanical and durability properties.

As far as geometrical configuration is concerned, possible cross-sectional shapes for steel fibres are circular, rectangular square, triangular, flat, polygonal, etc.; whereas to obtain better bond performance the longitudinal geometry of the fibre can be modified by roughening its surface or by inducing mechanical deformation. Thus, fibres can be smooth,

indented, crimped, twisted, hooked or paddled-end, etc. Typical examples of steel fibres according to Naaman (Naaman, 2003) are reported in Fig. 7.1.

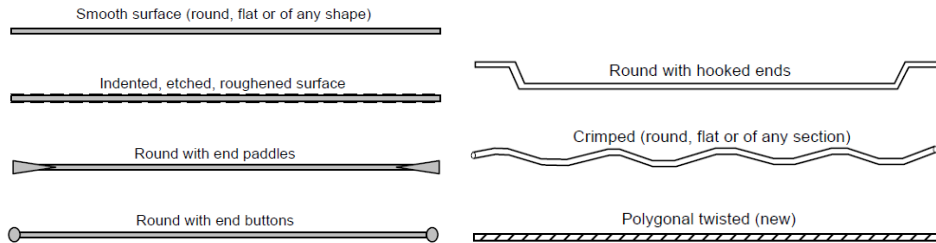


Figure 7.1 - Typical profiles of steel fibres used in concrete according to Naaman (Naaman, 2003)

Remarkable importance is also assumed by the *aspect ratio*, that is the ratio of length over diameter or equivalent diameter. Common values of the aspect ratio for steel fibres vary between 40 and 80, thus they can be considered small enough to be randomly dispersed in a concrete mixture through usual mixing procedures.

7.1.1 Mix design

Generally, SFRC can be produced using conventional concrete practices, even if some important differences should be taken into account (Bentur and Mindess, 2007). The standard ACI 544.3R-08 (ACI Committee 544, 2008) and the CNR instructions DT204-2006 (CNR, 2007) describe these differences, giving guide lines to cast an efficient SFRC. The basic problem is to find a good compromise between enhanced mechanical properties and workability. In fact, the volume fraction of uniformly dispersed fibres must be high enough to achieve the desired improvements in mechanical behaviour, while maintaining sufficient workability in the fresh mix to allow proper mixing, placing and finishing (Bentur and Mindess, 2007). The problems of both workability and uniform distribution increase with increasing fibre length, volume, and aspect ratio. Moreover, the introduction of steel fibres into a concrete mix adversely affects the packing density of the aggregates, limiting the maximum fibre content (Hoy and Bartos, 1999).

For all these reasons, the typical percentage of fibres volume fraction is within the range 0.5-2%. For relatively small fibre volumes ($\sim 0.5\%$), the conventional mix designs used for plain concrete, based on normal strength and durability considerations, might be adopted without further precautions. Conversely, for larger fibre volumes, mix design procedures which emphasise the workability of the SFRC seem to be more suitable (Bentur and Mindess, 2007).

7.1.2 Mechanical properties

A brief description of the mechanical properties of the SFRC is here reported, referring to paragraph 7.2 for the explanation of the test procedures commonly adopted to obtain them.

As for the behaviour of SFRC under compression, the fibres contribution cannot be considered significant in terms of strength (Fanella and Naaman, 1985). However, the presence of fibres substantially increases the post-cracking ductility, i.e. the energy absorption of the material (Nataraja, 1999). The direct tensile strength of the concrete, instead, can be strongly enhanced when fibres are aligned with respect to the direction of the tensile load (Grimaldi and Luciano, 2000), whereas, for a randomly fibres distribution, the increase in strength is much smaller, with many investigations indicating values around 30% (Hughes, 1981). As it happens in compression, steel fibres lead to major increases in the post-cracking behaviour or toughness of the composites (Bentur and Mindess, 2007).

As far as the mechanical behaviour of SFRC is concerned, the fibres are found to have much greater effect on the flexural strength than on either compressive or tensile strengths (Bentur and Mindess, 2007). The flexural strength is often related to the term $W \cdot l_e/d_s$, where W is the weight per cent of fibres and l_e/d_s is the aspect ratio, i.e. the ratio of the equivalent length of the fibre (l_e) over its diameter (d_s). Usually, the higher is this term, the larger is the flexural strength. However, for $W \cdot l_e/d_s > 600$, it has been observed that non-uniform fibre distribution or insufficient workability may occur, leading to unsatisfactory mechanical properties (Bentur and Mindess, 2007).

As a consequence of the improved material integrity provided by the fibre bridging effect, the shear resistance of SFRC is usually larger than that of plain concrete (Khaloo and Kim, 1997). Although many parameters have been found to affect the shear strength of SFRC (e.g. fibre volume fraction, aspect ratio, concrete compressive strength, tensile reinforcement ratio, and span-depth ratio (Slater et al., 2012)), Narayanan and Darwish (Narayanan and Darwish, 1987) assessed that SFRC beams with higher steel fibre volumes result in higher shear strengths regardless of the concrete strength and fibre aspect ratio. However, the prediction of the increase in shear strength due to the presence of steel fibre still represents a difficult task (Slater et al., 2012).

Although the improvement in strength provided by the addition of steel fibres to concrete matrices, the major advantage of FRC over its unreinforced counterpart lies in the enhanced flexural toughness (Banthia and Sappakittipakorn, 2007). Commonly, the flexural toughness is defined as the area under the load-deflection (or stress-strain) curve in flexure. It should be underlined that, as is the case of flexural strength, flexural toughness also increases with growing ratio $W \cdot l_e/d_s$. Details on the methods employed to measure the flexural toughness are provided in the forthcoming paragraph 7.3.

7.2.2.1 Hardening and softening responses

With regard to the tensile and flexure performances of FRC, either softening or hardening behaviour can be observed in the post-cracking response. If the maximum load capacity corresponds to the first crack strength, the composite is considered to have a softening post-crack behaviour (Figs. 7.2a and 7.2b). The softening response is usually associated to a concentration of deformation in a single crack. For the composites exhibiting a hardening behaviour (Figs. 7.2c and 7.2d), instead, the load carrying capacity increases after the first crack strength. The formation of multiple cracks with limited width characterises the hardening post-cracking response (Naaman and Reinhardt, 2003). These

composites are usually called ‘high-performance fibre-reinforced cement composite (HPFRCC)’, with ‘high-performance’ indicating growing stresses after the cracking strength (Shi et al., 2015).

The nature (i.e., softening or hardening) of the post-cracking response is dependent on the type, geometry, volume and properties of the fibres; the properties of the cementitious matrix; and the interface properties (Naaman, 2007).

The softening and hardening behaviour characterise both tensile and bending load responses (Fig. 7.2). When FRC exhibits a hardening response in tension (referred to as *strain-hardening*) (Fig. 7.2c) always results in a hardening response in bending (*deflection-hardening*) (Fig. 7.2d); whereas a FRC with a softening response in tension (referred to as *tension-softening*) (Fig. 7.2a) may lead to either a *deflection-softening* (Fig. 7.2b) or a *deflection-hardening* (Fig. 7.2d) response.

Typically, SFRC behaviour shows tension- and deflection-softening responses, even if the mix proportion can be modified in order to obtain a deflection-hardening response in bending. This can be done by increasing the volume fraction of fibres in the mix (Rizzuti and Bencardino, 2014). Commonly, fibre volume percentages lower than 2% result in a softening-deflection behaviour, while for higher volume fractions a hardening-deflection behaviour has been often detected (CNR, 2007). Clearly, this threshold value is not fixed, but it represents a good reference for predicting the behaviour of the material under consideration. With regard to SFRC, typical fibre volume percentages are lower than 2% especially due to the geometrical configurations and dimensions usually adopted. Thus, this kind of FRC is expected to exhibit tension-softening and deflection-softening responses.

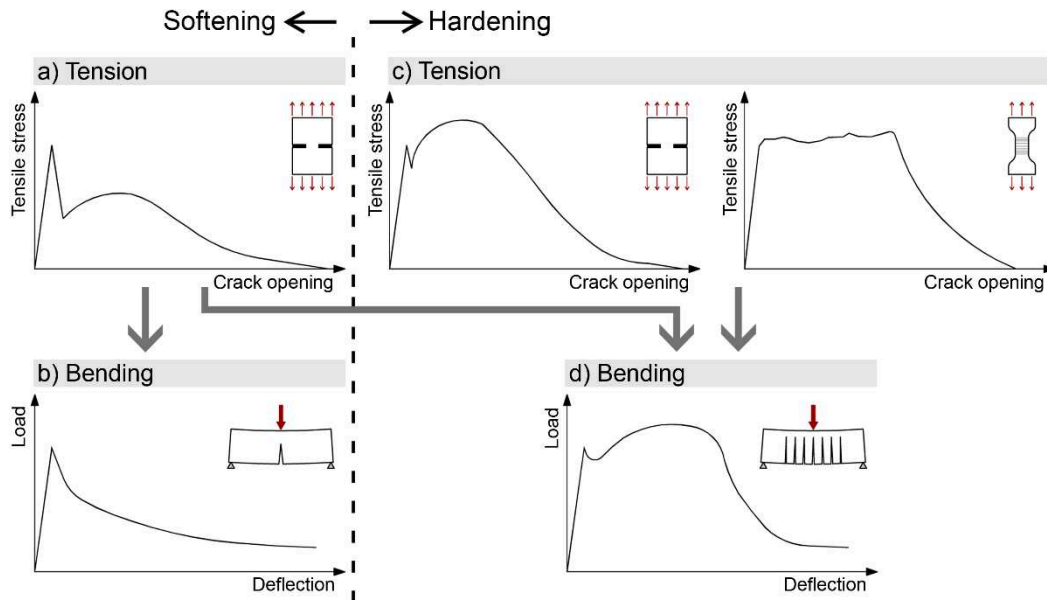


Figure 7.2 - Softening and hardening behaviour of FRC: a) tension-softening; b) deflection-softening; c) tension-hardening; and d) deflection-hardening

7.2.3 Durability

Another important aspect, which needs to be taken into account when SFRC is concerned, is durability. This is because, as in the case of traditional RC structures, steel reinforcements inside the concrete matrix may undergo corrosion, resulting in detrimental effects on mechanical and durability performances. In fact, corrosion represents the predominant deterioration process in RC structures and in the last years, the growing applications of SFRC led many studies to investigate the corrosion susceptibility of steel fibres (Granju and Balouch, 2005), (Balouch et al., 2010), (Berrocal et al., 2013).

A first result that has been widely reported is that in case of SFRC, steel fibre corrosion is much less severe comparing to steel reinforcing bars (Balouch et al., 2010). Since steel fibres are characterised by a large surface area-to-volume ratio, the layer around the reinforcement is able to screen more effectively steel fibres than large diameter bars (Granju and Balouch, 2005). Moreover, the presence of fibres reduces the permeability of cracked concrete due to a change in the crack profile which shifts from the formation of few large cracks to a multitude of closely spaced micro-cracks (Rapoport et al., 2002), (Ahmed and Mihashi, 2007). In fact, the concrete cracking promotes the chloride penetration, which, is one of the major forms of environmental attack to reinforced concrete and induces reinforcement corrosion (Shi et al., 2012). Clearly, the larger is the crack width, the easier are the chlorides penetration and transport inside the matrix. Thus, the fibre bridging action across micro-cracks before they coalesce is able to sensibly reduce the environmental attack, resulting in less susceptibility to reinforcement corrosion and more durability of SFRC with respect to plain concrete (Solgaard et al., 2010).

Despite these considerations, corrosion of fibres may occur in SFRC, producing micro-spalling of concrete, as well as the reduction of the sectional area of the fibres (Granju and Balouch, 2005). A recent study by Marcos-Meson et al. (Marcos-Meson et al., 2017) identified 4 main stages (Fig. 7.3) in the process of corrosion of steel fibres in a cracked concrete matrix:

- 1) The steel-matrix interfacial transition zone (ITZ) on steel fibres plays the role of a protective coating, preventing the access of aggressive agents, such as oxygen and chlorides (Fig. 7.3a). In fact, the ITZ for steel fibres appears more uniform and denser than that for conventional steel rebars;
- 2) As the matrix cracks due to exceeded tensile strength of concrete, the fibre-matrix bond is 'activated', resulting in increasing strains at the interface and damage at the ITZ. The extent of this damage is related to the strain (i.e. larger crack widths lead to greater damage at the ITZ) and the shape of the fibres. Granju and Balouch (Granju and Balouch, 2005) observed that deformed geometrical configurations (i.e. hooked-end fibres) are more susceptible of localised corrosion damages. The damaged ITZ would provide a preferential path for diffusion of the aggressive agents (Fig.7.3b);
- 3) As long as the composite does not reach a critical crack width, the damaged fibre-matrix interface would eventually heal, recovering similar conditions to the original state (stage 1) and recreating the passive layer (Homma et al., 2009) (Fig.

7.3c). Actually, as it happens in the case of steel rebars for low corrosion level, the expansive effect of the corrosion products would increase the fibre-matrix frictional bond, resulting in the improved residual-tensile strength observed by Granju and Balouch (Granju and Balouch, 2005);

- 4) When the damage at the fibre-matrix interface increases due to larger strain and exceeded crack width, the ITZ regions with greater damage (e.g. deformed regions, fibre-crack intersection) are characterised by progressive and localised reduction of the fibre cross-section due to corrosion (Fig. 7.3d). The ITZ is not able to heal anymore and once the critical cross-section is reached (i.e. the tensile capacity of the steel is lower than the fibre-matrix bond strength), the failure mode of the SFRC would shift from fibre pull-out to fibre yield, resulting in decreased residual-tensile strength.

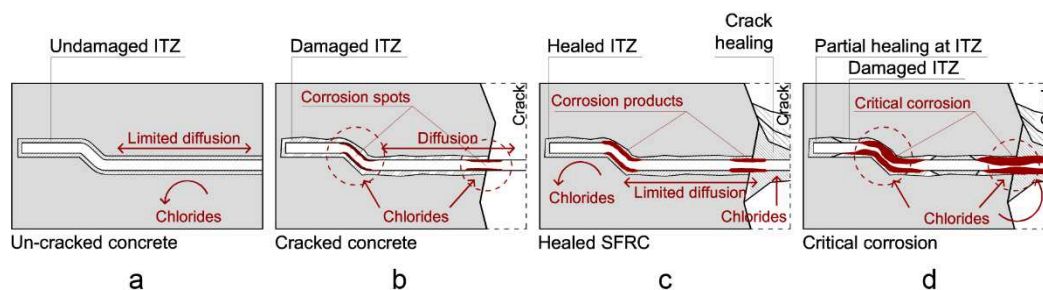


Figure 7.3 - Corrosion mechanisms on: a) un-cracked concrete; b) cracked concrete at an early stage; c) cracked concrete after autogenous healing; d) cracked concrete with critical corrosion on fibres [based on (Marcos-Meson et al., 2017)].

It is worth underlying that, as reported by many authors ((Bentur and Mindess, 2007); (Homma et al., 2009); (Kim et al., 2014)) and, more recently, by Marcos-Meson et al. (Marcos-Meson et al., 2017), there still is limited information about the processes induced by the fibre-matrix ITZ due to corrosion of steel fibres.

7.3 Overview of standardised test methods to characterise SFRC

This paragraph summarises some of the currently available test methods for measuring the mechanical properties of FRC materials. The FIB Model Code 2010 (fib, 2012b) provides the descriptions of testing and mechanical characterisation of FRC, emphasising the importance of defining suitable material parameters, including post-peak tensile behaviour.

As far as the behaviour in compression is concerned, the compressive relations valid for plain concrete apply to SFRC (fib, 2012b). RILEM Technical Committee TDF-162 (RILEM T.C. 162-TDF, 2002) suggests that the compressive strength of SFRC should be determined by means of standard tests, on either concrete cylinders or cubes.

With regard to the tensile behaviour, which is the most important aspect of SFRC, various test methods are possible. Three main categories of tests, are available to evaluate the behaviour in the post-cracking field (Paegle, 2015):

- Uni-axial tension tests: performed on notched FRC specimens for measuring the relation between tensile stresses and crack opening (Pereira et al., 2010); or on un-notched dogbone specimens for strain hardening FRC materials in order to provide the tensile stress-strain relationship (JSCE, 2008), (Paegle and Fischer, 2011);
- Flexural beam tests: three-point bending beam tests on notched specimens are suggested in the *fib* Model Code (fib, 2012b) and adopted from several standards, including the European standard EN 14651 (EN 14651, 2005), the RILEM Technical Committee guidelines (RILEM T.C. 162-TDF, 2002), the American ASTM C1609-C1609M-12 (ASTM C1609/C1609M-12, 2012), and the Italian guidelines for design, construction and production control of FRC structures (CNR, 2007). Similarly, many standards such as ASTM C1609-C1609M-12 (ASTM C1609/C1609M-12, 2012) and the Italian guidelines (CNR, 2007) contemplate also the four-point bending test on un-notched prisms;
- Flexural plate tests: the two most commonly used plate tests are standardised by ASTM C1550 (ASTM C1550 - 12a, 2012) which involves a round panel with 3 point supports, and by EN 14488-5 (EN 14488-5:2006, 2006) in which the specimens are square panels with continuous support.

In the present research, the three-point bending test (3PBT) on notched specimens according to EN 14651 (EN 14651, 2005) has been selected for characterising the tensile behaviour of the lightweight FRC with titanium alloy fibres here designed. Thus, a brief explanation of this test is made in the next paragraph, referring to the standard (EN 14651, 2005) for all the details.

7.3.1 Three-Point Bending Test (EN 14651)

The European Standard EN 14651 (EN 14651, 2005) describes the method for measuring the flexural tensile strength of metallic fibred concrete on moulded test specimen, with particular reference to the determination of the limit of proportionality (LOP) and of a set of residual flexural tensile strengths. This testing method and the relative specimen shape and size are intended for metallic fibres no longer than 60 mm and for concrete matrix with maximum size of aggregate less than or equal to 32 mm. The tensile behaviour of metallic fibre concrete is evaluated in terms of residual flexural tensile strength values determined from the load-crack mouth opening displacement curve or load-deflection curve, obtained by applying a centre-point load, F , on a simply supported notched prism. The definitions of the quantities relevant to this test, provided by the standard EN 14651 (EN 14651, 2005), are as follows:

- crack mouth opening displacement ($CMOD$): linear displacement measured by a transducer shown in the forthcoming Fig. 7.4b, on a prism subjected to a centre-point load F ;
- limit of proportionality (LOP): stress at the tip of the notch which is assumed to act in the un-cracked mid-span section, with linear stress distribution, of a prism subjected to the centre-point load F_L (i.e. the load value corresponding to the LOP);

- residual flexural tensile strength: fictitious stress at the tip of the notch which is assumed to act in the uncracked mid-span section, with linear stress distribution, of a prism subjected to the centre-point load F_j corresponding to $CMOD_j$, where $CMOD_j > CMOD_{FL}$, or to δ_j , where $\delta_j > \delta_{FL}$ ($j = 1,2,3,4$).

Fig. 7.4a shows the testing set-up and the specimen dimension details as standardised by the EN 14651 (EN 14651, 2005). The test specimens shall be prisms with a nominal size (width and depth) of 150 mm and a length, L , so that $550 \text{ mm} \leq L \leq 700 \text{ mm}$. A wet sawing should be used to notch the test specimens. Specimens shall be rotated over 90° around their longitudinal axis and then sawn through the width of specimen at mid-span. The notch width must be 5 mm or less, the distance h_{sp} shall be $125 \text{ mm} \pm 1 \text{ mm}$, as shown in Fig. 7.4b, which provides also details of the transducer (strain gauge) position.

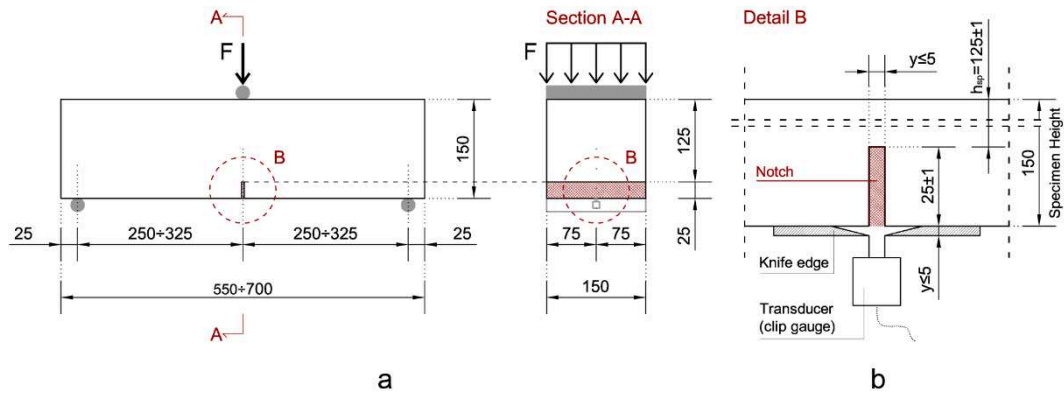


Figure 7.4 - Three-point bending test set-up according to EN 14651 (EN 14651, 2005): a) set up and specimen dimensions; b) details of the notch and the transducer

Results of the three-point bending test (3PBT throughout the thesis) are expressed in terms of $CMOD$, LOP and residual flexural tensile strength, $f_{R,j}$. Being y the distance between the bottom of the test specimen and the line of measurement individuated through the position of the transducer (Fig. 7.4b), the relation between $CMOD$ and deflection δ is given by the following Eq. (7.1) depending on the value of y , according to EN 14651 (EN 14651, 2005):

$$\delta = \begin{cases} 0.85 \cdot CMOD + 0.04 & y = 0 \\ 0.85 \cdot CMOD_y \cdot \frac{h}{h+y} + 0.04 & y > 0 \end{cases} \quad (7.1)$$

where:

$CMOD_y$ → $CMOD$ value, in millimetres, measured in case $y > 0$;

h → total height of the specimen in millimetres.

Eqs. (7.2) and (7.3) provide the LOP and the residual flexural tensile strength, respectively.

$$f_{ct,L}^f = LOP = \frac{3F_L l}{2bh_{sp}^2} \quad (7.2)$$

$$f_{R,j} = \frac{3F_j l}{2bh_{sp}^2} \quad (7.3)$$

where:

- $f_{ct,L}^f$ → LOP , in Newton per square millimeter;
- $f_{R,j}$ → residual flexural tensile strength corresponding to $CMOD = CMOD_j$ or $\delta = \delta_j$ ($j=1,2,3$ or 4), in Newton per square millimeters;
- F_L → load corresponding to the LOP , in Newton;
- F_j → load value corresponding to $CMOD = CMOD_j$ or $\delta = \delta_j$ ($j=1,2,3$ or 4), in Newton;
- l → span length, in millimetres;
- b → width of the specimen, in millimetres;
- h_{sp} → distance between the tip of the notch and the top of the specimen, in millimetres.

The load value F_L is determined by drawing a line at a distance of 0.05 mm and parallel to the load axis (y axis) of the load- $CMOD$ or load-deflection diagram and taking as F_L the highest load value in the interval $0 \leq CMOD \leq 0.05$ mm. An example of the identification of F_L is provided in Fig. 7.5. The load values F_j , instead, are those corresponding to the respective values of $CMOD$, as shown in Fig. 7.5.

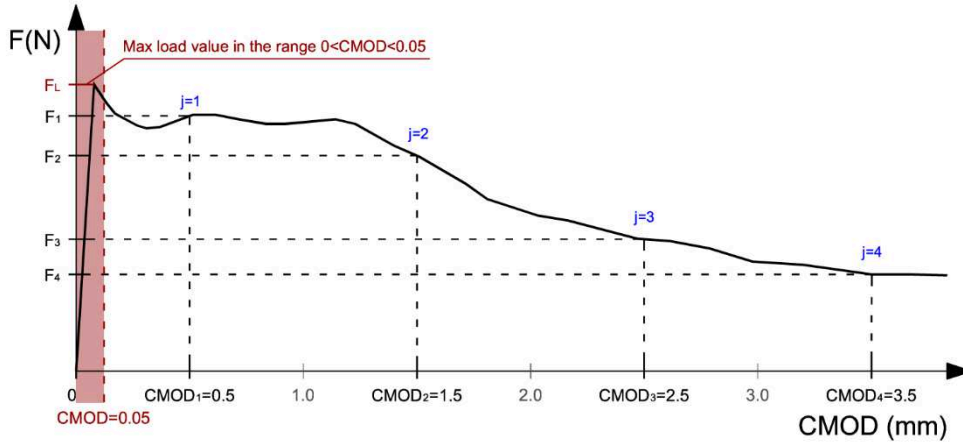


Figure 7.5 - Example of the load- $CMOD$ response of a 3PBT with the indication of F_L , $CMOD_j$ and the respective F_j

7.4 Experimental tests on TiFRC specimens

In this paragraph the experimental tests carried out on the composite material here denominated for brevity ‘TiFRC’ (titanium fibre reinforced lightweight concrete) are reported. Considering that no data have been found in the literature with respect to the

possibility of using titanium alloy fibres as reinforcement for FRC, several tests were performed in order to measure the mechanical characteristics of TiFRC. Moreover, tests on plain concrete intended for comparison have been carried out too.

7.4.1 Materials and fibres geometrical configuration

The materials employed in this experimental work are lightweight concrete (LWC) for the matrix and two different titanium alloys, i.e. Titanium Grade 2 (commercially pure titanium) and Titanium Grade 5 (titanium alloy Ti6Al4V) (ASTM B348-13, 2015) for the fibres. As far as LWC is concerned, the mix design adopted is the same as that reported in Table 6.2 of Chapter 6. The mechanical properties have been established by performing compressive and indirect tensile tests, as reported in the following paragraph 7.4.2. With regard to titanium, instead, two different alloys are employed for the fibres. The latter have been realised starting from titanium wires of diameter 1 and 0.9 mm for titanium grade 2 and grade 5, respectively. The geometrical configuration chosen is the double hooked-end shape, previously tested through single fibre pull-out test in Chapter 6 and shown in detail in Fig. 7.6. The mechanical properties are provided by the manufacturer and summarised in Table 7.1.

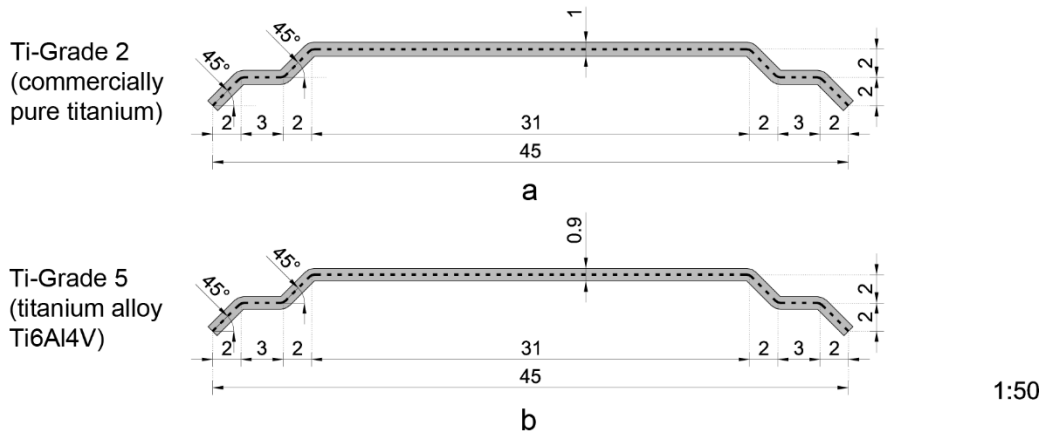


Figure 7.6 - Fibres geometry hooked-end configurations: a) Titanium Grade 2; b) Titanium Grade 5

Table 7.1 - Mechanical properties of the titanium wires provided by the manufacturer

Alloy	Nomenclature	Diameter	Length	Yield strength	Elongation
		ϕ (mm)	l (mm)	f_{ty} (MPa)	
Titanium Grade 2 (commercially pure titanium)	Ti-gr2	1.0	1000	345	20
Titanium Grade 5 (Ti6Al4V titanium alloy)	TI-gr5	0.9	450	820	6

7.4.2 Specimen preparation and test set-up

Three different batches have been casted, namely plain lightweight concrete, titanium grade 2 fibre reinforced lightweight concrete (Ti-gr2FRC throughout the thesis) and

titanium grade 5 fibre reinforced lightweight concrete (Ti-gr5FRC). For each batch, several groups of specimens were realised in order to perform compression, indirect tensile and three-point bending tests, depending on the batch. The following Table 7.2 and Figs. 7.7-7.9 summarise the specimens realised for each batch, providing also the nomenclature adopted hereafter and the tests they are intended for.

Table 7.2 - Cast details and specimen identification for each batch

Cast		Fibres		Compression test (CT)		Indirect tensile test (ITT)		Three-point bending test (3PBT)	
N°	Name	Geometry /material	V_f (%)	N°	Specimen	N°	Specimen	N°	Specimen
#1	Ti-gr2FRC	HE/ Ti-gr2	0.5	2	Ti-gr2_CT-1 Ti-gr2_CT-2 - -	- - - -	- - - -	4	Ti-gr2_3PBT-1 Ti-gr2_3PBT-2 Ti-gr2_3PBT-3 Ti-gr2_3PBT-4
#2	Ti-gr5FRC	HE/ Ti-gr5	0.5	2	Ti-gr5_CT-1 Ti-gr5_CT-2 - -	- - - -	- - - -	4	Ti-gr5_3PBT-1 Ti-gr5_3PBT-2 Ti-gr5_3PBT-3 Ti-gr5_3PBT-4
#3	Plain	-	-	3	P_CT-1 P_CT-2 P_CT-3	3	P_ITT-1 P_ITT-2 P_ITT-3	4	P_3PBT-1 P_3PBT-2 P_3PBT-3 P_3PBT-4

CAST #1 - Ti-gr2FRC

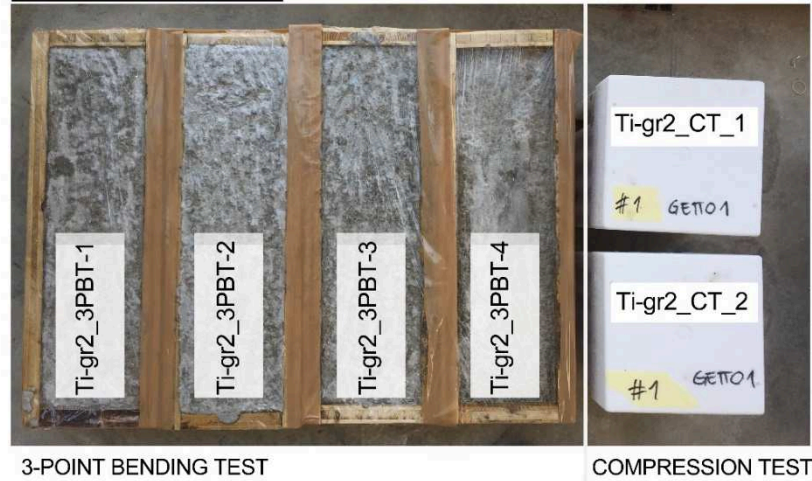


Figure 7.7 - Cast #1 (Ti-gr2FRC) scheme

CAST #2 - Ti-gr5FRC

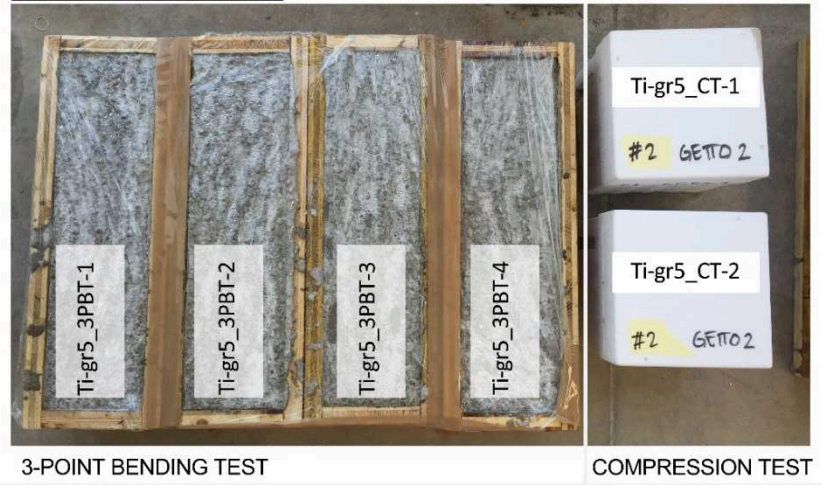


Figure 7.8 - Cast #2 (Ti-gr5FRC) scheme

CAST #3 - Plain concrete

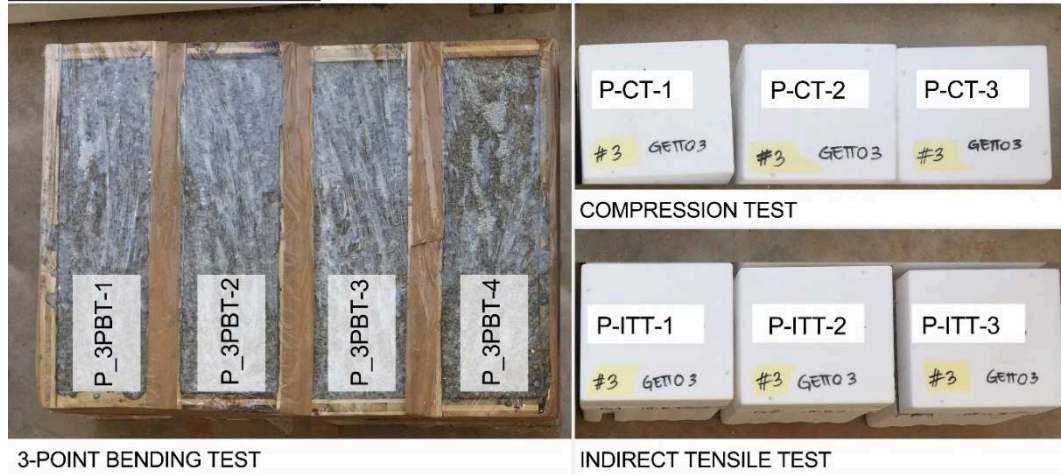


Figure 7.9 - Cast #3 (Plain concrete) scheme

Compression tests were performed according to the Italian-European standard UNI EN 12390-3 (UNI EN 12390-3:2009, 2009) on cubic specimens of dimensions 150×150×150 mm. The same dimensions were adopted for the plain concrete specimens intended for the indirect tensile test (UNI EN 12390-6:2010, 2010). Figs. 7.10a and 7.10b show the compression and indirect tensile tests set-up, respectively.

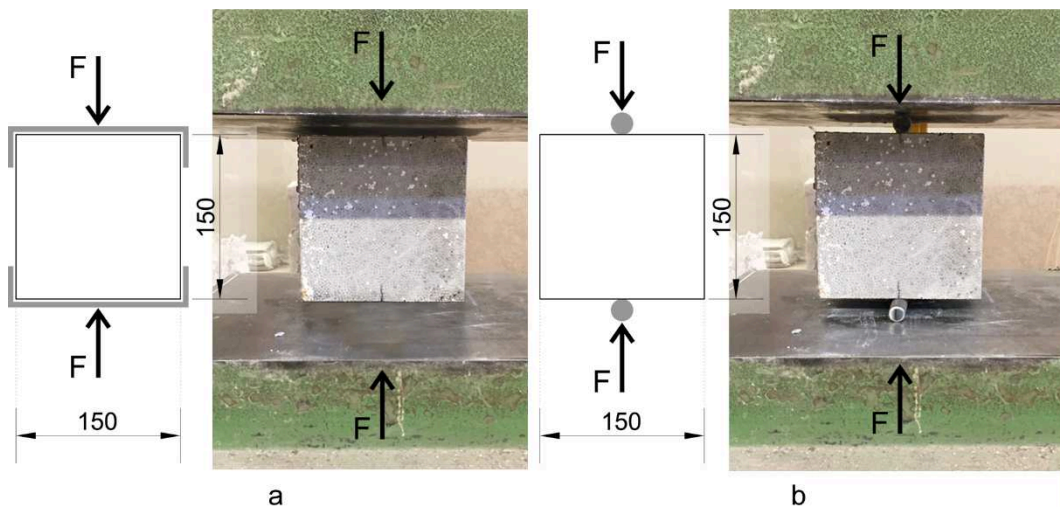


Figure 7.10 - Test set-up and execution: a) compression test; b) indirect tensile test

Three-point bending tests (3PBT) have been carried out on notched prismatic specimens of dimensions 150×150×550 mm, according to the European standard EN 14651 (EN 14651, 2005), as discussed in paragraph 7.3.1 of the present chapter. The specimen dimensions are reported in Fig. 7.11, whereas the 3PBT set-up is shown in Fig. 7.12.

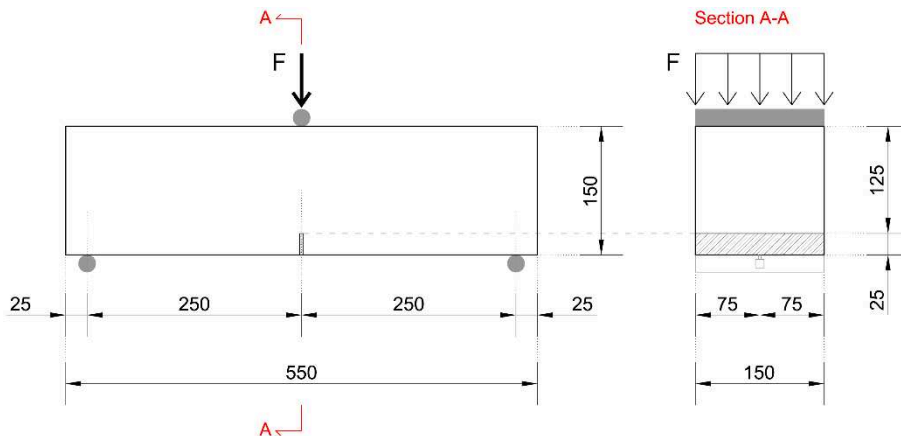


Figure 7.11 - Specimen dimensions for the three-point bending test

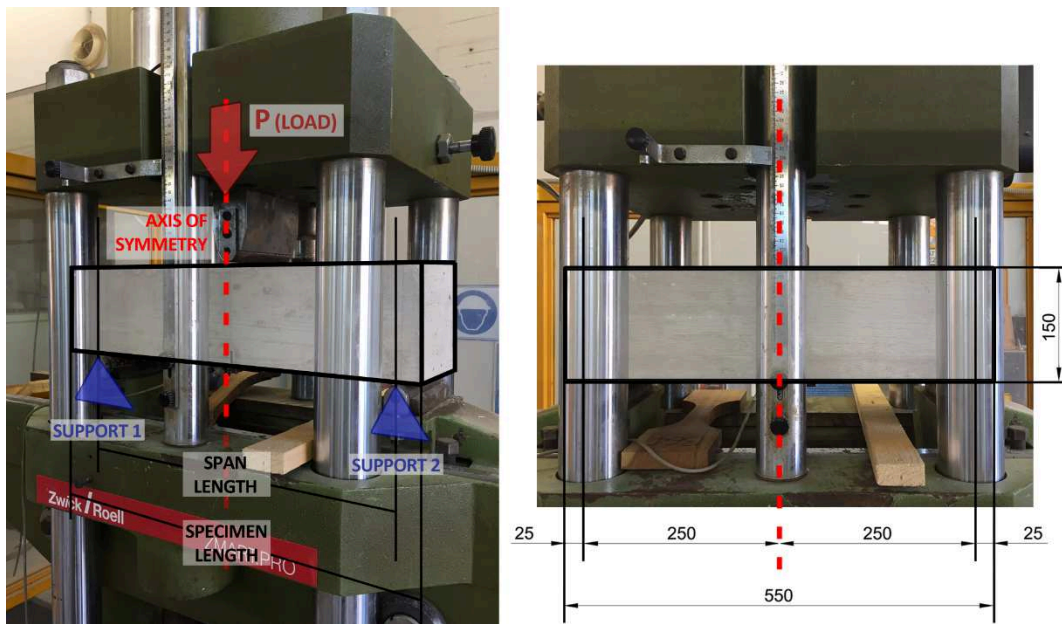


Figure 7.12 - Three-point bending test set-up

7.5 Experimental test results

Firstly, the specific weight of the three different batches has been measured. Table 7.3 summarises the measured weight of all the specimens after 28 days of curing. Thus, the specific weight of each concrete batch, i.e. the density, is the average value among the specific weights measured.

Table 7.3 - Specific weight of the three concrete batches

Cast	Specimen	Dimensions				Weight		Average
		Width	Depth	Length	Volume	Specimen weight	Specific weight	Specific weight
		(mm)	(mm)	(mm)	(m ³)	(kg)	(kg/m ³)	(kg/m ³)
#1 Ti-gr2FRC	Ti-gr2_CT-1	150	150	150	0.003375	6.30	1866.77	1882.92
	Ti-gr2_CT-1	150	150	150	0.003375	6.20	1837.04	
	Ti-gr2_3PBT-1	150	150	550	0.012375	24.00	1939.39	
	Ti-gr2_3PBT-2	150	150	550	0.012375	23.30	1882.83	
	Ti-gr2_3PBT-3	150	150	550	0.012375	23.45	1894.95	
	Ti-gr2_3PBT-4	150	135**	550	0.011138	20.90	1876.54	
#2 Ti-gr5FRC	Ti-gr5_CT-1	150	150	150	0.003375	6.40	1896.30	1877.44
	Ti-gr5_CT-1	150	150	150	0.003375	6.35	1881.48	
	Ti-gr5_3PBT-1	150	150	550	0.012375	23.05	1862.63	
	Ti-gr5_3PBT-2	150	150	550	0.012375	23.50	1898.99	
	Ti-gr5_3PBT-3	150	150	550	0.012375	22.75	1838.38	
	Ti-gr5_3PBT-4	150	150	550	0.012375	23.35	1886.87	
#3 Plain	P_CT-1	150	150	150	0.003375	6.40	1896.30	1893.60
	P_CT-2	150	150	150	0.003375	6.40	1896.30	
	P_CT-3	150	150	150	0.003375	6.30	1837.04	
	P_ITT-1	150	150	150	0.003375	6.50	1925.93	
	P_ITT-2	150	150	150	0.003375	6.35	1881.48	
	P_ITT-3	150	150	150	0.003375	6.45	1911.11	
	P_3PBT-1	150	150	550	0.012375	23.50	1898.99	
	P_3PBT-2	150	150	550	0.012375	23.35	1886.87	
	P_3PBT-3	150	150	550	0.012375	23.75	1919.19	
	P_3PBT-4	150	150	550	0.012375	23.30	1882.83	

** Reduced dimension

As reported in Table 7.3, specimen Ti-gr2_3PBT-4 presents a specimen with a reduced dimension, i.e. the width is equal to 135 mm instead of 150 mm. Thus, this aspect needs to be accounted for when *LOP* and residual flexural strength are computed.

With regard to the density of the three batches, it is possible to conclude that the presence of the fibres does not affect the specific weight of the lightweight concrete matrix. In the present case, actually, the specific weights of the fibre reinforced batches (1882.92 kg/m³ for Ti-gr2FRC and 1893.60 kg/m³ for Ti-gr5FRC) are lower than that of plain concrete (1893.60 kg/m³). However, it is not considered reasonable to conclude that fibres lighten the matrix, firstly because a relative small number of specimens have been casted, and, secondly, because the differences between the three batches are not significant and could be more reasonably credited to the heterogeneous nature of concrete.

7.5.1 Compression and indirect tensile tests

The results of the compression and indirect tensile tests are reported in Table 7.4 for Ti-gr2FRC, Ti-gr5FRC and Plain concrete. According to the standard UNI EN 12390-3 (UNI EN 12390-3:2009, 2009), the compressive strength, f_{cm} , is calculated through the following relation Eq. (7.4):

$$f_{cm} = \frac{F_{max}}{A_c} \quad (7.4)$$

where A_c is the area subjected to the force F , which, in the present case, corresponds to the specimen side squared, i.e. l^2 . From the indirect tensile tests, instead, the tensile strength, f_{ct} , is evaluated through Eq. (7.5), according to UNI EN 12390-6 (UNI EN 12390-6:2010, 2010).

$$f_{ct} = \frac{2F_{max}}{4l^2} \quad (7.5)$$

Table 7.4 - Compression and indirect tensile tests results

Specimen	CT Results		Average	ITT Results		Average
	F_{max} (kN)	f_{cm} (MPa)		F_{max} (kN)	f_{ct} (MPa)	
Ti-gr2_CT-1	1195	53.11	50.78	-	-	
Ti-gr2_CT-2	1090	48.44		-	-	
Ti-gr5_CT-1	1210	53.78	54.45	-	-	
Ti-gr5_CT-2	1240	55.11		-	-	
P_CT-1	1215	54.00	49.41	-	-	
P_CT-2	945	42.00		-	-	
P_CT-3	1175	52.22		-	-	
P_ITT-1	-	-		60	1.33	
P_ITT-2	-	-		65	1.44	1.22
P_ITT-3	-	-		40	0.89	

From Table 7.4, it is possible to see that the average compressive strength for plain concrete is slightly lower than that measured for TiFRC. Particularly, when titanium grade 5 fibres are employed, the compressive strength increases from 49.41 to 54.45 MPa. However, the fibres contribution is not significant in terms of compressive strength, as it happens in the case of steel fibres analysed in Section 7.2.2. Despite that, the observation of the broken specimens (Fig. 7.13) highlights a confinement effect provided by the presence of the fibres that tends to maintain the integrity of the specimen.

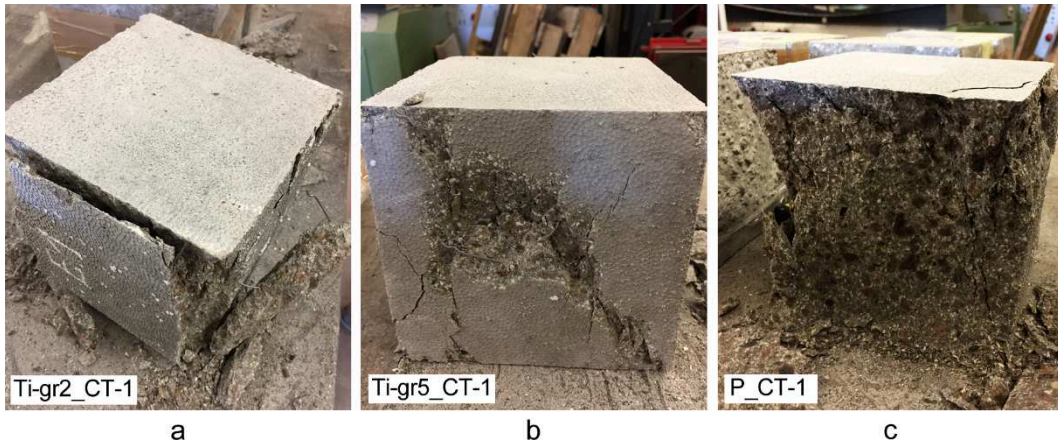


Figure 7.13 - Compression test broken specimens: a) Ti-gr2_CT-1; b) Ti-gr5_CT-1; c) P_CT-1

7.5.2 Three-point bending tests

The results of the three-point bending test are reported in terms of crack mouth opening displacement (*CMOD*) versus applied load (*F*). The curves obtained for the three batches are shown in Figs. 7.14-7.16, while the computation of the *LOP* and the residual flexural strength values for several *CMOD*s, according to Eqs. (7.2) and (7.3), respectively, are reported in Table 7.5.

It is necessary to underline that specimen P_3PBT-1 failed the test, due to a problem in the measurement apparatus at the beginning of the test. For the sake of completeness, the curve is reported but related data are not considered to evaluate the *LOP* and the residual flexural strength in Table 7.6.

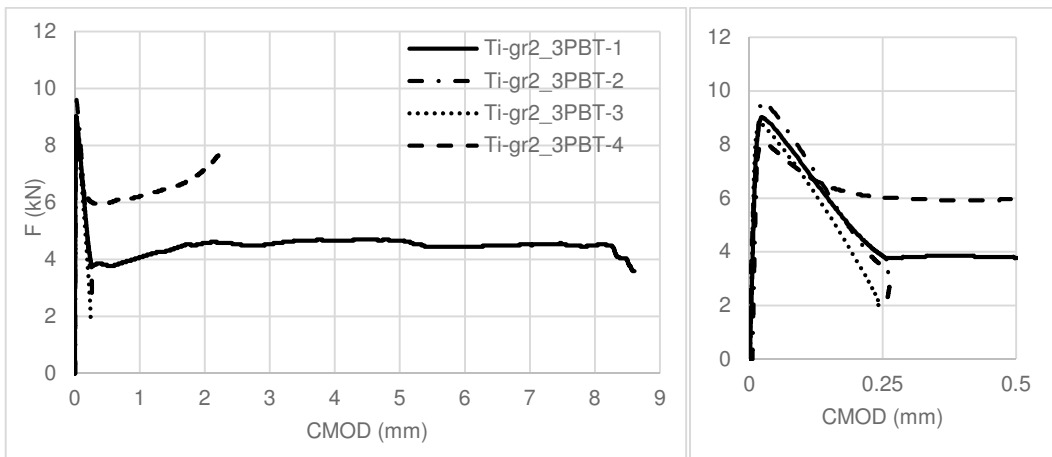


Figure 7.14 - Results of the 3PBT on Ti-gr2FRC (complete curves and zoom on the first part up to *CMOD*=0.5 mm)

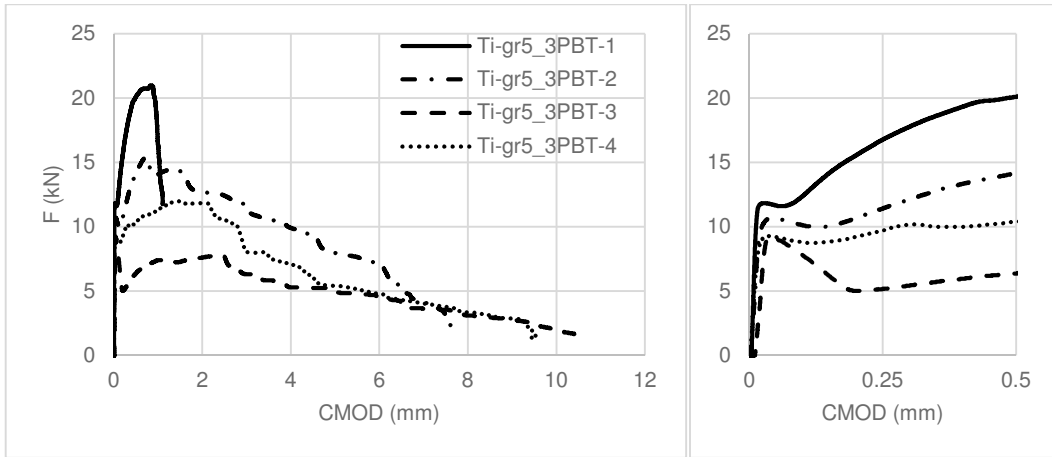


Figure 7.15 - Results of the 3PBT on Ti-gr5FRC (complete curves and zoom on the first part up to $CMOD = 0.5$ mm)

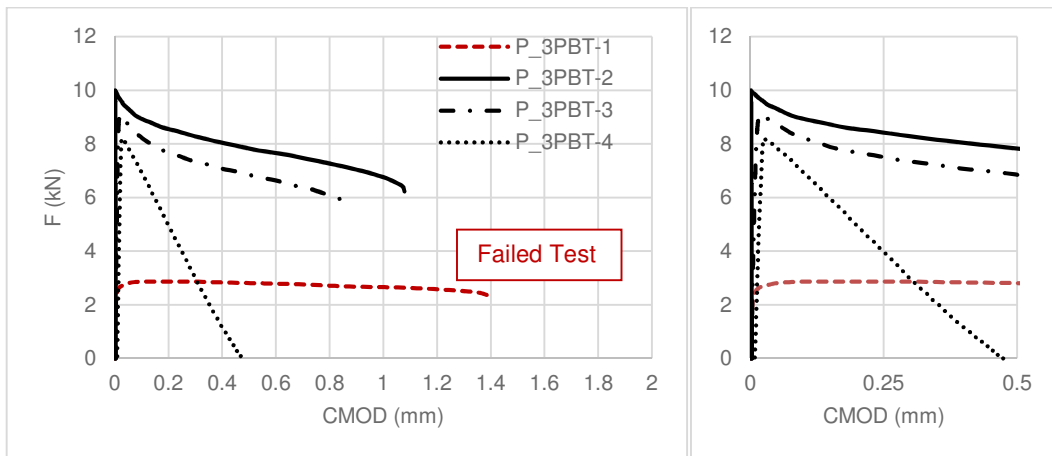


Figure 7.16 - Results of the 3PBT on Plain Concrete (complete curves and zoom on the first part up to $CMOD = 0.5$ mm)

Table 7.5 - 3PBT results

Specimen	F_L	$f_{ct,L}^f$ LOP (MPa)	F_j							$f_{R,j}$							
			(kN)							(MPa)							
			$CMOD_j$			$CMOD_j$				$CMOD_j$			$CMOD_j$				
			0.5	1	1.5	2	2.5	3	3.5	0.5	1	1.5	2	2.5	3	3.5	
Tigr2_3PBT	-1	9.02	2.89	3.77	4.08	4.35	4.58	4.53	4.53	4.67	1.21	1.31	1.39	1.46	1.45	1.45	1.49
	-2	9.60	3.07	-	-	-	-	-	-	-	-	-	-	-	-	-	-
	-3	8.84	2.83	-	-	-	-	-	-	-	-	-	-	-	-	-	-
	-4	8.03	2.86	5.97	6.24	6.60	7.18	-	-	-	2.12	2.22	2.35	2.55	-	-	-
	Average	8.87	2.91	4.87	5.16	5.47	5.88	4.53	4.53	4.67	1.66	1.76	1.87	2.01	1.45	1.45	1.49
Tigr5_3PBT	-1	11.85	3.79	20.10	16.38	-	-	-	-	-	6.43	5.24	-	-	-	-	-
	-2	10.73	3.43	14.18	14.09	14.32	12.70	12.43	11.62	10.59	4.54	4.51	4.58	4.06	3.98	3.72	3.39
	-3	9.24	2.96	7.40	7.40	7.27	7.63	7.67	6.33	5.83	2.37	2.37	2.33	2.44	2.46	2.02	1.87
	-4	9.29	2.97	10.41	11.31	11.98	11.85	10.55	8.08	7.72	3.33	3.62	3.83	3.79	3.37	2.58	2.47
	Average	10.28	3.29	13.03	12.30	11.19	10.73	10.22	8.68	8.05	4.17	3.93	3.58	3.43	3.27	2.78	2.58
P_3PBT	-1	FT*	FT*	FT*	-	-	-	-	-	-	FT*	-	-	-	-	-	-
	-2	10.01	3.20	7.76	-	-	-	-	-	-	2.48	-	-	-	-	-	-
	-3	9.11	2.92	6.78	-	-	-	-	-	-	2.17	-	-	-	-	-	-
	-4	8.21	2.63	0.00	-	-	-	-	-	-	0.00	-	-	-	-	-	-
	Average	8.89	2.92	4.85							1.55						

*FT: failed test

A first needed consideration concerns the group of specimens made of Ti-gr2FRC. The tests carried out could not well capture the post-peak phase of all the specimens due to a problem in the acquisition system. Therefore, the complete curves for only two specimens have been acquired satisfactory (Ti-gr2_3PBT-1 and Ti-gr2_3PBT-4). This problem did not occur for the specimens of the group Ti-gr5_3PBT, which exhibited the expected load-*CMOD* behaviour with significant residual flexural strength values. As for plain concrete, instead, the fragile behaviour exhibited by curves was expected and in this case is the natural outcome of that kind of batch. In fact, in this case the results have been considered for measuring the *LOP* and not the residual flexural strengths for different *CMOD*s.

Despite these aspects, some considerations can be drawn from the experimental 3PBTs. In terms of *LOP*, the experimental results highlighted that the presence of fibres give no or not significant contribution on average. When titanium grade 5 fibres are employed, however, a slightly increase in the average *LOP* has been observed. A synoptic view of the average *LOP*s for each concrete batch, measured according to Eq. (7.2) and reported in Table 7.5 for individual tests, is summarised in Table 7.6.

Table 7.6 - *LOP* comparison

	Ti-gr2FRC	Ti-gr5FRC	Plain concrete
$f_{ct,L}^f$ (<i>LOP</i>) (MPa)	2.91	3.29	2.92

The fibres major contribution intervenes when flexural residual strengths ($f_{R,j}$) are taken into account. At *CMOD*=0.5 mm, it is already clear that Ti-fr5FRC exhibits a much higher residual strength than plain concrete, even though at this stage flexural strength of Plain concrete is still not vanished, on average. As for the two successful tests on Ti-gr2FRC, the measured $f_{R,j}$ values demonstrate a different behaviour with respect to Ti-gr5FRC. In fact, for the latter all the curves exhibited a significant increase in the load bearing capacity after the first post-peak drop. For the Ti-gr2FRC specimens, instead, the residual force after the post-peak drop shows a slight increase, but in a gradual and slow manner.

The experimental behaviours exhibited by the three batches have been further investigated by visually analysing the broken specimens (Figs. 7.17-7.19). A significant aspect noticed in the case of the Ti-gr2FRC concerns the failure mechanism, that, in some cases (see Fig. 7.17, specimen Tigr2_3PBT-3), occurred for fibres rupture instead of fibre pull-out. This did not happen in the case of Ti-gr5FRC, thus it seems to depend on the mechanical characteristics of the fibres. In fact, titanium grade 2 fibres have a tensile yield strength equal to 345 MPa, which is much lower than that of titanium grade 5 fibres (820 MPa). When the dominant failure mechanism is the fibre rupture instead of the fibre pull-out, the ductility of the composite material is significantly reduced in favour of a more fragile behaviour (Bentur and Mindess, 2007), (Paegle, 2015). However, also in the case of Ti-gr2FRC, the fibre bridging action can be clearly appreciated from the concrete particles held by the fibres along the crack (Fig. 7.17, specimen Tigr2_3PBT-4).

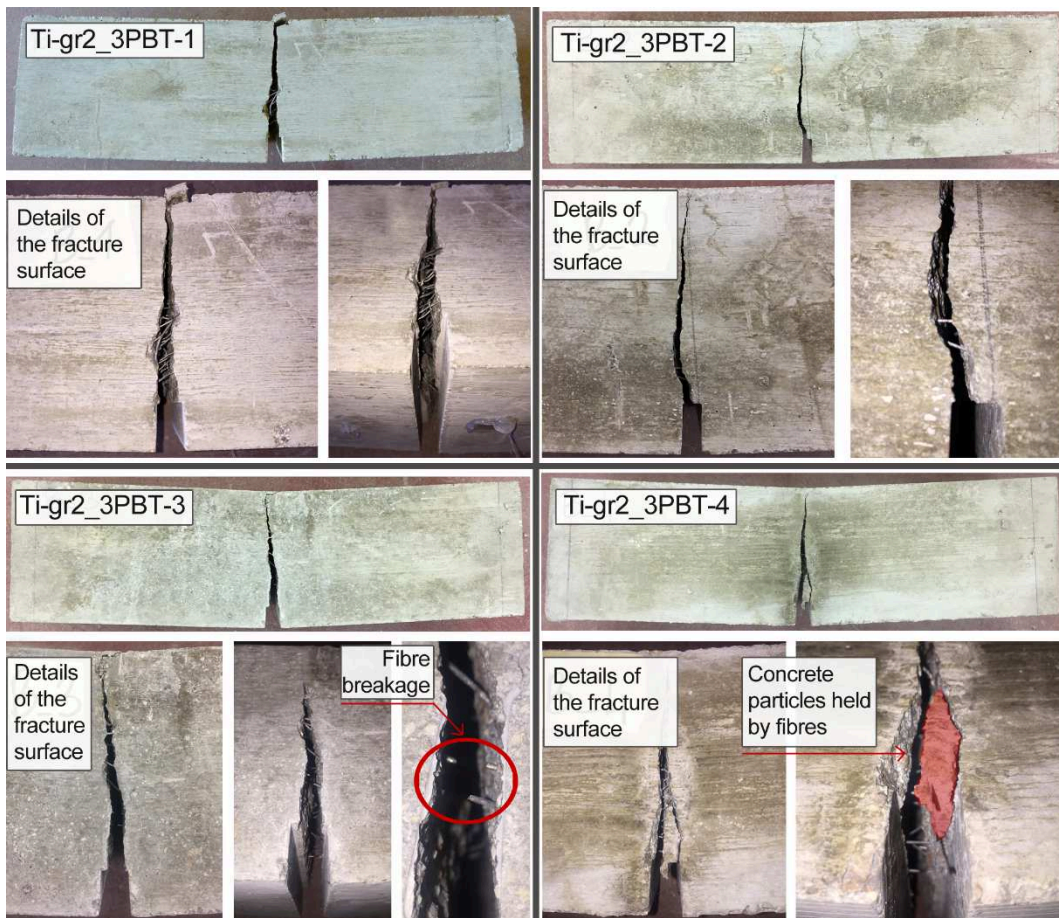


Figure 7.17 - Broken specimens after the 3PBT on Ti-gr2FRC

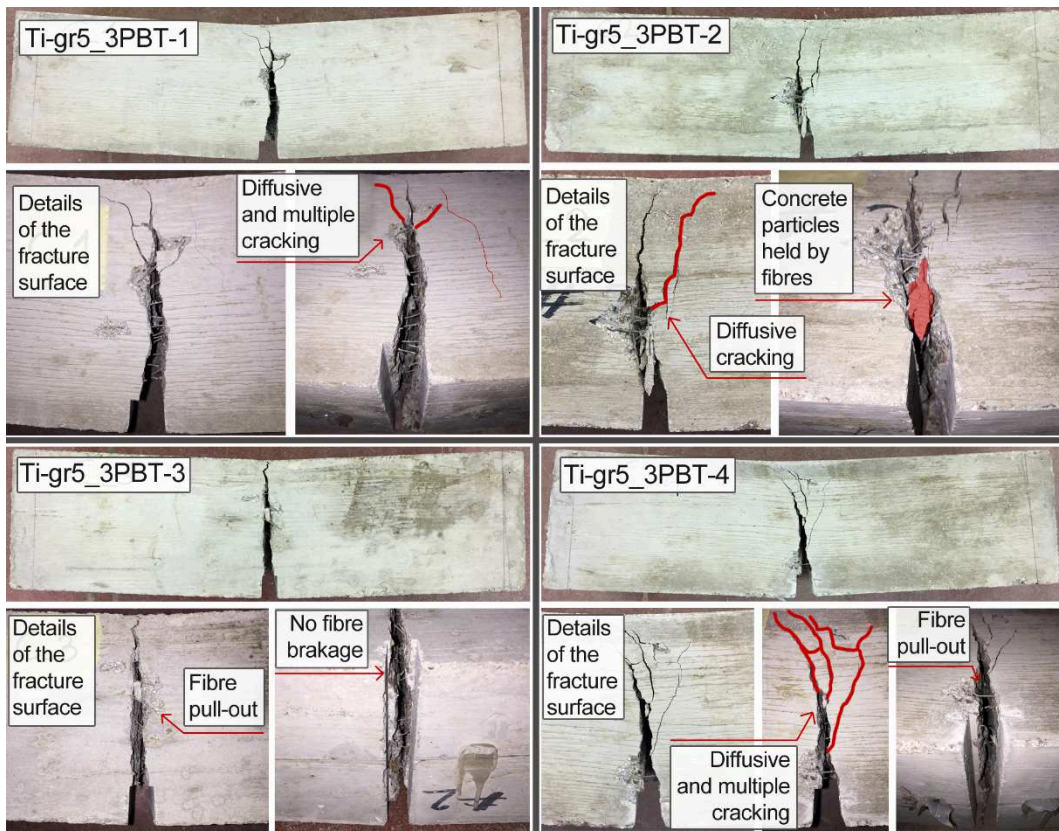


Figure 7.18 - Broken specimens after the 3PBT on Ti-gr5FRC

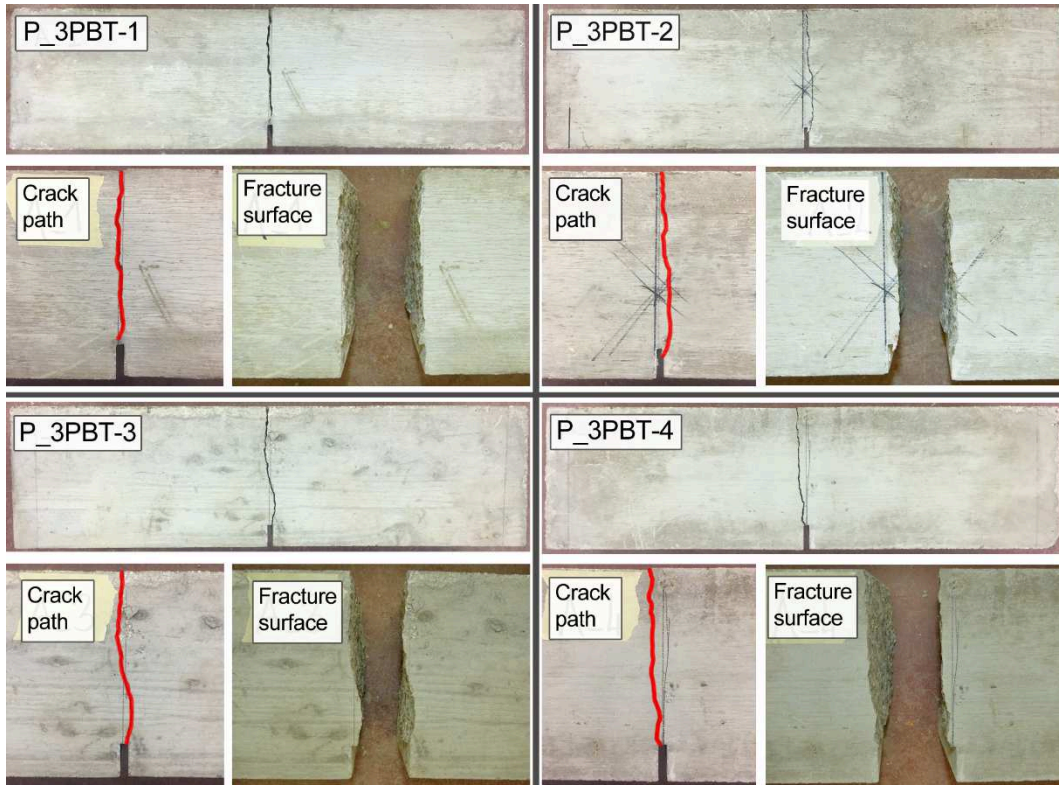


Figure 7.19 - Broken specimens after the 3PBT on Plain Concrete (P)

7.5.3 Comparison between TiFRC and SFRC

From the three-point bending tests, it can be deduced that, among the analysed cases, Ti-gr5FRC represents the most performant FRC in terms of *LOP* and residual flexural strength values. Therefore, further investigations have been conducted in order to compare its flexural toughness to that of the more traditional SFRC. To this end, the results of some studies presented in the literature on SFRC three-point bending tests under similar conditions have been taken into account, i.e. only those carried out according to the standard EN 14651 (EN 14651, 2005). Table 7.7 collects the data found in the literature and the comparison values obtained in the present experiments on Ti-gr5FRC. The quantities adopted for comparison are:

- $f_{ct,L}^f \rightarrow$ Limit of proportionality (*LOP*), which corresponds to the flexural strength at $CMOD=0.05$ mm;
- $f_{R,1} \rightarrow$ residual flexural strength at $CMOD_1$ ($CMOD=0.5$ mm) or deflection $\delta_{R,1}=0.46$ mm (RILEM T.C. 162-TDF, 2002);
- $f_{R,4} \rightarrow$ residual flexural strength at $CMOD_4$ ($CMOD=3.5$ mm) or deflection $\delta_{R,4}=3.00$ mm (RILEM T.C. 162-TDF, 2002).

It should be noted that only SFRC with hooked-end or double hooked-end fibres with different reinforcement index, RI , are considered. RI is defined accordingly Eq. (7.6):

$$RI = (l_e/\phi) \cdot V_f \quad (7.6)$$

where l_e/ϕ represents the aspect ratio (fibre equivalent length over diameter), and V_f is the fibre volume fraction.

Table 7.7 - Flexural strength and residual flexural strength comparison between Ti-gr5FRC and SFRC

	Concrete	Fibre			3PBT results				
	f_{cm} (MPa)	l_e/ϕ (-)	f_y (MPa)	shape	V_f (%)	RI (-)	$f_{ct,L}^f$ (MPa)	$f_{R,1}$ (MPa)	$f_{R,4}$ (MPa)
Ti-gr5FRC	49	50	820	DHE	0.50	0.25	3.29	4.17	2.58
SFRC:									
Bencardino et al. (Bencardino et al., 2010)	80.5	80	1050	HE	1.00	0.80	6.6	11.2	8.7
	78.2	80	1050	HE	2.00	1.60	6.5	13.8	12.9
Meskenas et al. (Meskenas et al., 2013)	43.10	50	-	HE	0.50	0.25	4.50	2.90	2.75
	44.80	50	-	HE	1.00	0.50	4.70	4.50	4.35
Pajak and Ponikiewski (Pajak and Ponikiewski, 2013)	98.20	37.5	1100	HE	0.50	0.19	3.80	3.61	1.97
	96.50	37.5	1100	HE	1.00	0.38	6.14	5.81	3.55
	88.60	37.5	1100	HE	1.50	0.56	8.31	8.09	5.09
Grimaldi et al. (Grimaldi et al., 2013)	48.40	66.67	-	HE	0.50	0.33	3.40	3.67	3.32
Soetens and Matthys (Soetens and Matthys, 2014)	55.04	80	2520	HE	0.25	0.20	3.92	5.27	5.60
	58.56	80	2520	HE	0.50	0.40	5.75	8.20	8.73
Amin et al. (Amin et al., 2015)	61.30	63.63	1340	HE	0.40		4.93	4.06	2.75
	63.80	63.63	1340	HE	0.80		7.46	7.07	4.62
Venkateshwaran et al. (Venkateshwaran et al., 2018)	38.90	66.67	1200	DHE	0.25	0.17	4.16	3.26	3.56
	39.70	66.67	1200	DHE	0.50	0.33	4.71	4.89	5.42
	46.10	66.67	1200	HE	0.25	0.17	4.24	3.31	3.55
	46.70	66.67	1200	HE	0.50	0.33	5.03	6.21	7.24

HE: hooked-end fibres;

DHE: double hooked-end fibres.

As it is possible to observe from Table 7.7, the values of the flexural strengths and residual flexural strengths found in the literature vary a lot among the cases taken into account. It can be assessed that the Tigr-5FRC performance in terms of flexural strength and residual flexural strength values is similar to that exhibited by SFRC. Particularly, when the same fibre volume fraction is adopted ($V_f=0.5\%$), $f_{ct,L}^f$ is equal to 3.29 MPa for Tigr-5FRC, which is lower than that found in the literature for SFRC (i.e. 3.40-5.75 MPa).

However, it should be considered that the reinforcement index, RI , is not always the same. In fact, in the present case it is equal to 0.25, while for the highlighted cases having $V_f=0.5\%$, RI goes from 0.19 ($f_{ct,L}^f=3.80$ MPa) to 0.40 ($f_{ct,L}^f=5.75$ MPa). Particularly, in the experiments reported by Pająk and Ponikiewski (Pająk and Ponikiewski, 2013), even if $RI=0.19$ (lower than 0.25 of Ti-gr5FRC), f_{cm} is much higher than that of Ti-gr5FRC (i.e. 98.20 vs. 49 MPa), and, as a consequence, it appears reasonable that the resultant $f_{ct,L}^f$ is slightly higher than that measured in the present experiments (3.80 vs. 3.29 MPa). Moreover, in this case $f_{ct,L}^f$ is the maximum flexural strength measured, whereas for Ti-gr5FRC the maximum flexural strength does not correspond to the limit of proportionality, but it occurs for a higher value of $CMOD$. Grimaldi et al. (Grimaldi et al., 2013), instead, obtained an average $f_{ct,L}^f$ equal to 3.40 MPa for a SFRC with $f_{cm}=48.40$ MPa, $V_f=0.5\%$ and $RI=0.33$. In this case, for similar compressive strengths, even if the RI is higher than that of Ti-gr5FRC, the obtained flexural strengths are comparable at all the $CMOD$ s considered. The results of the experiments carried out by Soetens and Matthys (Soetens and Matthys, 2014) and Venkateshwaran et al. (Venkateshwaran et al., 2018) showed better performances in terms of $f_{ct,L}^f$ than that obtained in the present work. However, in this two cases, for $V_f=0.5\%$, higher RI s were adopted with respect to that of Ti-gr5FRC.

In terms of first residual value, instead, Tigr-5FRC is characterised by higher values than those observed for SFRC in (Meskenas et al., 2013), (Pająk and Ponikiewski, 2013), and (Grimaldi et al., 2013); i.e. $f_{R,1}$ is equal to 4.17 MPa for Tigr-5FRC, while it varies from 2.90 to 3.67 for SFRC with $V_f=0.5\%$ and $0.19 < RI < 0.33$. Significantly higher values of $f_{R,1}$ (i.e. 8.20 MPa) were obtained by Soetens and Matthys (Soetens and Matthys, 2014), but they adopted steel fibres with very high yield strength (i.e. 2520 MPa). This aspect, in fact, strongly affects the SFRC performance, especially after the matrix first cracking.

As for the ultimate residual value (i.e. that corresponding to $CMOD=3.5$ mm or $\delta_{R,4}=3.00$ mm), Ti-gr5FRC has a similar value with respect to the SFRC with the same fibre volume fraction and similar RI ((Meskenas et al., 2013), (Pająk and Ponikiewski, 2013), and (Grimaldi et al., 2013)). On the contrary, in other cases (Soetens and Matthys, 2014) and (Venkateshwaran et al., 2018), even if same V_f was adopted, the higher yield strength of the fibres and the higher RI led to significantly greater values of residual ultimate flexural strength ($f_{R,4}$).

For the sake of completeness, also some values reported in the literature for higher volume fractions and higher reinforcement indices are reported (Bencardino et al., 2010), (Meskenas et al., 2013), (Pająk and Ponikiewski, 2013), (Amin et al., 2015). Obviously, in these cases, the flexural strength and its residual values at different deflection or crack mouth opening values, are much higher than those measured in the present experimental work.

To conclude, it is possible to assess that a remarkable variability was found in the literature concerning the flexural performance of SFRC. However, Ti-gr5FRC seems to

exhibit flexural strength values at different *CMOD* comparable to those of SFRC with similar characteristics.

In the next section, this material is further investigated in order to quantify its flexural strength under different geometrical conditions and, thus, to give a first evaluation of the size effect, which strongly affects the mechanical properties when fracture and cracking processes are involved.

7.6 Experimental test on a Ti-gr5FRC full-scale beam

As a final experimental work, a Ti-gr5FRC full-scale beam has been realised and tested under bending test conditions. The purpose of this test is to evaluate the flexural strength in the case of a full-scale beam without any other reinforcement, neither longitudinal reinforcing bars nor transversal stirrups. Thus, a comparison with respect to the flexural strength values measured for the Ti-gr5FRC specimens in the previous section, can be made.

7.6.1 Materials and geometrical details

The materials employed in the present experimental testing are lightweight concrete (LWC) for the matrix and the titanium alloy Ti6Al4V, i.e. titanium grade 5, for the fibres. The concrete mix is the same as that adopted in the previous experimental test, i.e. three-point bending test on Tigr-5FRC. With reference to this concrete batch the mechanical properties have been measured as explained in Section 7.4 of the present chapter and summarised in the following Table 7.8.

Table 7.8 - Mechanical properties of the concrete batch

	Compressive strength	Flexural strength (LOP)
	f_{cm}	$f_{ct,L}^f$
	(MPa)	(MPa)
Ti-gr5FRC	54.45	3.29

The hooked-end geometrical configuration presented in Fig. 7.6 is adopted for the titanium grade 5 fibres, whose dosage (V_f) has been set equal to 0.5% of the beam volume. Mechanical properties of the fibres are reported in Table 7.1 of the present chapter. Fig. 7.20 shows the full-scale beam geometry intended for the test.

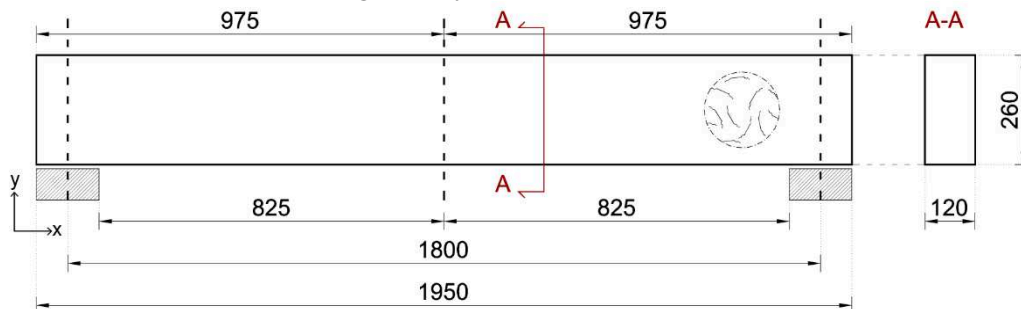


Figure 7.20 - Geometry of the Ti-gr5FRC full-scale beam

7.6.2 Test set-up

The test apparatus has been built in order to transfer a concentrated load to the mid-span cross-section of the beam through a steel beam (IPE120, (EN 10365:2017, 2017)) (Fig. 7.21c). The progressive increasing load has been simulated by incrementing the water level step-by-step (Fig. 7.21a). Each load-step consists of 50 l, up to a maximum of 1000 l (i.e. 1 m³), and two extensometers measure the mid-span deflection (y-direction, Fig. 7.21b) and the opening crack mouth (x-direction, Fig. 7.21c) of the correspondent cross-section, respectively. Therefore, the test is load-driven, meaning that the post-peak flexural behaviour cannot be captured. However, a first estimation of the flexural strength value on a full-scale Ti-gr5FRC beam can be obtained and compared to that obtained from the three-point bending tests on standardised specimens.

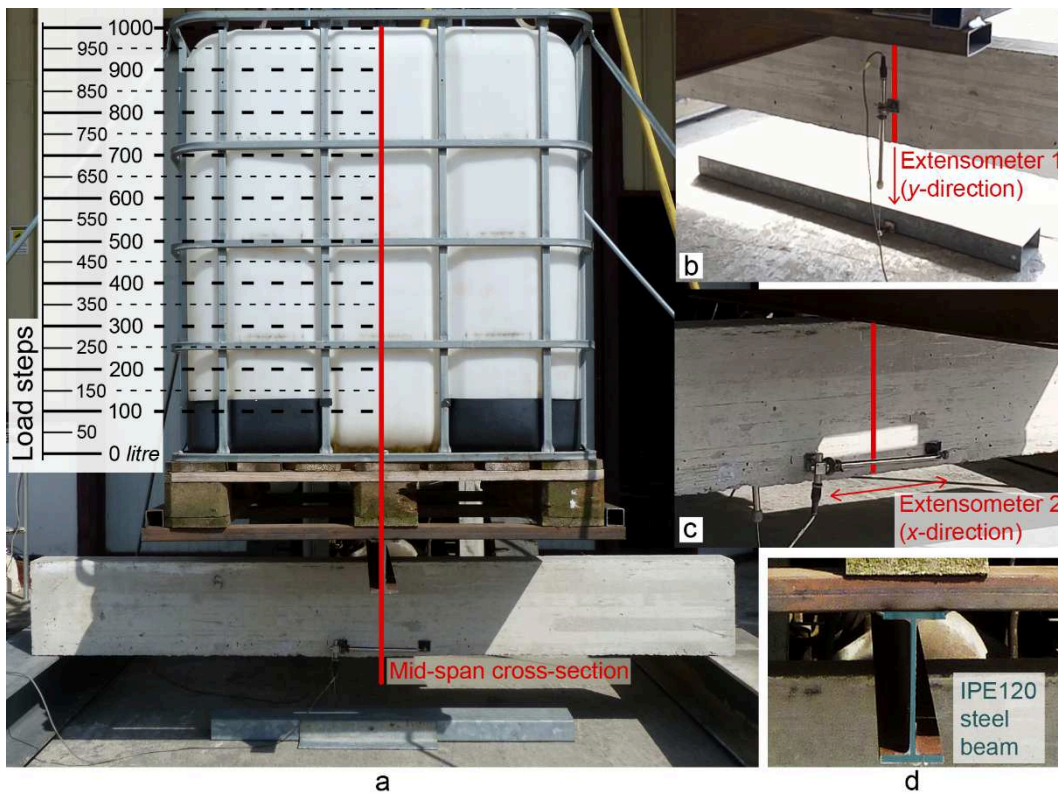


Figure 7.21 - Test set-up: a) test apparatus with load steps indication; b) position of the extensometer 1; c) position of the extensometer 2; and d) detail of the steel beam used to transfer the load

7.6.3 Test results

Table 7.9 summarises the beam test results. For each load step (LS), the corresponding applied load value (F_a), total load on the beam (F_T), and crack mouth opening displacement ($CMOD$) are reported. The $CMOD$ value is directly evaluated with extensometer 2, which measures the width in x -direction of the crack at mid-span. As for the deflection (δ_y), a

problem in the data acquisition occurred during the test, thus non-reliable data could be extracted from the measurement. Fig. 7.22 shows the beam mid-span at different load steps up to the failure.

Table 7.9 - Results of the test on the full-scale Ti-gr5FRC beam

<i>LS</i>	F_a (l)	F_a (kg)	F_T (kg)	F_T (kN)	<i>CMOD</i> (mm)
1	50	49.85	150.85	1.48	0.0409
2	100	99.7	200.7	1.97	0.0623
3	150	149.55	250.55	2.46	0.0718
4	200	199.4	300.4	2.95	0.0968
5	250	249.25	350.25	3.44	0.1533
6	300	299.1	400.1	3.92	0.1966
7	350	348.95	449.95	4.41	0.2359
8	400	398.8	499.8	4.90	0.3111
9	450	448.65	549.65	5.39	0.3691
10	475	473.575	574.575	5.64	0.4373
11	490	488.53	589.53	5.78	104.11

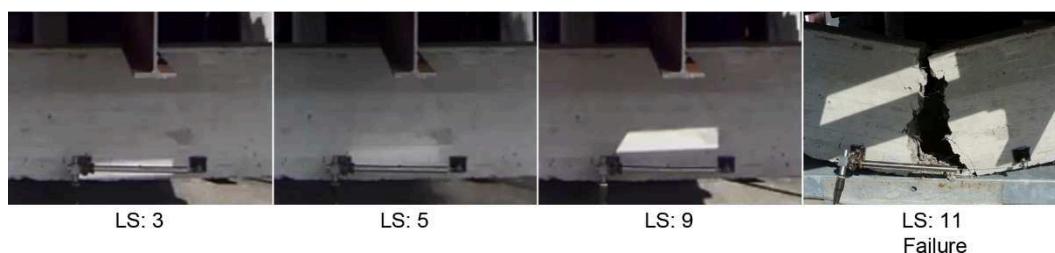


Figure 7.22 - Beam under progressive load-step

7.6.3.1 Flexural strength

The critical load value, corresponding to the beam failure, is equal to 5.78 kN. From this value, it is possible to compute the flexural strength, f_{ct}^f , of the beam through Eq. (7.7):

$$f_{ct}^f = \frac{F_{T,max} \cdot L}{4W} \quad (7.7)$$

where:

- $F_{T,max}$ → maximum total load acting on the beam mid-span, in Newton;
- L → beam length, in millimetres;
- W → section modulus, which, for a rectangular section corresponds to $bh^2/6$, in cubic millimetres.

Thus, for the present case, the obtained flexural strength, measured assuming that the stress distribution is linear over the depth (b) of the section, is approximately equal to 2.10 MPa. The resultant flexural strength is much lower than that measured with the three-point bending test on Ti-gr5FRC, which was equal to 3.29 MPa. Actually, this was expected, due to the trend of decreasing strength accompanying increasing size of quasi-brittle and brittle members is well recognised (Hillerborg et al., 1976). Even though the presence of fibres

may reduce the severity of size effect in concrete, they are not able to eliminate this fracture-based phenomenon entirely (Lepech and Li, 2004). This is because the FRC failure mechanism is similar to that of plain concrete, being it characterised by the development of a single crack that originates deformation localised at the single crack face (Lepech and Li, 2004). In fact, FRC with low fibre volume fraction, i.e. lower than 2%, exhibits a tension-softening behaviour that does not allow the material to fail in a proper ductile manner that would make the size effect negligible.

In terms of flexural strength, it has been reported in the literature (Li et al., 1998), (Balendran et al., 2002) that, as the specimen size increases, the flexural strength decreases. Moreover, the more brittle a concrete batch is, the more profound the size effect becomes. Thus, as far as lightweight concrete is concerned, the more brittle nature of the concrete matrix with respect to normal weight concrete tends to make the size effect even more prominent (Balendran et al., 2002). On the contrary, Ultra High Performance Fibre Reinforced Concrete (UHPFRC), specifically designed in order to significantly improve ductility (Eide and Hisdal, 2012), is usually less affected by the size effect in terms of flexural strength (Wille and Parra-Montesinos, 2012), (Mahmud et al., 2013).

To sum up, from these considerations, it can be assessed that the decrease in the flexural strength (i.e. from 3.29 MPa to 2.10 MPa) observed in the present experimental work when passing from specimens (150×150×550 mm) to a full-scale beam (120×260×1950 mm) is the natural outcome of the size effect.

7.6.3.2 Failure mechanisms

Despite the size effect observed in the flexural strength values, the mechanisms acting when specimens are subjected to three-point bending tests have been recognised also in the full-scale beam test here carried out. In particular, the multiple cracking (Fig. 7.23a), the plastic deformation of the fibres hooks (Fig. 7.23b), and the fibre bridging mechanism leading to the presence of concrete particles held by the fibres at the crack surfaces (Fig. 7.23c), have been detected.

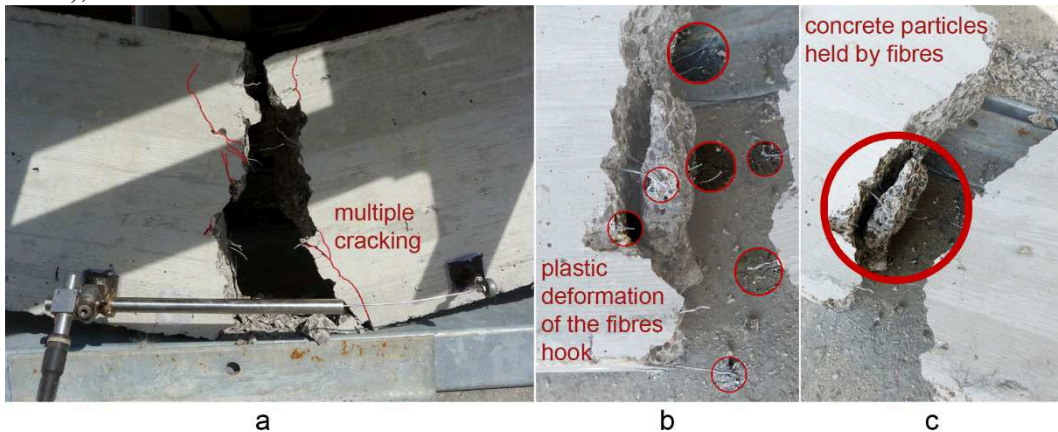


Figure 7.23 - Failure mechanisms: a) multiple and diffusive cracking; b) plastic deformation of the fibres hook; and c) bridging action of the fibres

It should be remarked that no longitudinal reinforcing bars have been used in the present test, leading to a much less ductile failure. This in order to understand the actual contribution of fibres in a full-scale beam.

The results obtained confirmed the expected lower flexural strength with respect to that measured for the Ti-gr5FRC specimens, while highlighted the same failure mechanisms, even if they occurred in a more brittle manner.

Chapter 8

Conclusions and future research

“...However, in the last decades the problems of unsatisfactory durability of structures, especially reinforced concrete structures, are in a dramatic increase. This causes not only economic impacts, because the repairing expenses of deteriorated structures are almost equal to the cost of construction of new ones, but also industrial, environmental and social problems due to decrease of reliability and safety. The durability deterioration due to corrosion remains a scientific and technological issue unresolved well in various fields such as civil engineering, offshore engineering, port structures and transportation infrastructure...”

These words have been written in 2016 by Prof. Apostolopoulos in his ‘*Special issue on durability of RC structures*’ (Apostolopoulos, 2016) and describe very well the necessity to find always novel solutions to the problem of durability of reinforced concrete structures, whose major cause of loss of performance is represented by corrosion of the embedded reinforcement. Apostolopoulos (Apostolopoulos, 2016) also reported, in fact, that “*Corrosion of steel reinforcement is the most serious durability problem of reinforced concrete structures. It impairs not only the appearance of the structure, but also its strength and safety, due to the reduction in the cross-sectional area of the reinforcement and to the deterioration of bond with the surrounding concrete.*”

Therefore, novel strategies for corrosion protection and materials less susceptible of corrosion than traditional carbon steel are under always increasing attention. In this context titanium and its alloys can represent a valuable and realistic option for special designs where avoiding rebar corrosion and reducing structure self-weight are crucial to the point to justify high expenses. In fact, titanium alloys exhibit an outstanding corrosion resistance

and one of the highest strength-to-density ratio among the metals (particularly, beta-alloys such as the most used Ti6Al4V).

8.1 Overview of findings and conclusions

In the present thesis, preliminary analyses towards the possibility to use titanium alloy reinforcement in concrete matrices has been investigated. Before any other considerations, it has been considered essential to assess whether titanium alloys and concrete could develop an efficient bond behaviour, because the latter is at the basis of the composite structural performance of both reinforced concrete and fibre reinforced concrete materials. Thus, particular attention has been focused on interfaces problems, which have been recently remarked as fundamental aspects, with reference to steel reinforcement, by Angst et al. in (Angst et al., 2017).

To this end, the first investigation carried out in this work concerned the interface between reinforcing bars made of the titanium alloy Ti6Al4V and two different mixtures of concrete, i.e. normal and lightweight concrete batches (NWC and LWC, respectively). Bond stress-slip relationships were extracted from pull-out tests conducted on $\phi 8$ and $\phi 16$ mm Ti6Al4V bars from NWC and LWC specimens. They exhibited the typical pull-out behaviour that reflects three mechanisms, i.e. chemical adhesion, friction and mechanical interlocking. Despite only plain bars have been tested in this study, visual and microscopic analyses of bar surfaces, sampled after pull-out tests, showed reasonable hints for the presence of cement particles adhering to the plain bar surface and subjected to crushing during the pull-out test, which may be identifiable, to some degree, as asperities. The presence of these asperities could explain also several features of the obtained bond-slip diagrams, such as evidence of non-negligible interlocking and dilatancy phenomena, which could not be justified by assuming ideally smooth bars. Moreover, SEM analyses of the bar-matrix interface after a slip equal to 55% of the bond length confirmed the assumed dilatant behaviour, providing also the problem ‘scale’ through the measure of the separation at the interface, whose magnitude was around 10-15 μm .

Experimental pull-out tests were then used to assess the bond strength between the two materials. In particular, it has been found that the bond strength between the titanium alloy used (Ti6Al4V) and concrete is similar or even higher than the bond strength between concrete and other materials widely used as reinforcement. In fact, the Ti6Al4V-concrete bond strength is similar to that of plain, smooth or even slightly sandblasted steel bars, whereas it is higher than that for stainless steel plain rebars (with greater roughness) and plain, smooth FRP bars. Tests provided another remarkable result in terms of bond strength: the comparison between NWC and LWC showed that in the first case the developed bond strength is significantly lower (about 40%). Both the visual and microscopic analyses of the pulled-out bars revealed the presence of a uniform layer of residual matrix materials in the case of LWC; conversely, sparse spots are clearly distinguishable in the case of NWC. This evidence and the observation of the specimen fracture surface, have led to formulate the hypothesis that the higher performance of bond in LWC is due to the more uniform

asperity degradation along the rebar-concrete interface, i.e. a homogeneous physical aggregate distribution improves the bond strength.

To demonstrate and simultaneously better investigate the physics behind the pull-out mechanism, a finite element (FE) model has been employed, simulating the interfacial failure through cohesive zone models (CZMs). Firstly, bilinear (Alfano and Crisfield, 2001) and exponential (Xu and Needleman, 1994) CZMs, two of the most used ones, have been used in the FE analysis, leading to good agreement between experimental and numerical responses in the range of the linear and immediate post-peak branches of the curves. However, in both cases the resulting force vanishes after the slip value at the completion of debonding, neglecting its residual value. Since the higher Poisson's ratio of titanium with respect to that of concrete and the absence of lateral pressure on the specimens, compression stresses did not originate at the interface. Therefore, also by adopting the CZM accounting for damage and friction proposed by Alfano and Sacco (Alfano and Sacco, 2006), the experimental residual pull-out force could not be captured with the FE analysis. In order to overcome this limitation and better represent the actual physics of the pull-out mechanism, two novel CZMs were formulated. The first one simulates the experimental behaviour observed by adding to the bilinear formulation of Alfano and Crisfield (Alfano and Crisfield, 2001) an exponential decreasing branch that goes from a first residual post-peak value of the tangential stress to a final residual value. With this model, which is based on empirical observations, the experimental curves could be accurately reproduced. However, a more physical description of the phenomenon has been reached by implementing in the FE model, the dilatant behaviour of the interface, assumed after experimental evidence, through the angle-degrading M-CZM proposed by Serpieri et al. in (Serpieri et al., 2015a), accounting for damage, friction, mechanical interlocking and wear. In the present thesis the angle-degrading model has been investigated in further detail by considering different area fraction for the three microplanes and, most importantly, an enhancement of this model has been proposed and validated. The enhancement consists of the due account of the reduction of the asperities depth, consistently with the microplanes angle degradation due to interface wear. With this model, here denominated '*enhanced degrading M-CZM*', sensitivity analyses have been carried out in order to understand the influence of each significant parameter. Thereafter, to fit the experimental curves, an identification procedure has been performed, leading to two optimal set of material interface parameters best fitting the tests with NWC and LWC, respectively, employing $\phi 16$ Ti6Al4V rebars. Furthermore, the validation of the enhanced degrading M-CZM was carried out by applying the sets of interface material parameters to simulate the tests with $\phi 8$ bars, achieving satisfactory agreement between experimental and numerical curves.

The investigation on the titanium alloys-concrete interface has been further conducted by carrying out pull-out test on titanium fibres from LWC specimens. In fact, understanding the behaviour of the single titanium alloy fibre pulled-out from a concrete matrix can be considered a fundamental step toward the possibility to combine titanium and concrete in a fibre reinforced concrete composite material. In the single fibre pull-out tests, two

different geometrical configurations of fibres made of titanium Grade 5, i.e. the alloy Ti6Al4V (ASTM B348-13, 2015), have been tested in order to compare the mechanisms activated by straight fibres and deformed ones. After analysing the literature on the advantages and limitations of various configurations, the choice has fallen upon a double hooked-end configuration, which better combines performance and realisation feasibility. Moreover, this double-bended hook geometry has been not yet thoroughly investigated in the literature, especially if compared to the most used hooked-end configuration, which presents a single bend for each end of the fibre. The bond-slip relationships obtained from the single fibre pull-out tests demonstrated that for straight fibres the same mechanisms as those identified in the case of bars, act at the interface during debonding. Even if a direct comparison could not be made due to the differences in the pull-out set up adopted for the two tests, some analogies were observed and further investigated by means of the FE analysis. Therefore, the enhanced degrading M-CZM here formulated was applied to the model representing the single straight fibre pull-out tests, leading to very good agreement between experimental and numerical curves. The differences in the model parameters values between bar and fibre pull-out simulations, turned out to be consistent with the physics of the phenomenon. In fact, the most significant result from this point of view was related to the asperities depth. For bars, the value of the asperities depth parameter more suitable was found to be 10-15 μm (confirmed also by SEM observations), while the same parameter for fibres was equal to 2 μm . The asperities depth parameter was related to the modified reinforcement-concrete interface that can be more or less rough due to the combined action of the surface roughness and the concrete particles attached to the former surface. Being the surface of the bars much wider than that of fibres, it appears reasonable to hypothesise that the fibre-concrete interface is less rough than that between bars and concrete, i.e. the asperities depth value has to be higher for the pull-out simulation of bars than for that involving fibres. Same arguments were reported for the other involved parameters.

The single fibre pull-out tests were used to assess also the contribution of hooked-end fibres with respect to straight ones. The tests highlighted that the hook contribution could occur for two main mechanisms, i.e. the hook rupture or the hook plastic deformation. Even though the average bond strength is approximately the same (i.e. around 4.75 MPa), in the second case the dissipated energy is clearly higher, and the failure happens for the progressive formation of plastic hinges in correspondence of the hook bends. When the hook undergoes rupture, instead, the interface failure is more fragile, and the bond-slip curve exhibited a drop in the pull-out force after the peak, which did not occur for fibres that could deform completely. The double hooked-end shape tested was thus adopted for further experiments aimed to quantify the fracture toughness of a composite material made of lightweight concrete and titanium fibres.

Finally, a lightweight fibre reinforced concrete with titanium alloys (TiFRC) randomly distributed fibres was designed and tests. Fibres made of both commercially pure titanium (titanium Grade 2) and the titanium alloy Ti6Al4V (titanium Grade 5), i.e. the alloy used for all the other tests, were realised with the double hooked-end configurations in order to evaluate also the effect of the titanium alloys properties into the final response of the

composite material. Three-point bending tests on TiFRC specimens highlighted that the flexural strength and the residual values of the flexural stress at different stages are much higher in the case of Ti-gr5FRC than those of Ti-gr2FRC, that in some cases was characterised by the fibre rupture at the interface. The properties obtained with the three-point bending tests on Ti-gr5FRC were compared to similar cases found in the literature where steel fibres are employed to reinforce concrete matrices. The comparison highlighted that the values of flexural strength and residual flexural strength at fixed values of crack mouth opening or deflection, were similar to those found in the present tests when fibre volume fraction, concrete compressive strength and reinforcement index are comparable.

As a final step, a full-scale beam made of Ti-gr5FRC was built without any other reinforcement and tested in order to evaluate its flexural strength. Thus, it was possible to compare the flexural strength measured for the specimens (on average equal to 3.29 MPa) to that obtained from the test on a full-size beam (equal to 2.10 MPa). In this respect, it has been reported in the literature (Balendran *et al.*, 2002), that as the specimen size increases the flexural strength decreases, with special reference to the FRC materials characterised by a low fibre volume fraction (i.e. lower than 2%) and thus exhibiting a tension-softening behaviour. Moreover, the more brittle a concrete batch is, the stronger the size effect becomes. Thus, as far as lightweight concrete is concerned, the more brittle nature of the concrete matrix with respect to normal weight concrete tends to make the size effect more prominent. These considerations led to assess that the decrease in the flexural strength observed in the present experimental work when passing from specimens (150×150×550 mm) to a full-scale beam (120×260×1950 mm) is the natural outcome of the size effect. Moreover, the size effect could be reliably measured since no further reinforcement in the full-scale beam was added.

8.2 Objectives achievement discussion

The objectives set at the beginning of the present thesis have been achieved. In fact, the interface between titanium alloy reinforcement and concrete has been experimentally and numerically characterised, providing also a comparison between the former and the behaviour of the most widely used interfaces found in the literature. Moreover, a novel material consisting of a lightweight concrete matrix and titanium alloy fibres has been designed and tested, comparing again its performance with that of the typically used FRCs. Particularly, the main results obtained in the present thesis are summarised as follows:

- pull-out tests on plain titanium grade 5 bars from NWC and LWC resulted in bond strength values comparable or even higher to those reported in the literature for other reinforcement materials usually employed. Particularly, Ti6Al4V-LWC interface exhibited higher bond strength than Ti6Al4V-NWC interface;
- an interlocking mechanism at microscale level and a dilatant behaviour of the interface was hypothesised through the analysis of the bond-slip relationships, the SEM images of the partially broken interface, and through the visual and microscopic observations of the sampled bar portions previously embedded into the concrete matrix;

- the former hypotheses were confirmed by means of the FE analysis, in which CZMs were adopted to simulate the interface failure. It has been demonstrated that only by adopting an empirical-based CZM (derived from the bilinear formulation of Alfano and Crisfield (Alfano and Crisfield, 2001)) or a micromechanics-based CZM accounting for dilatancy and interlocking, it was possible to reproduce the experimental results;
- the enhanced degrading M-CZM can represent the cases of pull-out of plain rebars made of other materials, since the interface mechanisms acting at the interface are the same as those identified for reinforcing plain bars made of steel or FRP, etc.. Thus, the experimental evidence and the numerical procedures here adopted can contribute to the comprehension of the micromechanisms acting when plain reinforcement and concrete matrices are subjected to interface failure;
- single Ti6Al4V fibre pull-out tests led to similar responses than those exhibited by bars in terms of debonding micromechanisms. In fact, FE analyses with the enhanced degrading M-CZM could capture the experimental results only by changing some parameter values, consistently with the different geometrical and physical configuration of the model;
- double hooked-end and straight fibres performances in terms of pull-out behaviour were also tested to measure the hook contribution. When Ti6Al4V hooked-end fibres were extracted from LWC specimens, the hook showed either rupture and plastic deformations, leading to different amount of dissipated energies but maintaining approximately the same average bond strength values. FE three-dimensional analyses reproduced the experimental results by adopting the modified Alfano and Crisfield model here formulated with the same parameter values for the two different geometrical configurations, i.e. straight and (double) hooked-end fibres;
- as far as fibre reinforcement is concerned, three-point bending tests on TiFRC specimens were carried out, resulting in higher flexural performance when titanium grade 5 fibres are employed with respect to titanium grade 2 ones. Moreover, the performance can be considered comparable in terms of peak and residual flexural strengths to those reported in the literature for steel fibres with the same dosage;
- finally, a full-scale beam made of Ti-gr5FRC was built without any other kind of reinforcement and tested to measure the flexural peak strength. The decrease noticed with respect to the value obtained from three-point bending tests on specimens could be considered the natural outcome of the size effect.

8.3 Future research

The results obtained in the present thesis provide information useful for those particular design problems in which titanium and its alloys can be considered a valid potential reinforcement for concrete (both in the forms of longitudinal bars and randomly distributed

fibres), i.e. when structures are exposed to very aggressive environments and durability is crucial enough to justify high costs.

From the experimental point of view, tests involving durability should be performed in order to actually measure the contribution of the outstanding corrosion resistance of titanium on the bond strength performance over time and under aggressive environmental conditions. Moreover, in order to describe more precisely the fracture toughness of a realistic beam, experiments on full-scale beams should be carried out in a displacement control regime.

From the numerical point of view, instead, the enhanced degrading M-CZM here formulated should be extended to the three-dimensional case, in order to extend its application to different geometrical configurations of the reinforcement (such as the double hooked-end configuration here adopted).

Finally, if the possibility to reinforce concrete with titanium-based reinforcement is considered, it would be necessary to perform a detailed cost-benefit analysis, properly accounting for the corrosion costs that would arise in particular environmental conditions and the actual cost of titanium. In this respect, in fact, some recent studies ((Higgins et al., 2017), (Platt, 2018)) highlighted that for some applications (e.g. bridge decks) the initial higher costs of the raw material would be repaid by the long term savings in maintenance. This still appears to be an open issue that would require further analyses when specific applications of titanium alloys for reinforcing concrete are taken into account. However, the possibility to use titanium as an alternative to steel reinforcement for concrete structures (both in the forms of bars and fibres) does not seem to be unrealistic and could be considered an innovative and challenging perspective for those particular designs where avoiding corrosion and lightening the structure self-weight (for example by combining titanium and lightweight concrete) are particularly crucial in terms of reliability and safety (e.g. transportation infrastructures, offshore engineering, buildings with strategic importance such as hospitals, firehouses, etc.).

References

- © ANSYS, I., 2015. ANSYS Mechanical APDL Theory Reference.
- Abdallah, S., Fan, M., 2017. Anchorage mechanisms of novel geometrical hooked-end steel fibres. *Mater. Struct. Constr.* 50, 1–11. <https://doi.org/10.1617/s11527-016-0991-5>
- Abdallah, S., Fan, M., Rees, D.W.A., 2018. Bonding Mechanisms and Strength of Steel Fiber-Reinforced Cementitious Composites: Overview. *J. Mater. Civ. Eng.* 30, 04018001. [https://doi.org/10.1061/\(ASCE\)MT.1943-5533.0002154](https://doi.org/10.1061/(ASCE)MT.1943-5533.0002154)
- Abdallah, S., Fan, M., Rees, D.W.A., 2016a. Analysis and modelling of mechanical anchorage of 4D/5D hooked end steel fibres. *Mater. Des.* 112, 539–552. <https://doi.org/10.1016/j.matdes.2016.09.107>
- Abdallah, S., Fan, M., Zhou, X., 2017. Pull-Out Behaviour of Hooked End Steel Fibres Embedded in Ultra-high Performance Mortar with Various W/B Ratios. *Int. J. Concr. Struct. Mater.* 11, 301–313. <https://doi.org/10.1007/s40069-017-0193-8>
- Abdallah, S., Fan, M., Zhou, X., 2016b. Effect of Hooked-End Steel Fibres Geometry on Pull-Out Behaviour of Ultra-High Performance Concrete 10, 1594–1599.
- Abdulle, F., Xiao, R., 2014. Testing and nonlinear numerical modelling of fibre pull-out mechanism from cementitious materials.
- Abdulridha, A., Palermo, D., Foo, S., Vecchio, F.J., 2013. Behavior and modeling of superelastic shape memory alloy reinforced concrete beams. *Eng. Struct.* 49, 893–904. <https://doi.org/10.1016/j.engstruct.2012.12.041>
- Achillides, Z., 1998. BOND BEHAVIOUR OF FRP BARS IN CONCRETE.
- Achillides, Z., Pilakoutas, K., 2004. Bond behavior of fiber reinforced polymer bars under direct pullout conditions. *J. Mater. Civ. Eng.* 4, 173–181. [https://doi.org/10.1061/\(ASCE\)1090-0268\(2004\)8:2\(173\)](https://doi.org/10.1061/(ASCE)1090-0268(2004)8:2(173))
- ACI Committee 211, 1998. ACI 211.4R-93 Guide for Selecting Proportions for High-Strength Concrete with Portland Cement and Fly Ash. *Man. Concr. Pract.* 93, 13.
- ACI Committee 213, 2003. Guide for Structural Lightweight-Aggregate Concrete.
- ACI Committee 408, 2003. ACI 408R-03 Bond and Development of Straight Reinforcing Bars in Tension. *Am. Concr. Inst.* 1–49.
- ACI Committee 544, 2008. Guide for Specifying , Proportioning , and Production of Fiber-Reinforced Concrete.
- ACI Committee 544, 1999. Measurement of Properties of Fiber Reinforced Concrete, Aci.
- Ahlborn, T., DenHartigh, T., 2002. A Comparative Bond Study of Stainless Steel Reinforcement in Concrete. Houghton, MI.
- Ahmed, S.F.U., Mihashi, H., 2007. A review on durability properties of strain hardening fibre reinforced cementitious composites (SHFRCC). *Cem. Concr. Compos.* 29, 365–376. <https://doi.org/10.1016/j.cemconcomp.2006.12.014>
- Al-shannag, M.J., Charif, A., 2017. Bond behavior of steel bars embedded in concretes made with natural lightweight aggregates. *J. King Saud Univ. - Eng. Sci.* 29, 365–372. <https://doi.org/10.1016/j.jksues.2017.05.002>

- Al-Sulaimani, G.J., Kaleemullah, M., Basunnul, I.A., Rasheeduzzafar, A.A.-M., 1990. Influence of corrosion and cracking on bond behaviour and strength of reinforced concrete members. *ACI Struct. J.*
- Alfano, G., 2006. On the influence of the shape of the interface law on the application of cohesive-zone models. *Compos. Sci. Technol.* 66, 723–730. <https://doi.org/10.1016/j.compscitech.2004.12.024>
- Alfano, G., Crisfield, M.A., 2001. Finite element interface models for the delamination analysis of laminated composites: Mechanical and computational issues. *Int. J. Numer. Meth. Eng.* 50, 1701–1736.
- Alfano, G., Sacco, E., 2006. Combining interface damage and friction in a cohesive-zone model. *Int. J. Numer. Methods Eng.* 68, 542–582. <https://doi.org/10.1002/nme.1728>
- Allix, O., Corigliano, A., 1996. Modeling and simulation of crack propagation in mixed-modes interlaminar fracture specimens. *Int. J. Fract.* 77, 111–140. <https://doi.org/10.1007/BF00037233>
- Allix, O., Ladevéze, P., Corigliano, A., 1995. Damage analysis of interlaminar fracture specimens. *Compos. Struct.* 31, 61–74. [https://doi.org/10.1016/0263-8223\(95\)00002-X](https://doi.org/10.1016/0263-8223(95)00002-X)
- Almusallam, A.A., Al-Gahtani, A.S., Aziz, A.R., 1996. Effect of reinforcement corrosion on bond strength. *Constr. Build. Mater.* 10, 123–129. [https://doi.org/10.1016/0950-0618\(95\)00077-1](https://doi.org/10.1016/0950-0618(95)00077-1)
- Alwan, J., Naaman, A., Guerrero, P., 1999. Effect of mechanical clamping on the pull-out response of hooked steel fibers embedded in cementitious matrices. *Concr. Sci. Eng.* 1, 15–25.
- Alwan, J.M., Naaman, A.E., Hansen, W., 1991. Pull-out work of steel fibers from cementitious composites: Analytical investigation. *Cem. Concr. Compos.* 13, 247–255. [https://doi.org/10.1016/0958-9465\(91\)90030-L](https://doi.org/10.1016/0958-9465(91)90030-L)
- Amin, A., Foster, S.J., Muttoni, A., 2015. Derivation of the σ -w relationship for SFRC from prism bending tests. *Struct. Concr.* 16, 93–105. <https://doi.org/10.1002/suco.201400018>
- Amleh, L., Ghosh, A., 2006. Modeling the effect of corrosion on bond strength at the steel–concrete interface with finite-element analysis. *Can. J. Civ. Eng.* 33, 673–682. <https://doi.org/10.1139/106-052>
- Anderson, T.L., 2012. *Fracture Mechanics: Fundamentals and Applications*, Taylor & Francis Group. <https://doi.org/10.1016/j.jmps.2010.02.008>
- Angst, U.M., Geiker, M.R., Michel, A., Gehlen, C., Wong, H., Isgor, O.B., Elsener, B., Hansson, C.M., François, R., Hornbostel, K., Polder, R., Alonso, M.C., Sanchez, M., Correia, M.J., Criado, M., Sagüés, A., Buenfeld, N., 2017. The steel–concrete interface. *Mater. Struct. Constr.* 50. <https://doi.org/10.1617/s11527-017-1010-1>
- Annapoorna, G.V., Suresh, S., 2017. Experimental Study on Bond Behavior of Reinforcing Bars in Plain and Fiber Reinforced Concrete. *Int. J. Adv. Mech. Civ. Eng.* ISSN 2394-2827 4, 83–86.

- Antonietta Aiello, M., Leone, M., Pecce, M., 2007. Bond Performances of FRP Rebars-Reinforced Concrete. *J. Mater. Civ. Eng.* 19, 205–213. [https://doi.org/10.1061/\(ASCE\)0899-1561\(2007\)19:3\(205\)](https://doi.org/10.1061/(ASCE)0899-1561(2007)19:3(205))
- Anwar Hossain, K.M., 2008. Bond characteristics of plain and deformed bars in lightweight pumice concrete. *Constr. Build. Mater.* 22, 1491–1499. <https://doi.org/10.1016/j.conbuildmat.2007.03.025>
- Apostolopoulos, C., 2016. Special issue on durability of RC structures. *Int. J. Struct. Integr.* 7, IJSI-02-2016-0006. <https://doi.org/10.1108/IJSI-02-2016-0006>
- Ardanuy, M., Claramunt, J., Toledo Filho, R.D., 2015. Cellulosic fiber reinforced cement-based composites: A review of recent research. *Constr. Build. Mater.* 79, 115–128. <https://doi.org/10.1016/j.conbuildmat.2015.01.035>
- ASTM B348-13, 2015. Standard Specification for Titanium and Titanium Alloy Bars and Billets. *Astm.* <https://doi.org/10.1520/B0348-13.2>
- ASTM C1550 - 12a, 2012. Standard Test Method for Flexural Toughness of Fiber Reinforced Concrete (Using Centrally Loaded Round Panel).
- ASTM C1609/C1609M-12, 2012. Standard Test Method for Flexural Performance of Fiber-Reinforced Concrete.
- Baena, M., Torres, L., Turon, A., Barris, C., 2009. Experimental study of bond behaviour between concrete and FRP bars using a pull-out test. *Compos. Part B Eng.* 40, 784–797. <https://doi.org/10.1016/j.compositesb.2009.07.003>
- Bakis, C.E., Bank, L.C., Brown, V.L., Cosenza, E., Davalos, J.F., Lesko, J.J., Machida, A., Rizkalla, S.H., Triantafillou, T.C., 2002. Fiber-Reinforced Polymer Composites for Construction—State-of-the-Art Review. *J. Compos. Constr.* 6, 73–87. [https://doi.org/10.1061/\(ASCE\)1090-0268\(2002\)6:2\(73\)](https://doi.org/10.1061/(ASCE)1090-0268(2002)6:2(73))
- Balendran, R. V, Zhou, F.P., Nadeem, A., Leung, A.Y.T., 2002. Influence of steel fibres on strength and ductility of normal and lightweight high strength concrete 37, 1361–1367.
- Balouch, S.U., Forth, J.P., Granju, J.L., 2010. Surface corrosion of steel fibre reinforced concrete. *Cem. Concr. Res.* 40, 410–414. <https://doi.org/10.1016/j.cemconres.2009.10.001>
- Bank, L.C., Campbell, T.I., Dolan, C.W., 2003. Guide for the Design and Construction of Concrete Reinforced with FRP Bars Reported by ACI Committee 440. *Concrete* 1–42. [https://doi.org/10.1061/40753\(171\)158](https://doi.org/10.1061/40753(171)158)
- Banthia, N., Sappakittipakorn, M., 2007. Toughness enhancement in steel fiber reinforced concrete through fiber hybridization. *Cem. Concr. Res.* 37, 1366–1372. <https://doi.org/10.1016/j.cemconres.2007.05.005>
- Banthia, N., Trottier, J.N., 1994. Concrete reinforced with deformed steel fibres, Part I: bond slip mechanism. *ACI Mater. J.* 91, 435–446.
- Barenblatt, G., 1959. The formation of equilibrium cracks during brittle fracture. General ideas and hypotheses. Axially-symmetric cracks. *J. Appl. Math. Mech.* 23, 622–636. [https://doi.org/10.1016/0021-8928\(59\)90157-1](https://doi.org/10.1016/0021-8928(59)90157-1)
- Barenblatt, G.I., 1962. The Mathematical Theory of Equilibrium Cracks in Brittle Fracture. *Adv. Appl. Mech.* 7, 55–129. [https://doi.org/10.1016/S0065-2156\(08\)70121-2](https://doi.org/10.1016/S0065-2156(08)70121-2)

- Bastidas-Arteaga, E., 2018. Reliability of Reinforced Concrete Structures Subjected to Corrosion-Fatigue and Climate Change. *Int. J. Concr. Struct. Mater.* 12. <https://doi.org/10.1186/s40069-018-0235-x>
- Bažant, Z.P., Desmorat, R., 1994. Size Effect in Fiber or Bar Pullout with Interface Softening Slip. *J. Eng. Mech.* 120, 1945–1962. [https://doi.org/10.1061/\(ASCE\)0733-9399\(1994\)120:9\(1945\)](https://doi.org/10.1061/(ASCE)0733-9399(1994)120:9(1945))
- Bazant, Z.P., Sener, S., 1988. Size Effect in Pullout Tests. *ACI Mater. J.* 85, 347–351. <https://doi.org/10.14359/2257>
- Beddar, M., 2002. Fibre-reinforced concrete: Past, present and future.
- Bencardino, F., Rizzuti, L., Spadea, G., Swamy, R.N., 2010. Experimental evaluation of fiber reinforced concrete fracture properties. *Compos. Part B Eng.* 41, 17–24. <https://doi.org/10.1016/j.compositesb.2009.09.002>
- Bentur, A., Mindess, S., 2007. *Fibre Reinforced Cementitious Composites*. Taylor & Francis, 2 Park Square, Milton Park, Abingdon, Oxon OX14 4RN.
- Berrocal, C., Lundgren, K., Löfgren, I., 2013. Influence of Steel Fibres on Corrosion of Reinforcement in Concrete in Chloride Environments: A Review. *Fibre Concr.* 2013 1–10.
- Błaszczyszki, T., Przybylska-Fałek, M., 2015. Steel Fibre Reinforced Concrete as a Structural Material. *Procedia Eng.* 122, 282–289. <https://doi.org/10.1016/j.proeng.2015.10.037>
- Böhni, H., 2005. *Corrosion in Reinforced Concrete Structures*. Elsevier Science Ltd.
- Bolzon, G., Cocchetti, G., 2003. Direct assessment of structural resistance against pressurized fracture. *Int. J. Numer. Anal. Methods Geomech.* 27, 353–378. <https://doi.org/10.1002/nag.276>
- Brandt, A.M., 2008. Fibre reinforced cement-based (FRC) composites after over 40 years of development in building and civil engineering. *Compos. Struct.* 86, 3–9. <https://doi.org/10.1016/j.compstruct.2008.03.006>
- Bresler, B., Bertero, V., 1968. Behavior of Reinforced Concrete under Repeated Load. *J. Struct. Div. ASCE* 94, 1567–1590.
- Brocks, W., Cornec, A., Scheider, I., 2007. Computational Aspects of Nonlinear Fracture Mechanics, *Comprehensive Structural Integrity*. <https://doi.org/10.1016/B0-08-043749-4/03102-5>
- Budiansky, E., Rice, J.R., 1973. Conservation laws and energy release rates. *J. Appl. Mech.* 40, 201–203.
- Burdekin, F.M., Stone, D.E.W., 1966. The crack opening displacement approach to fracture mechanics in yielding materials. *J. Strain Anal. Eng. Des.* 1, 145–153.
- Cabrera, J.G., 1996. Deterioration of concrete due to reinforcement steel corrosion. *Cem. Concr. Compos.* [https://doi.org/10.1016/0958-9465\(95\)00043-7](https://doi.org/10.1016/0958-9465(95)00043-7)
- Caggiano, A., Xargay, H., Folino, P., Martinelli, E., 2015. Experimental and numerical characterization of the bond behavior of steel fibers recovered from waste tires embedded in cementitious matrices. *Cem. Concr. Compos.* 62, 146–155. <https://doi.org/10.1016/j.cemconcomp.2015.04.015>

- Cairns, J., Du, Y., Law, D., 2007. Influence of corrosion on the friction characteristics of the steel/concrete interface. *Constr. Build. Mater.* 21, 190–197. <https://doi.org/10.1016/j.conbuildmat.2005.06.054>
- Cairns, J., Du, Y., Law, D., 2006. Residual bond strength of corroded plain round bars. *Mag. Concr. Res.* 58, 221–231. <https://doi.org/10.1680/mac.2006.58.4.221>
- Camacho, G.T., Ortiz, M., 1996. Computational modelling of impact damage in brittle materials. *Int. J. Solids Struct.* 33, 2899–2938. [https://doi.org/10.1016/0020-7683\(95\)00255-3](https://doi.org/10.1016/0020-7683(95)00255-3)
- Cao, Y.Y.Y., Yu, Q.L., 2018. Effect of inclination angle on hooked end steel fiber pullout behavior in ultra-high performance concrete. *Compos. Struct.* 201, 151–160. <https://doi.org/10.1016/j.compstruct.2018.06.029>
- Carol, I., López, C.M., Roa, O., 2001. Micromechanical analysis of quasi-brittle materials using fracture-based interface elements. *Int. J. Numer. Methods Eng.* 52, 193–215. <https://doi.org/10.1002/nme.277>
- Castellano, M.G., 2005. Seismic protection of monuments by shape memory alloy devices and shock transmitters 1229–1234.
- Castellano, M.G., Martelli, A., 2000. The Influence of Shape Memory Alloy Ties on the Seismic Behaviour of Historical Masonry Buildings, in: *Proceedings of the IASS Symposium on “Bridging Large Spans.”* pp. 271–280.
- CEB-FIP Report, 2000. Bond of reinforcement in concrete: State of the art. *FIB Bull.* 10 434. <https://doi.org/10.1680/mac.11.00091>
- Cecconi, G., Cerasuolo, C., Salva, R., Torricelli, P., 2008. *Quaderni Trimestrali Consorzio Venezia Nuova.*
- Červenka, J., Chandra Kishen, J.M., Saouma, V.E., 1998. Mixed mode fracture of cementitious bimaterial interfaces. *Eng. Fract. Mech.* 60, 95–107. [https://doi.org/10.1016/S0013-7944\(97\)00094-5](https://doi.org/10.1016/S0013-7944(97)00094-5)
- Chaboche, J.L., Girard, R., Schaff, A., 1997. Numerical analysis of composite systems by using interphase/interface models. *Comput. Mech.* 20, 3–11. <https://doi.org/10.1007/s004660050209>
- Champaney, L., Valoroso, N., 2001. Evaluation of interface models for the analysis of non-linear behaviour of adhesively bonded joints, in: *Proceedings European Conference on Computational Mechanics (ECCM)*. Cracow, Poland.
- Chandra, N., Li, H., Shet, C., Ghonem, H., 2002. Some issues in the application of cohesive zone models for metal-ceramic interfaces. *Int. J. Solids Struct.* 39, 2827–2855. [https://doi.org/10.1016/S0020-7683\(02\)00149-X](https://doi.org/10.1016/S0020-7683(02)00149-X)
- Chandramouli K., Rao, S.S., Pannirselvam N, Sekhar, S.T., Sravana P, 2010. Strength Properties of Glass Fibre Concrete. *J. Eng. Appl. Sci.* 5, 1–6.
- Chanvillard, G., 1999. Modeling the pullout of wire-drawn steel fibers. *Cem. Concr. Res.* 29, 1027–1037. [https://doi.org/10.1016/S0008-8846\(99\)00081-2](https://doi.org/10.1016/S0008-8846(99)00081-2)
- Chanvillard, G., Aitcin, P.C., 1996. Pull-out behavior of corrugated steel fibers qualitative and statistical analysis. *Adv. Cem. Based Mater.* 4, 28–41. [https://doi.org/10.1016/1065-7355\(96\)00036-3](https://doi.org/10.1016/1065-7355(96)00036-3)

- Cheng, A., Huang, R., Wu, J.K., Chen, C.H., 2005. Effect of rebar coating on corrosion resistance and bond strength of reinforced concrete. *Constr. Build. Mater.* 19, 404–412. <https://doi.org/10.1016/j.conbuildmat.2004.07.006>
- Cherepanov, G.P., 1967. Crack propagation in continuous media. *J. Appl. Math. Mech.* 31, 503–512. [https://doi.org/https://doi.org/10.1016/0021-8928\(67\)90034-2](https://doi.org/https://doi.org/10.1016/0021-8928(67)90034-2)
- Chess, P., Grønvold & Karnov (Eds.), 1998. *Cathodic Protection of Steel in Concrete*. E & FN SPON, London EC4P 4EE.
- Choi, O.C., Hadje-Ghaffari, H., Darwin, D., McCabe, S.L., 1991. Bond of epoxy-coated reinforcement: Bar parameters. *ACI Mater. J.* 88, 207–217.
- Chung, D.D.L., 2000. Cement reinforced with short carbon fibers: A multifunctional material. *Compos. Part B Eng.* 31, 511–526. [https://doi.org/10.1016/S1359-8368\(99\)00071-2](https://doi.org/10.1016/S1359-8368(99)00071-2)
- Chung, L., Jay Kim, J.H., Yi, S.T., 2008. Bond strength prediction for reinforced concrete members with highly corroded reinforcing bars. *Cem. Concr. Compos.* 30, 603–611. <https://doi.org/10.1016/j.cemconcomp.2008.03.006>
- Clemena, G.G., Jackson, D.R., 2002. *Cathodic Protection of Concrete Bridge Decks Using Titanium Mesh*. Charlottesville, Virginia.
- CNR, 2007. *CNR-DT 204/2006 Guide for the Design and Construction of Fiber-Reinforced Concrete Structures* 57.
- Cocchetti, G., Maier, G., Shen, X.P., 2002. Piecewise linear models for interfaces and mixed mode cohesive cracks. *C. - Comput. Model. Eng. Sci.* 3, 279–298.
- Coccia, S., Imperatore, S., Rinaldi, Z., 2016. Influence of corrosion on the bond strength of steel rebars in concrete. *Mater. Struct. Constr.* 49, 537–551. <https://doi.org/10.1617/s11527-014-0518-x>
- Cominoli, L., Failla, C., Plizzari, G.A., 2007. Steel and synthetic fibres for enhancing concrete toughness and shrinkage behaviour, in: Kraus, R.N., Naik, T.R., Claisse, P., Pouya, H.S. (Eds.), *Proc. Int. Conf: Sustainable Construction Materials and Technologies*. UW Milwaukee CBU, Coventry, pp. 231–240.
- Corneec, A., Scheider, I., Schwalbe, K.H., 2003. On the practical application of the cohesive model. *Eng. Fract. Mech.* 70, 1963–1987. [https://doi.org/10.1016/S0013-7944\(03\)00134-6](https://doi.org/10.1016/S0013-7944(03)00134-6)
- Cosenza, E., Manfredi, G., Realfonzo, R., 1995. Analytical modelling of bond between FRP reinforcement and concrete, in: L. Taerwe (Ed.), *Non-Metallic (FRP) Reinforcement for Concrete Structures*. E & FN SPON, London SE 8HN.
- Cox, H.L., 1952. The elasticity and strength of paper and other fibrous materials. *Br. J. Appl. Phys.* 3.
- Cox, J.V., Hermann, L.R., 1992. Confinement stress dependent bond behavior, Part II: A two degree of freedom plasticity model, in: *Proceedings of the International Conference*. Riga, Latvia.
- Cox, S.B., 2015. *The Influence of Concrete Heterogeneity on the Pull-out Behaviour of Steel Fibres*. Eindhoven University of Technology.
- Croci, G., 1998. The Basilica of St. Francis of Assisi after the September 1997 Earthquake. *Struct. Eng. Int.* 8, 56–58. <https://doi.org/10.2749/101686698780489667>

- Cunha, V.M.C.F., 2010. Steel Fibre Reinforced Self-Compacting Concrete (from Micro-Mechanics to Composite Behaviour). University of Minho.
- Cunha, V.M.C.F., Barros, J.A.O., Sena-Cruz, J.M., 2010. Pullout Behavior of Steel Fibers in Self-Compacting Concrete. *J. Mater. Civ. Eng.* 22, 1–9. [https://doi.org/10.1061/\(ASCE\)MT.1943-5533.0000001](https://doi.org/10.1061/(ASCE)MT.1943-5533.0000001)
- Dakanali, I., Stavrakas, I., Triantis, D., Kourkoulis, S.K., 2016. Pull-out of threaded reinforcing bars from marble blocks. *Procedia Struct. Integr.* 2, 2865–2872. <https://doi.org/10.1016/j.prostr.2016.06.358>
- Darwin, D., Idun, E.K., Zuo, J., Tholen, M.L., 1998. Reliability-based strength reduction factor for bond. *ACI Struct. J.* 95, 434–443.
- Dawes, M.G., 1985. *The COD design curve: Limitations, Finite Size and Application.* Cambridge.
- Del Piero, G., Raous, M., 2010. A unified model for adhesive interfaces with damage, viscosity, and friction. *Eur. J. Mech. A/Solids* 29, 496–507. <https://doi.org/10.1016/j.euromechsol.2010.02.004>
- Diamond, S., Huang, J., 2001. The ITZ in concrete - a different view based on image analysis and SEM observations 23, 179–188.
- Dolce, M., Nigro, D.S., Ponzio, F.C., Marinetto, R., 2001. Il miglioramento sismico dei beni monumentali con il sistema CAM, in: X° Convegno Nazionale ANIDIS - l'Ingegneria Sismica in Italia. Potenza/Matera, pp. 1–4.
- Donachie, M.J., 2000. Titanium: A Technical Guide, 2nd Edition | Introduction to Selection of Titanium Alloys. *ASM Int.* 180, 5–11. <https://doi.org/10.1361/tatg2000p005>
- Dong, S., Zhao, B., Lin, C., Du, R., Hu, R., Zhang, G.X., 2012. Corrosion behavior of epoxy/zinc duplex coated rebar embedded in concrete in ocean environment. *Constr. Build. Mater.* 28, 72–78. <https://doi.org/10.1016/j.conbuildmat.2011.08.026>
- Dugdale, D.S., 1960. Yielding of steel sheets containing slits. *J. Mech. Phys. Solids* 8, 100–104. [https://doi.org/10.1016/0022-5096\(60\)90013-2](https://doi.org/10.1016/0022-5096(60)90013-2)
- Eide, M.B., Hisdal, J.-M., 2012. Ultra High Performance Fibre Reinforced Concrete (UHPFRC) – State of the art.
- Elices, M., Guinea, G. V., Gomez, J., Planas, J., 2002. The cohesive zone model: advantages , limitations and challenges. *Eng. Fract. Mech.* 69, 137–163. [https://doi.org/DOI: 10.1016/S0013-7944\(01\)00083-2](https://doi.org/DOI: 10.1016/S0013-7944(01)00083-2)
- EN 10365:2017, 2017. Hot rolled steel channels, I and H sections - Dimensions and masses.
- EN 14488-5:2006, 2006. Testing sprayed concrete - Part 5: Determination of energy absorption capacity of fibre reinforced slab specimens.
- EN 14651, 2005. Test method for metallic fibered concrete - Measuring the flexural tensile strength (limit of proportionality (LOP), residual).
- Erdem, S., Kağnıcı, T., Blankson, M.A., 2015. Investigation of Bond between Fibre Reinforced Polymer (FRP) Composites Rebar and Aramid Fibre-Reinforced Concrete 5, 148–154. <https://doi.org/10.5923/j.cmaterials.20150506.02>
- Ertzibengoa, D., Matthys, S., Taerwe, L., 2012. Bond behaviour of flat stainless steel rebars in concrete. *Mater. Struct. Constr.* 45, 1639–1653. <https://doi.org/10.1617/s11527-012-9862-x>

- Fanella, D.A., Naaman, A.E., 1985. Stress-Strain Properties of Fiber Reinforced Mortar in Compression. *J. Am. Concr. Inst.* 82, 475–483.
- Fang, C., Lundgren, K., Chen, L., Zhu, C., 2004. Corrosion influence on bond in reinforced concrete. *Cem. Concr. Res.* 34, 2159–2167. <https://doi.org/10.1016/j.cemconres.2004.04.006>
- Feldman, L.R., Bartlett, F.M., 2005. Bond Strength Variability in Pullout Specimens with Plain Reinforcement. *ACI Struct. J.* 102, 860–867. <https://doi.org/10.14359/14794>
- fib, 2012a. CEB-FIP Model Code 2010. Lausanne, Switzerland : International Federation for Structural Concrete (fib), 2012.
- fib, 2012b. Model Code for Concrete Structures 2010 - Final draft, fib Bulletin No. 65 and 66.
- Fischer-Cripps, A.C., 2007. Linear Elastic Fracture Mechanics, in: *Introduction to Contact Mechanics*. p. 221. https://doi.org/10.1007/978-0-387-68188-7_2
- Franchi, A., Fratesi, R., Moriconi, G., Plizzari, G.A., 1999. Caratteristiche meccaniche e di aderenza al calcestruzzo di barre di armatura in acciaio zincato, in: *Giornate AICAP*. Torino, pp. 53–62.
- Fratesi, R., Moriconi, G., Coppola, L., 1990. The Influence of Steel Galvanization on Rebars Behaviour in Concrete, in: Page, C.L., Bamforth, P.B., Figg, J.W. (Eds.), *Corrosion of Reinforcement in Concrete Constructions*. The Royal Society of Chemistry, pp. 630–641.
- Geubelle, P.H., Baylor, J.S., 1998. Impact-induced delamination of composites: a 2D simulation. *Compos. Part B Eng.* 29, 589–602. [https://doi.org/10.1016/S1359-8368\(98\)00013-4](https://doi.org/10.1016/S1359-8368(98)00013-4)
- Giambanco, G., Mroz, Z., 2001. The Interphase Model for the Analysis of Joints in Rock Masses and Masonry Structures. *Meccanica* 36, 111–130. <https://doi.org/https://doi.org/10.1023/A:1011957217840>
- Gopalaratnam, V.S., Shah, S.P., 1987. Failure Mechanisms and Fracture of Fiber Reinforced Concrete. *ACI Spec. Publication* 105, 1–26.
- Granju, J.L., Balouch, S.U., 2005. Corrosion of steel fibre reinforced concrete from the cracks. *Cem. Concr. Res.* 35, 572–577. <https://doi.org/10.1016/j.cemconres.2004.06.032>
- Grimaldi, A., Luciano, R., 2000. Tensile stiffness and strength of fiber-reinforced concrete. *J. Mech. Phys. Solids* 48, 1987–2008. [https://doi.org/10.1016/S0022-5096\(99\)00079-4](https://doi.org/10.1016/S0022-5096(99)00079-4)
- Grimaldi, A., Meda, A., Rinaldi, Z., 2013. Experimental behaviour of fibre reinforced concrete bridge decks subjected to punching shear. *Compos. Part B Eng.* 45, 811–820. <https://doi.org/10.1016/j.compositesb.2012.09.044>
- Grunewald, S., 2004. Performance-based design of self-compacting fibre reinforced concrete. Delft Univ. Press. Delft University of Technology (The Netherlands).
- Guohua Xing, Cheng Zhou, TaoWu, and B.L., 2015. Experimental study on bond behavior between Plain Reinforcing Bars and concrete. *Adv. Mater. Sci. Eng.* 18, 745–752. <https://doi.org/10.1016/j.conbuildmat.2004.04.026>

- Gylltoft, K., 1989. Fracture Mechanics Applied to Bond Failure in Pull-out Tests, in: Elfgren, L. (Ed.), *Fracture Mechanics of Concrete Structures: From Theory to Applications (RILEM Report 3)*. Chapman and Hall, Stockholm, pp. 258–262.
- Hadje-Ghaffari, H., Darwin, D., Choi, O.C., Darwin, D., McCabe, S.L., 1994. Bond of Epoxy-Coated Reinforcement : Cover , Casting Position , Slump , and Consolidation. *ACI Struct. J.* 91, 59.
- Hamoush, S., Abu-lebdeh, T., Cummins, T., Zornig, B., A, N.C., Street, E.M., 2010. Pullout Characterizations of Various Steel Fibers Embedded in Very High-Strength Concrete Department of Civil , Architectural and Environmental Engineering , US Army Corps of Engineers , Concrete and Materials Division , Vicksburg , MS 39183 Manhattan Con. Am. J. Eng. Appl. Sci. 3, 418–426.
- Hansson, C.M., Mammoliti, L., Hope, B.B., 1998. Corrosion inhibitors in concrete - part I: the principles. *Cem. Concr. Res.* 28, 1775–1781. [https://doi.org/https://doi.org/10.1016/S0008-8846\(98\)00142-2](https://doi.org/https://doi.org/10.1016/S0008-8846(98)00142-2)
- Hao, Y., Hao, H., 2017. Pull-out behaviour of spiral-shaped steel fibres from normal-strength concrete matrix. *Constr. Build. Mater.* 139, 34–44. <https://doi.org/10.1016/j.conbuildmat.2017.02.040>
- Hao, Y., Hao, H., Chen, G., 2014. Experimental investigation of the behaviour of spiral steel fibre reinforced concrete beams subjected to drop-weight impact loads. *Mater. Struct.* 49, 353–370. <https://doi.org/10.1617/s11527-014-0502-5>
- Harajli, M., Hamad, B., Karam, K., 2002. Bond-slip Response of Reinforcing Bars Embedded in Plain and Fiber Concrete. *J. Mater. Civ. Eng.* 14. [https://doi.org/https://doi.org/10.1061/\(ASCE\)0899-1561\(2002\)14:6\(503\)](https://doi.org/https://doi.org/10.1061/(ASCE)0899-1561(2002)14:6(503))
- Hashin, Z., 1963. Theory of Mechanical Behavior of Heterogeneous Media. *Appl. Mech. Rev.* 17, 1–9.
- Hayfield, P.C.S., Warne, M.A., 1989. Titanium based mesh anode in the cathodic protection of reinforcing bars in concrete. *Constr. Build. Mater.* [https://doi.org/10.1016/0950-0618\(89\)90007-X](https://doi.org/10.1016/0950-0618(89)90007-X)
- Hester, C.J., Salamizavaregh, S., Darwin, D., McCabe, S.L., 1993. Bond of Epoxy-Coated Reinforcement : Splices.
- Higgins, C., Knudtsen, J., Amneus, D., Barker, L., 2017. Shear and Flexural Strengthening of Reinforced Concrete Beams with Titanium Alloy Bars, in: *Proceedings of the 2nd World Congress on Civil, Structural, and Environmental Engineering (CSEE' 17)*. pp. 1–8. <https://doi.org/10.11159/icsenm17.141>
- Hill, R., 1963. Elastic properties of reinforced solids: Some theoretical principles. *J. Mech. Phys. Solids* 11, 357–372. [https://doi.org/https://doi.org/10.1016/0022-5096\(63\)90036-X](https://doi.org/https://doi.org/10.1016/0022-5096(63)90036-X)
- Hillerborg, A., Modéer, M., Petersson, P.E., 1976. Analysis of crack formation and crack growth in concrete by means of fracture mechanics and finite elements. *Cem. Concr. Res.* 6, 773–781. [https://doi.org/10.1016/0008-8846\(76\)90007-7](https://doi.org/10.1016/0008-8846(76)90007-7)
- Homma, D., Mihashi, H., Nishiwaki, T., 2009. Self-Healing Capability of Fibre Reinforced Cementitious Composites. *J. Adv. Concr. Technol.* 7, 217–228. <https://doi.org/10.3151/jact.7.217>

- Horne, A.T., Richardson, I.G., Brydson, R.M.D., 2007. Quantitative analysis of the microstructure of interfaces in steel reinforced concrete 37, 1613–1623. <https://doi.org/10.1016/j.cemconres.2007.08.026>
- Hoy, C.W., Bartos, P.J.M., 1999. Interaction and packing of fibres: effects on the mixing process, in: Reinhardt, H.W., Naaman, A.E. (Eds.), PRO 6: 3rd International RILEM Workshop on High Performance Fiber Reinforced Cement Composites (HPFRCC3). RILEM Publications, pp. 181–191.
- Hughes, B.P., 1981. Experimental test results for flexure and direct tension of fibre cement composites. *Int. J. Cem. Compos. Light. Concr.* 3, 13–18. [https://doi.org/10.1016/0262-5075\(81\)90018-X](https://doi.org/10.1016/0262-5075(81)90018-X)
- Hughes, B.P., Fattuhi, N.I., 1975. Fiber bond strengths in cement and concrete. *Mag. Concr. Res.* 27, 161–166.
- Ibrahim, K.I.M., 2016. Mechanical Properties of Glass Fiber Reinforced Concrete (GFRC). *IOSR J. Mech. Civ. Eng.* 13, 47–50. <https://doi.org/10.9790/1684-1304054750>
- Ingraffea, A.R., Gerstk, W.H., Gergely, P., Saouma, V., 1984. Fracture Mechanics of Bond in Reinforced Concrete. *J. Struct. Eng.* [https://doi.org/10.1061/\(ASCE\)0733-9445\(1984\)110:4\(871\)](https://doi.org/10.1061/(ASCE)0733-9445(1984)110:4(871))
- Isla, F., Ruano, G., Luccioni, B., 2015. Analysis of steel fibers pull-out. Experimental study. *Constr. Build. Mater.* 100, 183–193. <https://doi.org/10.1016/j.conbuildmat.2015.09.034>
- Jaffer, S.J., Hansson, C.M., 2009. Chloride-induced corrosion products of steel in cracked-concrete subjected to different loading conditions. *Cem. Concr. Res.* 39, 116–125. <https://doi.org/10.1016/j.cemconres.2008.11.001>
- Jorge, S., Dias-da-Costa, D., Júlio, E.N.B.S., 2012. Influence of anti-corrosive coatings on the bond of steel rebars to repair mortars. *Eng. Struct.* 36, 372–378. <https://doi.org/10.1016/j.engstruct.2011.12.028>
- JSCE, 2008. Recommendations for Design and Construction of High Performance Fiber Reinforced Cement Composites with Multiple Fine Cracks (HPFRCC). *Concr. Eng. Ser.* 82, Testing Method 6-10.
- Kabir, M.R., Islam, M., 2014. Bond stress behavior between concrete and steel rebar: Critical investigation of pull-out test via Finite Element Modeling. *Int. J. Civ. Struct. Eng.* 5, 80–90. <https://doi.org/10.6088/ijcser.2014050008>
- Karanassos, K., 2014. Criteri di reintegrazione strutturale nel restauro dei monumenti dell'Acropoli di Atene. *Problemi metodologici e scelte progettuali.* Thiasos 3, 43–54.
- Kepler, J.L., Locke, C.E., 2000. Evaluation of Corrosion Protection Methods for Reinforced Concrete Highway Structures. *Corrosion* 231.
- Keuser, M., Mehlhorn, G., 1987. Finite Element Models for Bond Problems. *J. Struct. Eng.* 113. [https://doi.org/https://doi.org/10.1061/\(ASCE\)0733-9445\(1987\)113:10\(2160\)](https://doi.org/https://doi.org/10.1061/(ASCE)0733-9445(1987)113:10(2160))
- Khaloo, A.R., Kim, N., 1997. Influence of Concrete and Fiber Characteristics on Behavior of Steel Fiber Reinforced Concrete under Direct Shear. *ACI Mater. J.* 94, 592–601.
- Kim, D.J., Kang, S.H., Ahn, T.H., 2014. Mechanical Characterization of High-Performance Steel-Fiber Reinforced Cement Composites with Self-Healing Effect. *Materials (Basel).* 7, 508–526. <https://doi.org/10.3390/ma7010508>

- Knudtsen, J., 2016. Shear Strengthening Reinforced Concrete Bridge Girders Using Near-Surface Mounted Titanium Alloy Bars. <https://doi.org/10.15713/ins.mmj.3>
- Koch, G., Varney, J., Thompson, N., Moghissi, O., Gould, M., Payer, J., 2016. International Measures of Prevention , Application , and Economics of Corrosion Technologies Study. *NACE Int.* 216.
- Kondo, D., Weleman, H., Cormery, F., 2007. Basic concepts and models in continuum damage mechanics. *Rev. Eur. Génie Civ.* 11, 927–943. <https://doi.org/10.1080/17747120.2007.9692970>
- Kumar, K., Ritu, E., 2015. Effect Of Acrylic Fiber On The Flexural Strength And Durability Of Pavement Quality Concrete : A Review 4, 77–81.
- Lancioni, G., Donnini, J., Corinaldesi, V., 2017. A variational model for determining fracture modes in FRCM Systems. *Procedia Struct. Integr.* 3, 354–361. <https://doi.org/10.1016/j.prostr.2017.04.031>
- Landes, J.B.D., Begley, J.A., 1976. Serendtrity and the J integral. *Int. J. Fract.* 12, 764–766. <https://doi.org/10.1007/BF00037923>
- Lawrence, P., 1972. Some theoretical considerations of fibre pull-out from an elastic matrix. *J. Mater. Sci.* 7, 1–6.
- Lee, H.S., Noguchi, T., Tomosawa, F., 2002. Evaluation of the bond properties between concrete and reinforcement as a function of the degree of reinforcement corrosion. *Cem. Concr. Res.* 32, 1313–1318. [https://doi.org/10.1016/S0008-8846\(02\)00783-4](https://doi.org/10.1016/S0008-8846(02)00783-4)
- Lee, J.-H., Kighuta, K., 2017. Twin-twist effect of fibers on the pullout resistance in cementitious materials. *Constr. Build. Mater.* 146, 555–562. <https://doi.org/10.1016/j.conbuildmat.2017.04.147>
- Lee, Y., Kang, S., Kim, J., 2010. Pullout behavior of inclined steel fiber in an ultra-high strength cementitious matrix. *Constr. Build. Mater.* 24, 2030–2041. <https://doi.org/10.1016/j.conbuildmat.2010.03.009>
- Lemaitre, J., 1992. *A Course on Damage Mechanics*. Springer Berlin Heidelberg, Berlin, Heidelberg. <https://doi.org/10.1007/978-3-662-02761-5>
- Lepech, M., Li, V.C., 2004. Size effect in EEC structural members in flexure. *Fram. Fract. Mech. Concr. Struct.* 1059–1066.
- Leyens, C., Peters, M., 2003. *Titanium and Titanium Alloys*, Titanium and Titanium Alloys. <https://doi.org/10.1002/3527602119>
- Li, V.C., Chan, Y., 1994. Determination of Interfacial Debond Mode for Fiber-Reinforced Cementitious Composites. *J. Eng. Mech.* 120, 707–719. [https://doi.org/10.1061/\(ASCE\)0733-9399\(1994\)120:4\(707\)](https://doi.org/10.1061/(ASCE)0733-9399(1994)120:4(707))
- Li, V.C., Lin, Z.L., Matsumoto, T., 1998. Influence of fiber bridging on structural size-effect. *Int. J. Solids Struct.* 35, 4223–4238. [https://doi.org/10.1016/S0020-7683\(97\)00311-9](https://doi.org/10.1016/S0020-7683(97)00311-9)
- Li, V.C., Stang, H., Krenchel, H., 1993. Micromechanics of crack bridging in fibre-reinforced concrete. *Mater. Struct.* 26, 486–494. <https://doi.org/10.1007/BF02472808>
- Lilliu, G., van Mier, J.G.M., 2003. 3D lattice type fracture model for concrete. *Eng. Fract. Mech.* 70, 927–941. [https://doi.org/10.1016/S0013-7944\(02\)00158-3](https://doi.org/10.1016/S0013-7944(02)00158-3)

- Lin, G., Geubelle, P.H., Sottos, N.R., 2001. Simulation of fiber debonding with friction in a model composite pushout test. *Int. J. Solids Struct.* 38, 8547–8562. [https://doi.org/10.1016/S0020-7683\(01\)00085-3](https://doi.org/10.1016/S0020-7683(01)00085-3)
- Löfgren, I., 2005. Fibre-reinforced Concrete for Industrial Construction - a fracture mechanics approach to material testing and structural analysis. Chalmers University of Technology. <https://doi.org/91-7291-696-6>
- Lourenco, P.J.B.B., 1996. Computational strategies for masonry structures.
- Luccioni, B., Oller, S., 2003. A directional damage model. *Comput. Methods Appl. Mech. Eng.* 192, 1119–1145. [https://doi.org/10.1016/S0045-7825\(02\)00577-7](https://doi.org/10.1016/S0045-7825(02)00577-7)
- Ludirdja, D., Young, J.F., 1992. Synthetic Fiber Reinforcement for Concrete. USACERL Tech. Rep. FM- 93/ 02.
- Lundgren, K., 2007. Effect of corrosion on the bond between steel and concrete: an overview. *Mag. Concr. Res.* 59, 447–461. <https://doi.org/10.1680/mac.2007.59.6.447>
- Lundgren, K., 2005. Bond between ribbed bars and concrete. Part 1: Modified model. *Mag. Concr. Res.* 57, 371–382. <https://doi.org/10.1680/mac.2005.57.7.371>
- Lundgren, K., Gylltoft, K., 2000. A model for the bond between concrete and reinforcement. *Mag. Concr. Res.* 52, 53–63. <https://doi.org/10.1680/mac.2000.52.1.53>
- Maage, M., 1977. Interaction between steel fibres and cement-based matrices. *Mater. Struc- tures, Res. Test.* 10, 297–301.
- Mahmud, G.H., Yang, Z., Hassan, A.M.T., 2013. Experimental and numerical studies of size effects of Ultra High Performance Steel Fibre Reinforced Concrete (UHPFRC) beams. *Constr. Build. Mater.* 48, 1027–1034. <https://doi.org/10.1016/j.conbuildmat.2013.07.061>
- Marcos-Meson, V., Michel, A., Solgaard, A., Fischer, G., Edvardsen, C., Skovhus, T.L., 2017. Corrosion resistance of steel fibre reinforced concrete - A literature review. *Cem. Concr. Res.* <https://doi.org/10.1016/j.cemconres.2017.05.016>
- Markovic, I., 2006. High-Performance Hybrid-Fibre Concrete.
- Masiani, R., Tocci, C., 2012. Ancient and modern restorations for the column of Marcus Aurelius in Rome. *Int. J. Archit. Herit.* <https://doi.org/10.1080/15583058.2011.593254>
- Mazars, J., Pijaudier-Cabot, G., 2001. Bridges between Damage and Fracture Mechanics, in: *Handbook of Materials Behavior Models*. Elsevier, pp. 542–548. <https://doi.org/10.1016/B978-012443341-0/50060-0>
- McDonald, D.B., Sherman, M.R., Pfeifer, D.W., Virmani, Y.P., 1995. Stainless steel reinforcing as corrosion protection. *Concr. Int.* 17, 65–70.
- Meaud, C., Jurkiewicz, B., Ferrier, E., 2014. Steel-concrete bonding connection: An experimental study and non-linear finite element analysis. *Int. J. Adhes. Adhes.* 54, 131–142. <https://doi.org/10.1016/j.ijadhadh.2014.05.010>
- Meskenas, A., Gelazius, V., Kaklauskas, G., Gribniak, V., Rimkus, A., 2013. A new technique for constitutive modeling of SFRC. *Procedia Eng.* 57, 762–766. <https://doi.org/10.1016/j.proeng.2013.04.096>

- Mi, Y., Crisfield, M.A., Davies, G.A.O., 1998. Progressive Delamination using interface elements. *J. Compos. Mater.* 32, 1246–1272. <https://doi.org/https://doi.org/10.1177/002199839803201401>
- Mimura, Y., Yoshitake, I., Zhang, W., 2011. Uniaxial Tension Test of Slender Reinforced Early Age Concrete Members. *Materials (Basel)*. 4, 1345–1359. <https://doi.org/10.3390/ma4081345>
- Mo, K.H., Alengaram, U.J., Jumaat, M.Z., Liu, M.Y.J., 2015. Contribution of acrylic fibre addition and ground granulated blast furnace slag on the properties of lightweight concrete. *Constr. Build. Mater.* 95, 686–695. <https://doi.org/10.1016/j.conbuildmat.2015.07.048>
- Mo, Y.L., Chan, J., 1996. Bond and Slip of Plain Rebars in Concrete. *J. Mater. Civ. Eng.* 8, 208–211. [https://doi.org/10.1061/\(ASCE\)0899-1561\(1996\)8:4\(208\)](https://doi.org/10.1061/(ASCE)0899-1561(1996)8:4(208))
- Mosler, J., Scheider, I., 2011. A thermodynamically and variationally consistent class of damage-type cohesive models. *J. Mech. Phys. Solids* 59, 1647–1668. <https://doi.org/10.1016/j.jmps.2011.04.012>
- Muley, P., Varpe, S., Ralwani, R., 2015. Chopped Carbon Fibers Innovative Material for Enhancement of Concrete Performances. *Int. J. Sci. Eng. Appl. Sci.* 2395–3470.
- Muñoz, M.B., 2011. STUDY OF BOND BEHAVIOUR BETWEEN FRP REINFORCEMENT AND CONCRETE.
- Naaman, A.E., 2007. Deflection-Softening and Deflection-Hardening FRC Composites: Characterization and Modeling. *ACI Spec. Publication* 248, 53–66.
- Naaman, A.E., 2003. Engineered Steel Fibers with Optimal Properties for Reinforcement of Cement Composites. *J. Adv. Concr. Technol.* 1, 241–252. <https://doi.org/10.3151/jact.1.241>
- Naaman, A.E., 1985. Fiber Reinforcement for Concrete. *Concr. Int.* 7, 21–25.
- Naaman, A.E., Najm, H., 1991. Bond-slip mechanisms of steel fibers in concrete. *ACI Mater. J.* 88, 135–145.
- Naaman, A.E., Namur, G., Najm, H., Alwan, J., 1989. Bond Mechanisms in Fiber Reinforced Cement-Based Composites.
- Naaman, A.E., Namur, G.G., Alwan, J.M., Najm, H.S., 1991. Fiber Pullout and Bond Slip. I: Analytical Study. *J. Struct. Eng.* 117, 2769–2790. [https://doi.org/10.1061/\(ASCE\)0733-9445\(1991\)117:9\(2769\)](https://doi.org/10.1061/(ASCE)0733-9445(1991)117:9(2769))
- Naaman, A.E., Reinhardt, H.W., 2003. High Performance Fiber Reinforced Cement Composites HPRCC-4: International RILEM Workshop. *Mater. Struct.* 36, 710–712. <https://doi.org/10.1007/BF02479507>
- Naaman, A.E., Shah, S.P., 1976. Pull-Out Mechanism in Steel Fiber-Reinforced Concrete. *J. Struct. Div. ASCE* 102, 1537–1548.
- Namur, G.G., Alwan, J.M., Najm, H.S., 1991. Fiber pullout and bond slip. I: Analytical study. *J. Struct. Eng.* 117, 2769–2790.
- Nanni, A., Al-Zaharani, M.M., Al-Dulaijan, S.U., Bakis, C.E., Boothby, T.E., 1995. Bond of FRP reinforcement to concrete - experimental results, in: Taerwe, L. (Ed.), *Non-Metallic (FRP) Reinforcement for Concrete Structures*. E & FN SPON, London SE1 8HN.

- Narayanan, R., Darwish, Y.S., 1987. Use of Steel Fibers as Shear Reinforcement. *ACI Struct. J.* 84, 216–227.
- Nataraja, M., 1999. Stress–strain curves for steel-fiber reinforced concrete under compression. *Cem. Concr. Compos.* 21, 383–390. [https://doi.org/10.1016/S0958-9465\(99\)00021-9](https://doi.org/10.1016/S0958-9465(99)00021-9)
- Navarro, I., Yepes, V., Martí, J., 2018. Life Cycle Cost Assessment of Preventive Strategies Applied to Prestressed Concrete Bridges Exposed to Chlorides. *Sustainability* 10, 845. <https://doi.org/10.3390/su10030845>
- Needleman, A., 2013. Some issues in cohesive surface modeling. *Procedia IUTAM* 10, 221–246. <https://doi.org/10.1016/j.piutam.2014.01.020>
- Nemat-Nasser, S., Hori, M., 1993. *Micromechanics: Overall Properties of Heterogeneous Materials*, 2nd Editio. ed. North Holland, Amsterdam. <https://doi.org/10.1115/1.2788912>
- Neville, A.M., 2011. Properties of Concrete, *Journal of General Microbiology*. <https://doi.org/10.4135/9781412975704.n88>
- Ngo, D., Scordelis, A.C., 1967. Finite element analysis of reinforced concrete beams. *ACI J.* 64, 152–163.
- Oliveira, D. V., Lourenço, P.B., 2004. Implementation and validation of a constitutive model for the cyclic behaviour of interface elements. *Comput. Struct.* 82, 1451–1461. <https://doi.org/10.1016/j.compstruc.2004.03.041>
- Orangun, C.O., Jirsa, J.O., Breen, J.E., 1977. A Reevaluation of Test Data on Development Length and Splices. *J. Am. Concr. Inst.* 74, 114–122. <https://doi.org/10.14359/10993>
- Ortiz, M., Pandolfi, A., 1999. Finite-deformation irreversible cohesive elements for three-dimensional crack-propagation analysis. *Int. J. Numer. Methods Eng.* 44, 1267–1282. [https://doi.org/10.1002/\(SICI\)1097-0207\(19990330\)44:9<1267::AID-NME486>3.0.CO;2-7](https://doi.org/10.1002/(SICI)1097-0207(19990330)44:9<1267::AID-NME486>3.0.CO;2-7)
- Paegle, I., 2015. Characterization and modeling of fiber reinforced concrete for structural applications in beams and plates. Technical University of Denmark.
- Paegle, I., Fischer, G., 2011. Shear crack formation and propagation in reinforced Engineered Cementitious Composites, in: *International Rilem Conference on Advances in Construction Materials Through Science and Engineering*.
- Pająk, M., Ponikiewski, T., 2013. Flexural behavior of self-compacting concrete reinforced with different types of steel fibers. *Constr. Build. Mater.* 47, 397–408. <https://doi.org/10.1016/j.conbuildmat.2013.05.072>
- Park, K., Paulino, G.H., 2013. Cohesive Zone Models: A Critical Review of Traction-Separation Relationships Across Fracture Surfaces. *Appl. Mech. Rev.* 64, 060802. <https://doi.org/10.1115/1.4023110>
- Park, K., Paulino, G.H., Roesler, J.R., 2009. A unified potential-based cohesive model of mixed-mode fracture. *J. Mech. Phys. Solids* 57, 891–908. <https://doi.org/10.1016/j.jmps.2008.10.003>
- Parrinello, F., Failla, B., Borino, G., 2009. Cohesive-frictional interface constitutive model. *Int. J. Solids Struct.* 46, 2680–2692. <https://doi.org/10.1016/j.ijsolstr.2009.02.016>

- Pereira, E., Fischer, G., Barros, J.A.O., Lepech, M., 2010. Crack formation and tensile stress-crack opening behavior of Fiber Reinforced Cementitious Composites (FRCC), in: 7th International Conference on Fracture Mechanics of Concrete and Concrete Structures (FraMCoS 7).
- Pernicova, R., Dobias, D., Pokorny, P., 2017. Problems Connected with use of Hot-dip Galvanized Reinforcement in Concrete Elements. *Procedia Eng.* 172, 859–866. <https://doi.org/10.1016/j.proeng.2017.02.086>
- Pijaudier-Cabot, G., Mazars, J., Pulikowski, J., 1991. Steel-concrete bond analysis with nonlocal continuous damage. *J. Struct. Eng.* 117, 862–882.
- Pineau, A., 2006. Development of the Local Approach to Fracture over the Past 25 years: Theory and Applications. *Int. J. Fract.* 138, 139–166. <https://doi.org/10.1007/s10704-006-0035-1>
- Platt, S.L., 2018. Galvanic corrosion potential and material and bond properties of titanium reinforcing bars. University of Pittsburgh.
- Rabbat, B.G., Russell, H.G., 1985. Friction Coefficient of Steel on Concrete or Grout. *J. Struct. Eng.* 111, 505–515. [https://doi.org/10.1061/\(ASCE\)0733-9445\(1985\)111:3\(505\)](https://doi.org/10.1061/(ASCE)0733-9445(1985)111:3(505))
- Ragueneau, F., Dominguez, N., Ibrahimbegovic, A., 2006. Thermodynamic-based interface model for cohesive brittle materials: Application to bond slip in RC structures. *Comput. Methods Appl. Mech. Eng.* 195, 7249–7263. <https://doi.org/10.1016/j.cma.2005.04.022>
- Raous, M., Ali Karray, M., 2009. Model coupling friction and adhesion for steel-concrete interfaces. *Int. J. Comput. Appl. Technol.* 34, 42–51. <https://doi.org/10.1504/IJCAT.2009.022701>
- Raous, M., Cangémi, L., Cocu, M., 1999. A consistent model coupling adhesion, friction, and unilateral contact. *Comput. Methods Appl. Mech. Eng.* 177, 383–399. [https://doi.org/10.1016/S0045-7825\(98\)00389-2](https://doi.org/10.1016/S0045-7825(98)00389-2)
- Raous, M., Raous, M., Mécanique, R., Raous, M., 2011. Interface models coupling adhesion and friction To cite this version : HAL Id : hal-00647853 Interface models coupling adhesion and friction 333, 491–501.
- Rapoport, J., Aldea, C.-M., Shah, S.P., Ankenman, B., Karr, A., 2002. Permeability of Cracked Steel Fiber-Reinforced Concrete. *J. Mater. Civ. Eng.* 14, 355–358. [https://doi.org/10.1061/\(ASCE\)0899-1561\(2002\)14:4\(355\)](https://doi.org/10.1061/(ASCE)0899-1561(2002)14:4(355))
- Reinhardt, H.W., Blaauwendraad, J., Vos, E., 1984. Prediction of bond between steel and concrete by numerical analysis. *Matériaux Constr.* <https://doi.org/10.1007/BF02479089>
- Rice, J.R., 1968. A Path Independent Integral and the Approximate Analysis of Strain Concentration by Notches and Cracks. *J. Appl. Mech.* 35, 379–386.
- Rice, J.R., Wang, J.-S., 1989. Embrittlement of interfaces by solute segregation. *Mater. Sci. Eng. A* 107, 23–40. [https://doi.org/10.1016/0921-5093\(89\)90372-9](https://doi.org/10.1016/0921-5093(89)90372-9)
- RILEM T.C. 162-TDF, 2002. RILEM T.C. 162-TDF: Test and design methods for steel fibre reinforced concrete - Bending test - Final recommendations. *Mater. Struct.* 35, 579–582. <https://doi.org/10.1007/BF02483127>

- RILEM TC, 1983. RC 6 Bond test for reinforcement steel. 2. Pull-out test, 1983, in: RILEM (Ed.), RILEM Recommendations for the Testing and Use of Constructions Materials. E & FN SPON, pp. 218–220. <https://doi.org/10.1617/2351580117.081>
- Rizzuti, L., Bencardino, F., 2014. Effects of fibre volume fraction on the compressive and flexural experimental behaviour of SFRC. *Contemp. Eng. Sci.* 7, 379–390. <https://doi.org/10.12988/ces.2014.4218>
- Robins, P., Austin, S., Jones, P., 2002. Pull-out behaviour of hooked steel fibres. *Mater. Struct.* 35, 434–442. <https://doi.org/10.1007/BF02483148>
- Rots, J.G., 1989. Bond of reinforcement, in: *Fracture Mechanics of Concrete Structures: From Theory to Applications*. St. Edmund Press Ltd, Suffolk, pp. 245–262.
- Roylance, D., 2001. Introduction to Fracture Mechanics [WWW Document]. URL <http://web.mit.edu/course/3/3.11/www/modules/frac.pdf>
- RTI, 2013. Titanium Alloy Guide 43–74.
- Schwalbe, K.-H., Scheider, I., Cornec, A., 2013. Guidelines for Applying Cohesive Models to the Damage Behaviour of Engineering Materials and Structures, SpringerBriefs in Applied Sciences and Technology. Springer-Verlag Berlin Heidelberg. <https://doi.org/10.1007/978-3-642-29494-5>
- Seara-Paz, S., González-Fontebo, B., Eiras-López, J., Herrador, M.F., 2014. Bond behavior between steel reinforcement and recycled concrete. *Mater. Struct.* 47, 323–334. <https://doi.org/10.1617/s11527-013-0063-z>
- Serpieri, R., Alfano, G., 2011. Bond-slip analysis via a thermodynamically consistent interface model combining interlocking, damage and friction. *Int. J. Numer. Methods Eng.* 85, 164–186. <https://doi.org/10.1002/nme.2961>
- Serpieri, R., Alfano, G., Sacco, E., 2015a. A mixed-mode cohesive-zone model accounting for finite dilation and asperity degradation. *Int. J. Solids Struct.* 67–68, 102–115. <https://doi.org/10.1016/j.ijsolstr.2015.04.005>
- Serpieri, R., Sacco, E., Alfano, G., 2015b. A thermodynamically consistent derivation of a frictional-damage cohesive-zone model with different mode I and mode II fracture energies. *Eur. J. Mech. A/Solids* 49, 13–25. <https://doi.org/10.1016/j.euromechsol.2014.06.006>
- Serpieri, R., Varricchio, L., Sacco, E., Alfano, G., 2014. Bond-Slip Analysis via a Cohesive-Zone Model Simulating Damage, Friction and Interlocking. *Frat. ed Integrità Strutt.* 29, 284–292. <https://doi.org/10.3221/IGF-ESIS.29.24.284>
- Shafaei, Y., Shaikh, F.U.A., Sarker, P.K., 2017. Effect of the Fibre Geometry on Pull-out Behaviour of HVFA Mortar Containing Nanosilica. *Procedia Eng.* 171, 1535–1541. <https://doi.org/10.1016/j.proeng.2017.05.042>
- Shen, D., Shi, X., Zhang, H., Duan, X., Jiang, G., 2016. Experimental study of early-age bond behavior between high strength concrete and steel bars using a pull-out test. *Constr. Build. Mater.* 113, 653–663. <https://doi.org/10.1016/j.conbuildmat.2016.03.094>
- Shi, C., Wu, Z., Xiao, J., Wang, D., Huang, Z., Fang, Z., 2015. A review on ultra high performance concrete: Part I. Raw materials and mixture design. *Constr. Build. Mater.* 101, 741–751. <https://doi.org/10.1016/j.conbuildmat.2015.10.088>

- Shi, X., Xie, N., Fortune, K., Gong, J., 2012. Durability of steel reinforced concrete in chloride environments: An overview. *Constr. Build. Mater.* 30, 125–138. <https://doi.org/10.1016/j.conbuildmat.2011.12.038>
- Shih, C.F., 1981. Shih, Relationship between the J-integral and the COD for stationary and extending cracks. *J. Mech. Phys. Solids* 29, 305–326.
- Silva Filho, L.C.P., Vale Silva, B., Dal Bosco, V.I., Gomes, L.E.S., Barbosa, M.P., Lorrain, M., 2012. Analysis of the influence of rebar geometry variations on bonding strength in the pull-out test. *Bond Concr.* 2012 1–General, 63–68.
- Simo, J.C., Hughes, T.J.R., 1998. *Computational Inelasticity*. Berlin.
- Slater, E., Moni, M., Alam, M.S., 2012. Predicting the shear strength of steel fiber reinforced concrete beams. *Constr. Build. Mater.* 26, 423–436. <https://doi.org/10.1016/j.conbuildmat.2011.06.042>
- Soetens, T., Gysel, A. Van, Matthys, S., Taerwe, L., 2013. A semi-analytical model to predict the pull-out behaviour of inclined hooked-end steel fibres. *Constr. Build. Mater.* 43, 253–265. <https://doi.org/10.1016/j.conbuildmat.2013.01.034>
- Soetens, T., Matthys, S., 2012. Implementation of fibre pull-out behaviour in a finite element model for SFRC 941–946.
- Soh, C.K., Chiew, S.P., Dong, Y.X., 1999. Damage Model for Concrete-Steel Interface. *J. Eng. Mech.* 125, 979–983. [https://doi.org/https://doi.org/10.1061/\(ASCE\)0733-9399\(1999\)125:8\(979\)](https://doi.org/https://doi.org/10.1061/(ASCE)0733-9399(1999)125:8(979))
- Solgaard, A., Küter, A., Edvardsen, C., 2010. Durability Aspects of Steel Fibre Reinforced Concrete in Civil Infrastructure. 2nd Int. Symp. Serv. Life Des. Infrastructures 229–236.
- Sørensen, B.F., Lilholt, H., 2016. Fiber pull-out test and single fiber fragmentation test - Analysis and modelling. *IOP Conf. Ser. Mater. Sci. Eng.* 139. <https://doi.org/10.1088/1757-899X/139/1/012009>
- Söylev, T.A., Richardson, M.G., 2008. Corrosion inhibitors for steel in concrete: State-of-the-art report. *Constr. Build. Mater.* 22, 609–622. <https://doi.org/10.1016/j.conbuildmat.2006.10.013>
- Stang, H., Li, Z., Shah, S.P., 1990. Pullout Problem: Stress versus Fracture Mechanical Approach. *J. Eng. Mech.* 116, 2136–2150. [https://doi.org/10.1061/\(ASCE\)0733-9399\(1990\)116:10\(2136\)](https://doi.org/10.1061/(ASCE)0733-9399(1990)116:10(2136))
- Trad, A., Ghanem, H., Ismail, R., 2018. Bond Behaviour of Structural Lightweight Concrete Bond Behaviour of Structural Lightweight Concrete. <https://doi.org/10.1007/978-3-319-59471-2>
- Treece, R.A., Jirsa, J.O., 1989. Bond strength of epoxy-coated reinforcing bars. *ACI Mater. J.* 86, 167–174. <https://doi.org/10.14359/2341>
- Tvergaard, V., 1990. Effect of fibre debonding in a whisker-reinforced metal. *Mater. Sci. Eng. A* 125, 203–213. [https://doi.org/10.1016/0921-5093\(90\)90170-8](https://doi.org/10.1016/0921-5093(90)90170-8)
- Tvergaard, V., Hutchinson, J.W., 1992. The relation between crack growth resistance and fracture process parameters in elastic-plastic solids. *J. Mech. Phys. Solids* 40, 1377–1397. [https://doi.org/10.1016/0022-5096\(92\)90020-3](https://doi.org/10.1016/0022-5096(92)90020-3)

- Uchida, Y., Takeyama, T., Dei, T., 2010. Ultra high strength fiber reinforced concrete using aramid fiber. *Korea Concr. Inst.* 978–89.
- UNI EN 12390-3:2009, 2009. Prove sul calcestruzzo indurito - Parte 3: Resistenza alla compressione dei provini.
- UNI EN 12390-6:2010, 2010. Prove sul calcestruzzo indurito - Parte 6: Resistenza a trazione indiretta dei provini.
- UNI EN ISO 6892-1:2009, 2009. Prova di trazione - Parte 1: Metodo di prova a temperatura ambiente.
- Uomoto, T., Mutsuyoshi, H., Katsuki, F., Misra, S., 2002. Use of Fiber Reinforced Polymer Composites as Reinforcing Material for Concrete. *J. Mater. Civ. Eng.* 14, 191–209. [https://doi.org/10.1061/\(ASCE\)0899-1561\(2002\)14:3\(191\)](https://doi.org/10.1061/(ASCE)0899-1561(2002)14:3(191))
- Urbanski, M., Lapko, A., Garbacz, A., 2013. Investigation on concrete beams reinforced with basalt rebars as an effective alternative of conventional R/C structures. *Procedia Eng.* 57, 1183–1191. <https://doi.org/10.1016/j.proeng.2013.04.149>
- Van Gysel, A., 1999. A pull-out model for hooked end steel fibres, in: Reinhardt, H.W., Naaman, A.E. (Eds.), *Proceedings of the Third International Workshop on High Performance Fiber Reinforced Cement Composites (HPFRCC3)*, Proc. RILEM, PRO 6. RILEM Publications, Bagnaux, France, pp. 351–360.
- Venkateshwaran, A., Tan, K.H., Li, Y., 2018. Residual flexural strengths of steel fiber reinforced concrete with multiple hooked-end fibers. *Struct. Concr.* 19, 352–365. <https://doi.org/10.1002/suco.201700030>
- Verderame, G.M., Ricci, P., Carlo, G. De, Manfredi, G., 2009. Cyclic bond behaviour of plain bars . Part I: Experimental investigation. *Constr. Build. Mater.* 23, 3499–3511. <https://doi.org/10.1016/j.conbuildmat.2009.07.002>
- Vervuurt, A., Van Mier, J.G.M., 1995. Interface fracture in cement-based materials, in: Wittmann, F.H. (Ed.), *Proceedings FRAMCOS-2*. AEDIFICA TIO Publishers, Freiburg, pp. 295–304.
- Vetturini, R., 2014. Campanile del Complesso monumentale di S.Pietro in Perugia [WWW Document]. URL <https://divisare.com/projects/247982-riccardo-vetturini-campanile-del-complesso-monumentale-di-s-pietro-in-perugia>
- Virmani, Y.P., Clemena, G.G., 1998. Corrosion protection concrete bridges.
- Voyiadjis, Z., Kattan, P.I., 2008. A Comparative Study of Damage Variables in Continuum Damage Mechanics. *Int. J. Damage Mech.* 18, 315–340. <https://doi.org/https://doi.org/10.1177/1056789508097546>
- Wang, Y., Li, V.C., Backer, S., 1988. Modelling of fibre pull-out from a cement matrix. *Int. J. Cem. Compos. Light. Concr.* 10, 143–149. [https://doi.org/10.1016/0262-5075\(88\)90002-4](https://doi.org/10.1016/0262-5075(88)90002-4)
- Wille, K., Parra-Montesinos, G.J., 2012. Effect of beam size, casting method, and support conditions on flexural behavior of ultra-high-performance fiber-reinforced concrete. *ACI Mater. J.* 109.
- Xiao, J., Falkner, H., 2007. Bond behaviour between recycled aggregate concrete and steel rebars 21, 395–401. <https://doi.org/10.1016/j.conbuildmat.2005.08.008>

- Xu, X.P., Needleman, A., 1994. Numerical simulations of fast crack growth in brittle solids. *J. Mech. Phys. Solids* 42, 1397–1434. [https://doi.org/10.1016/0022-5096\(94\)90003-5](https://doi.org/10.1016/0022-5096(94)90003-5)
- Yankelevsky, D.Z., 1985. New Finite Element for Bond-Slip Analysis. *J. Struct. Eng.* 111. [https://doi.org/https://doi.org/10.1061/\(ASCE\)0733-9445\(1985\)111:7\(1533\)](https://doi.org/https://doi.org/10.1061/(ASCE)0733-9445(1985)111:7(1533))
- Yeih, W., Huang, R., Chang, J.J., Yang, C.C., 1997. Pullout test for determining interface properties between rebar and concrete. *Adv. Cem. Based Mater.* 5, 57–65. [https://doi.org/10.1016/S1065-7355\(96\)00004-1](https://doi.org/10.1016/S1065-7355(96)00004-1)
- Yeomans, S.R., 2013. Galvanized Steel Reinforcement in Concrete: An Overview Galvanized Steel Reinforcement in Concrete :
- Zacharda, V., Němeček, J., Štemberk, P., 2017. Micromechanical performance of interfacial transition zone in fiber-reinforced cement matrix. *IOP Conf. Ser. Mater. Sci. Eng.* 246. <https://doi.org/10.1088/1757-899X/246/1/012018>
- Zhang, H., Yu, R.C., 2016. Inclined fiber pullout from a cementitious matrix: A numerical study. *Materials (Basel)*. 9, 19–21. <https://doi.org/10.3390/ma9100800>
- Zhou, Y., Gencturk, B., Willam, K., Attar, A., 2014. Carbonation-Induced and Chloride-Induced Corrosion in Reinforced Concrete Structures Carbonation-Induced and Chloride-Induced Corrosion in Reinforced Concrete Structures. *Am. Soc. Civ. Eng.* 27, 17. [https://doi.org/10.1061/\(ASCE\)MT.1943-5533.0001209](https://doi.org/10.1061/(ASCE)MT.1943-5533.0001209).
- Zuo, J., Darwin, D., 2000. Splice strength of conventional and high relative rib area bars in normal and high-strength concrete. *ACI Struct. J.* 97, 630–641. <https://doi.org/10.14359/7428>